SANDIA REPORT

SAND2015-9432
Unlimited Release
Printed September 2015

Active Suppression of Drilling System Vibrations for Deep Drilling

David W. Raymond, Stephen Buerger, Avery Cashion,
Mikhail Mesh, William Radigan and Jiann-Cherng Su

Prepared by
Sandia National Laboratories
Albuquerque, New Mexico 87185 and Livermore, California 94550

Sandia National Laboratories is a multi-program laboratory managed and operated by Sandia Corporation, a wholly owned subsidiary of Lockheed Martin Corporation, for the U.S. Department of Energy's National Nuclear Security Administration under contract DE-AC04-94AL85000.

Issued by Sandia National Laboratories, operated for the United States Department of Energy by Sandia Corporation.

Available to DOE and DOE contractors from
U.S. Department of Energy
Office of Scientific and Technical Information
P.O. Box 62
Oak Ridge, TN 37831

Telephone: (865) 576-8401
Facsimile: (865) 576-5728
E-Mail: reports@osti.gov
Online ordering: http://www.osti.gov/scitech

Available to the public from
U.S. Department of Commerce
National Technical Information Service
5301 Shawnee Rd
Alexandria, VA 22312

Telephone: (800) 553-6847
Facsimile: (703) 605-6900
E-Mail: orders@ntis.gov
Online order: http://www.ntis.gov/search

SAND2015-9432
Unlimited Release
Printed September 2015

ACTIVE SUPPRESSION OF DRILLING SYSTEM VIBRATIONS FOR DEEP DRILLING

David W. Raymond, Avery Cashion and Jiann-Cherng Su
Geothermal Research Department

Stephen Buerger
Intelligent Systems Controls

Mikhail Mesh
Analytical Structural Dynamics

William Radigan
Radigan Engineering

Sandia National Laboratories
P.O. Box 5800
Albuquerque, New Mexico 87185-MS1033

Abstract

The dynamic stability of deep drillstrings is challenged by an inability to impart controllability with ever-changing conditions introduced by geology, depth, structural dynamic properties and operating conditions. A multi-organizational LDRD project team at Sandia National Laboratories successfully demonstrated advanced technologies for mitigating drillstring vibrations to improve the reliability of drilling systems used for construction of deep, high-value wells. Using computational modeling and dynamic substructuring techniques, the benefit of controllable actuators at discrete locations in the drillstring is determined. Prototype downhole tools were developed and evaluated in laboratory test fixtures simulating the structural dynamic response of a deep drillstring. A laboratory-based drilling applicability demonstration was conducted to demonstrate the benefit available from deployment of an autonomous, downhole tool with self-actuation capabilities in response to the dynamic response of the host drillstring. A concept is presented for a prototype drilling tool based upon the technical advances.

The technology described herein is the subject of U.S. Patent Application No. 62219481, entitled “DRILLING SYSTEM VIBRATION SUPPRESSION SYSTEMS AND METHODS,” filed September 16, 2015.

ACKNOWLEDGMENTS

This work was sponsored by the Department of Energy Laboratory Directed Research and Development program. Sandia National Laboratories is a multi-program laboratory operated and managed by Sandia Corporation, a wholly owned subsidiary of Lockheed Martin Corporation, for the U.S. Department of Energy's National Nuclear Security Administration under contract DE-AC04-94AL85000.

Sandia core values were exemplified by the individuals comprising the research and development team. The team was a diverse mix of capabilities in structural dynamic analysis; dynamics modeling and controls; electro-mechanical design, fabrication and assembly; and data acquisition, testing, and analysis. While the project was managed from within the Geothermal Research Department (06916), critical contributions were made from Robotics (06533), Engineering Sciences (01523), and laboratory-support contractors. The diversity of the project team enabled innovative discussions on the nature of drilling vibrations and preferred mitigation solutions.

The authors are indebted to the efforts of our Sandia colleagues for their engineering and laboratory contributions in making this work possible: Doug Blankenship, Keith Barrett, Tim Blada, David Chavira, Adam Foris, Jeff Greving, Mark Grubelich, Dennis King, Steve Knudsen, Steven Spencer, Jim Uhl, and Elton Wright.

CONTENTS

FIGURES

TABLES

This page intentionally left blank.

NOMENCLATURE

BHA	Bottom Hole Assembly
dB	decibel
DD	Detournay and Defourny (model)
DDS	Drilling Dynamics Simulator
DOE	Department of Energy
FEM	Finite Element Models
FRF	Frequency Response Function
FFT	Fast Fourier Transform
HPU	Hydraulic Power Unit
HRDF	Hard Rock Drilling Facility
LDRD	Laboratory Directed Research and Development
SMA	Shape Memory Alloys
SNL	Sandia National Laboratories
TMD	Tuned Mass Damper
VRS	Variable Rate Spring
VRSF	Variable Rate Spring Fixture
WOB	Weight On Bit

This page intentionally left blank.

1. INTRODUCTION

1.1. Executive Summary

Sandia
National Laboratories has been tasked with developing technology to improve the reliability of conventional drilling systems for construction of deep, high value wells. Disposal of high-level radioactive waste in large diameter boreholes in crystalline rock to depths of 16,400 ft. (5 km) is one possible example. Conventional drilling operations are troubled by vibrations throughout the drill stem that contribute to performance reductions, hardware failures, and increased drilling costs. Technology is needed to actively control drillstring vibrations to both enforce stability and reduce vibrations, thereby increasing the reliability of the overall well construction process.

With rotary drilling, one would like to apply prescribed forces to the bottom hole assembly to advance drilling. However, the reaction at the bit depends upon rock failure mechanisms and when compared to input forces applied at the surface, these reactive forces at the rock-bit interface create force imbalances that have the potential to introduce vibration into the drill stem. Compounding the problem, rock is heterogeneous and different rocks types have different failure rates. The dynamic stability of deep drillstrings is also challenged by an inability to impart controllability with ever-changing conditions introduced by depth, structural dynamic properties and operating conditions.

Sandia seeks to develop autonomous controllable modules that alter the physical dynamics of a drillstring in order to prevent or suppress damaging and inefficient structural vibrations. One way to mitigate vibrations is by controlling the elasticity or stiffness of the components composing the drill stem. Conceptually, instability (i.e., chatter) can be mitigated by prescribing the preferred dynamic response of components in the bottom hole assembly (BHA). A controllable system would allow the dynamic response of the overall drillstring to be tailored as desirable since the response of the overall system depends on many parameters including the properties of the components composing the drillstring (e.g., length, diameter, materials, etc.), the bit configuration, the rock properties and the operating conditions. Additionally, since communication between downhole tools and surface controls is challenging during drilling operations, the ideal system should be fully or semi-autonomous to allow accommodation of the breadth of conditions encountered. A controllable element is needed in the BHA that exhibits controllable stiffness to enforce dynamic stability for the overall drillstring. Sandia has developed a solution using an innovative application of smart materials to the drilling vibrations problem that allows modification of drillstring element structural stiffnesses to preferential values for suppression of drilling vibrations.

The technology developed has broad impact as it is applicable to the entire drilling sector. Current science and technology has not solved this problem due to telemetry limitations during drilling operations making field observation of the problem challenging; difficulty with laboratory simulation of the problem due to geometric limitations in the laboratory; and the challenge of developing controls/tools with autonomous features. The team employed an advanced computer-controlled drilling dynamic simulator within the resident Sandia Hard Rock Drilling Facility to simulate deep drillstrings in the laboratory to facilitate the technology

developments. Technical advances have been filed and intellectual property protection is being pursued.

1.2. Background and Application

A high-reliability drilling system is needed for construction of a deep borehole disposal system reaching depths of 16,400 ft. (5 km) in continental crystalline basement rock. Drillstring vibrations are one potential cause of trouble relative to deep hole drilling as they increase the technical risks and final costs of well construction. They are a constant issue in all drilling operations and cause increases in drilling trouble and damaged components, and decreases in the rate of penetration, and bit and tool life. While the drilling industry routinely attempts to deal with these problems using fixed-rate damping tools, the consequences are exacerbated when drilling deep wells due to increased drillstring flexibility and greater times to replace worn or damaged components. Vibrations are particularly problematic in high strength rock where the risk of tool failure increases dramatically. Drillstring stabilization is imperative for improved reliability and drilling performance.

Drilling vibrations have been observed at the bit using downhole measurement tools on the longitudinal, rotational and lateral axes. Longitudinal vibrations can cause bit bouncing that can result in severe impact loading on the bit cutting structure. Likewise, severe rotational vibrations can include stick-slip wherein the rotary motion of the bit is completely stopped as the drillstring winds up. The drill bit service industry has developed whirl-resistant bit designs and balanced cutting structures to mitigate whirling and severe lateral vibration. Yet the coupling between the bit cutting structure and the dynamic response of the drillstring cannot be ignored. To accurately reflect reality, vibration modes should be considered on all axes. However, for the purposes of this work, the scope is limited to the representation of the axial mode of the drillstring. Coupling between the axial and rotational degrees of freedom is given due consideration.

Well construction for the Deep Borehole Disposal Program is a similar application to drilling large diameter wellbores for geothermal wellbore construction [Ref. 25]. Since conventional drilling operations are troubled by vibrations that result in well construction cost increases, improved reliability is needed to improve the performance of deep drilling operations in hard rock. Since identification and development of a valid radioactive waste disposal concept is of vital interest to the United States Department of Energy and the mission of Sandia National Laboratories - the Laboratory Directed Research and Development (LDRD) office funded the work herein to develop advanced technology to improve the reliability of deep drilling operations. As an LDRD-funded project, the team remained focused upon the needs of the Deep Borehole Disposal Program while addressing the problem of drilling vibrations encountered by the drilling industry at large.

1.3. The Drilling Vibrations Problem

1.3.1. Problem Statement

Drillstring vibrations are a leading cause of non-productive time in the drilling industry. Isolation can be used to change the transmissibility of forces into the drillstring. Similarly, it is generally

understood that instability due to self-excitation can result if modes of vibration exist within the operating range. The instability problem is summarized in Figure 1-1 cutter forces at the rock-bit interface are modulated by the dynamic response of the bit producing a variable cutting force that self-excites the modes of vibration of the drillstring, G.

Conditions observed up-hole can be radically different than what actually occurs downhole. While variations in operating conditions are available to change vibration levels, the preferred operating conditions are not always obvious due to the inconsistency between up-hole observations and downhole conditions. This problem is compounded by an inability to timely adjust operating conditions in response to deleterious conditions. The approach herein is to introduce variable compliance in the Bottom Hole Assembly (BHA) to achieve the preferred dynamic response of the drillstring. Given the challenges of drillstring telemetry, it must be accomplished autonomously without operator intervention. A computational model of the drillstring is needed to provide a detailed understanding of the dynamic response. The influence of variable compliance can then be evaluated.

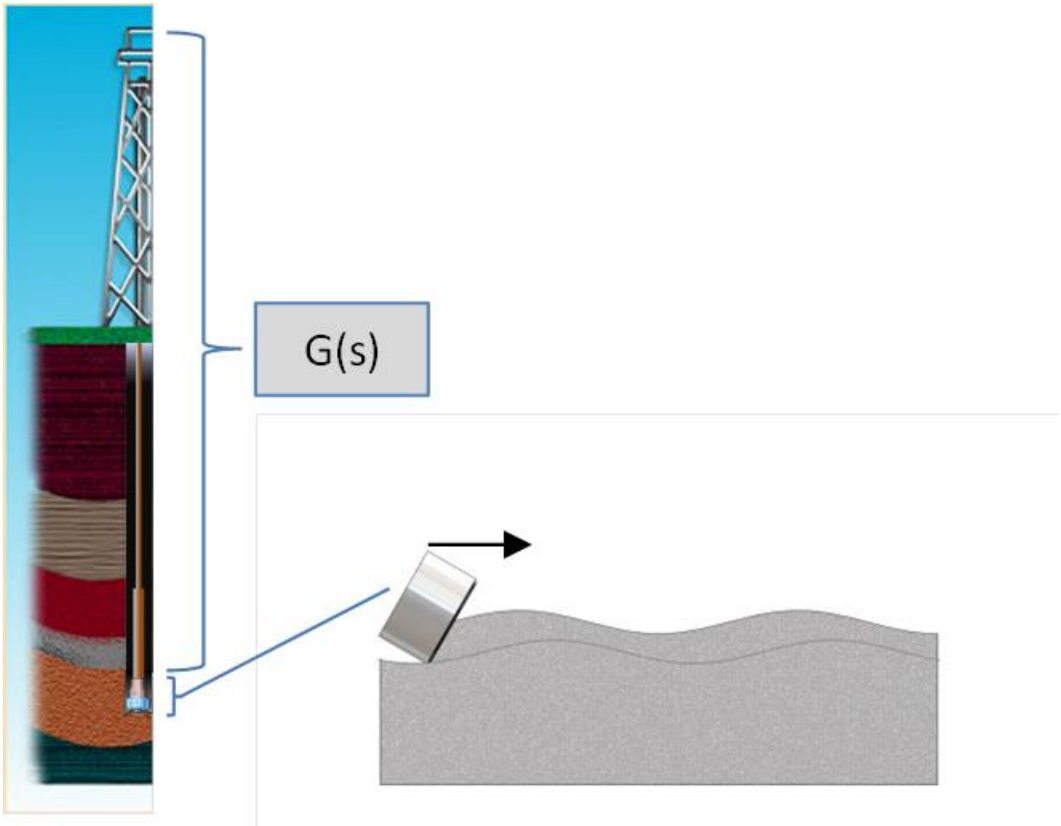

Figure 1-1. Drilling instability produced by periodic cutter forces self-exciting drillstring modes of vibration.

1.3.2. Explanation/Theory of Instability

As mentioned above, drilling operations, like many material removing processes, can become subject to unstable self-excited vibration. A theory of instability in machining developed by

J. Tlusty is presented in [Ref. 16] and its application to the drilling vibration problem is described in [Ref. 3].

One of the key points of the paper is derivation of the force acting on the drill bit. That force is described by the following equation [Ref. 16]:

$$F(t) = 1.5dK_r[c - u(t) + u(t-\tau)] \qquad \text{(Eq. 1-1)}$$

Considering a single degree-of-freedom system excited by such a force, the equation of motion is (after eliminating constant term):

$$m\ddot{x} + \beta\dot{x} + K_d x = 1.5dK_r[-x(t) + x(t-\tau)] \qquad \text{(Eq. 1-2)}$$

where m is the mass of the drill bit, β – damping in the system, K_d – stiffness of the drill string, K_r – a constant dependent on the rock properties and drilling parameters and d – drill bit diameter. Equations of this type have been studied extensively and detailed analysis is available, for example, in [17]. Solution of this equation is sought in the form $Ae^{\sigma t}$ which leads to the following characteristic equation:

$$m\sigma^2 + \beta\sigma + (K_d + 1.5dK_r) + 1.5dK_r e^{-\tau} = 0 \qquad \text{(Eq. 1-3)}$$

(Eq. 1-3 is transcendental equation and may have infinite number of complex roots. Stability of the solution is determined by the real part of the roots. Negative real part results in stable solution, positive - in unstable, while purely imaginary roots correspond to stable oscillatory solution. This situation is similar to the stability of conventional linear systems except that in case of systems with delay, the number of roots may be infinite. This similarity means that some of the traditional methods of the stability analysis of linear systems can be applied to the systems with delay.

There are also important differences. Free term in the (Eq. 1-3 depends on both rock constant and drill string stiffness. As a result, frequency of the self-excited drill string vibration also depends on both parameters. This effect was observed experimentally in laboratory conditions.

1.3.2.1.1. The Limit of Stability

Direct analysis of the characteristic equation of the multi degree-of-freedom system is difficult because of the transcendental nature of the equation. At the same time, frequency – based methods of the stability analysis are still applicable. Drill string with the excitation force described by (Eq. 1-1 can be represented as a system with feedback and delay in the feedback loop as follows:

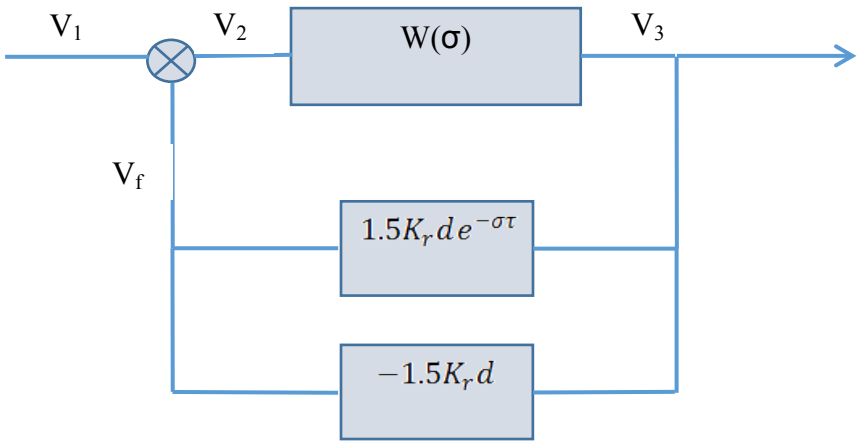

Figure 1-2. Drillstring equivalent feedback loop system.

Here W(σ) is transfer function of the drillstring itself. Following block diagram and symbolic variables V_i

$$V_f = 1.5dK_rV_3(1 - 1.5K_r de^{-\sigma\tau})$$
$$V_3 = W(\sigma)V_2$$
$$V_2 = V_1 - V_f$$

and transfer function of the system with the feedback is

$$\frac{V_3}{V_1} = \frac{W(\sigma)}{1+1.5dK_rW(\sigma)(1-e^{-\sigma\tau})} \qquad \text{(Eq. 1-4)}$$

Usual frequency-based stability criteria (Nyquist, Mikhailov) can now be applied to study stability of the drill string vibration, but using them to calculate stability zone boundaries in the parameter space can be cumbersome. Direct analysis of the transfer function turns is more efficient for that purpose.Drillstring will become unstable when denominator of (Eq. 1-4 is equal to zero, or the following is true:

$$Re[1.5dK_rW(\sigma)(1 - e^{-\sigma\tau})] = -1$$
$$Im[1.5dK_rW(\sigma)(1 - e^{-\sigma\tau})] = 0$$

Let's introduce $W_R = Re[W(\sigma)]$ and $W_I = Im[W(\sigma)]$. We are interested in the limit case of the stationary vibration which corresponds to pure imaginary $\sigma = j\omega$. If $\sigma = p + j\omega$ is complex, then vibration is going to be decreasing or increasing depending on sign of p. For purely imaginary $\sigma = j\omega$

$$W_R - W_R\cos\omega\tau - W_I\sin\omega\tau = \frac{-1}{1.5dK_r}$$
$$W_I - W_I\cos\omega\tau + W_R\sin\omega\tau = 0$$

or

$$W_R(1-\cos\omega\tau) - W_I\sin\omega\tau = \frac{-1}{1.5dK_r}$$
$$W_I(1-\cos\omega\tau) + W_R\sin\omega\tau = 0$$

or by reducing trigonometric function to half-angle

$$2W_R\sin^2\frac{\omega\tau}{2} - 2W_I\sin\frac{\omega\tau}{2}\cos\frac{\omega\tau}{2} = \frac{-1}{1.5dK_r}$$
$$W_I\sin^2\frac{\omega\tau}{2} = -W_R\sin\frac{\omega\tau}{2}\cos\frac{\omega\tau}{2}$$

leads to

$$2W_R\sin^2\frac{\omega\tau}{2} + 2W_R\cos^2\frac{\omega\tau}{2} = \frac{-1}{1.5dK_r}$$
$$W_I\sin\frac{\omega\tau}{2} = -W_R\cos\frac{\omega\tau}{2}$$

and finally

$$Re(W(s)) = W_R = \frac{-1}{3dK_r}$$

or

$$d_{\lim} = \frac{-1}{3K_r Re(W(s))} \qquad \text{(Eq. 1-5)}$$

While the same result was obtained in [Ref. 3],our derivation is simple and straightforward and does not require any qualitative reasoning.

1.4. State of the Art in Drilling Vibration Management

The drilling industry invests considerable resources in design and specification of the bottom hole assembly for deep drilling operations. The BHA includes a variety of components including the drill bit, stabilizers, potentially a directional drilling assembly including a downhole motor, possibly a measurements tool, and drill collars. Drill bit designs are tailored for the rock types they are intended to penetrate. Polycrystalline Diamond Compact (PDC) bits are often specifically custom designed for the formations they are intended to drill. These bits are enhanced with features including dual rows of cutters, impact arrestors, and components to control depth of cut to prevent over-torqueing the drillstring during operation. The service companies have advanced software prediction capabilities that balance the forces across the bit face to reduce the tendencies of the bit to induce modes of vibration, including axial bit bounce, torsional vibrations including stick-slip, and whirl.

Additionally, drill bit service companies provide analysis services to energy companies and operators to predict the dynamic response of the bottom hole assembly subject to operating conditions and wellbore trajectories. These computational predictions are based, in part, upon data from extensive laboratory testing that enable a detailed understanding of the interaction between the bit and the rock. These analysis services enable the drilling operators to anticipate

problematic conditions (i.e., predict drillstring dynamics) that may be encountered during the course of drilling a particular interval throughout the well construction process.

Shock subs may be emplaced in the BHA as well to protect the BHA and measurement tools from shock and vibration encountered during drilling. However, these shock subs typically have a fixed spring constant and damping characteristic and cannot be changed once the BHA is tripped into the hole. Furthermore, given the telemetry challenge of jointed pipe operations, very little control operations are available to change the dynamic response of the BHA once it is tripped into the hole. Since tripping in and out of the hole results in non-productive time, it can be a major contributor to drilling costs. Consequently, the drilling industry has few options to improve drilling dynamics once the bottom hole assembly is tripped into the wellbore. Some service companies have developed advanced devices to mitigate downhole vibrations [Ref. 27] to prevent overloading the bit during drilling dysfunctions. However, many of these devices are passive and real-time control of the dynamics of the downhole assembly is not available.

The drilling industry also uses monitoring of surface drilling parameters as a valid means to reduce downhole vibrations. The reliability of this approach may be compromised as drilling progresses to great depths as the drillstring acts as a filter in transmitting dynamic forces as the drillstring lengthens. The inability to precisely monitor and control the downhole environment suggests that technology can be improved by introducing an autonomous solution that adapts as needed for downhole conditions.

1.5. Technical Approach

The phenomena of drillstring vibrations and their effect on drilling performance have been the subject of extensive analytical and field investigation for almost 50 years. The approach emanating from this LDRD project team presents an innovative solution: modify the properties of the drilling system autonomously using controls and smart material enabled actuators in response to measurement of downhole vibrations that cannot be detected timely or adequately from the surface.

Various concepts have been conceived to mitigate vibrations within the drilling system using controllable springs, adaptive structures, and smart materials. This fundamentally requires the ability to analyze the dynamics of a system consisting of an unmodified drillstring and one or more controllable modules, inserted at some location(s) within the drillstring, in numerous different states. However, the dynamics of long drillstrings are complicated and require high fidelity finite element models to be fully accounted for. It is impractical to explore and iterate multi-state designs and control strategies purely in a finite element design space. Therefore it is desirable to independently represent the dynamics of several subsystems (e.g. drillstring elements and controllable modules) and to then combine them in a simple way to enable streamlined analysis of the composite system dynamics. A branch of system dynamic theory known as *substructuring* provides a means of doing this.

Dynamic substructuring allows subsystems, represented with frequency response functions (FRFs), to be combined into composite systems, producing FRFs for the composite systems. Using the FRFs resulting from computational models, a procedure has been demonstrated for

finite element and modal models of a drillstring in a port function-based simulation that allows for re-assembly of dynamic substructures for rapid and iterative exploration of actuator alternatives. This approach also represents the system dynamics in a format suitable for the application of control theory and methods to enable the design of automatic module controllers. The method is demonstrated on a representation of a 2200 m (7200 ft.) drillstring common in the literature and validated in the laboratory using simplified spring-mass systems. The project team developed computational models to understand the details of drillstring dynamics. These models were substructured to investigate the benefit of actuator mechanics at distributed locations throughout the drill stem. Various actuator options were surveyed, evaluated, and prototyped for deployment and specification within the drillstring.

Various prototype controllable tool concept/mitigation strategies were considered including controllable stiffness in the BHA via a selective spring stack, shape memory alloy (SMA) springs, and liquid springs. Damping is also desirable in the bottom hole assembly to mitigate vibrations; Sandia has previously developed controllable damping concepts for BHA deployment using magnetorheological (MR) fluids. This intellectual property has already been licensed by Sandia National Laboratories to APS Technologies who currently markets a downhole tool based upon the concept. Application of MR fluids is considered herein for inclusion in a downhole variable spring rate tool to enhance overall drillstring stability yet they are not the primary focus of this work. Other concepts evaluated include Tuned Vibration Absorbers (TVA) to absorb vibration and Inertial Exciters (IE) in the bottom hole assembly to actively cancel vibration. While the focus is on the introduction of these technologies to the BHA, the substructuring approach allows them to be considered for application to other areas of the drillstring as well to form an integrated approach to drillstring vibration management.

Test fixtures were developed that allowed the application space to be addressed. Prototype models were developed and tested that allowed proof-of-concept demonstrations and evaluation of critical effects governing performance. A drilling applicability demonstration provided proof of the benefits available. These activities will support eventual development of prototype downhole tools based upon demonstrated proofs of concept.

The LDRD project team worked diligently to understand the nature of the drilling vibrations problem via literature reviews, participation in academic and industry colloquia, interacting with energy services industry representatives, development of simple to complex drillstring models, reviewing complex rock-bit interaction theories, and reproducing and observing drilling vibrations within the laboratory. The team applied creativity by addressing alternative solutions to vibration suppression while maintaining focus on the committed deliverables of the internally-funded project. Working synergistically, the team achieved several milestones during the three-year LDRD-funded project including a proof-of-concept demonstration of the benefits available by deployment of vibration suppression tools within the drillstring in year one, a critical function evaluation of the technology parameter space in year two, and a laboratory-based drilling applicability demonstration in year three.

1.6. Scope and Organization

This report is subdivided into sections that summarize major work areas throughout the LDRD project. Chapter 2 addresses drillstring modeling and substructuring methods to evaluate physical dynamics governing the response of deep drillstrings and the dynamic influence that can be achieved by introduction of controllable actuators. Chapter 3 addresses drilling process modeling and simulations of instability using rock-bit interaction models and representative drillstring properties derived in the computational modeling effort. Chapter 4 includes a summary of hardware demonstrations to conduct proof-of-concept demonstrations of prototype downhole tools and demonstrate their performance in mitigating drillstring vibrations in physical structures that were constructed to emulate critical and characteristic properties of vibrating drillstrings. Chapter 5 includes results of actual laboratory drilling simulations using state of the art PDC bits with a deep drilling simulation in Sandia's Hard rock Drilling Facility. Chapter 6 outlines an approach to development of a downhole Variable Rate Spring prototyped using the advanced concepts developed in this study. This concept makes use of a demonstrated design concept, advanced processing techniques for determining the dynamic characteristics of host drillstrings, and a conceptual control system for the tool. Chapter 7 is a summary of lessons learned during the course of this work and recommendations for additional research.

This page intentionally left blank.

2. DRILLSTRING MODELING

2.1. Drillstring Substructuring

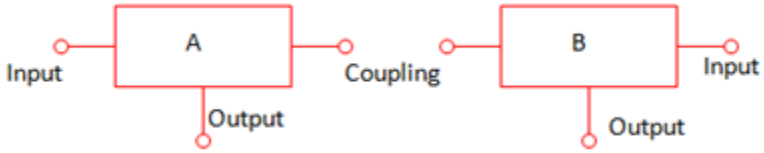

Figure 2-1. Schematic of two subsystems representing coupled dynamic systems.

By applying dynamic substructuring, a dynamic system composed of several individually quantified subsystems may be analyzed by systematically combining the subsystem models. For example, subsystems A and B, shown in Figure 2-1., each have one or more locations where input forces are applied, one or more locations where output is measured (in any form: force, displacement, velocity, etc.), and one or more locations where the subsystem can be coupled to other subsystems. Each can be represented by a matrix frequency response function (FRF) that relates inputs to outputs across frequency. For example, the matrix function H_A in (Eq. 2-1) relates input forces applied to subsystem A at the "Input" (F_{Ai}) and "Coupling" (F_{Ac}) locations to generic outputs at the "Output" (d_{Ao}) and "Coupling" (d_{Ac}) locations:

$$\begin{bmatrix} d_{Ao} \\ d_{Ac} \end{bmatrix} = \begin{bmatrix} H_{Ao,Ai} & H_{Ao,Ac} \\ H_{Ac,Ai} & H_{Ac,Ac} \end{bmatrix} \begin{bmatrix} F_{Ai} \\ F_{Ac} \end{bmatrix} \qquad \text{(Eq. 2-1)}$$

Subsystem B can be represented with an analogous expression. The subsystems are combined by connecting them at the coupling location according to two boundary conditions, *compatibility* and *equilibrium*. Compatibility requires that the displacement at the coupling points on both subsystems is the same:

$$d_{Ac} = d_{Bc} \qquad \text{(Eq. 2-2)}$$

Equilibrium requires that forces are equal and opposite at the coupling point:

$$F_{Ac} + F_{Bc} = 0 \qquad \text{(Eq. 2-3)}$$

This expresses Newton's second law at the interface. When subsystems A and B are so connected, their composite dynamics can be represented using a combination of the matrix functions H_A and H_B. The resulting expression and its derivation proceed from a method outlined in de Klerk, Rixen & Voormeeren, 2008 [Ref 1]. Thus the subsystems may each be represented in a compact form using FRFs while the ability to combine the systems and analyze their composite dynamics is retained.

2.1.1. Impedance and Admittance Representations

Mechanical impedance and its inverse, *mechanical admittance*, offer FRF representations of systems and subsystems with advantageous properties. Impedance and admittance characterize the static and dynamic behavior of a system as it appears at a single spatial location or *port of interaction*. Impedance is defined as the force produced in response to an imposed velocity at a port, and may be linear or nonlinear, time varying or invariant. Admittance is the velocity in response to an imposed force. Both are defined in terms of power conjugate variables (force times velocity equals power), which, unlike block diagram analysis, enables analytical methods that are not impacted by the instantaneous direction of energy flow and that seamlessly handle connection of multiple subsystems without the need to consider impedance matching or subsystems loading one another. In this formulation, coupled dynamic systems may be understood and manipulated on the basis of their apparent dynamics at a particular point, regardless of what physical or control elements actually create those dynamics. This formulation is well-suited to the drillstring problem, which can be formulated as a set of dynamic systems coupled in series. Each subsystem is only exposed to those properties of neighboring subsystems that are represented by its behavior at the ports of interaction where the subsystems are connected, defined by its *port function*. This approach potentially enables application of an extensive literature on impedance control [Ref 2] to the problem of developing control algorithms for the controllable module.

When a subsystem interacts with other subsystems (or the environment "outside" the system) through more than one port of interaction, it has multiple inputs and multiple outputs and therefore its port function is a matrix. In the case of the drillstring, most subsystems are modeled as two-port matrix functions, because they interact with a lower portion of the drillstring on one end, and a higher portion of the drillstring on the other end. An example of a two-port impedance function is shown below:

$$\begin{bmatrix} F_1 \\ F_2 \end{bmatrix} = \begin{bmatrix} Z_{11} & Z_{12} \\ Z_{21} & Z_{22} \end{bmatrix} \begin{bmatrix} \dot{x}_1 \\ \dot{x}_2 \end{bmatrix} \qquad \text{(Eq. 2-4)}$$

This representation is a special case of a dynamic subsystem analogous to equation (1), where in this case the inputs are velocities at two different locations and the outputs are forces at those same locations. When two subsystems defined by port functions are connected at their ports of interaction, *causality* must be complementary, meaning that one subsystem must be represented with an impedance function and the other with an admittance function. This ensures that the "output" of a subsystem (e.g. force if the system is represented with an impedance function) is equivalent to the "input" of a connected subsystem (force is an input to an admittance function). Thus when a series of two-port elements are connected in series, as for the drillstring model, the subsystem representations must alternate in causality between impedance and admittance functions.

2.1.2. Drillstring Split Model Formulation

To represent a drillstring with a controllable module or "actuator" inserted at an arbitrary location, we use the general model formulation shown in Figure 2-2. A drillstring model is split into the subsystems G1 and G2. The bottom of G1 terminates at the point where the bit contacts

the rock, while the top of G2 terminates at the drilling rig on the surface. The top of G1 and the bottom of G2 terminate at opposite ends of the actuator module A.

A drillstring may be modeled as a serial collection of compliant and inertial elements. In the topology of Figure 2-2, G1 and G2 may each be such a collection of elements. The actuator model might include a wide variety of dynamics intended to reduce or eliminate structural vibrations. Applying impedance substructuring methods, each of the subsystems G1, G2 and A may comprise arbitrarily complex dynamic models without increasing the dimensionality of the system. This may be seen by examining the port functions for each of the subsystems. One formulation for the port functions of G2, A, and G1, respectively, is as follows:

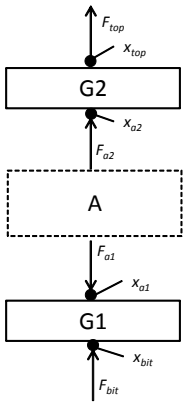

Figure 2-2. Representation of Substructured Drillstring with integral actuator A.

$$\begin{bmatrix} \dot{x}_{top} \\ \dot{x}_{a2} \end{bmatrix} = \begin{bmatrix} Y_{G2\_11} & Y_{G2\_12} \\ Y_{G2\_21} & Y_{G2\_22} \end{bmatrix} \begin{bmatrix} F_{top} \\ F_{a2} \end{bmatrix}$$

$$\begin{bmatrix} F_{a1} \\ F_{a2} \end{bmatrix} = \begin{bmatrix} Z_{A\_11} & Z_{A\_12} \\ Z_{A\_21} & Z_{A\_22} \end{bmatrix} \begin{bmatrix} \dot{x}_{a1} \\ \dot{x}_{a2} \end{bmatrix} \qquad \text{(Eq. 2-5)}$$

$$\begin{bmatrix} \dot{x}_{bit} \\ \dot{x}_{a1} \end{bmatrix} = \begin{bmatrix} Y_{G1\_11} & Y_{G1\_12} \\ Y_{G1\_21} & Y_{G1\_22} \end{bmatrix} \begin{bmatrix} F_{bit} \\ F_{a1} \end{bmatrix}$$

In equation (Eq. 2-5) causality constraints are satisfied by representing G1 and G2 with admittance functions, and A with an impedance function (the opposite formulation would also satisfy causality). All of the Y_{G1} and Y_{G2} terms can be derived from a finite element model and together provide a model of a drillstring. Each term is a function of frequency (e.g. of the Laplace variable), and may in principle be arbitrarily complex. Thus increasing the dynamic order of G1 or G2 does not increase the dimensionality of the model at the interfaces; it does however increase the order of these terms. The actuator impedance terms Z_A are defined based on design dynamics for the actuator module, for example a variable rate spring.

With representations for each of the three subsystems per equation (Eq. 2-5), a composite system representation may be formed. This is shown in Figure 2-3. and can be implemented and simulated directly as drawn using Simulink (The MathWorks). The Z and Y blocks in Figure 2-3. are simply filled in with the terms from equation (Eq. 2-5). When the subsystems are connected, the resulting composite system represents the entire drillstring and interfaces to the outside world only through the up-hole and downhole ends of the drillstring. Mathematically, the composite system is a two-input, two-output admittance port function defined by the following equation:

$$\begin{bmatrix} \dot{x}_{top} \\ \dot{x}_{bit} \end{bmatrix} = \begin{bmatrix} Y_{S\_tt} & Y_{S\_tb} \\ Y_{S\_bt} & Y_{S\_bb} \end{bmatrix} \begin{bmatrix} F_{top} \\ F_{bit} \end{bmatrix} \quad \text{(Eq. 2-6)}$$

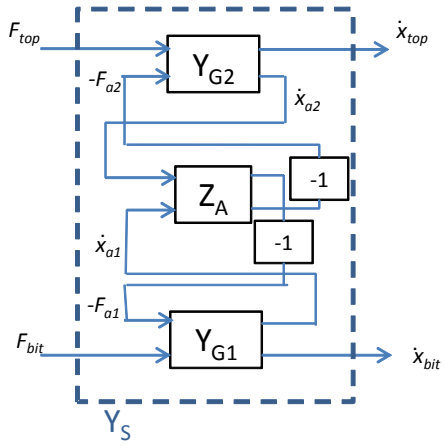

Figure 2-3. Coupled system with G1, A and G2 subsystems represented by admittance and impedance port functions.

This formulation provides a straightforward means of representing drillstring dynamics extracted from a finite element simulation in simple matrix functions so that they can be combined with many different actuator dynamics and simulated much more rapidly than either running repeated complete finite element analyses or deriving new closed-form equations for each new dynamic configuration. The port function that represents the actuator dynamics, Z_A, may readily be replaced with alternative dynamics without changing the other system blocks. For any given actuator location, the finite element analysis need only be run once to generate the port functions for G1 and G2. This formulation is also useful for application of control algorithms. The actuator dynamics may be treated as variable control dynamics, and conventional block diagram-based control methods may be applied to the system as represented in Figure 2-3.. Impedance control methods may be used to sculpt the actuator dynamics to balance performance and vibration suppression.

2.1.3. Actuator System models

While the drillstring (G1 and G2) model port function elements are derived from finite element models, the actuator must also be modeled with a two-port function. The structure of this function depends on the dynamic structure of the actuator. In some cases, certain subsystems may not be able to be represented in one causality or the other. This might produce infinite matrix function terms, or could simply cause simulation problems by creating improper transfer functions (in port functions, physically realistic systems might have improper transfer function representations). In these cases, it is generally possible to either switch causality of all elements in a system to make the system work, or to change the causality of subsystem models by adding elements such as extremely stiff springs in series that do not change the relevant dynamic modes but that do make alternate causalities feasible.

2.1.4. Parallel Spring and Damper

The actuator structure of greatest interest is a linear spring with parallel linear damping. If the spring has stiffness k_a and the damper has damping coefficient c_a, the Laplace-domain two-port function in impedance causality is as follows (where s is the Laplace variable):

$$\begin{bmatrix} F_{a1} \\ F_{a2} \end{bmatrix} = \begin{bmatrix} \frac{c_a s + k_a}{s} & -\left(\frac{c_a s + k_a}{s}\right) \\ -\left(\frac{c_a s + k_a}{s}\right) & \frac{c_a s + k_a}{s} \end{bmatrix} \begin{bmatrix} sX_{a1} \\ sX_{a2} \end{bmatrix} \quad \text{(Eq. 2-7)}$$

2.1.5. Tuned Damper

A tuned vibration absorber includes a parallel mass that is outside the main load chain and couples to the drillstring through a spring. This is shown in Figure 2-4.. A two-port impedance function in the Laplace domain for the tuned vibration absorber in Figure 2-4. would be a 2x2 matrix in which each term equals:

$$m_p s + \frac{k_e}{s} - \frac{k_e^2}{m_e + k_e s} \quad \text{(Eq. 2-8)}$$

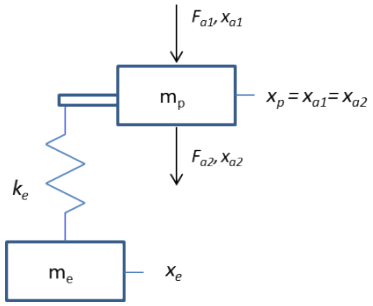

Figure 2-4. Tuned vibration absorber.

2.1.6. Active Cancellation (using Inertial Excitation)

An inertial exciter is very similar to the model shown in Figure 2-4., except that the spring k_e would be replaced with an actuator force source $F_e(t)$.

We turn now to the development of the drillstring model.

2.2. Drillstring Computational Modeling

2.2.1. Model Simulations

2.2.1.1. Tlusty Drillstring

A drillstring model that is common in the literature [Ref. 3] is a normal modes characterization of a drillstring comprised of 7200 ft. (2200 m) of 4-1/2 in. (11.4 cm) diameter drill pipe and 780 ft. (240 m) of 6-1/2 inch (16.5 cm) diameter drill collar - herein referred to as the "Tlusty Drillstring." The properties of the rig supporting this drillstring are also modeled at the top of the drillstring. The normal modes model was prepared by discretizing this system into a series of spring mass elements. The traveling block, swivel, and kelly are represented by a mass of 22600 lb. (10250 kg), and the draw works cable with spring stiffness of 52500 lb./in. (9.2 E6 N/m). The 7200 ft. (2200 m) drill pipe section is modeled using 19 lumped mass components with a mass of 5600 lb. (2500 kg) and stiffness of 28000 lb./in. (4.9 E6 N/m). The interface between the drill pipe and drill collar is modeled using a mass of 7720 lb. (3500 kg) and stiffness of 28000 lb./in. (4.9 E6 N/m). The drill collar section is modeled using 7 lumped mass components with a mass of 9800 lb. (4400 kg) each and stiffness of 700000 lb./in. (122 E6 N/m).

Modal damping is used to apply uniform damping throughout the model. The assumption of proportional damping is commonly used in structural applications and facilitates diagonalization of the system of equations. It is also standard in many commercial finite element modal analysis software programs.

This structural dynamics model has been reproduced using a discretization of the spring mass system into a normal modes model in MATLAB. Additionally, the finite element model for the bar-element formulation was implemented in a custom MATLAB script and the MSC Nastran commercial software package was executed for validation. A finite element model using several versions of the MSC Nastran beam elements (CBEAM, CBAR, CTUBE) was created with 110 equal length elements for the drillstring and 12 elements for the drill collar; the type of elements used did not have any influence on predicted results. The bar-element model was configured in MATLAB with a variable number of elements. Both FEM models were used to calculate normal modes and frequency response functions at various points on the structure due to the excitation applied at the drill bit and substructuring locations. Both modeling approaches were validated by comparing to each other and by comparing to the earlier published data [Ref. 4]. Eigenfrequencies and response produced by both models are identical.

The bar element model more readily accommodates length variations and spatial discretization and is used for further evaluations. The frequency response function computed using both the spring-mass and bar element approaches is shown in Figure 2-5 and provides sufficient evidence that both the MSC Nastran model and MATLAB FEM implementation are validated and can be used for further analysis. Dareing et al. [Ref.3] indicates the response of this system is dominated by six modes and demonstrates that changes to a drillstring that result in shifting modes to have positive real transfer function values prevent the development of self-excitation by these modes. Figure 2-6 demonstrates that a particular value of a spring in the BHA (5E6 N/m in this example) can be used to modulate the transfer function of the overall drillstring.

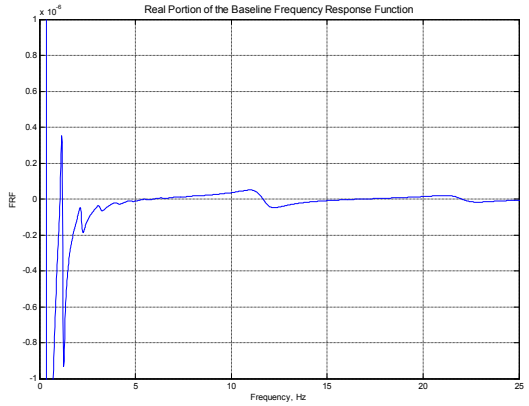

Figure 2-5. Transfer function computed in MATLAB agrees with publication.

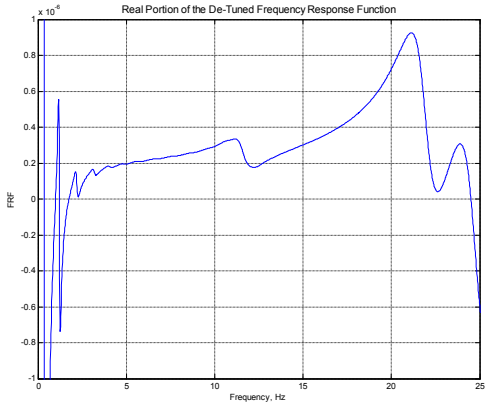

Figure 2-6. Detuned Frequency Response Function.

2.2.1.1.1. Analysis of the 7200 ft. Drill String.

Analysis efforts were concentrated initially on the 7200 ft. (2200 m) drill string system described in [Ref. 3] because of the wealth of the published data and experience gained from this reference. Methodologies used for simulation are not model specific and can be easily applied to other drill strings. Based on description provided in [Ref. 3], parameters of the 7200 ft. (2200 m) drill string were assumed as follows:

Drill pipe OD	0.374 ft. (0.114 m)
Drill pipe length	7200 ft. (2200 m)
Drill pipe sections	19
Drill pipe section mass	5633 lb. (2555 kg)
Drill pipe section stiffness	3.38×10^5 lb./ft. (4.94×10^6 N/m)
Drill collars OD	0.541 ft. (0.165 m)
Drill collars length	780 ft. (240 m)
Drill collar sections	7
Drill collar section mass	9848 lb. (4467 kg)
Drill collar section stiffness	8.50×10^6 lb./ft. (1.24×10^8 N/m)
Drill collar to Drill pipe interface	
Mass	7740 lb. (3511 kg)
Stiffness	3.38×10^5 lb./ft. (4.94×10^6 N/m)
Traveling block, swivel, kelly mass	22681 lb. (10288 kg)
Draw works stiffness	6.3×10^5 lb./ft. (9.2×10^6 N/m)

Data provided in [Ref. 3] does not explicitly define important parameters such as drill pipe and drill collar wall thickness, nor does it explicitly state what material the pipes were made of. A natural assumption is that it was steel with standard steel properties. It turns out that it is impossible to match exactly the properties described above assuming pipes of round section,

constant thickness along the length of the pipes and steel properties. While the most likely reason for that is variation of the shape of the pipes near the tool joint interface, it was easier to accommodate that by slightly adjusting material properties for both drill collar and drill string while maintaining mass and stiffness parameters. It is also necessary to have actual dimensions because the lump parameter model used in the paper is replaced by a finite element model with much finer discretization and the calculation of the element stiffness and mass matrix requires complete knowledge of the material properties and geometry.

To find the best possible approximation for the properties described in [Ref. 3], an optimization was performed in Excel by modifying the material properties and dimensions not specified in the paper in order to match the properties listed above. The following properties were determined by that procedure and used in the analysis:

Drill string material Young's modulus	2.97×10^7 psi (2.05×10^{11} Pa)
Drill string material Poisson ratio	0.3
Drill string material density	0.2845 lb./in.^{3} (7874 kg/m^3)
Drill string ID	0.31871 ft. (0.09714 m)
Drill string OD	0.374 ft. (0.114 m)
Drill collar material Young's modulus	3.23×10^7 psi (2.23×10^{11} Pa)
Drill collar material Poisson ratio	0.3
Drill collar material density	0.2464 lb./in.^{3} (6819 kg/m^3)
Drill collar ID	0.1782 ft. (0.0543 m)
Drill collar OD	0.541 ft. (0.165 m)

A finite element model utilizing several versions of the MSC.NASTRAN beam elements (CBEAM, CBAR, CTUBE) was created with 110 equal length elements for the drill string and 12 elements for the drill collar. The type of the elements used did not have any effect on the results and CTUBE elements were used in the final production model. A Matlab code implementing the same FEA model (with an arbitrary number of elements) was also used in the simulation.

2.2.1.1.2. Analysis Results.

Both normal modes and frequency response analysis was performed using the MSC. NASTRAN and Matlab code results. The normal modes results were identical. A comparison of the analysis results to those in the literature is presented in Table 2-1. Slight discrepancies in the results are due to a more accurate discretization of the model used in the present FEA versus the simplified scheme of the [Ref. 3]. The velocity transfer function is presented in Figure 2-7.

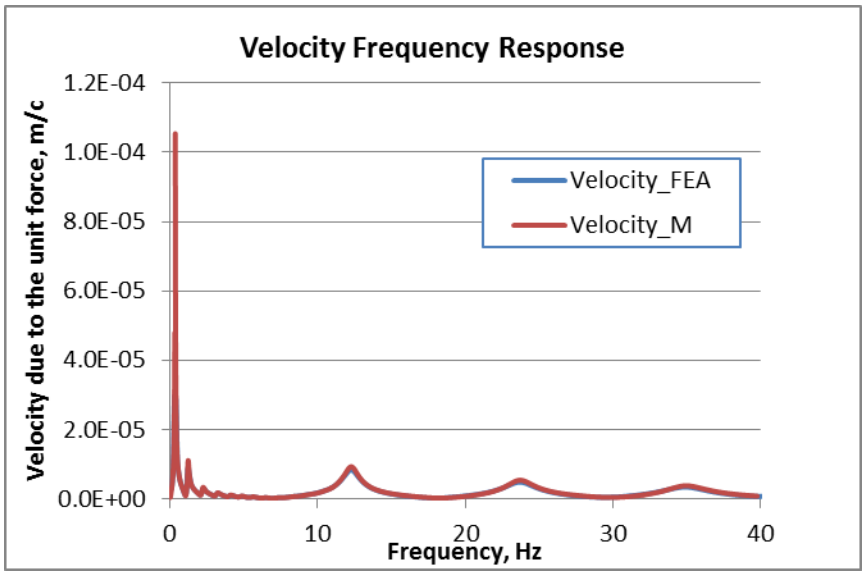

Figure 2-7. Velocity transfer function of the Tlusty drillstring.

Table 2-1. Comparison Of Normal Modes Results.

Normal Mode Frequency, Hz MSC.NASTRAN	Normal Mode Frequency, Hz MATLAB	Absolute Error, Hz	Results from Tlusty
0.346	0.346	1.1E-07	0.345
1.216	1.216	3.4E-07	1.25
2.205	2.205	9.3E-08	2.29
3.181	3.181	2.0E-07	
4.062	4.062	2.2E-07	
4.812	4.812	8.8E-09	
5.586	5.586	1.0E-07	
6.480	6.480	1.4E-07	
7.462	7.462	4.5E-08	
8.503	8.503	6.7E-08	
9.579	9.579	1.1E-08	
10.674	10.674	4.5E-07	10.4
11.764	11.764	1.4E-07	
12.279	12.279	1.4E-07	
12.930	12.930	8.1E-08	
14.037	14.037	3.4E-07	
15.155	15.155	1.7E-07	
16.275	16.275	2.9E-08	
17.395	17.395	1.8E-07	
18.513	18.513	9.8E-08	
19.630	19.630	9.0E-08	19.8
20.743	20.743	2.9E-08	
21.854	21.854	1.7E-09	
22.960	22.960	1.4E-07	
23.709	23.709	1.4E-07	
24.066	24.066	1.8E-07	
25.163	25.163	1.7E-07	
26.257	26.257	1.8E-07	
27.346	27.346	1.4E-08	
28.430	28.430	9.1E-08	
29.509	29.509	3.1E-08	
30.581	30.581	3.7E-09	

2.2.1.2. 5 km Drillstring

While the initial model and code development work was done using the published description of the 7200 ft. drill string system, the actual target application is a 5 km drill string system for the

Deep Borehole Disposal Program. An initial simplified design of that system has the following parameters:

Drill string material Young's modulus	2.97×10^7 psi (2.05×10^{11} Pa)
Drill string material Poisson ratio	0.3
Drill string material density	0.2816 lb./in.^{3} (7793 kg/m^3)
Drill string ID	0.49708 ft. (0.15151 m)
Drill string OD	0.55207 ft. (0.16827 m)
Drill collar material Young's modulus	3.23×10^7 psi (2.23×10^{11} Pa)
Drill collar material Poisson ratio	0.3
Drill collar material density	0.2816 lb./in.^{3} (7793 kg/m^3)
Drill collar ID	0.148 ft. (0.045 m)
Drill collar OD	0.9167 ft. (0.2794 m)
Drill pipe length	15231.0 ft. (4642.4 m)
Drill pipe sections	491
Drill collars length	1799.18 ft. (548.39 m)
Drill collar sections	58
Drill collar to Drill pipe interface	
Mass	673.1 lb. (305.3 kg)
Stiffness	3.38×10^5 lb./ft. (4.94×10^6 N/m)
Traveling block, swivel, kelly mass	34022 lb. (15432 kg)
Draw works stiffness	6.3×10^5 lb./ft. (9.2×10^6 N/m)

An analysis of this configuration was conducted using the developed Matlab code to calculate the normal modes of the system. Modes up to 30Hz are listed in the table below.

Normal Mode Frequencies of the 5 km Drill String System, Hz						
0.518	4.770	9.379	14.029	18.653	23.186	27.665
0.985	5.123	9.597	14.148	18.721	23.360	28.009
1.461	5.593	10.091	14.640	19.179	23.691	28.164
1.938	6.079	10.594	15.144	19.681	24.189	28.656
2.410	6.572	11.098	15.649	20.183	24.687	29.149
2.872	7.068	11.603	16.153	20.685	25.185	29.641
3.318	7.568	12.108	16.658	21.187	25.682	30.133
3.747	8.068	12.614	17.162	21.688	26.179	30.624
4.172	8.569	13.119	17.666	22.189	26.675	31.115

2.2.2. Bar Element Model

Computational models provide the opportunity to analytically explore various aspects of the drill string operation such as resonance vibration, self-excitation due to rock/bit interaction and loss of

stability. Models can also be used for identifying critical modes of the structure and selecting the optimal type and parameters of vibration mitigation devices. Several types of models can be employed for these purposes including linear and non-linear Finite Element Models (FEM), multibody dynamics models, and specialized models utilizing custom methods to solve equations describing the vibration of the drillstring system; initial work in this area has focused on linear FEM implemented in both commercial code (MSC Nastran) and custom implementation of the FEM in MATLAB (The MathWorks). While simple to implement, linear models provide plentiful information about the fundamental dynamics of the system, such as the onset of instability, and can be easily used in the substructuring approach and corresponding control algorithms. Attention is initially focused on axial vibration of the drill string. Coupling of the rotational and off-axis motions is ignored for the sake of simplicity.

Stiffness and mass matrix for the basic bar element are as follows:

$$K = \frac{EA}{L}\begin{bmatrix} 1 & -1 \\ -1 & 1 \end{bmatrix} \qquad M = \frac{\rho LA}{2}\begin{bmatrix} 1 & -1 \\ -1 & 1 \end{bmatrix} \qquad \text{(Eq. 2-9)}$$

These element stiffness matrices are assembled into the global stiffness matrix along with special elements such as collar – string interface stiffness and mass, draw works stiffness, etc. and used in a normal modes analysis. Boundary conditions used are free-free at the bit and supported at the drill rig draw works.

2.2.3. Vibration Mitigation Options Evaluation

In conventional structural dynamics problems, several common solutions are used to mitigate vibrations. Measures such as tuned dynamic dampers (TMDs) or detuning the structure from the frequencies of the excitation forces by appropriate structural modifications are commonly employed with good results. Unfortunately, most of these methods suffer from a common problem - they assume a particular operating conditions or structure which does not change during operation. Neither of these is correct for the drill string during deep well drilling. A change of the length of the drill string results in the change of the dynamic properties due to both mass and stiffness changes. Operation conditions can change at any time due to changes of the rock properties, the rotational speed of the drill bit and other factors. Whatever solution is selected for vibration mitigation purposes, it must have the ability to be adjusted as conditions change. All of the options to be reviewed are designed with such ability in mind. While analysis is still performed for a given set of properties and conditions to demonstrate applicability of the solution, it is understood that as conditions change, a vibration mitigation device will have its properties adjusted to account for that change. Several different vibration mitigation concepts will be demonstrated below including detuning, TMD and an inertial exciter. It is important to note that parameters in all these examples, in the absence of the specific design requirements, are selected arbitrarily just to show the possibility of addressing vibration in the realistic system by using realistic vibration mitigation measures.

2.2.3.1. Detuning of the drillstring from excitation frequencies.

Since the highest level of vibration due to the periodic force (such as one produced by the rotational motion of the drill bit/drill string system) is usually achieved at the resonance of a normal mode, an obvious approach is detuning that mode from the excitation force frequency by modifying structural properties. To achieve that goal, a spring of variable stiffness can be introduced near the drill bit in the drill collar structure. To evaluate the feasibility of such a solution, a spring with stiffness 2.06 x 10^6 lb./ft. (3 x 10^7 N/m) was introduced in the FEM of the 7200 ft. (2200 m) string approximately 65.6 ft. (20.0 m) away from the drill bit end and the response of the drill bit was evaluated. Displacement, velocity and acceleration frequency response functions are presented in Figure 2-8. It can be seen that the structural modification by inserting a spring of realistic parameters can modify the modes in the range of interest and significantly change the response of a drill bit. Structural modifications will reduce vibrations at some frequencies and increase them at others, so this, as other approaches considered below can only be effective in an adaptive system.

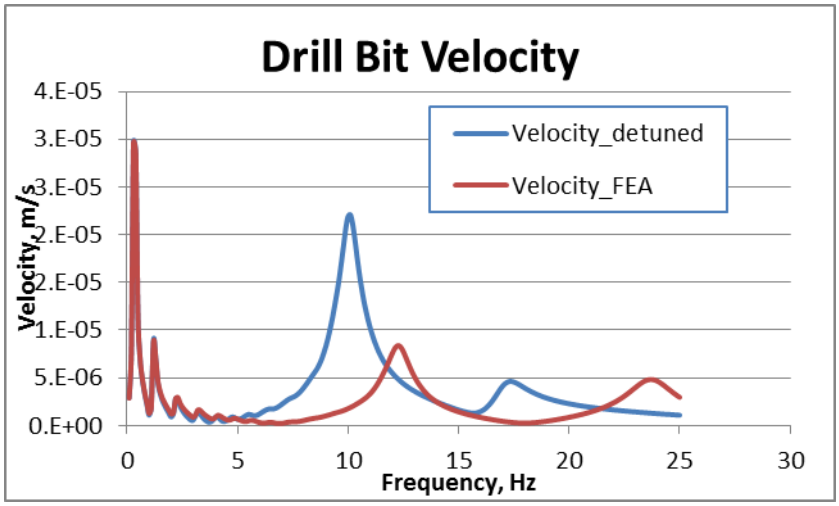

Figure 2-8. Velocity and acceleration of the detuned system.

2.2.3.2 Tuned Dynamic Damper.

Another common vibration mitigation approach is adding a TMD to the structure. A TMD consists of a mass/spring/damper system tuned to perform optimally either at the frequency of the excitation force or the frequency of the mode contributing substantially to the response. A detailed analysis of the TMD is presented in Appendix A. It is important to realize that certain freedom exists in choosing the location and mass of TMD. To demonstrate the concept, only first order tuning is used. Better tuning can be achieved by using a rigorous optimization procedure to find TMD parameters. The tables below summarize the results of the vibration reduction due to the application of the TMD targeting modes # 3, 14 and 25. The data clearly shows the effects of the mass of the TMD as well as placing it in the sub-optimal location. Yet, even a suboptimal TMD can provide a substantial reduction in the vibration level. It can be seen that a TMD of less than 1% of the mass of drill string system can reduce vibration by factor of 2 or greater.

Mode # 2, Frequency 1.22Hz				
Point	Mass	Damping	Resp	% Nominal
82	2000	0.05	4.00E-05	67%
82	1000	0.03	4.90E-05	82%

Mode # 14, Frequency 12.28Hz				
Point	Mass	Damping	Resp	% Nominal
9	1000	0.2	2.30E-04	35%
9	500	0.15	3.00E-04	46%
9	250	0.09	3.60E-04	55%
18	1000	0.19	3.00E-04	46%
18	500	0.15	3.40E-04	52%

Mode #25, Frequency 23.7				
Point	Mass	Damping	Resp	% Nominal
9	500	0.1	5.40E-04	75%
9	250	0.13	4.40E-04	61%
9	125	0.06	5.00E-04	69%

2.2.3.2. Inertial Exciter

An Inertial Exciter (IEx) is one additional option that was considered for vibration mitigation. This device applies an oscillatory load to the structure with the goal of reducing vibration. See Appendix A for a brief theoretical overview of the application of the device. Just as was the case of the TMD, placement within the structure plays a very important role. Several exciters may

have to be placed at different locations if resonance of more than one mode is to be addressed. To illustrate the effectiveness of an inertial exciter, a load was applied at a location 65.6 ft. (20.0 m) away from the drill bit and tuned to reduce vibration at mode #26 (24.07 Hz). At the same time, however, an inertial exciter can increase vibration at other frequencies, so that an adaptive approach must be used with this option as well. An inertial exciter has the advantage of ease with which frequency and amplitude can be manipulated. At the same time, the amount of force it can produce is limited by its design and may or may not be sufficient to mitigate the vibration at particular modes.

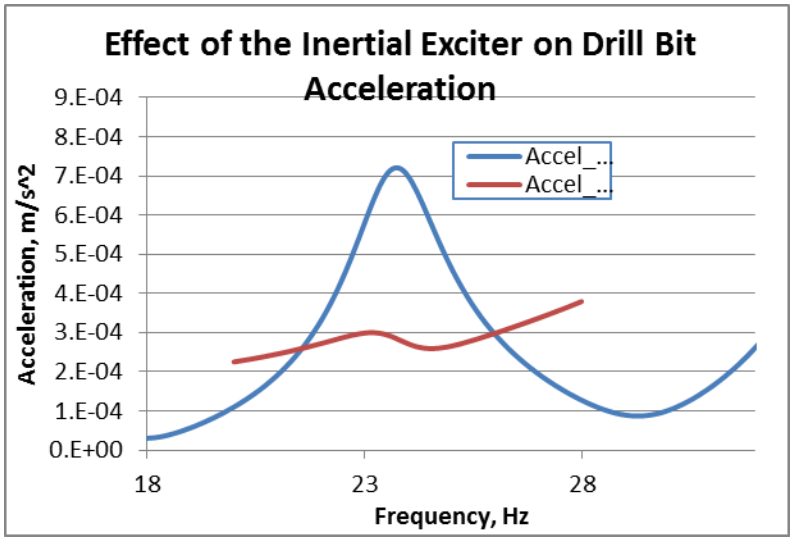

Figure 2-9. Effect of the Inertial Exciter on Drill Bit vibration.

2.2.4. Drillstring Modeling Conclusions

Three vibration mitigation options were reviewed with computational modeling – system detuning, Inertial Exciter and TMD. All options seem to be feasible for the drill string application. The parameters of those devices are the realistic ranges for the typical system and multiple tuning options exist. Specific design requirements must be defined before the best option (or combination of several options tuned to address vibration at several frequencies) can be selected.

2.3. Drillstring Substructuring using Normal Modes

In order to validate the process for simulating a drillstring using port functions in Simulink, representations of several different systems with varying levels of complexity were used and validated through several different solution methods. These models and the resulting simulations are described below.

A simple four-mass chain of masses in series with a parallel spring-damper in between each mass (4DOF model) was used for initial validation. This model included a force input on the first mass and a terminating spring to a rigid boundary on the final mass. This model has basic dynamic characteristics similar to a drillstring, but is simple enough to allow solution by hand to validate the other solution approaches. It is included in Appendix C as a validation exercise. With the completion of this validation, we move onto substructuring the drillstring model.

2.3.1. Tlusty Drillstring Modeling

Structural dynamics FEM was used to evaluate the influence of controllable elements on the entire drillstring. The normal modes analysis produces as many modes as inertial elements in the drillstring. From these modes, the important modes must be selected for simulation in MATLAB / Simulink for control design. In the current configuration, Simulink functions well with up to approximately 20 modes – with significantly more modes, it experiences numeric problems. The normal modes coefficients were used to develop impedance / admittance based transfer functions of the drill string in MATLAB. For example, for G1, a two-port admittance transfer function was used as seen below.

$$\begin{bmatrix} V_{bit} \\ V_{act} \end{bmatrix} = \begin{bmatrix} Y_{11} & Y_{12} \\ Y_{21} & Y_{22} \end{bmatrix} \begin{bmatrix} F_{bit} \\ F_{act} \end{bmatrix} \qquad \text{(Eq. 2-10)}$$

The coefficients for this matrix function were derived from the normal mode (eigenvector) coefficients ϕ according to the following expressions (see Appendix A):

$$\begin{aligned} Y_{11} &= s \sum_{l=1}^{r} \frac{\phi_{nl} * \phi_{nl}}{m_l s^2 + c_l s + k_l} \\ Y_{12} &= s \sum_{l=1}^{r} \frac{\phi_{nl} * \phi_{1l}}{m_l s^2 + c_l s + k_l} \\ Y_{21} &= s \sum_{l=1}^{r} \frac{\phi_{1l} * \phi_{nl}}{m_l s^2 + c_l s + k_l} \\ Y_{22} &= s \sum_{l=1}^{r} \frac{\phi_{1l} * \phi_{1l}}{m_l s^2 + c_l s + k_l} \end{aligned} \qquad \text{(Eq. 2-11)}$$

In these expressions, *n* represents the G1 grid point, *r* represents the number of modes incorporated into the MATLAB / Simulink analysis, while *l* represents the number of masses in G1 (the dimensionality of the system).

The G2 transfer function used a single-port admittance (the drill rig boundary condition was defined internally to the normal modes model for the top portion of the drillstring). With n representing the G2 grid point and q representing the number of modes, the admittance for G2 was defined as follows:

$$Y_{G2} = s \sum_{l=1}^{q} \frac{\phi_{nl} * \phi_{nl}}{m_l s^2 + c_l s + k_l} \qquad \text{(Eq. 2-12)}$$

These transfer functions were broken into two parts, the numerator and denominator. This allowed them to be called from within a Simulink transfer function block as shown in Figure 2-10. Figure 2-10 is a direct implementation of the schematic in Figure 2-3, with the exception that the drill rig dynamics have been incorporated into the representation of G2 rather than treated as a separate input and output.

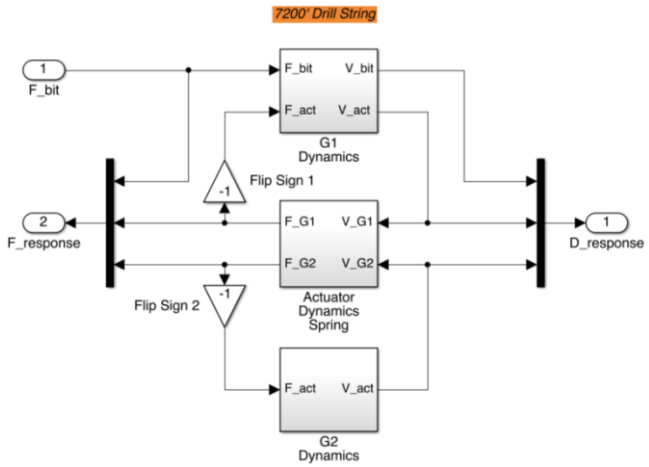

Figure 2-10. Simulink implementation of three-subsystem substructured representation of drillstring with a variable rate spring actuator module.

Bode plots were generated for G2 in order to validate the approach to generating impedance transfer functions. The normal modes frequency response was plotted with MATLAB's Bode plot using the ϕ coefficients to verify there was no loss of system dynamics. As can be seen in Figure 2-11, the two plots overlay.

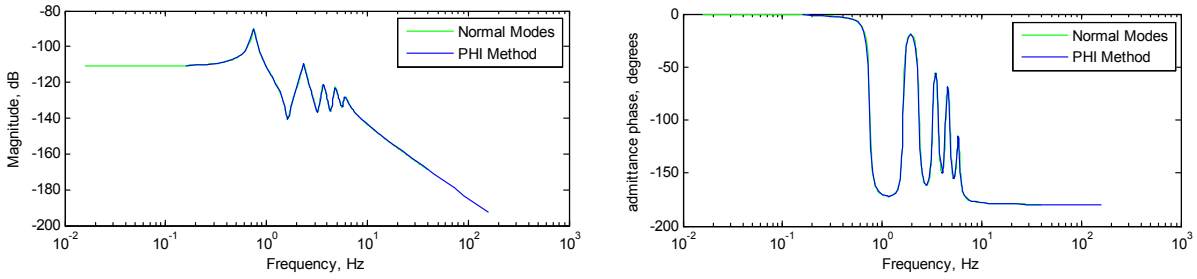

Figure 2-11. Normal Modes FRF vs PHI Method Bode G2 (plots overlay).

2.3.2. DDS Modeling

Since the response of a deep drillstring is dominated by a few fundamental modes of vibration, the Sandia LDRD team conceived a spring/mass suite analog to replicate the dynamic properties of the Tlusty drillstring in the laboratory. This system allows for independent assessment of prototype tools using a passive simulation of the dynamic compliance of a field drillstring. The Sandia Drillstring Dynamics Simulator (DDS) is used to reproduce the frequency response of a simulated drillstring in the laboratory. The simulator consists of a spring-mass system (Figure 2-12.) designed to represent a scaled FRF of the Tlusty drillstring in a structural steel frame (Figure 2-13). A variable rate spring can be introduced below the spring-mass system to evaluate the influence on the transfer function.

2.3.2.1. DDS Simulation Results

The DDS was designed to include five resonant frequencies in G2 that closely matched the dominant frequencies in the Tlusty drill string model. The system was broken up into three pieces—G1, variable spring, and G2. G1 consisted of mass M_1 and the actuator force. The variable rate spring and its natural damping are represented by K_{vs} and C_{vs}. G2 consisted of the remaining masses and springs. The equations of motion for this system are shown below.

(Note: In the actual DDS as-tested (described later), an additional spring was added to prevent Mass 6 from coming out of contact with the spring that retained it to Mass 5. This spring coupled Mass 6 to Mass 2, causing a slight change to the dynamics for the highest-frequency mode.)

$$M_{DDS} = \begin{bmatrix} m_1 & 0 & 0 & 0 & 0 & 0 \\ 0 & m_2 & 0 & 0 & 0 & 0 \\ 0 & 0 & m_3 & 0 & 0 & 0 \\ 0 & 0 & 0 & m_4 & 0 & 0 \\ 0 & 0 & 0 & 0 & m_5 & 0 \\ 0 & 0 & 0 & 0 & 0 & m_6 \end{bmatrix} \quad \text{(Eq. 2-13)}$$

$$K_{DDS} = \begin{bmatrix} K_{vs} & -K_{vs} & 0 & 0 & 0 & 0 \\ -K_{vs} & K_{vs} + K_{ps} + K_3 + K_6 & -K_3 & 0 & 0 & -K_6 \\ 0 & -K_3 & K_3 + K_4 & -K_4 & 0 & 0 \\ 0 & 0 & -K_4 & K_4 & 0 & 0 \\ 0 & 0 & 0 & 0 & K_5 & -K_5 \\ 0 & -K_6 & 0 & 0 & -K_5 & K_5 + K_6 \end{bmatrix} \quad \text{(Eq. 2-14)}$$

$$C_{DDS} = \begin{bmatrix} C_{vs} & -C_{vs} & 0 & 0 & 0 & 0 \\ -C_{vs} & C_{vs} + C_{ps} + C_3 + C_6 & -C_3 & 0 & 0 & -C_6 \\ 0 & -C_3 & C_3 + C_4 & -C_4 & 0 & 0 \\ 0 & 0 & -C_4 & C_4 & 0 & 0 \\ 0 & 0 & 0 & 0 & K_5 & -K_5 \\ 0 & -C_6 & 0 & 0 & -C_5 & C_5 + C_6 \end{bmatrix} \quad \text{(Eq. 2-15)}$$

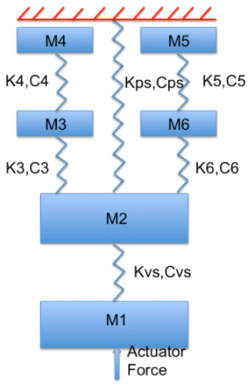

Figure 2-12. Tlusty Drillstring Analog.

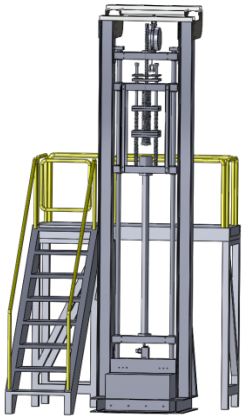

Figure 2-13. Drillstring Dynamics Simulator with Tlusty Drillstring Analog.

The mass and spring values were iteratively adjusted in order to reasonably match the DDS' G2 resonant frequencies with the five dominant Tlusty resonant frequencies. The comparison can be seen in Table 2-2.

Table 2-2. Tlusty vs DDS Resonant Frequencies in Hertz.

Mode #	Tlusty	DDS
1	0.345	0.673
2	1.25	1.22
3	2.29	2.35
4	10.4	9.22
5	19.8	28.3

To achieve these frequencies, the mass and spring values in Table 2-3 were used.

Table 2-3. DDS Mass and Spring Values.

G1	M_1	62.9 kg		
Actuator	K_{vs}	7530- 120,660 N/m		
G2	M_2	100 kg	K_{ps}	3502 N/m
	M_3	23.9 kg	K_3	1751 N/m
	M_4	17.3 kg	K_4	1751 N/m
	M_5	8.7 kg	K_5	59192 N/m
	M_6	4.3 kg	K_6	59192 N/m

2.3.2.2. Simulink DDS Block Diagram

The DDS model was implemented into Simulink for simulation and analysis. The layout of the DDS model can be seen in Figure 2-14.

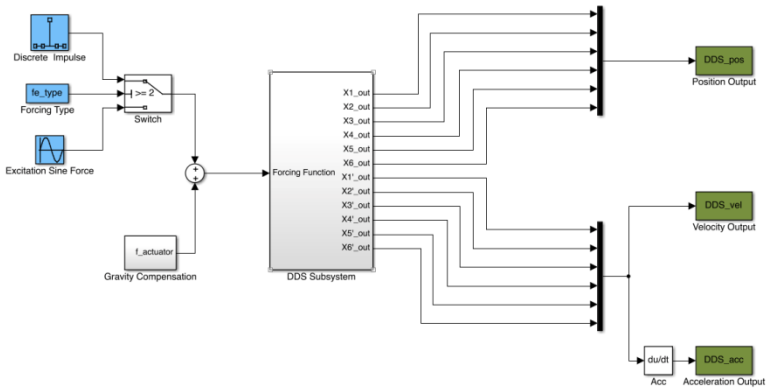

Figure 2-14. DDS Simulink Model Overview

The dynamic DDS subsystem can be seen in Figure 2-15.

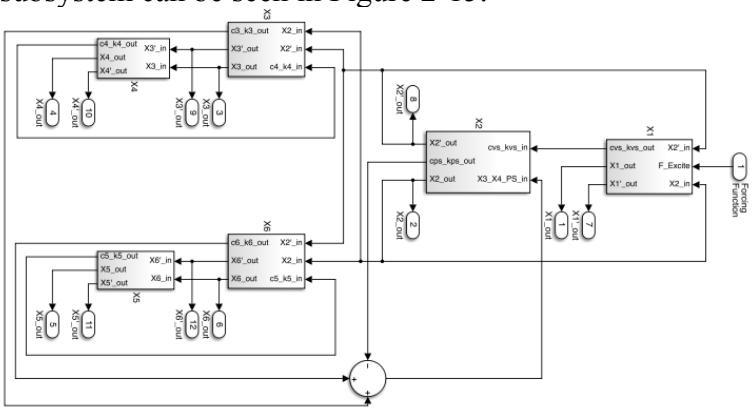

Figure 2-15. DDS Dynamic Subsystem.

2.3.3. Variable Spring Rate and Bode

In order to better understand the effect of the variable spring rate on the resonant frequencies, an analysis of Bode frequency response plots was performed. The result of the variable rate spring shifting the resonant frequencies can be seen in Figure 2-16. The blue plot is the original DDS frequency response with the variable rate spring at K_{vs}=120,660 N/m. Shifting the spring to K_{vs}=76,000 N/m, results in a shift of a resonant peak from ~8 Hz to ~6 Hz, as can be seen in the upper right panel. Thus, if the system was being driven at 8 Hz and the variable rate spring was shifted to the aforementioned value, the system would no longer exhibit the ill effects of driving near an 8 Hz resonance. This can be replicated to move each of the critical system modes. Shifting the spring to lower values of K_{vs}, as shown in the other plots, significantly shifts the problematic resonances in the vicinity of 2-10 Hz, providing a means of preventing excitation of these major structural modes.

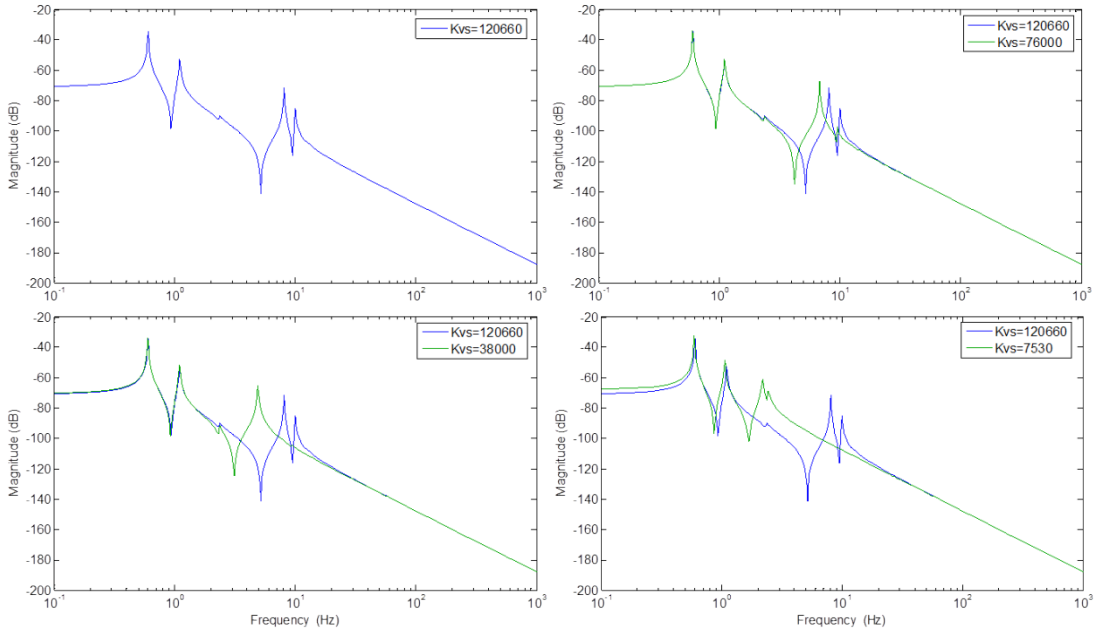

Figure 2-16. FRF magnitude of original DDS (blue) and change due to compliance(green).

2.3.4. Simulation and Results

The DDS was simulated with a driving frequency at each of the six resonant frequencies. At time t=100 seconds, the variable spring rate was shifted from an initial rate to a different rate to show how a shift in spring rate not only shifts the system out of resonance, but reduces the transmissibility of forces throughout the system. Below are the responses of each mass from its initial rest position, driven at each of the system's resonant frequencies from Table 2-2:

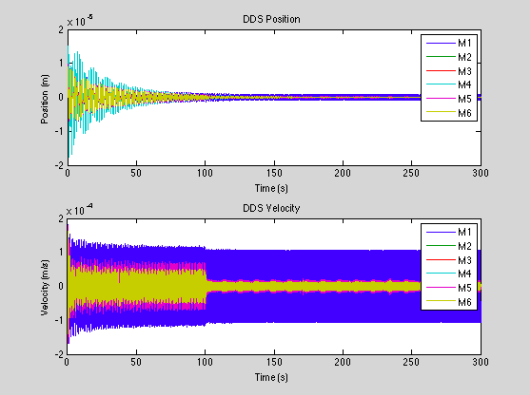

Figure 2-17. Mode 1: Kvs@t=0: 122000 N/m, Kvs@t=100: 7502 N/m

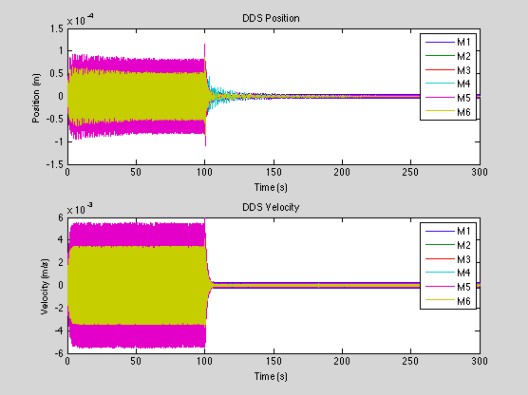

Figure 2-18. Mode 2: Kvs@t=0: 122000 N/m, Kvs@t=100: 7502 N/m

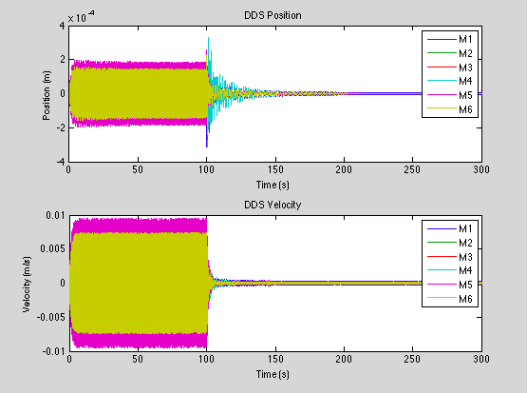

Figure 2-19. Mode 3: Kvs@t=0: 122000 N/m, Kvs@t=100: 7502 N/m

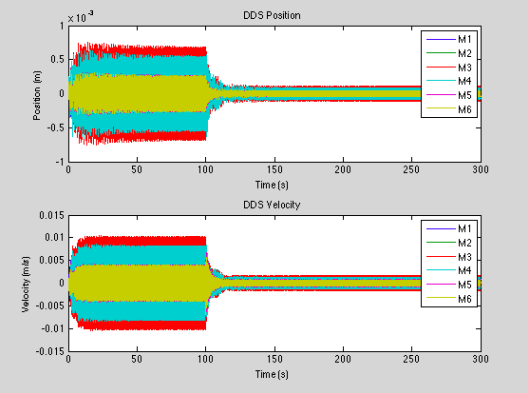

Figure 2-20. Mode 4: Kvs@t=0: 7502 N/m, Kvs@t=100: 50000 N/m

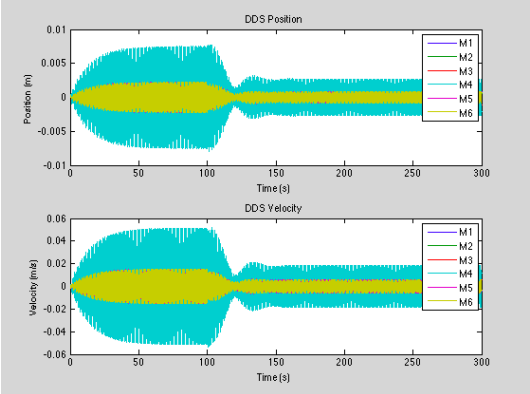

Figure 2-21. Mode 5: Kvs@t=0: 122000 N/m, Kvs@t=100: 7502 N/m

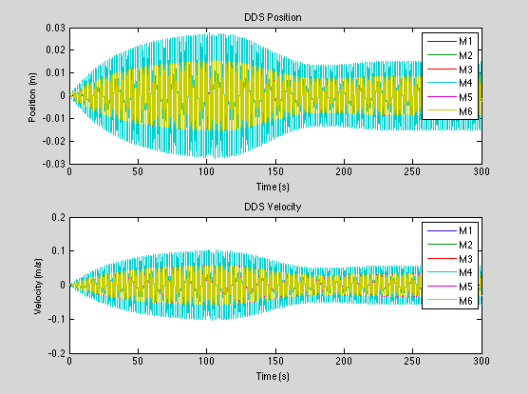

Figure 2-22. Mode 6: Kvs@t=0: 122000 N/m, Kvs@t=100: 7502 N/m

As can be seen, in each case the system exhibits resonance until time, t=100 seconds. Shifting the variable spring rate shifts the resonant frequencies of the system, moving the system into a non-resonant state.

2.3.5. Drillstring (G1 & G2) System ID

Several of the potential control approaches proposed for down-hole autonomous use require a dynamic model of the drillstring to be developed in real-time from measured data, a process known as system identification. Using a substructured drillstring model, simulations were conducted to demonstrate the ability to perform system identification on a drillstring and to explore the nuances of doing so.

- Figure 2-23 shows a Simulink model of a substructured drillstring, with annotations indicating where it is possible to measure force and motion signals on either side of an actuator sub. These measurements represent the inputs (forces) and outputs (velocities) to both the G1 and G2 transfer functions. Ideally, system identification methods could be used to identify both the G1 and G2 sides of a drillstring. In-situ system identification of a drillstring differs from more common system identification methods in several important ways: In typical system identification, the inputs are controlled and sculpted in order to achieve the desired excitation frequency content. In the drillstring arrangement, longitudinal excitation originates from forces applied to the bit (which result from rotary motion of the drillstring), and is not directly controllable. The input forces to G1 and G2 are transformed from the bit forces by intermediate dynamics. In real drilling, it will be essentially impossible to produce a desired frequency band at the G1 and G2 inputs; it may only be possible to identify dynamics within the excited bands.

- The excitation forces (and motion) at the bit are not directly measured in this arrangement.

- Because the subsystem represented by the G1 transfer function is located between the excitation (at the bit) and the measurements (at the bottom end of the actuator), it is not possible to identify the G1 dynamics by this method. Instead, the relationship between input and output at that interface is dominated by the dynamics above the point of measurement (further “downstream” from the excitation). This is shown below.

Given these unusual properties, simulations were conducted to understand the feasibility of system identification. Several different types of wideband excitations were applied at the bit, and the inputs and outputs to G1 and G2 at the actuator interface were recorded. The resulting data vectors were used to generate transfer functions using Matlab’s tfestimate function. Figure 2-24 shows the results of two simulations, one using a chirp excitation (from 0.1 to 100 Hz) and the other a step excitation (which should excite all frequencies equally). The top two plots in each column show the magnitude and phase versus frequency of the nominal model (blue line) along with the model identified from simulation data (green line). The bottom plot shows the coherence versus frequency, which is a measure of the correlation between the input and output signals and serves as an indicator of estimate quality; when the coherence is close to 1, the estimate should be accurate. In this case, the step appears to provide a better estimate at the

lowest frequencies, which is expected as the chirp does not excite frequencies below 0.1 Hz. However, at intermediate frequencies (between ~1 and 20 Hz), the chirp excitation produces better estimates, and correctly identifies the key peaks of the magnitude spectrum in spite of fluctuating coherence. Neither excitation produces an accurate estimate of phase above 10 Hz.

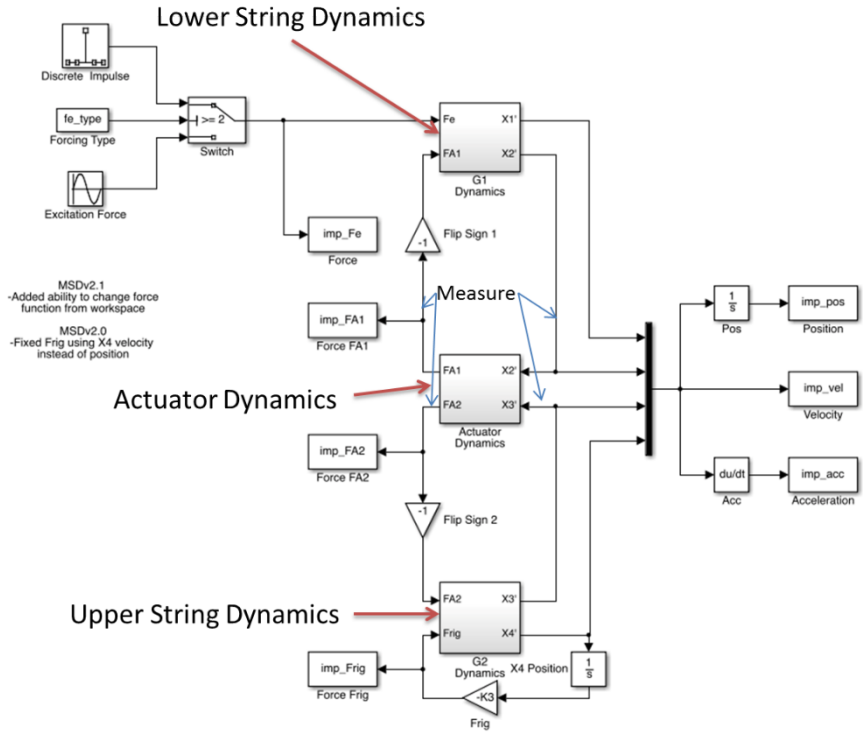

Figure 2-23. Simulink model of a drillstring with measurement points indicated for system identification.

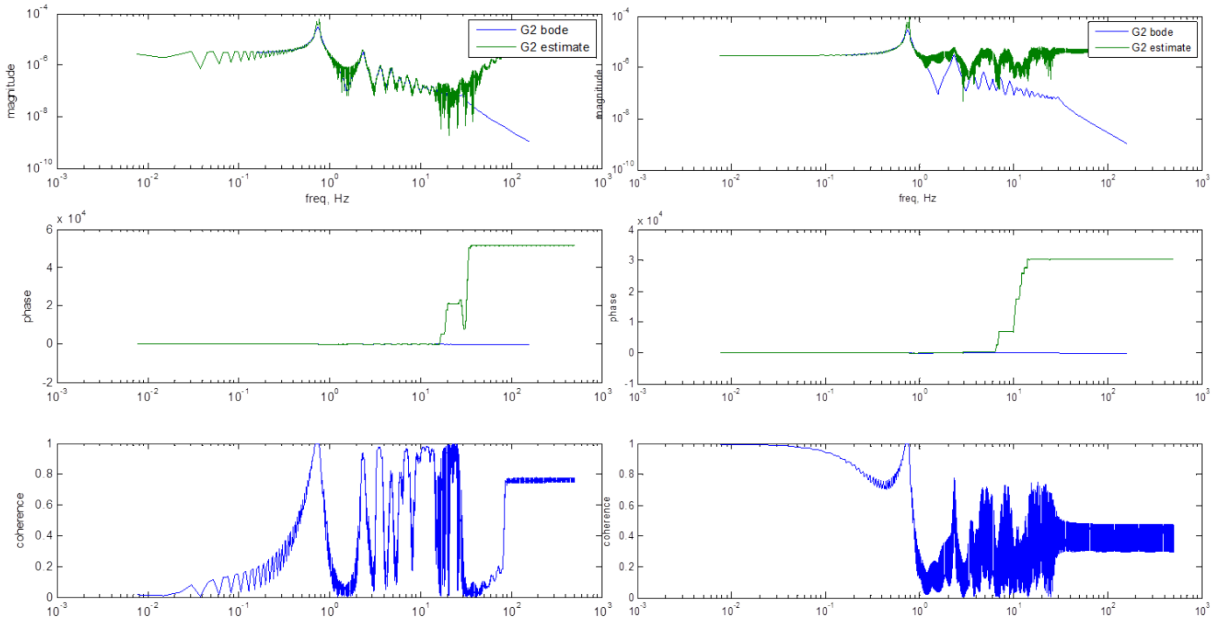

Figure 2-24. Results of simulated G2 system identification using a chirp (left) and step (right) excitation. Plots compare the magnitude and phase of the estimate derived from simulated data (green) and the nominal model (blue).

While estimate quality is imperfect, these results indicate that the G2 dynamics may conceivably be estimated in situ, in spite of the unusual properties of this arrangement. In order to evaluate the potential for instability, it is insufficient to identify the magnitude spectrum; the real part of the transfer function must be determined [Ref. 16]. Figure 2-25 plots the estimated real part of the transfer function along with the nominal model. The curves agree and, critically, the zero crossings that define the potentially unstable regions are accurately estimated.

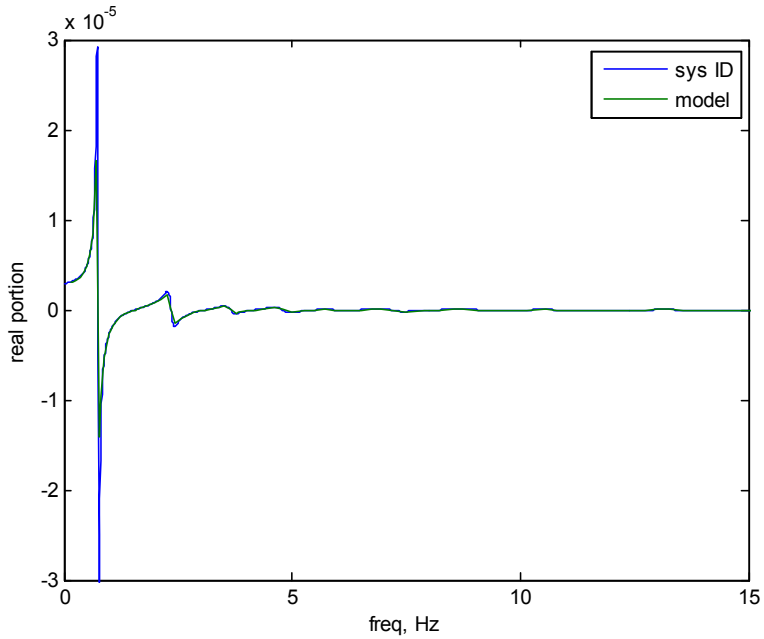

Figure 2-25. Real portion of G2 admittance transfer function, determined by applying Matlab's tfestimate function to simulated data.

While these results are encouraging, simulations also revealed that estimate quality is extremely sensitive to several practical parameters that may be difficult or impossible to control in an actual drilling situation. For example, estimate quality improves significantly when the excitation and data acquisition time window is extended. This is illustrated by the left and right panels of Figure 2-26, which shows estimates derived from simulations with a chirp excitation of 40 seconds and 400 seconds, respectively. The longer window results in a much more accurate fit of estimate to the nominal system dynamics.

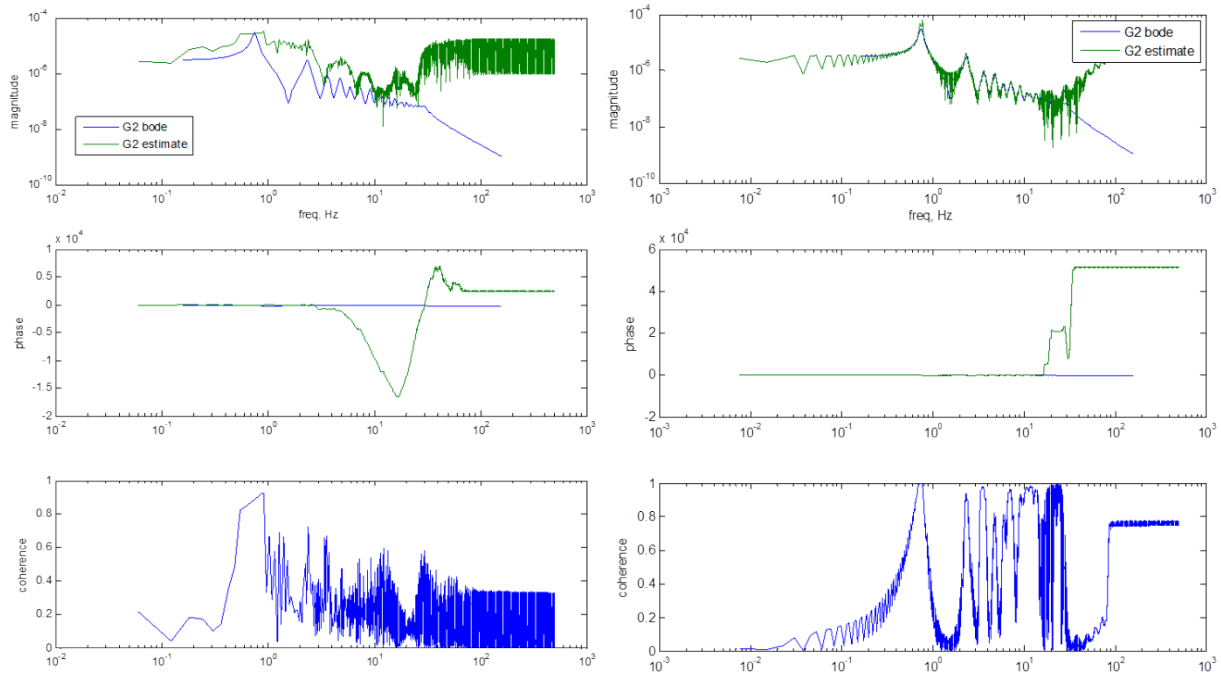

Figure 2-26. The effect of excitation time window on estimate quality. Transfer function estimates from a chirp excitation 40 sec (left) and 400 sec (right) in duration.

The quality of system identification estimates is also heavily influenced by the details of the drillstring dynamics, as illustrated by Figure 2-27. The excitation for the two simulations shown in this figure was identical; the only difference is that the variable actuator spring stiffness was reduced by 10x in the right panel as compared to the left panel. The quality of estimate improved significantly with a softer spring, as particularly evidenced by the dramatic increase in coherence at most frequencies. This may suggest that the stiff, lightly damped mode introduced by the actuator spring causes problems for system identification.

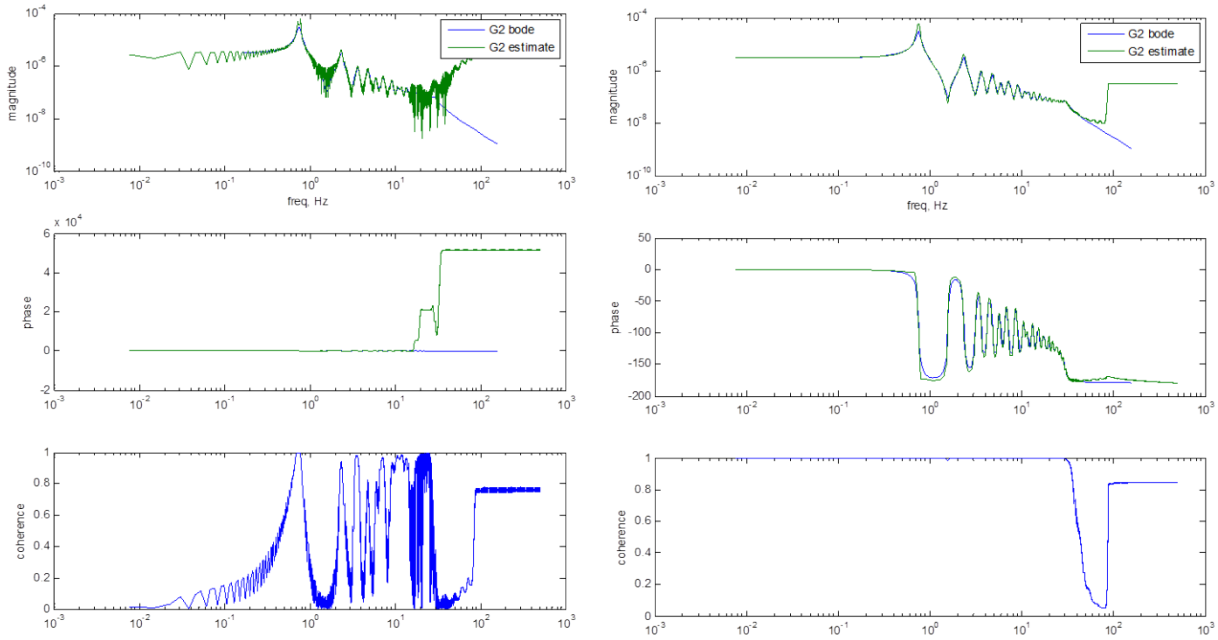

Figure 2-27. Simulated system identification G2 estimates with a stiff actuator spring (left) and a softer spring (right).

Given the practical limitations of system identification, another possibility worth considering is to locate the resonant modes of the G2 subsystem by other simpler means, and to infer the model structure from these modes. For example, potentially the frequency content of one or both of the measured G2 signals (force or motion) may alone provide this information. To test this idea, data from the same chirp-excited simulation was processed in several ways and compared to the nominal model. The results are shown in Figure 2-28, which plots the nominal model (G2 bode), the estimate derived from both the force and velocity signals using tfestimate (G2 estimate), and the fast fourier transforms (FFT) of both the force and velocity. The input force at G2 yields little information about its modes. The velocity FFT locates most of the lower frequency modes with reasonable accuracy. However, the actual system identification estimate tracks the nominal model much better. Because these curves are derived from the exact same data, this indicates that the system identification tools provide a significant analytical benefit.

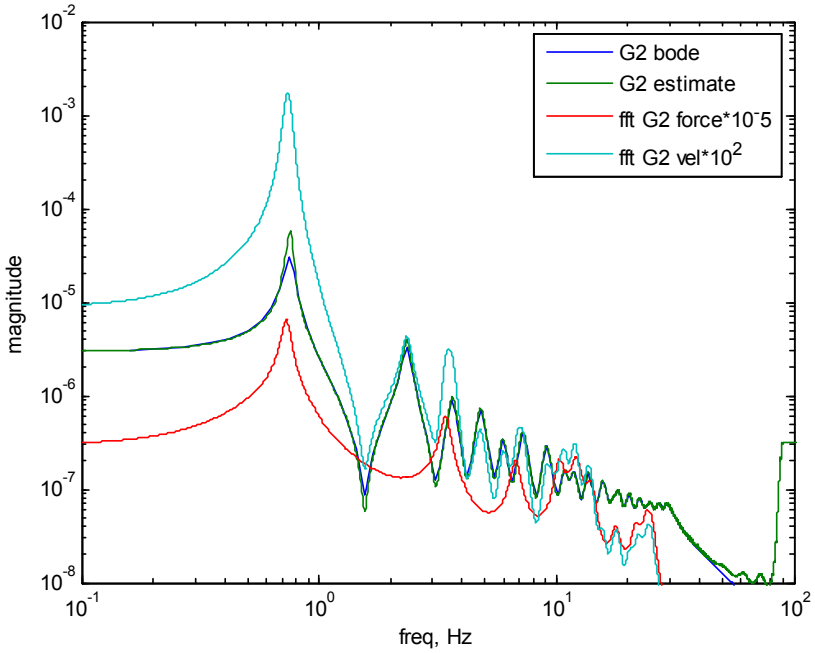

Figure 2-28. Comparison of nominal resonance locations, estimated resonances, and raw force and velocity FFTs for G2.

As noted above, it is not possible to identify the dynamics of G1 by exciting at the bit and measuring the force and motion at the bottom of the actuator. If system identification tools (e.g. Matlab's tfestimate function) are applied to the force and velocity measured at this location, the resulting estimate reflects the dynamics of the system *above* the point of measurement (i.e., the actuator and G2). This is shown by the example plotted in Figure 2-29. In this case, the estimate (blue line) is plotted along with the nominal model of the actuator spring. It is clear that the actuator dynamics dominate the estimate. Because the G1 subsystem is located between the point of excitation and the location where the input and output signals are measured, its dynamics are not observable from this location. Therefore it may not be possible to estimate the dynamics of G1 in situ – or at the very least, alternative methods would be required to do so.

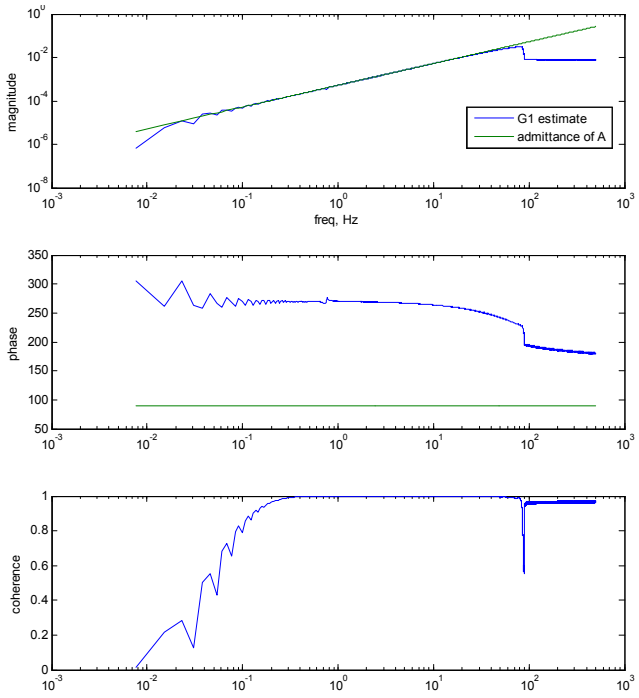

Figure 2-29. Attempts to estimate G1 dynamics instead represent dynamics above the point of measurement.

3. DRILLING PROCESS MODELING & SIMULATIONS

3.1. Rock/Bit Interaction

Due consideration must be given to the rock bit interaction process to understand how it contributes to drillstring vibration. The variety of bit types -- roller cones, impregnated diamond, and PDC bits -- produce a diverse range of excitations. Generally, roller cones generate excitation forces at frequencies that are proportional to rotary speed, with rotary frequencies corresponding to cone rotation superimposed upon the dominant rotary frequency; the tooth distribution across the cones generates reaction forces at frequencies that are superimposed upon these rotary frequencies. Impregnated diamond bits also are rotary rate dependent yet have very little tooth exposure. Conversely, PDC bits have high tooth exposure. As shown in Section 1 (see Nyquist instability diagram), this interaction makes the forces generated via rock-cutter interaction depth of cut dependent. Since PDC bits self-excite the modes of vibration of the support drillstring, the frequencies of the reactive forces appear at the natural frequencies of the drillstring.

Glowka (Sandia) has measured individual PDC cutter rock forces as a function of depth of cut and rock type [Ref. 26] using an instrumented linear mill. Empirical correlations of these force measurements as a function of depth of cut formed the basis for the development of the computational code PDCWEAR [Ref. 26] that enables prediction of the integrated bit response at different operating conditions in various rock types for stable drilling. While the detailed cutter-specific force predictions enabled by PDCWEAR are useful, we seek a simplified approach for preliminary evaluations to predict the onset of stability as the bit interacts with the rock and drillstring.

Detournay and Defourny [Ref. 10] used the Glowka cutter data as the basis for a phenomenological model for the drilling action of PDC bits. This model has also been validated by Sandia using field data and is used herein as a valid representation of rock-cutter interaction forces. We use it to evaluate the response of the test bits evaluated in the drilling applicability demonstration. We also use it to develop an instability model that predicts rock-cutter interaction forces when subject to drillstring vibration.

This Detournay and Defourny model, hereafter referred to as the DD model, assumes the rock-cutter interaction at their interface to consist of two processes, cutting and friction; Cutting is characterized by two constants, ε, and ζ, and friction by one parameter, μ, where

ε = intrinsic specific energy necessary to cut a volume of rock [psi];
ζ = ratio of vertical to horizontal cutter forces in the absence of friction [-].
μ = friction coefficient at the wearflat/rock contact [-];

The horizontal, F_s, and vertical, F_n, force components for cutting (Figure 3-1) are:

$$F_s^c = \varepsilon A \qquad \text{(Eq. 3-1)}$$

and

$$F_n^c = \zeta \varepsilon A \quad \text{(Eq. 3-2)}$$

For a blunt cutter (Figure 3-2), frictional processes are related by a coefficient of friction:

$$F_s^f = \mu F_n^f \quad \text{(Eq. 3-3)}$$

The horizontal force component including friction is expressed as:

$$F_s = \varepsilon A + \mu F_n^f \quad \text{(Eq. 3-4)}$$

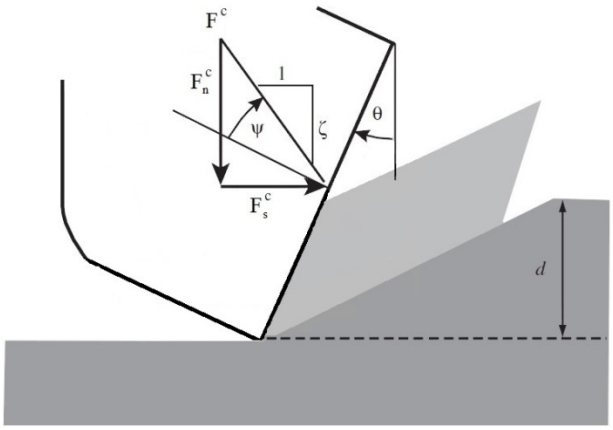

Figure 3-1. Sharp cutter (Ref. 10).

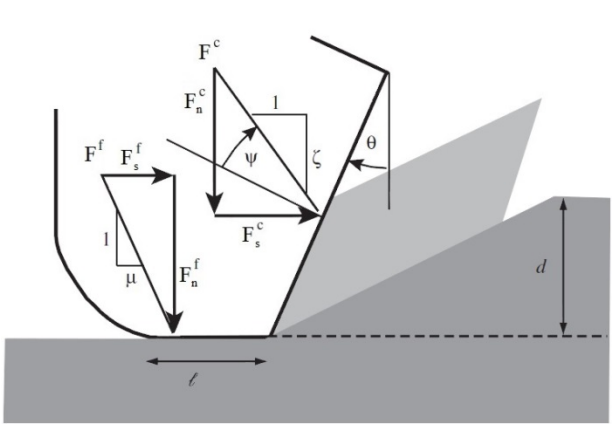

Figure 3-2. Blunt Cutter (Ref. 10).

By introducing the quantities

$$E = \frac{F_s}{A} \quad \text{(Eq. 3-5)}$$

and

$$S = \frac{F_n}{A} \quad \text{(Eq. 3-6)}$$

Detournay shows a linear relation, between E & S, where for a sharp cutter

$$E = \varepsilon \quad \text{(Eq. 3-7)}$$

and

$$S = \zeta A \quad \text{(Eq. 3-8)}$$

For a blunt cutter, a linear relation exists between E & S:

$$E = E_0 + \mu S \quad \text{(Eq. 3-9)}$$

where

$$E_0 = (1 - \mu\zeta)\varepsilon \quad \text{(Eq. 3-10)}$$

The E-S diagram is depicted in Figure 3-3.

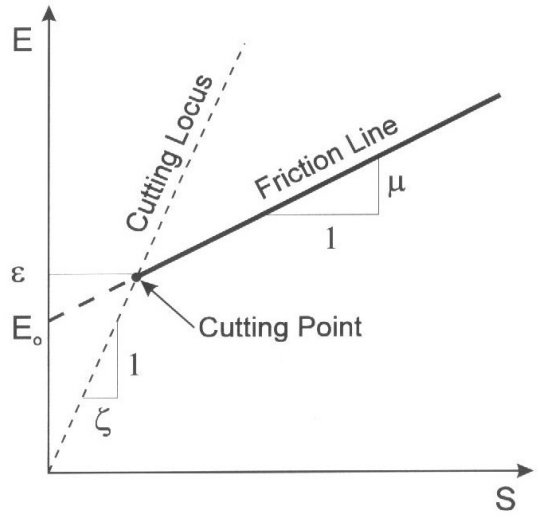

Figure 3-3. Specific Energy vs Drilling Strength Diagram.

Using the Sandia single cutter data [Ref. 26], Detournay shows that a sharp cutter (Figure 3-4), defines the cutting locus and a worn cutter (Figure 3-5), defines the friction line.

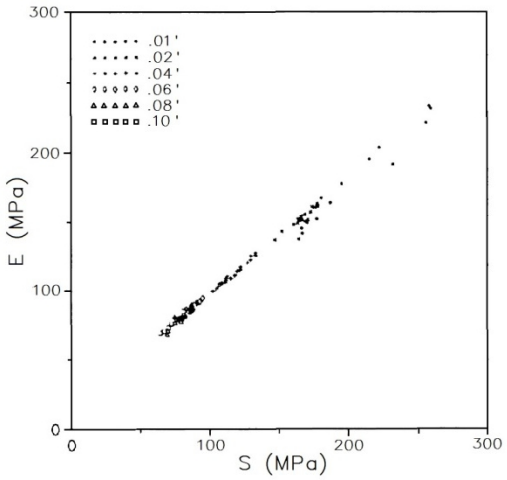

Figure 3-4. E-S diagram with results of Glowka's single-cutter experiments in Berea Sandstone using cutter I (Ref. 10).

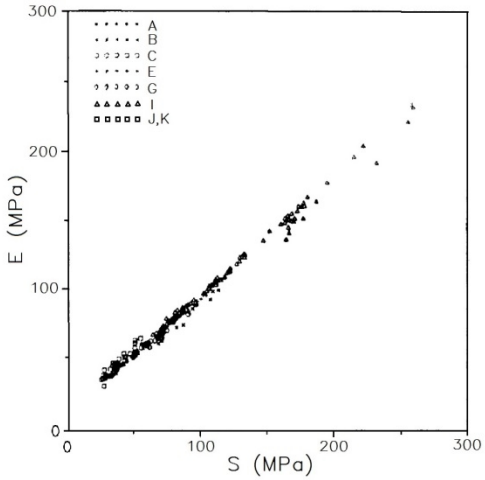

Figure 3-5. E-S diagram with results of all single-cutter experiments in Berea Sandstone reported by Glowka (Ref. 10).

The model of a PDC bit is a generalization of the model of the cutter response [Ref. 10]. Again assuming the coexistence of cutting action and frictional contact for the cutters comprising a bit, the cutting forces for the bit can be resolved to

$$T^c = \frac{1}{2}\varepsilon\delta a^2 \qquad \text{(Eq. 3-11)}$$

$$W^c = \zeta \varepsilon \delta a \quad \text{(Eq. 3-12)}$$

where

$$\delta = \frac{2\pi v}{\omega} \quad \text{(Eq. 3-13)}$$

where v is the rate of penetration and ω is the rotary speed.

The frictional forces on the bit are accounted for by introducing a new parameter, γ, where

$$\gamma = \frac{2T^f}{\mu a W_f} \quad \text{(Eq. 3-14)}$$

The model for the bit response can be characterized by again using the E-S diagram, where for the bit:

$$E = \frac{2T}{a^2 \delta} \quad \text{(Eq. 3-15)}$$

and

$$S = \frac{W}{a\delta} \quad \text{(Eq. 3-16)}$$

where a is the bit radius.

The linear relation between E & S for a bit is:

$$E = E_0 + \mu S \quad \text{(Eq. 3-17)}$$

where

$$E_0 = (1 - \beta)\varepsilon \quad \text{(Eq. 3-18)}$$

with

$$\beta = \gamma \mu \zeta \quad \text{(Eq. 3-19)}$$

The E-S diagram for a bit is similar to the one for a cutter except the slope of the friction line is replaced by the product μγ, where the constant, γ, embodies the influence of the bit design on its mechanical response.

Sandia has validated this model using laboratory data for a three cutter bit (Figure 3-6) in the HRDF (Figure 3-7). Figure 3-9 is a plot of specific energy versus drilling strength for the PDC bit response (shown in Figure 3-8). Also plotted in Figure 3-9 is the locus of cutting points. The cutting locus has a slope of 1/ζ, where ζ is the ratio of vertical to horizontal cutter forces in the absence of friction (i.e., pure cutting). With increasing weight on bit, the response of the bit approaches the cutting locus. The cutting locus, characterized by ζ, falls within a range of values of 0.7 – 0.9 for several rock types [Ref. 10]. Glowka's data predicts an average value of 1.1 [Ref. 31] for Sierra White Granite for depths of cut up to 0.06 inches (0.15 cm). A cutting line

with an average value of ζ=1.1 is plotted in Figure 3-9 and shows that the HRDF bit is capable of drilling slightly faster than 30 ft./hr. (2.54 mm/s).

Figure 3-6. HRDF 3-1/4" Diameter PDC Bit.

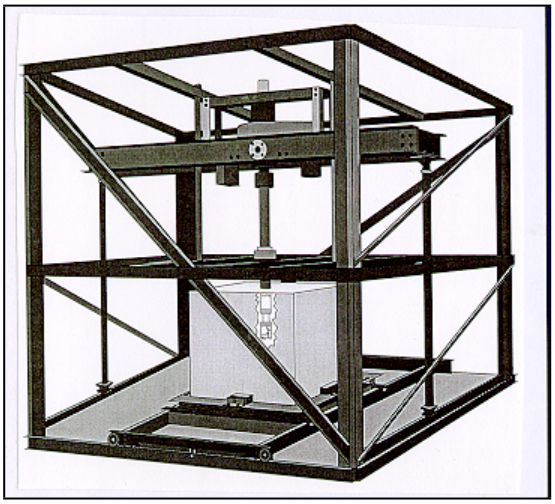

Figure 3-7. Sandia's Hard Rock Drilling Facility.

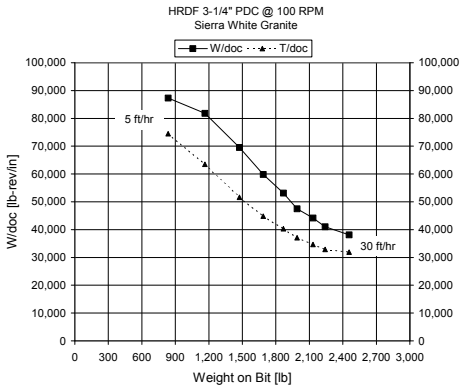

Figure 3-8. W/doc and T/doc vs. weight on bit for the HRDF 3-1/4" PDC bit.

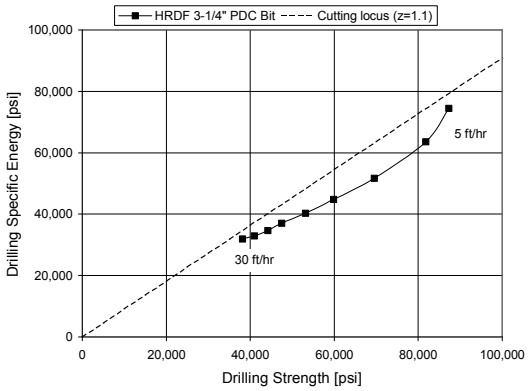

Figure 3-9. Drilling specific energy and drilling strength diagram for the HRDF 3-1/4" PDC bit.

By contrast, the "Tlusty model" assumes that the rock cutter interaction forces are a simple proportionality relationship. The DD model will be used herein to evaluate the onset of instability. The deviation of the bit response from the linear relation predicted by this model forms a basis for predicting the onset of vibration.

3.2. Numerical Drilling Simulations of Instability

The substructured drillstring models were expanded to provide real-time simulations of instability. As described in [Ref. 16], the mechanism that causes unstable longitudinal vibrations

in a drillstring involves a delay introduced by the drill bit's cutters repeatedly traversing the same angular positions over multiple revolutions. Therefore realistic simulations of this mechanism of instability must include models of the rotary and longitudinal cutter positions, a record of past cutter positions, and a rock-bit model that relates the instantaneous depth of cut (defined by the difference between the current longitudinal cutter position and the previous cutter position at the same angle) to the longitudinal force applied to the bit. Simulations have been developed using a simple spring-like rock-bit model as used in [Ref. 16], as well as the more complex, widely-accepted model for drag bit drilling found in [Ref. 10]. These real-time simulations could be used to design and simulate real-time controllers for variable stiffness or variable damping controllable elements.

Simulations were developed and performed for simple harmonic oscillator drillstring models, with and without an additional spring-mass-damper system in series. Thanks to the substructuring approach, it would be easy to extend the methods to more complex drillstring models. The simple harmonic oscillator matches that simulated in Reference 4, with a mass of 1613 lb. (732 kg), a stiffness of 5500 lb./in. (963000 N/m), and a damping ratio of 0.4, which produces the following FRF at the bit:

$$\frac{1/5500}{0.0007562s^2 + 0.022s + 1}$$

The added series module includes a spring of stiffness 3060 lb./in. (536000 N/m), a mass of 180 lb. (82 kg), and damping ratio also tuned to 0.4. The real and imaginary components of the FRF, with and without the additional module, are plotted along with the FRF magnitudes versus frequency in Figure 3-10. The addition of the spring module in series clearly increases the real portion of the FRF at frequencies up to approximately 13 Hz, and eliminates the negative real parts of the FRF in these frequency ranges. At higher frequencies, the opposite effect occurs, and the real part becomes more negative (this point will be discussed later).

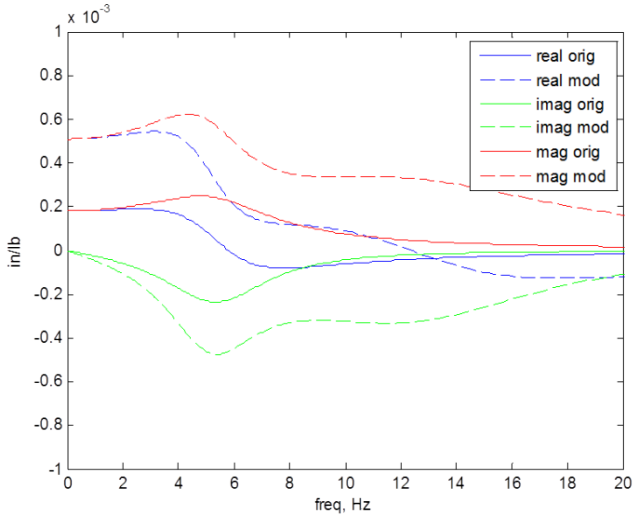

Figure 3-10. Real (blue), imaginary (green) and magnitude (red) components of frequency response function without (solid) and with (dashed) a stabilizing spring-mass-damper.

Using the substructuring approach described above, models of a simple harmonic oscillator with and without an additional series module, and interacting with rock through a bit, were implemented in Simulink. Top level block diagrams of these models are shown in Figure 3-11 and Figure 3-12. Figure 3-11 shows the simple harmonic oscillator without a series module. All of the drillstring dynamics are contained in the "G2 Dynamics" block. This block is coupled to a "RockBitDynamics" block that contains one of several mathematical representations that relate the instantaneous longitudinal bit velocity to the longitudinal force at the rock. Figure 3-12 shows a drillstring that includes the same simple harmonic oscillator in the "G2 Dynamics" block, but also includes a parallel spring-damper in the "Actuator Dynamics Spring" block and the added mass in the "G1 Dynamics" block. Again, this system interacts with one of several rock-bit models captured in the "RockBitDynamics" block.

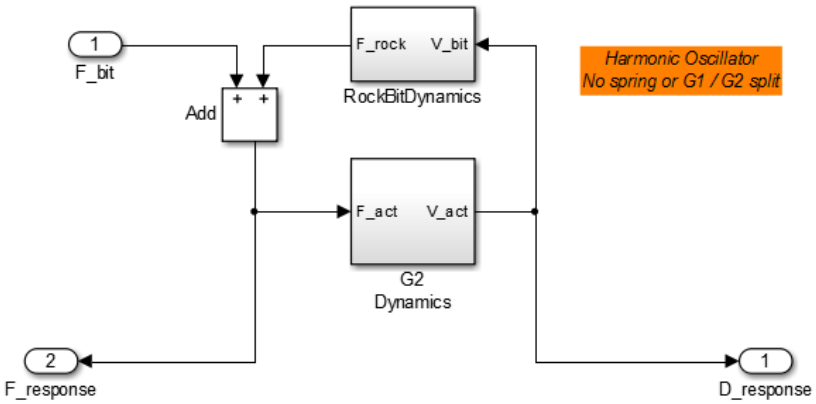

Figure 3-11. Simulink block diagram for simple harmonic oscillator simulation without additional spring / mass in series.

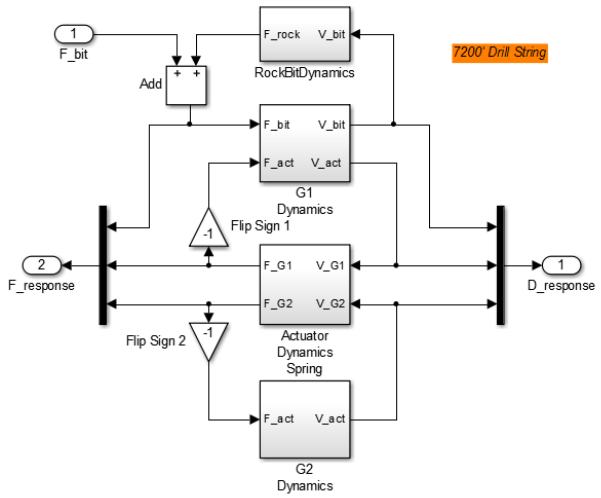

Figure 3-12. Simulink block diagram for simple harmonic oscillator simulation with additional spring / mass in series.

3.3. System Identification

To validate the Simulink representations of the substructured dynamic models with respect to instability models, system identification methods were applied to the simulated drillstring systems. A chirp force profile was applied in place of the bit, and the response force was measured and analyzed with Matlab's tfestimate function. The dynamics were found to match the analytically derived FRFs. The real portions of the simulated and analytically derived FRFs, both with and without the spring module, are plotted in Figure 3-13.

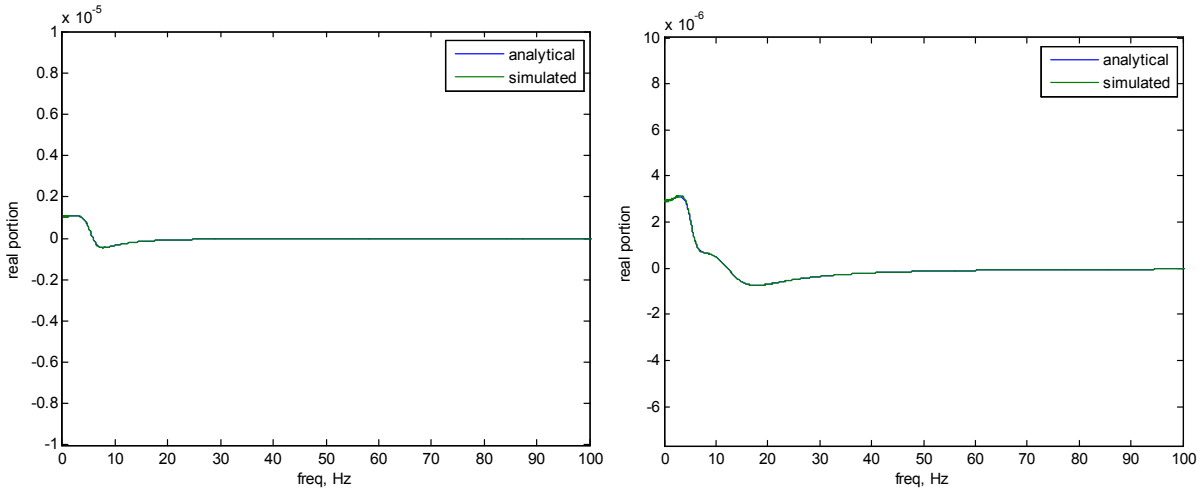

Figure 3-13. Comparison of simulated (green) and analytically derived (blue) real parts of transfer functions without (left) and with (right) additional spring and mass.

3.3.1. Real-Time Tlusty Instability Simulations

Initial simulations of induced instability used the simplified rock-bit interaction model used in [Ref. 16]. Equation 1 in [Ref. 16] defines the longitudinal reaction force applied to the drillstring by the rock as proportional to the depth of cut, the total length of the bit's cutting edges, and a constant termed the "specific cutting force" (K) which depends on rock strength. Thus for any given bit with a fixed length of cutting edge, the rock behaves like a spring, applying a force that is proportional to depth of cut.

Figure 3-14 shows a Simulink schematic of the rock-bit dynamic model that implements this Tlusty relationship. This code module takes in the instantaneous longitudinal bit velocity V_bit (in the lower left corner) and returns the instantaneous longitudinal reaction force applied by the rock F_rock (lower right). V_bit is immediately integrated and the rest of the calculations are based on the bit position "heightnew." The (fixed) angular velocity of the drill is specified for each run (Ang. Velocity block in the center left). The two Matlab Function blocks and the Lookup Table block in the center of the figure are used to store the geometry of the bottom of the hole from the previous pass, and to provide a means of looking up the cut position from the previous pass (heightold) based on the current angular position. The difference between the cutter's current position (heightnew) and its position on the previous pass (heightold) is the instantaneous depth of cut. This value is multiplied by the effective rock stiffness (determined by

using values from the literature for the specific cutting force K, and assuming a cutter length), producing the force F_rock, which is the instantaneous weight on bit.

This implementation includes several simplifying assumptions. First, the weight on bit and depth of cut are assumed to have zero bias, meaning that they may be either positive or negative at any point in time. In a real drilling application, there would be a positive bias weight on bit which would produce a positive depth of cut. Because the governing equations are linear, and we are only interested in vibrations, this assumption does not corrupt the results except that it does not account for the effects of the bit coming out of contact with the rock. Therefore the model is only valid if the bit stays in contact with the rock. A second simplifying assumption is that the bit has only one cutter, with a length equal to the bit radius. It is trivial to scale results to multiple cutters simply by dividing the simulation's angular velocity by the number of cutters – for example, the results from a bit with a single cutter operating at 20 rad/sec are equivalent to the results from a bit with 4 cutters operating at 5 rad/sec.

In order to induce nonzero vibrations, an initial "kick" is provided to the system via initial conditions stored in the "currState" Matlab Function block. This is equivalent to assuming that the bottom of the hole has an existing longitudinal pattern with which the bit interacts on its first revolution. Depending on the stability of vibrations, the initial condition response either grows or decays.

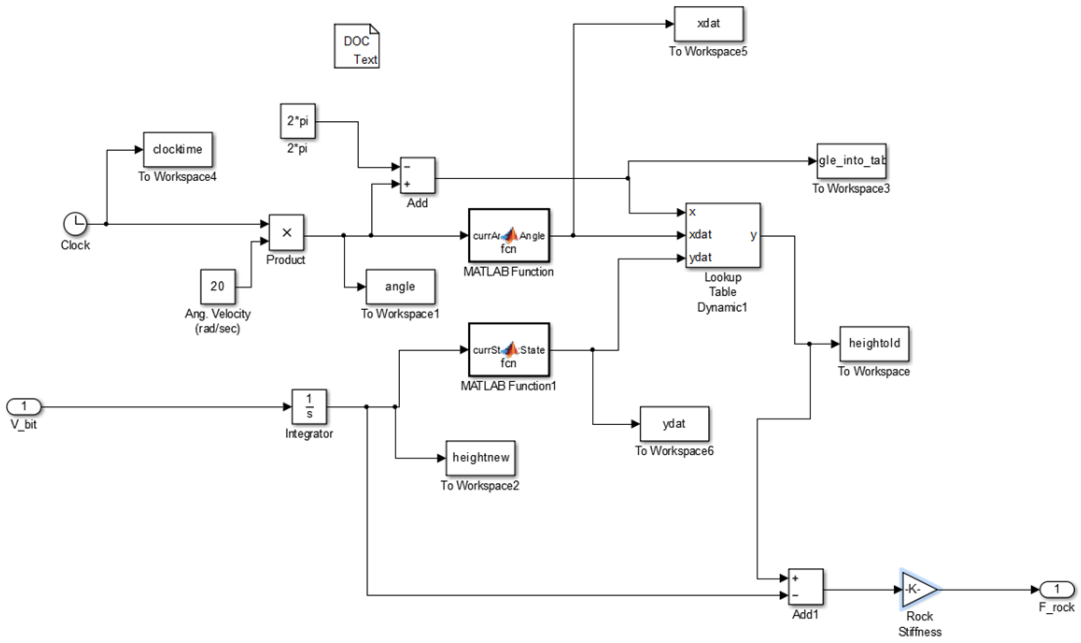

Figure 3-14. Simulink diagram of rock-bit interaction portion of Tlusty-based instability simulations.

As expected, the simulations produce both stable and unstable vibrations as the rotary speed and bit diameter are varied. Figure 3-15 shows examples of stable, decaying oscillations (left panel) and unstable, growing oscillations (right panel). In each case, the longitudinal bit position at the current time and on the previous revolution are plotted together to illustrate the alignment of the

bottom hole geometry between successive passes, which may provide some indication of whether vibrations are reinforced or suppressed by the cut geometry.

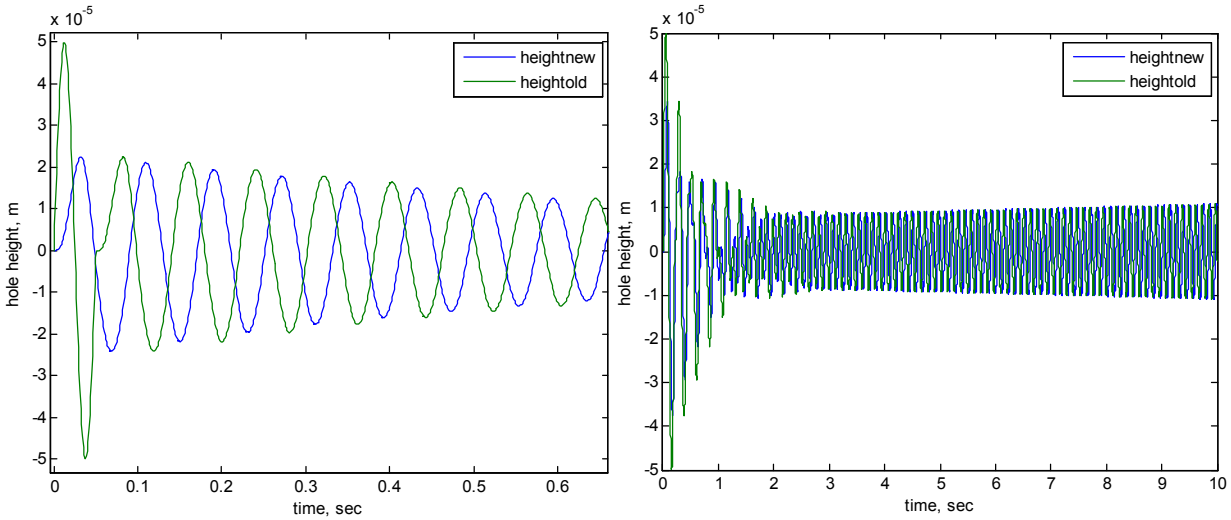

Figure 3-15. Examples of stable and unstable bit trajectories using Tlusty-based instability simulations.

To explore the variation in stability conditions and the effect of the series spring module, simulations were conducted across a wide variety of angular velocities. At each velocity, the bit diameter was varied. At small diameters, vibrations are stable, and at large diameters, vibrations are unstable. At each simulated angular velocity, the maximum bit diameter at which vibrations were stable was determined. Aggregate results, with and without the spring module, are plotted in Figure 3-16.

Figure 3-16 resembled the "lobing diagrams" in [Ref. 16]; however it is important to note a significant difference between the two types of diagrams. Figure 3-16 plots the stability boundary versus the *excitation* frequency. In contrast, the Tlusty analysis [Ref. 16] assumes that oscillations are present at each frequency, and then evaluates the stability limit in the presence of those oscillations. Therefore Tlusty's diagrams define *potential* or *necessary* conditions for instability, whereas Figure 3-16 documents *actual simulated stability boundaries*.

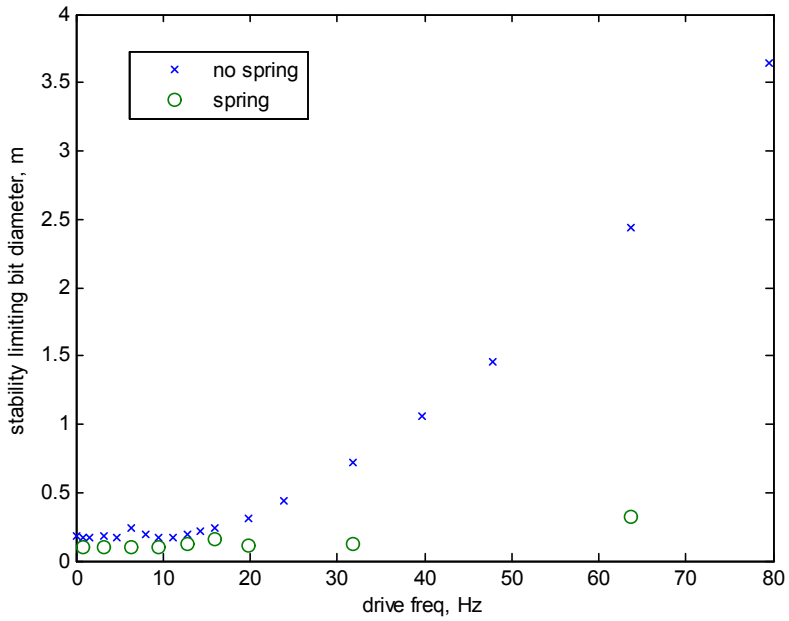

Figure 3-16. Maximum stable bit diameter versus drive frequency, with and without a stabilizing spring.

Figure 3-16 indicates that at all drive frequencies, the stability boundary occurs at smaller bit diameters with the spring module than without. Because the addition of the spring shifts the real value of the transfer function positive at frequencies below 12 Hz, intuitively one would expect this to improve stability, perhaps particularly at lower drive frequencies. However, there are several explanations that indicate there is greater nuance than the earlier literature (e.g., [Ref. 16]) may suggest.

One potential explanation is suggested by examining the dominant frequencies of the growing / unstable vibrations at the stability boundary for each drive frequency. These are plotted in Figure 3-17. When the spring module is present, all of the "unstable" vibrations occur at frequencies greater than 13 Hz. From Figure 3-10, we expect that oscillations at these higher frequencies will in fact be made less stable by the introduction of the spring. So if vibrations are excited at these frequencies (and the simulations appear to predict that they will be), the spring could have a destabilizing effect. If true, this suggests that the interaction between a series compliance and the drillstring is more nuanced than previously reported.

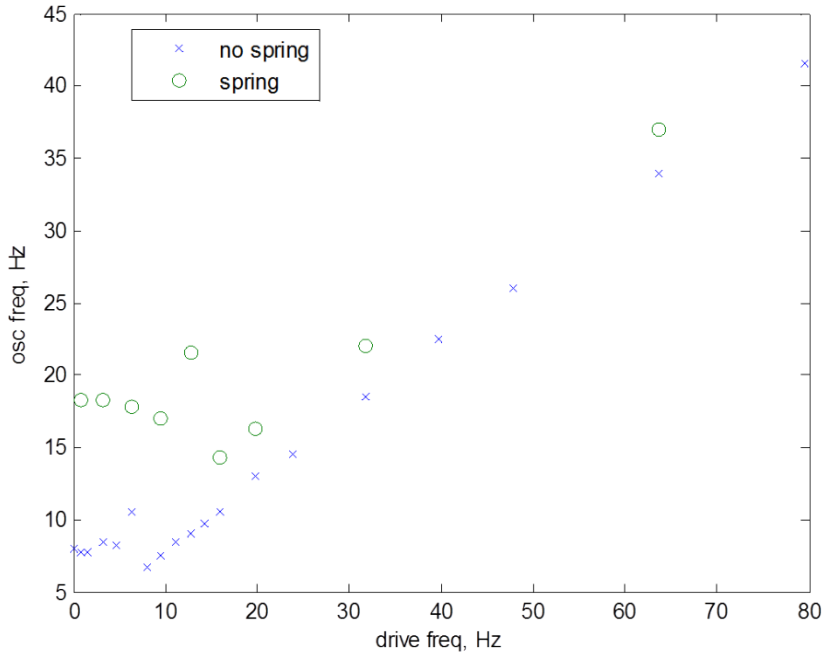

Figure 3-17. Approximate frequencies of dominant growing oscillations at the stability boundaries defined in Figure 3-16.

A second possibility is that this presentation incorrectly interprets the stability boundary from the simulations. For our purposes, we define vibrations as stable if their magnitude decays over time, and unstable if their magnitude grows over time. However, since the simulated system is greater than second order, multiple vibrations may come into play. Figure 3-18 shows an example that initially appears stable, but on a longer time horizon appears to be unstable. The initial gross oscillations decay steadily, but an initially smaller, high-frequency vibration emerges and grows over time. It is uncertain at this time whether this vibration is real or results from a numeric artifact. Furthermore, the determination of stability depends on the time horizon used. To generate Figure 3-16, a maximum time horizon (50 seconds) was assumed in order to limit simulation time. However, examples like that shown in Figure 3-18 cast some doubt on the results of Figure 3-16.

Ultimately, it is likely that both of these explanations apply to some extent. The higher-frequency oscillations may be initially induced through numeric issues (rather than from the system's physics), and then may grow because they are physically unstable. This would mean that the simulation is producing apparently unstable results when the system is physically stable. On the other hand, this does suggest that even if stable under normal conditions, the system is vulnerable to potential instability if higher-frequency vibrations are induced, even transiently. These results make clear that the selection of an optimal spring is nuanced, and trivial solutions such as just selecting the most compliant spring that is physical tolerable (as may be implied by a quick reading of [Ref. 16] are unlikely to succeed. This provides additional justification for the approach of making a wide range of spring rates available within a single down-hole tool, to enable stabilization under a wide variety of conditions without making physical changes to the drill that would require pulling the drillstring out of the hole.

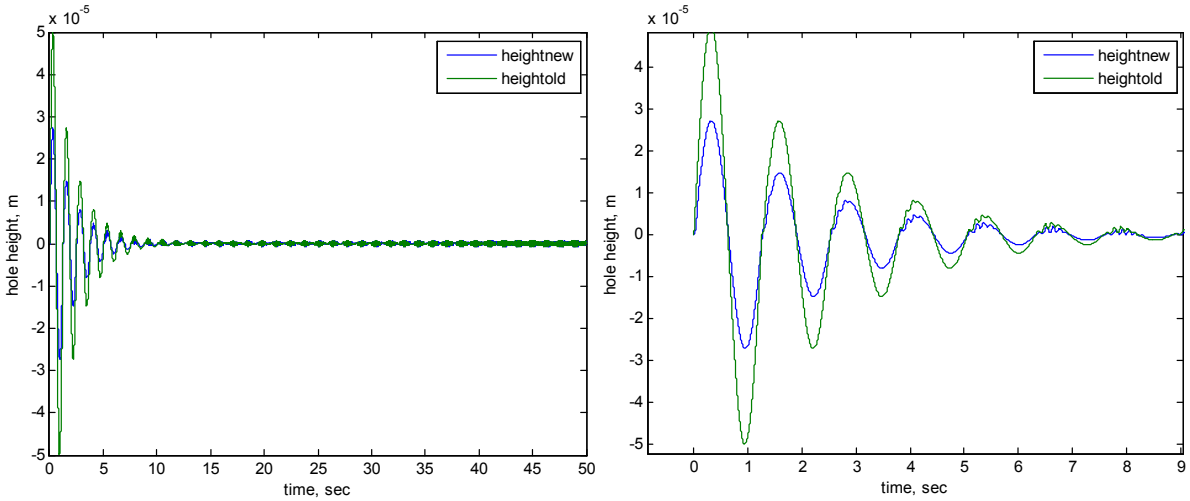

Figure 3-18. Uncertainty in defining stability from these simulations.

3.3.2. Integrated Tlusty / Detournay Instability Simulations

Additional simulations included a more sophisticated model for rock-bit interactions as described in Section 3.1 and presented in [Ref. 10, Ref. 11]. The model presented in [Ref. 10] defines a manifold on which rotary drag bit drilling conditions exist (the "friction line"). This manifold describes the interaction of both productive "cutting" interactions and frictional, lossy interactions between bit and rock. A subsequent contribution from the same lead author presents a complete set of linear relations between the weight on bit (or longitudinal force between rock and bit), the torque on bit, the rate of penetration, and the angular velocity [Ref. 11]. We have developed an implementation of this model that calculates the instantaneous weight on bit (force) from the instantaneous depth of penetration and the angular velocity. The angular velocity is assumed to be constant and set by an operator. The instantaneous depth of penetration is determined by comparing the current position of the bit to the cut position from the previous pass, just as described in the previous section. Thus this approach integrates, for the first time (to the authors' knowledge), an instability model derived from drillstring dynamics and a retained history of the bottom hole geometry, with the widely accepted Detournay model for rock-bit interactions.

Figure 3-19 shows a Simulink block diagram, analogous to Figure 3-14, of the rock-bit dynamics portion of the model that implements the Detournay model. Most of this diagram is identical to the Tlusty implementation, with the exception being the calculation of force from depth of cut shown in the lower right. In this case, the force depends on a set of parameters specific to the rock-bit model, captured in the "params" block, and on the angular velocity of the bit. The force is calculated using an embedded Matlab function that implements the Detournay model equations described above.

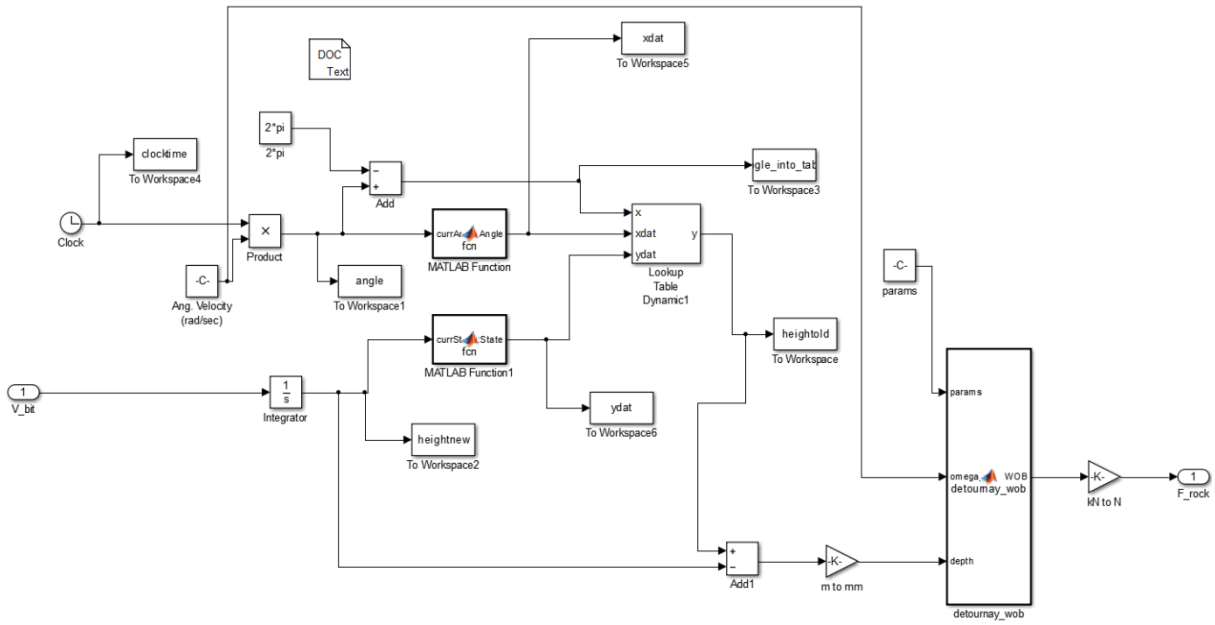

Figure 3-19. Simulink diagram of rock-bit interaction portion of Detournay-based instability simulations.

Additional simulations of drillstring vibrations were conducted using this revised rock-bit model. As before, the simple harmonic oscillator depicted in Figure 3-11 and Figure 3-12 was used as an example drillstring. In this case, simulations were conducted at a fixed rotary drilling speed (angular velocity), and the stiffness of a series spring was varied to explore the impact on the stability boundary. Under a particular set of drillstring dynamics and at a particular rotary drilling speed, vibrations are stable when the bit radius is small and eventually become unstable for larger bit radii. For the purposes of this analysis, the stability boundary is defined as the bit radius at which the vibrations are marginally stable.

Figure 3-20 shows a plot of this stability boundary versus series spring stiffness for a drill rotating at 4 rad/sec. The green line indicates the stability boundary for the baseline simple harmonic oscillator, with no series spring-mass-damper present. The blue circles indicate the stability boundaries for the same system with the addition of a spring-mass-damper module, with a mass of 180 lb., a stiffness that varies as indicated in the plot, and damper tuned to a damping ratio of 0.4 for the spring-mass combination. Figure 3-20 shows a very interesting result. Very soft springs actually make the system *less* stable, reducing the bit radius at which stability is maintained. Very stiff springs converge to the same limit as the nominal system; they introduce a high-frequency mode that does not affect stability. However, springs of intermediate values can significantly increase the radius at which stability is maintained (here by 50%). This shows that the selection of a spring may not be reduced to a trivial result (e.g. selecting the softest spring possible); in fact the “intermediate” valued springs that stabilize the system will vary dramatically with the drillstring dynamics. This strongly argues for the ability to make real-time adjustments to the stiffness, as we propose.

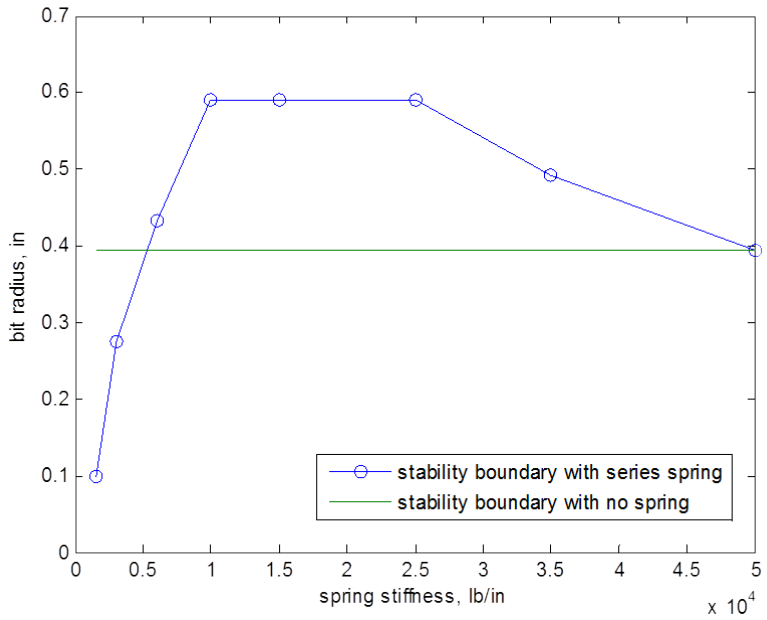

Figure 3-20. Plot of bit radius at which vibrations are marginally stable versus series spring stiffness.

This result may be further understood in the context of Tlusty's analysis [Ref. 16] by again examining the real portion of the transfer function versus frequency for each of these systems. These are plotted in Figure 3-21. Per Tlusty, in general the transfer function will be more stable at a particular frequency if the real portion is more positive. While soft springs (e.g. as shown by the green and red curves) dramatically increase the real portion at low frequencies, they significantly decrease the real portion starting at relatively modest frequencies. Our simulations predict that this will have a significant negative impact on stability, introducing unstable vibrations just above 10 Hz. On the other hand, the intermediate valued springs (k = 10,000 to 25,000 lb./in) tend to modestly boost the real portion across a broad range of frequencies, only reducing the real portion above ~25 Hz. The results shown in Figure 3-20, interpreted with the plots in Figure 3-21, indicate that the frequency region of 10-25 Hz is problematic for this particular oscillator system at this particular speed, and that an effective stabilizing spring must boost the real portion in this frequency range. This hints at a potential local control approach. The frequencies of the most problematic vibrations should be relatively easy to measure. The spring stiffness could then be selected (based on a model or system ID data from the drillstring) to boost the real portion of the transfer function in that specific frequency region.

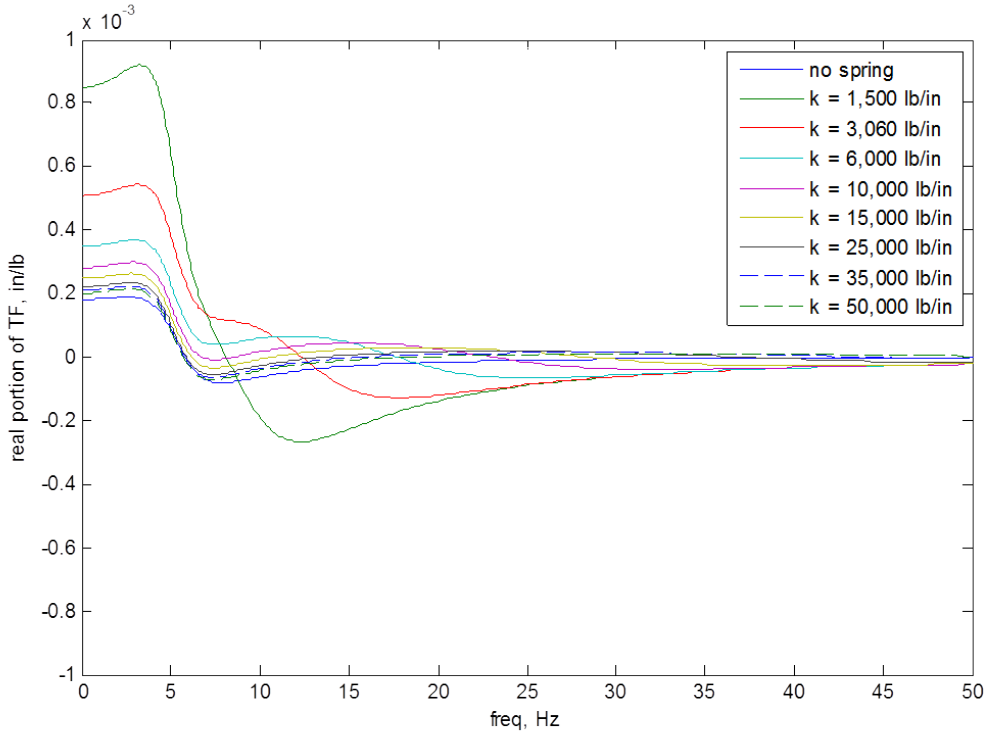

Figure 3-21. Real portion of transfer function versus frequency for baseline simple harmonic oscillator (solid blue line) and for harmonic oscillator with series spring-mass-damper with variety of stiffness values.

3.4. Time Domain Modeling with FEM/MBD

Another modeling approach investigated was application of the multi body dynamics (MBD) tools to the problem of drillstring vibrations. Since MSC. ADAMS MBD code was readily available at Sandia, it was selected as a modeling tool. Initial attempts to construct a model of the drillstring using native ADAMS elements, such as beams, were unsuccessful. Much better results were achieved by using ADAMS/Flex capability. The approach based upon ADAMS/Flex requires constructing the conventional FE model described earlier, then importing Craig-Bampton reduction of the model into ADAMS, augmenting flexible model with some additional features and performing the simulation in ADAMS. After drillstring FE model was imported into ADAMS, a forcing function defined by (Eq. 1-1) was added to the model and a simulation performed in the wide range of values of delay parameters to find both stable and unstable solutions. Results presented in Figure 3-22 include both stable and unstable vibration of the drillstring. While that effort was successful, it was not pursued any further because similar results were achieved already using the Matlab bar element model and the Simulink model for the stability analysis. As the complexity of the model grows, certain advantages of the MBD approach may become more significant. ADAMS for example has a great variety of specialized robust non-linear dynamics solvers compared to Simulink. Externally built FEM of the drillstring can be of any desired complexity and detail, while the custom Matlab bar element

model would be much more difficult to expand. For future development it is recommended to further explore switching to the MBD model with Simulink used to control it.

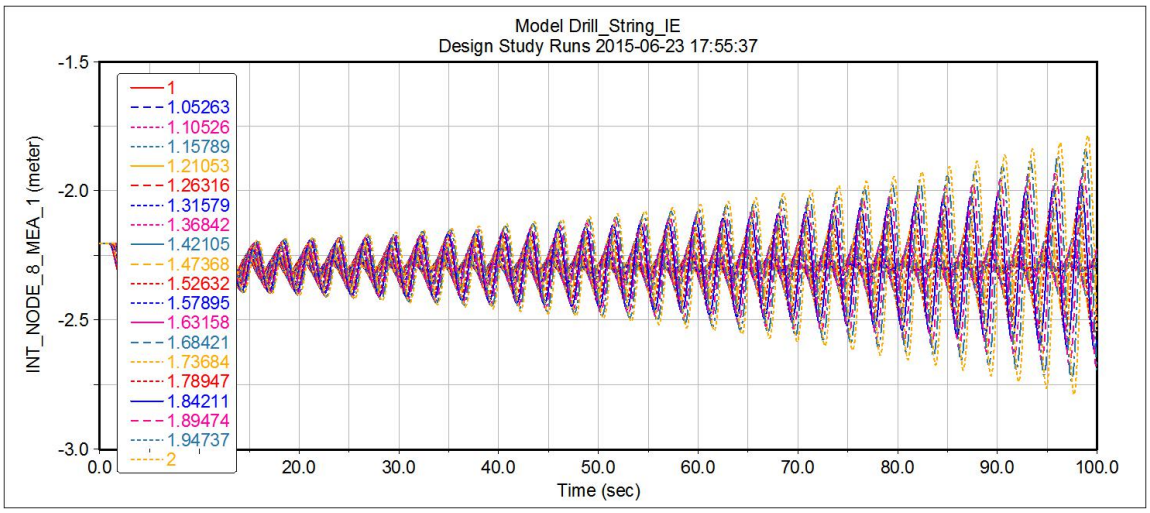

Figure 3-22. Onset of instability in Tlusty Drillstring as a Function of a Delay.

This page intentionally left blank.

4. HARDWARE DEVELOPMENTS & DEMONSTRATIONS

Hardware was developed to enable a detailed understanding of the limitations and benefits available by the introduction of controllable stiffness to a drilling assembly.

4.1. Variable Rate Spring (VRS) Prototype (Year 1 – Proof of Concept Demonstration)

A Variable Rate Spring (VRS) was designed and developed to accommodate fixture based testing on the benefits of a controllable spring installed in the bottom hole assembly (BHA) of a drillstring. Developing a variable rate spring in the form factor of a drillstring is challenging because the natural load path of such an element is serial through the drill stem. Combining these elements sequentially mandates that the stiffness will combine serially as well. That is, all spring elements will be subject to the same load. Physically, this means that the stiffnesses of the component springs will combine "in parallel" since their rates are subject to the same load. Ideally, one would like the stiffnesses to combine serially, such that a solid-state spring could be prescribed by selective activation of the preferred states. The form factor of a drillstrings makes this a challenge. Hence, considerable effort is required to conceive a solid state spring assembly that enables selective activation of the spring rate.

Sandia contracted with Radigan Engineering to design a prototype Variable Rate Spring, subject to Sandia specified design requirements. Design goals for the variable rate spring included the following:

- Spring rates between 20 lb./in. (3503 N/m) and 600 lb./in. (105000 N/m)
- Total weight less than 150 lb (68 kg)
- Less than 50 lb. (23 kg) moving mass
- Minimum of 2 in. (5 cm) available deflection
- Attachment points for "MTS" load frames and the Sandia Drilling Dynamics Simulator (DDS).

Five unique load rates were specified, roughly double between modules that allowed a solid-state spring to be designed as specified for the Drilling Dynamics Simulator (DDS) in Table 2-3. Target spring rates for the Variable Rate Spring were 20, 40, 80, 160 & 320 lb./in. (3500, 7000, 14000, 28000, & 56000 N/m) resulting in a controllable range of 520 – 8270 lb./ft. (7530 – 120660 N/m). Actual spring values of 22, 50, 96, 161 & 339 lb./in. (3583, 8757, 16813, 28196, & 59370 N/m) were identified and used. This allowed for 32 spring states, detailed in Figure 4-1 resulting in the net overall spring rate shown in Figure 4-2. The springs are located on a mandrel within each module stage (Figure 4-3), activated by a rotating spline (Figure 4-4), and stacked on a central shaft (fig ref). If the splines are aligned, motion is resisted by the module spring. If the splines are not aligned, the spline teeth pass through and do not engage the spring. The motion of the outer can of the assembly moves the bottom plate to potentially load lower spring modules as well. Photographs of actual components are shown in Figure 4-5 and Figure 4-6. The spring spindles are stacked upon one another around a central rod to form an integrated assembly (Figure 4-7). The assembly is fitted with a load cell and displacement transducer to monitor

response. The resulting design is shown loaded into a load frame in Figure 4-8. The design of the Variable Rate Spring (VRS) is documented in detail in 0.

Binary Load Selections

	Case 1		Case 2		Case 3		Case 4		Case 5		Case 6		Case 7		Case 8		Case 9		Case 10
	22 lbf/in		50 lbf/in		72 lbf/in		96 lbf/in		118 lbf/in		146 lbf/in		168 lbf/in		161 lbf/in		183 lbf/in		211 lbf/in
	44 lbf		100 lbf		144 lbf		192 lbf		236 lbf		292 lbf		336 lbf		322 lbf		366 lbf		422 lbf
1		2		3		4		5		6		7		8		9		10	
1	44	0	0	1	44	0	0	1	44	0	0	1	44	0	0	1	44	0	0
0	0	1	100	1	100	0	0	0	0	1	100	1	100	0	0	0	0	1	100
0	0	0	0	0	0	1	192	1	192	1	192	1	192	0	0	0	0	0	0
0	0	0	0	0	0	0	0	0	0	0	0	0	0	1	322	1	322	1	322
0	0	0	0	0	0	0	0	0	0	0	0	0	0	0	0	0	0	0	0

	Case 11		Case 12		Case 13		Case 14		Case 15		Case 16		Case 17		Case 18		Case 19		Case 20
	233 lbf/in		257 lbf/in		279 lbf/in		307 lbf/in		329 lbf/in		339 lbf/in		361 lbf/in		389 lbf/in		411 lbf/in		435 lbf/in
	466 lbf		514 lbf		558 lbf		614 lbf		658 lbf		678 lbf		722 lbf		778 lbf		822 lbf		870 lbf
11		12		13		14		15		16		17		18		19		20	
1	44	0	0	1	44	0	0	1	44	0	0	1	44	0	0	1	44	0	0
1	100	0	0	0	0	1	100	1	100	0	0	0	0	1	100	1	100	0	0
0	0	1	192	1	192	1	192	1	192	0	0	0	0	0	0	0	0	1	192
1	322	1	322	1	322	1	322	1	322	0	0	0	0	0	0	0	0	0	0
0	0	0	0	0	0	0	0	0	0	1	678	1	678	1	678	1	678	1	678

	Case 21		Case 22		Case 23		Case 24		Case 25		Case 26		Case 27		Case 28		Case 29		Case 30		Case 31
	457 lbf/in		485 lbf/in		507 lbf/in		500 lbf/in		522 lbf/in		550 lbf/in		572 lbf/in		596 lbf/in		618 lbf/in		646 lbf/in		668 lbf/in
	914 lbf		970 lbf		1014 lbf		1000 lbf		1044 lbf		1100 lbf		1144 lbf		1192 lbf		1236 lbf		1292 lbf		1336 lbf
21		22		23		24		25		26		27		28		29		30		31	
1	44	0	0	1	44	0	0	1	44	0	0	1	44	0	0	1	44	0	0	1	44
0	0	1	100	1	100	0	0	0	0	1	100	1	100	0	0	0	0	1	100	1	100
1	192	1	192	1	192	0	0	0	0	0	0	0	0	1	192	1	192	1	192	1	192
0	0	0	0	0	0	1	322	1	322	1	322	1	322	1	322	1	322	1	322	1	322
1	678	1	678	1	678	1	678	1	678	1	678	1	678	1	678	1	678	1	678	1	678

Figure 4-1. Binary load selections available from 32 state spring.

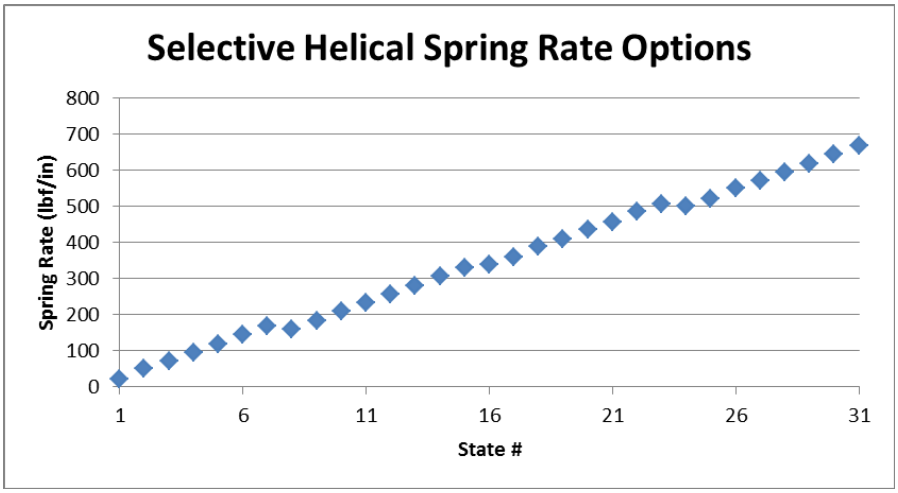

Figure 4-2. Net spring rate corresponding to spring state activation.

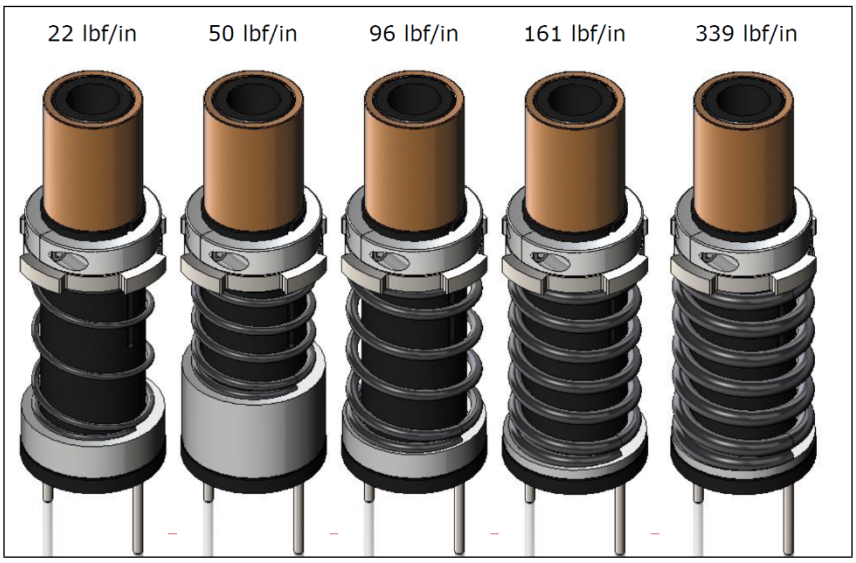

Figure 4-3. Stage Modules comprising Variable Rate Spring Assembly.

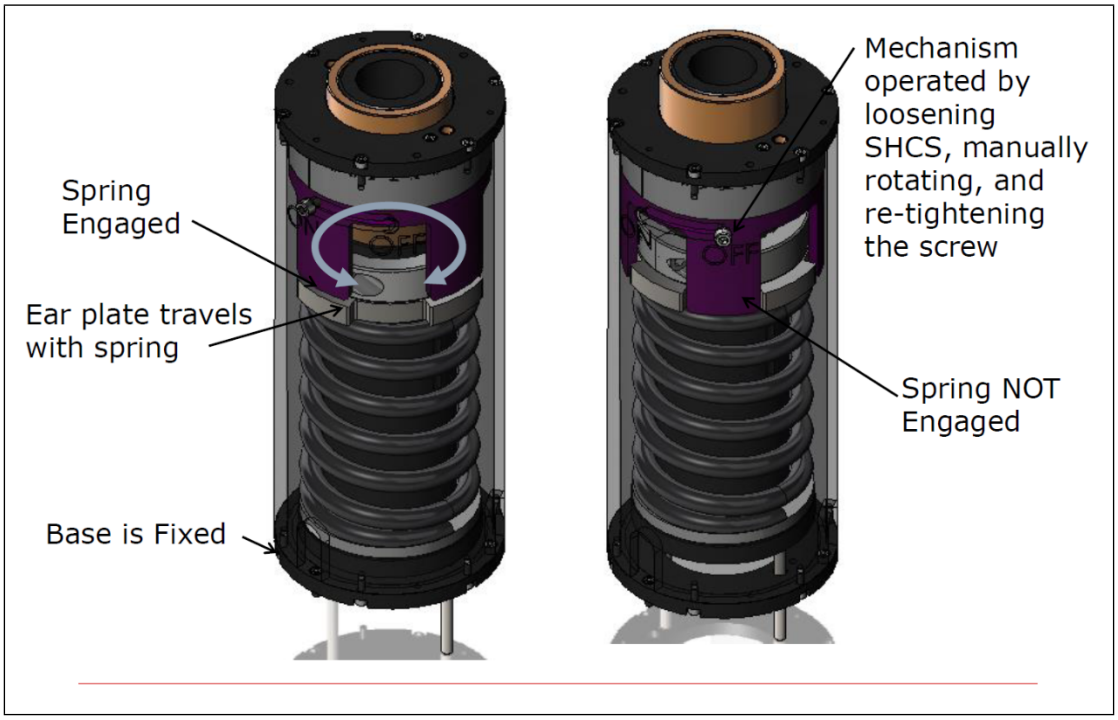

Figure 4-4. Stage module activation mechanism.

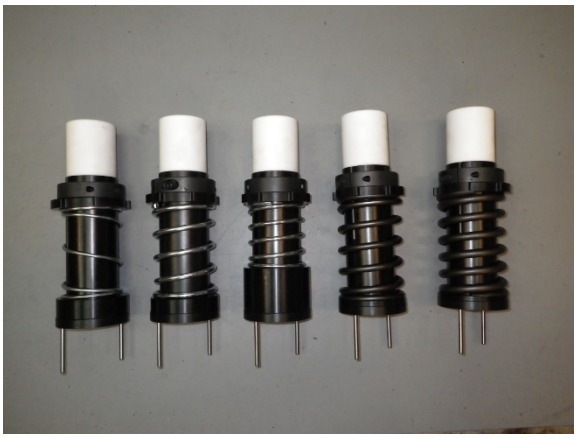

Figure 4-5. VRS – Multiple Modules.

Figure 4-6. VRS – Module Components.

Figure 4-7. VRS Completed Assembly.

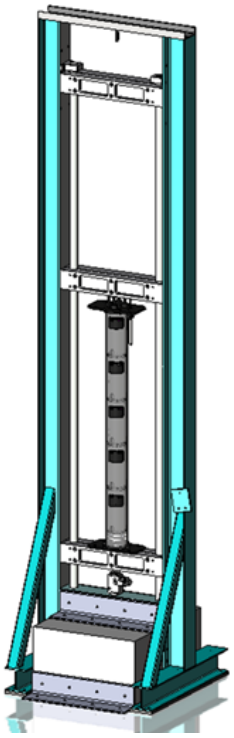

Figure 4-8. Variable Rate Spring Assembly illustrated as installed in developmental DDS Load Frame.

4.2. DDS Development (Year 1 – Proof of Concept Demonstration)

4.2.1. Drilling Dynamics Simulator Summary

The Drillstring Dynamics Simulator (DDS) will be used to demonstrate and evaluate developmental concepts for active suppression of drilling vibrations. The DDS will accommodate critical function evaluation of developmental concepts in scaled settings under representative drilling vibration conditions. These results will be used to advance overall designs that can be tested in a more prototypical actual drilling configuration.

The Sandia Drillstring Dynamics Simulator (DDS) described in Section 2.3.2 is designed and constructed to reproduce the frequency response of a drillstring in a laboratory setting. The simulator consists of a spring-mass system (Figure 2-12) designed to represent a scaled frequency response function (FRF) of the Tlusty drillstring in a structural steel frame (Figure 2-13). A variable rate spring can be introduced below the spring-mass system to evaluate the influence on the transfer function.

At the start of the LDRD project, the DDS consisted only of a structural steel frame that had been used previously for loading test specimens. The Drilling Dynamics Simulator consists of various subsystems, described in greater detail in the following sections. The vibration suppression concepts are introduced and monitored to facilitate detailed understanding of their response.

4.2.2. DDS Structure

The DDS structure is comprised of the following components:

- Frame: A specially designed structural steel frame is used to support the test articles and the spring-mass simulation of the drillstring. It includes guide shafts that are supported on structural steel columns. It was designed and manufactured by Sandia personnel in Organization 06916. The frame is anchored to the slab and a large rock is situated between the rails and used as the reaction mass within the assembly. Mounting holes in the surface of the rock support hinges that allow the guide shaft assembly, or "mast," to be rotated with respect to the frame. A structural stability and stress analysis was conducted to evaluate the safety of mast rotation.

- Mast: The mast consists of the parallel guide shafts with bushings and beams mounted on the guide shafts to support the springs, and masses comprising the drillstring simulation. The mast of the DDS is mounted on hinges so the mast can be lowered to accommodate insertion of the spring mass assembly and the vibration suppression concepts to be tested. A winch and load arrestor, described below, are used to accommodate this process. This rotation feature is included as an engineered safety mechanism in the overall design intent of the test layout to protect personnel from overhead masses when preparing test setups within the DDS assembly.

- Winch System: A winch is used to provide the motive force to raise and lower the mast. The winch is mounted on the frame rail and wire rope extends over a clevis at the top of the frame to allow the mast to be raised and lowered to accommodate accessing components. The winch is rated for a 1500 lb. (6670N) tensile load; this capacity exceeds the maximum load anticipated by the test operation for the lifting/lowering operation (see Stress Analysis of Frame).

- Clevis: The clevis is mounted to the upper structural support and is used to support the mast during raising and lowering operations; it is rated at 4000 lb. (17800 N).

- Load Arrestor: A load arrestor act as a load restraint to ensure the mast load is restrained in the event of an unplanned failure of the winch system. Should this mode of failure occur, the operator would refrain from further use of the mast operations until the load has been properly supported. The load arrestor is mounted at the top of the structural steel frame.

- Upper Structural Support: A specially designed structural support system has been designed to support the load arrestor on the top of the DDS frame; it is designed for a load rating of 5000 lb. (22000 N) in accordance with manufacturer's specifications.

- Mezzanine: A personnel platform is used to access the upper heights of the DDS. It is an OSHA-compliant design. It has not been modified from manufacturer's specifications.

4.2.3. Xcite Systems Integration

The DDS is fitted with XCite Systems actuators as described below:

- Xcite Actuator (Exciter Head): The Xcite systems actuators are used to provide a known force or displacement input to the drilling simulation. These inputs can be operated under either load control or stroke control. It consists of a hydraulically driven actuator with an integral fast-acting servo hydraulic valve. The valve is controlled by an input line from the master controller. The actuator is equipped with an integral load cell and displacement transducer to monitor response.

- Hydraulic Power Unit (HPU): A Hydraulic Power Unit (HPU) is used to generate fluid power to drive the Xcite systems actuator. It consists of variable volume, pressure-compensated pump loop. The variable volume pump produces approximately 15 gpm (0.95 L/s) at 3000 psi (20.6 MPa). It includes a low-volume pressure relief valve at the output of the pump. A pressure relief valve is included on the HPU for overpressure relief. Hydraulic hoses are used to route hydraulic fluid supply and return flows from the HPU to the DDS actuators.

- Master Controller: The master controller is used to provide input control signals to the HPU for startup/shutdown and to the actuator for rod control. The master controller provides voltage control to the Xcite actuator to control response in either load control or stroke control. The master controller has an interface to the control computer used to

control the testing. The HPU can be disabled using plug and cord via a pin-sleeve connection to the electrical facility connect. The system is disconnected from the 480V source to maintain the unit. When powered for service, the HPU is controlled from the master controller.

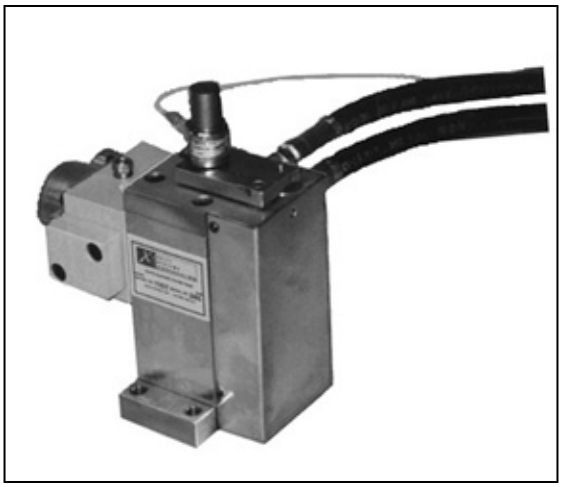

Figure 4-9. Servo-hydraulic Actuator (Exciter).

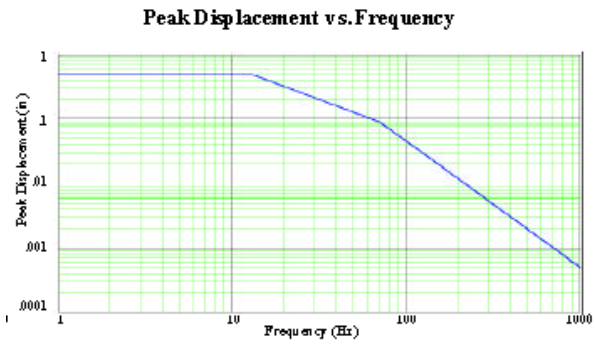

Figure 4-10. Xcite Systems Exciter – Displacement Capability.

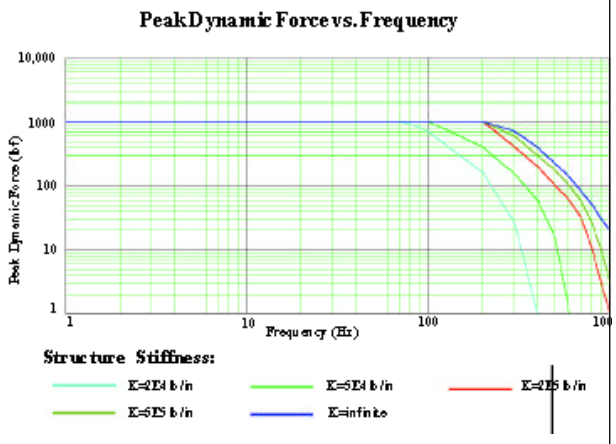

Figure 4-11. Xcite Systems Exciter – Load Capability.

Figure 4-12. Xcite Systems Master Controller

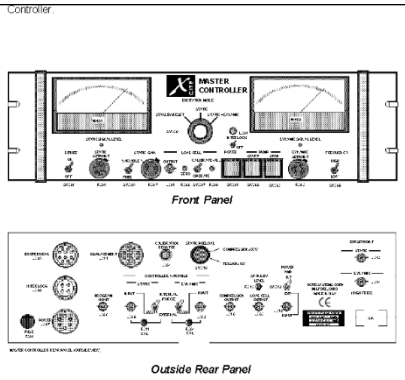

Figure 4-13. Master Controller – Front and Back Panels

4.2.4. Data-Acquisition/Control System

A personal computer-based data acquisition system is used to monitor the operating conditions of the Drilling Dynamics Simulator. The system is setup within the facility on an anthro-cart and connected to facility power. A 19-inch equipment rack is used to house the master controllers and the data acquisition interface cards. The display system consists of a Dell computer with a Windows 7 operating system. A monitor is used for both workstation control programming and data display. The display system is based upon a National Instruments Lab View processor developed by Prime Core. The display system reads data from the Xcite actuators and a variety of sensors deployed throughout the DDS system. A variety of plotting options can be user-configured to track parameters of interest. The computer is used to control the force and displacement inputs into the actuator; it also operates in a monitoring mode to record the acceleration and displacement response of the spring mass system with the DDS in addition to various other parameters of interest throughout the system. Force and displacement outputs from the computer are fed to the Master Controller. The master controller provides the appropriately conditioned output and connects directly to the Xcite Systems actuator. A variety of sensors are deployed throughout the DDS to monitor performance. These sensors include accelerometers, displacement transducers, and load cells. A data acquisition system was installed on the DDS as per the following table (Table 4-1).

Table 4-1. DDS DAQ System.

Compact DAQ layout

Slot	1	2	3	4	5	6	7	8
Card	NI-9469 Chassis Sync	NI 9234 Accel	NI 9234 Accel	NI 9234 Accel	NI 9219 Universal I/O	NI 9219 Universal I/O	NI 9402 Timer Access	
Channels		4	4	4	4	4	4	

Slot	1	2	3	4	5	6	7	8
Card	NI-9469 Chassis Sync t	NI 9229 Analog Input	NI 9229 Analog Input	NI 9269 Analog Output	NI 9269 Analog Output	NI 9402 Timer Access		
Channels		4	4	4	4	4		

Summary

Type	Channels	Bits	Rate per Channel (K)
Accelerometer	12	24	51
DAC Voltage	8	16	25
ADC Voltage	8	24	50
Universal I/O	8	24	.1
Counter/Timers	8	32	

4.2.5. Tlusty Equivalent Simulation

The physical construction of the DDS differs somewhat from the modeled description in Section 2. An additional spring was added grounding Mass 6 directly to Mass 2 for improved mechanical function. Also, the notation of Masses 5 and 6 were flipped in the Section 2 model with respect to the constructed fixture but the symmetry of the system led to no effect on the derived modes. The spring-mass diagram for the constructed system and relevant dynamics derivation are below. Table 4-2 compares the computed mode frequencies from the below model using mass and spring rate values from Table 2-3 to the model described in Section 2 and to the physically measured mode frequency values from the constructed system.

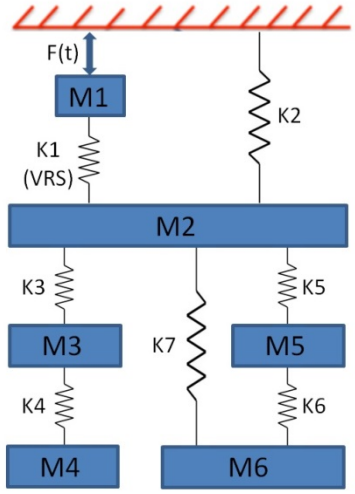

Figure 4-14. Modal equivalent spring-mass diagram of constructed DDS system.

Table 4-2. Computed vs Measured Mode Frequency Comparison.

Computed From Original Model (Hz)	Computed w/ Additional Spring (Hz)	Physically Measured (Hz)
0.59	0.59	x
1.06	1.06	1.2
2.2	2.2	2.6
2.41	2.4	2.6
9.23	15.7	15
28.3	28.7	28

$$M\frac{d^2}{dt^2}\begin{bmatrix}x_1\\x_2\\x_3\\x_4\\x_5\\x_6\end{bmatrix}=\begin{bmatrix}-k_1 & k_1 & 0 & 0 & 0 & 0\\ k_1 & -(k_1+k_2+k_3+k_5+k_7) & k_3 & 0 & k_5 & k_7\\ 0 & k_3 & -(k_3+k_4) & k_4 & 0 & 0\\ 0 & 0 & k_4 & -k_4 & 0 & 0\\ 0 & k_5 & 0 & 0 & -(k_5+k_6) & k_6\\ 0 & k_7 & 0 & 0 & k_6 & -(k_6+k_7)\end{bmatrix}\begin{bmatrix}x_1\\x_2\\x_3\\x_4\\x_5\\x_6\end{bmatrix}$$

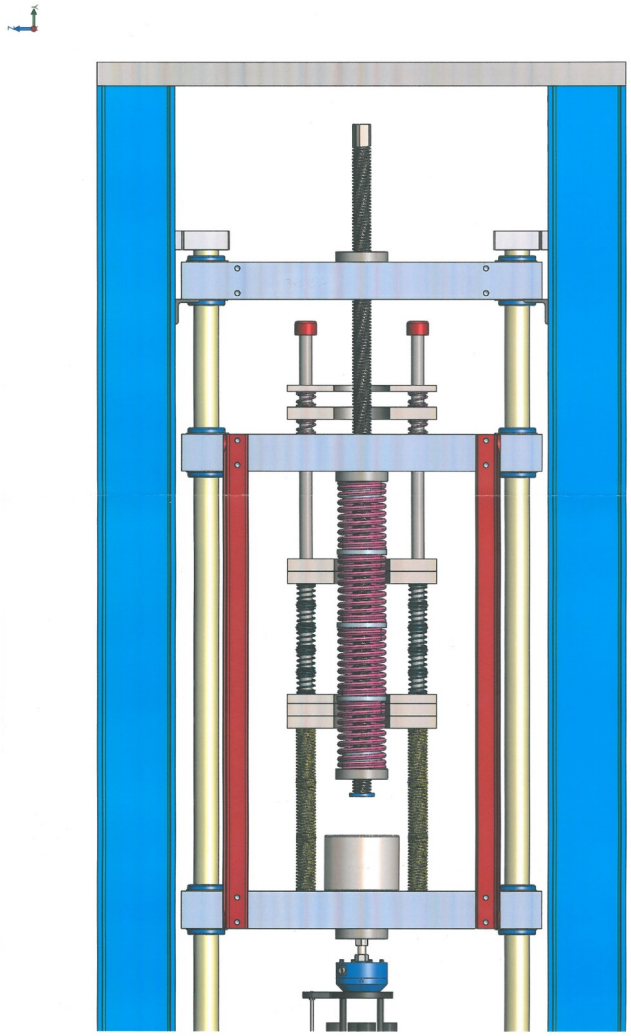

Figure 4-15. Spring-Mass SolidWorks Representation of Tlusty Equivalent.

4.3. DDS/VRS Integration & Testing (Year 1&2 – Proof of Concept Demonstration)

Integration of the VRS into the DDS was a multi-step process. The DDS was characterized in the "stiff" configuration using a solid rod attaching the Mass 1 to Mass 2. This simulated the DDS without any effect of the spring. Afterwards, the solid rod was replaced with the VRS to demonstrate the impact of the variable spring stiffness on the DDS dynamic behavior.

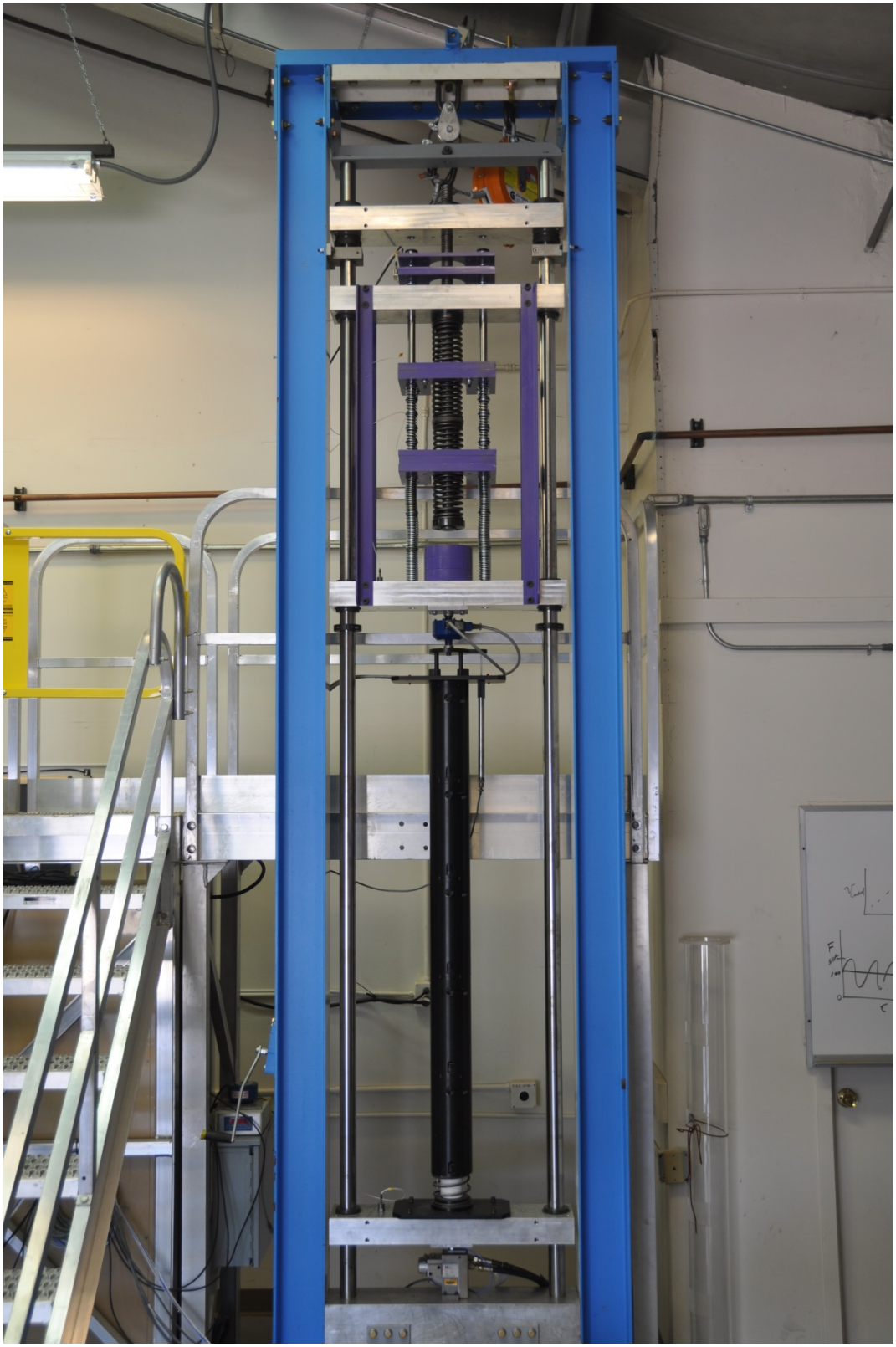

Figure 4-16. Photograph of the DDS with the VRS installed ready for testing.

4.3.1. Excitation and Measurements

Several excitation methods were used to drive the bottom actuator. These included random excitation and overlaid sinusoids. The random excitation signal was generated using the Matlab rand() function. The sampling frequency was 1024 Hz. A digital filter was used to limit the frequency content of the excitation signal. For the expected frequency response range of the DDS, a 50 Hz cutoff was used. A typical excitation signal is shown in Figure 4-17 below.

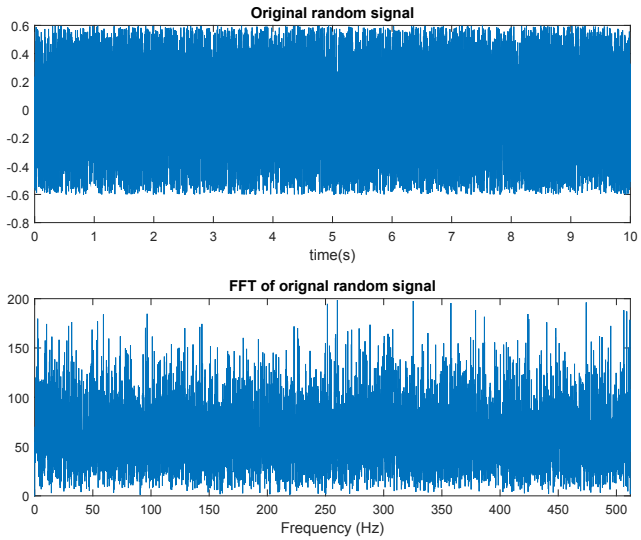

Figure 4-17. Random excitation signal pre-filtered

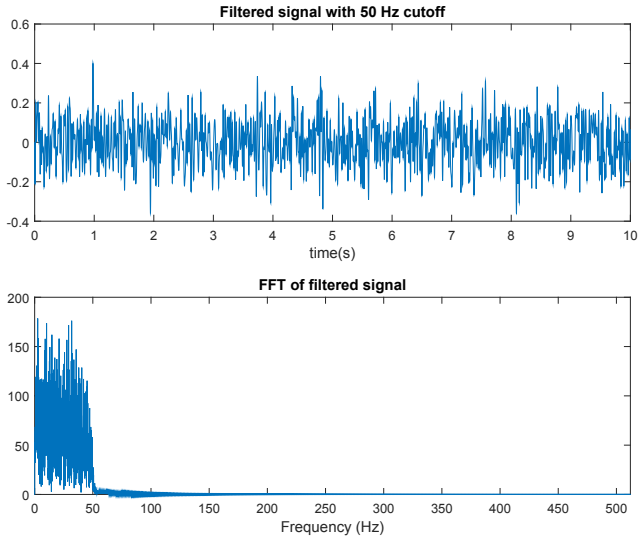

Figure 4-18. Filtered excitation signal with 50 Hz cutoff

4.3.2. FRF Characterization & Identification (DDS System ID)

Initial System Identification Experiments

A series of system identification experiments were conducted on the DDS, with two goals: to characterize the as-built dynamics and FRF of the DDS, and to begin experimentally exploring the feasibility of conducting system identification on a drillstring-like system. For these experiments, the Xcite actuator was used to generate controlled position trajectories with broadband frequency content (e.g. pseudorandom or chirp trajectories) at the base of the DDS. The induced response forces were measured using two load cells connected by rigid elements: one load cell that is integral to the Xcite actuator, and a second load cell at the base of the VRS. It was expected that these two load cells would produce very similar results.

In initial experiments, the coherence was poor at low frequencies. Figure 4-19 shows the coherence versus frequency for identification using the Xcite load cell (left) and the VRS load cell (right). The system was excited with frequency content nominally ranging from 0.01 Hz to 100 Hz. With the Xcite load cell, the coherence is below the desired level (~0.9) for all frequencies below 6 Hz. The coherence using the VRS load cell is even worse, and is below 0.9 for all frequencies below 20 Hz.

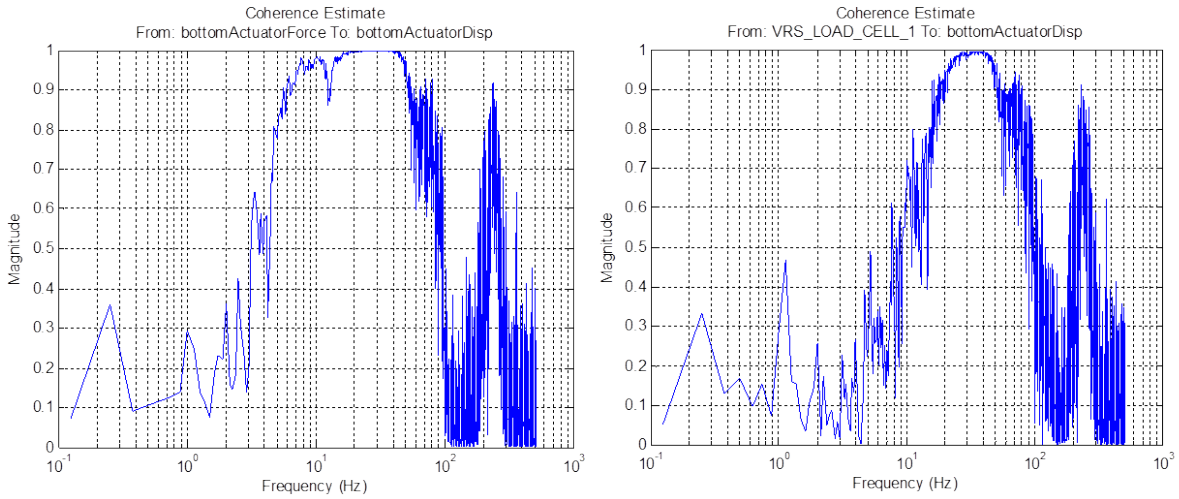

Figure 4-19. Coherence versus frequency for initial DDS system identification experiments. Data using Xcite load cell (left) and VRS load cell (right).

The resulting FRF estimates are plotted in Figure 4-20 for both load cells. The vertical green lines indicate the regions of high coherence, which is the only range in which the estimates should be trusted. The estimate from the Xcite load cell indicates a resonance in the 12-13 Hz range. The estimate from the VRS load cell indicates a possible resonance in the 30 Hz range. The possible modes that appear are highly damped, and there is little evidence of the other expected modes. Because the two load cells are coupled by a very rigid member, it is unclear why they produce such different results. Regardless, the estimates from these initial experiments were disappointing in that they did not reflect most of the dynamics intended to be implemented.

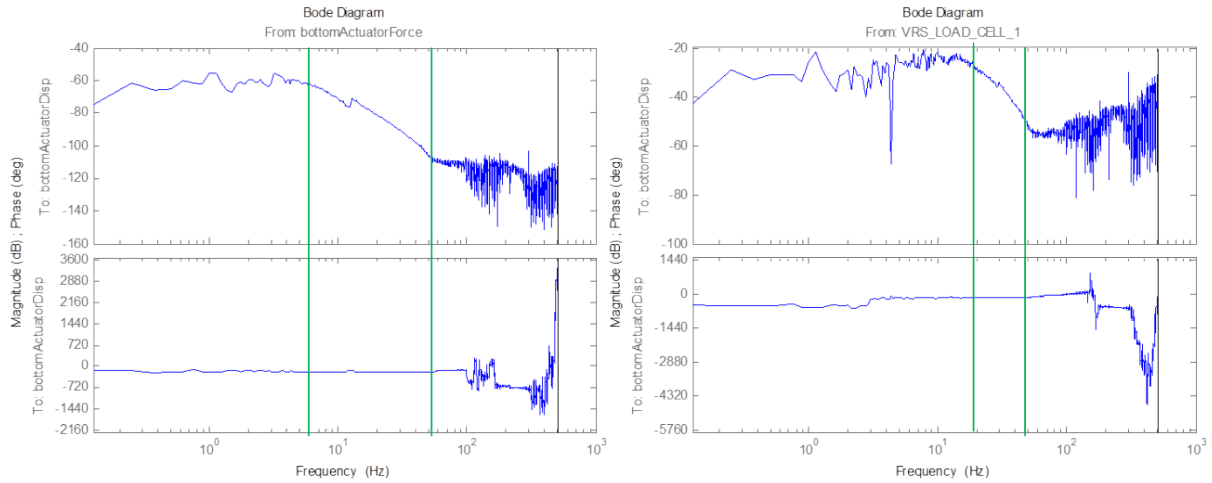

Figure 4-20. Estimated DDS FRF magnitude and phase from initial system identification experiments. Xcite load cell (left) and VRS load cell (right).

Improvements to DDS and System Identification Process

A number of changes were explored in order to improve both the function of the DDS and the system identification process. An effort was undertaken to improve the alignment and reduce friction in the DDS. Adjustments were made to the alignment of the main parallel guide shafts. Lubricated bronze bushings were used as shaft guides for the moving masses in place of the original Delrin guides (Figure 4-21).

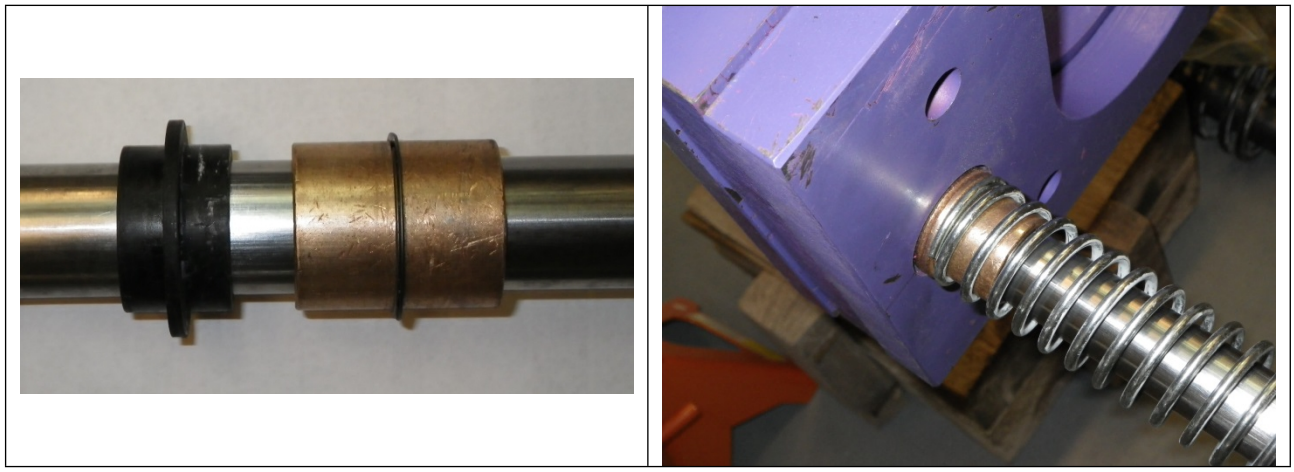

Figure 4-21. Delrin shaft guides vs. lubricated bronze guides.

The Xcite actuator includes several settings that were systematically optimized for improving system identification. With these changes in place, the signal coherence was improved throughout the interest frequency, particularly at lower frequencies.

In addition to the physical changes, the configuration of the Xcite actuator and data acquisition system was explored. The Xcite actuator includes several settings that are not fully understood.

Experiments were conducted that varied Xcite's "high / low" setting and turned "dither" on and off. These did not have a significant effect on system identification outcomes. A filter on the data acquisition system was removed. Additionally, the overall frequency response data was collected in segments in an attempt to improve the signal to noise ratio at low frequencies.

With these changes in place, new data was taken. The results of the system improvements and data collection techniques are shown below. The DDS was excited by sin sweeps in three overlapping frequency ranges: 0.1Hz-6Hz, 3Hz-20Hz, and 5Hz-35Hz.

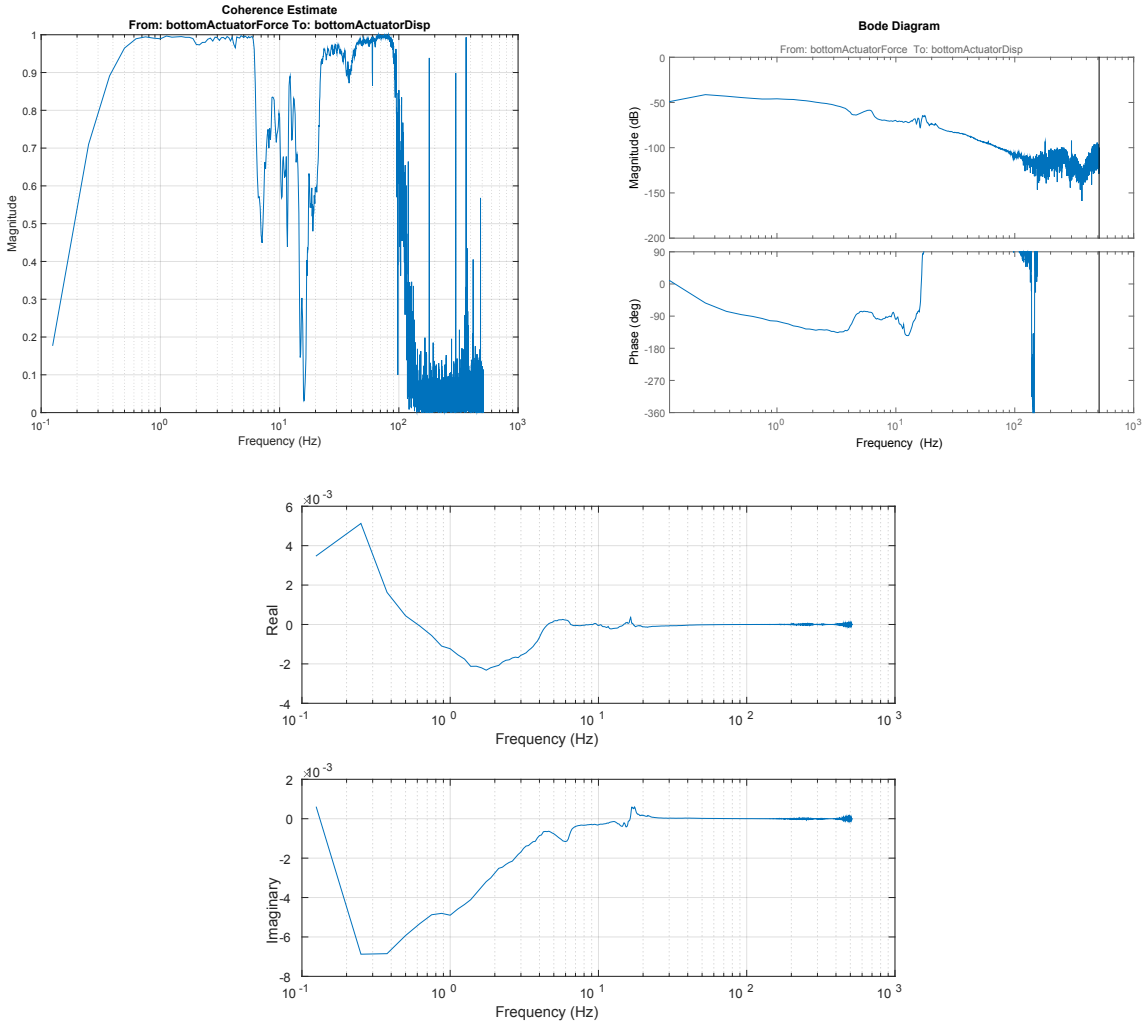

Figure 4-22. Sin sweep excitation 0.1Hz - 6Hz.

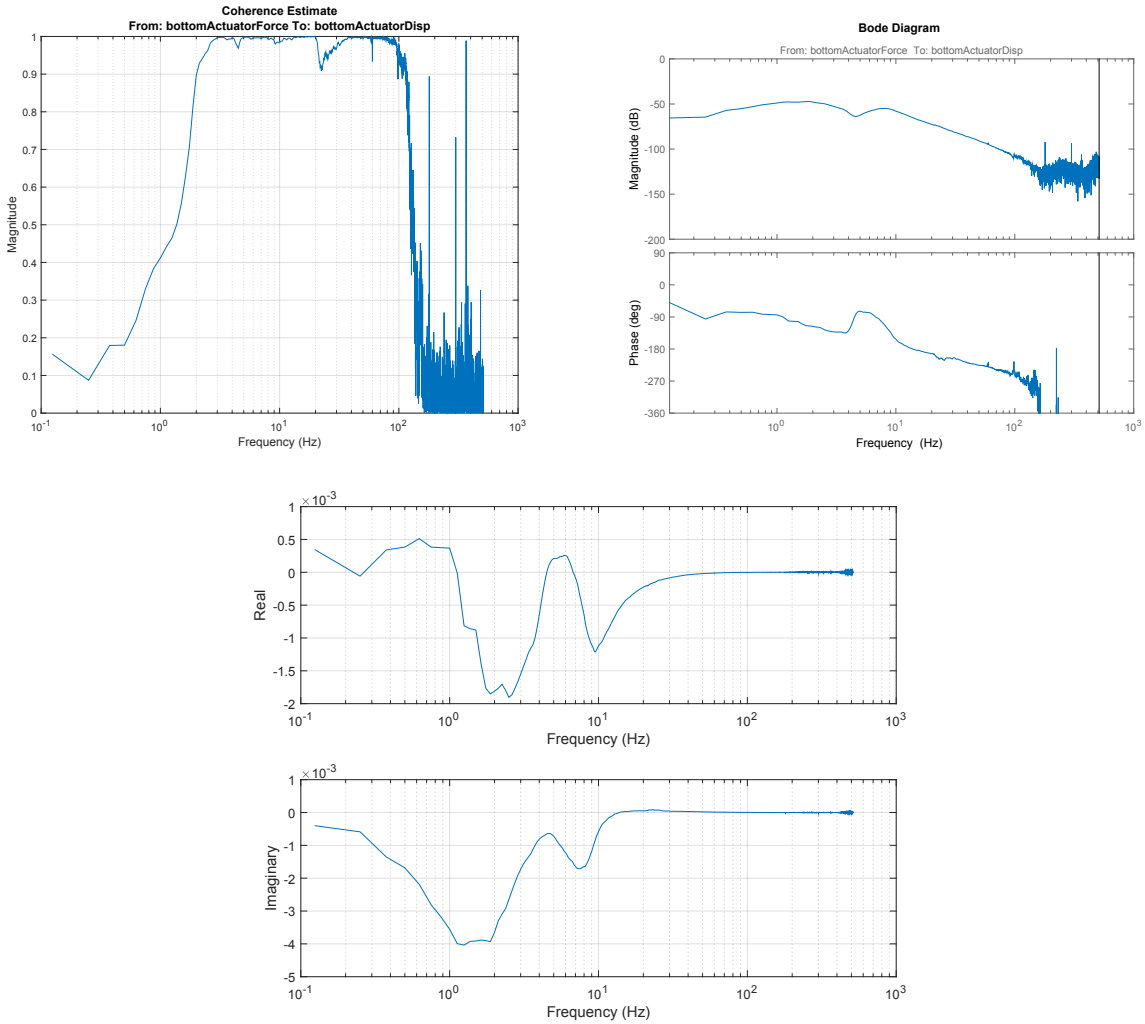

Figure 4-23. Sin sweep excitation 3Hz - 20Hz.

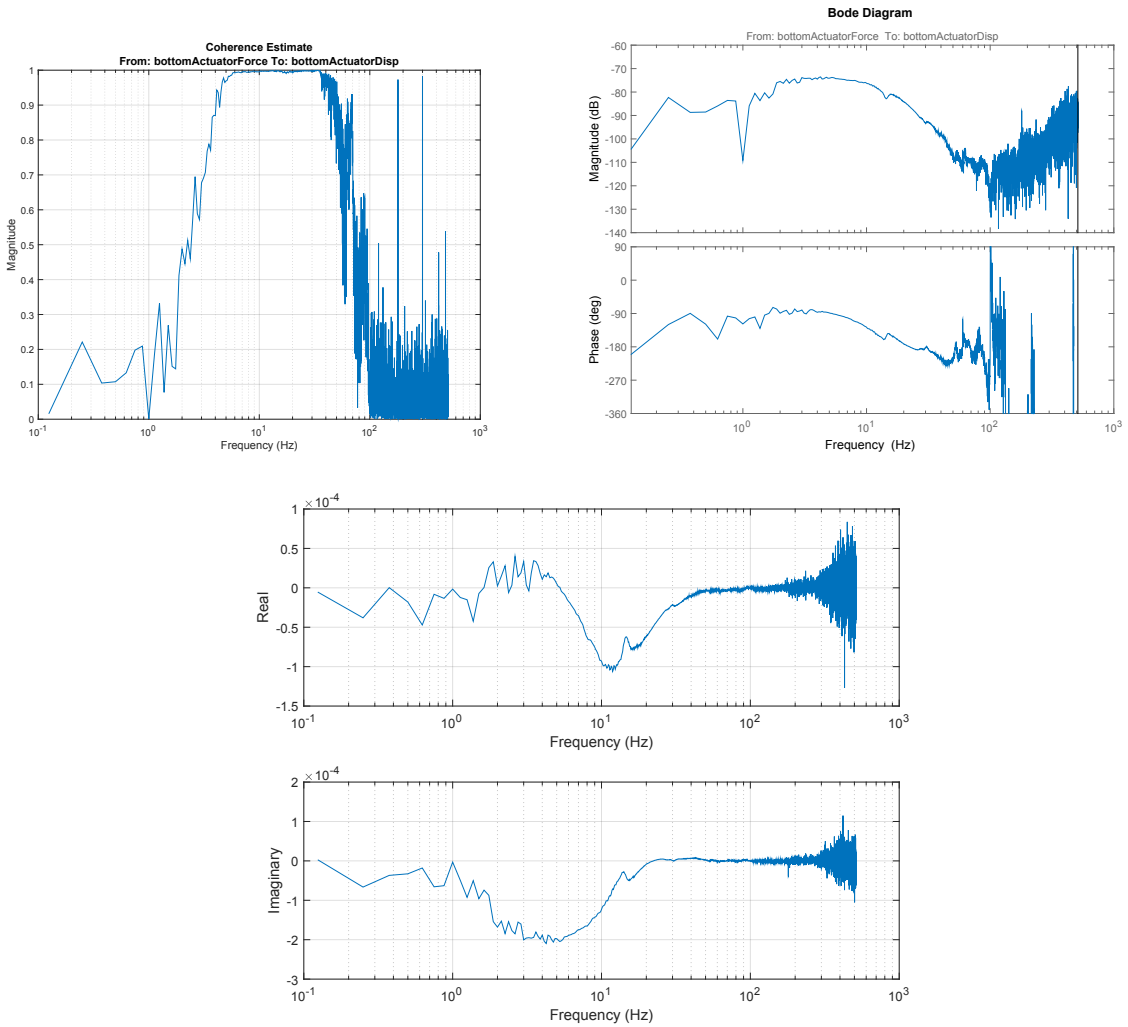

Figure 4-24. Sin sweep excitation 5Hz – 35Hz.

The combined frequency response functions capture modes at approximately 1Hz, 8Hz, 15Hz, and 30Hz. These modes are obtained by inspecting the imaginary portion of the response and observing where minimum values occur in the range of good coherence. Some modes of the system were not discernable from the data.

4.4. DDS Instability Simulation

To simulate drilling conditions, a model of axial drilling instability developed by Tlusty [Ref. 3] was implemented on the DDS. Axial displacement data of the simulated bit (Xcite Actuator) was logged and used to modify current actuator force using displacement data from the previous pass of a simulated cutter blade. This modulation leads to bit vibrations that grow as resonant modes are excited in the DDS system. The model was implemented in LabView (Figure 4-25) and was logged and controlled using a National Instruments PCI-6229 card installed in the DDS PC.

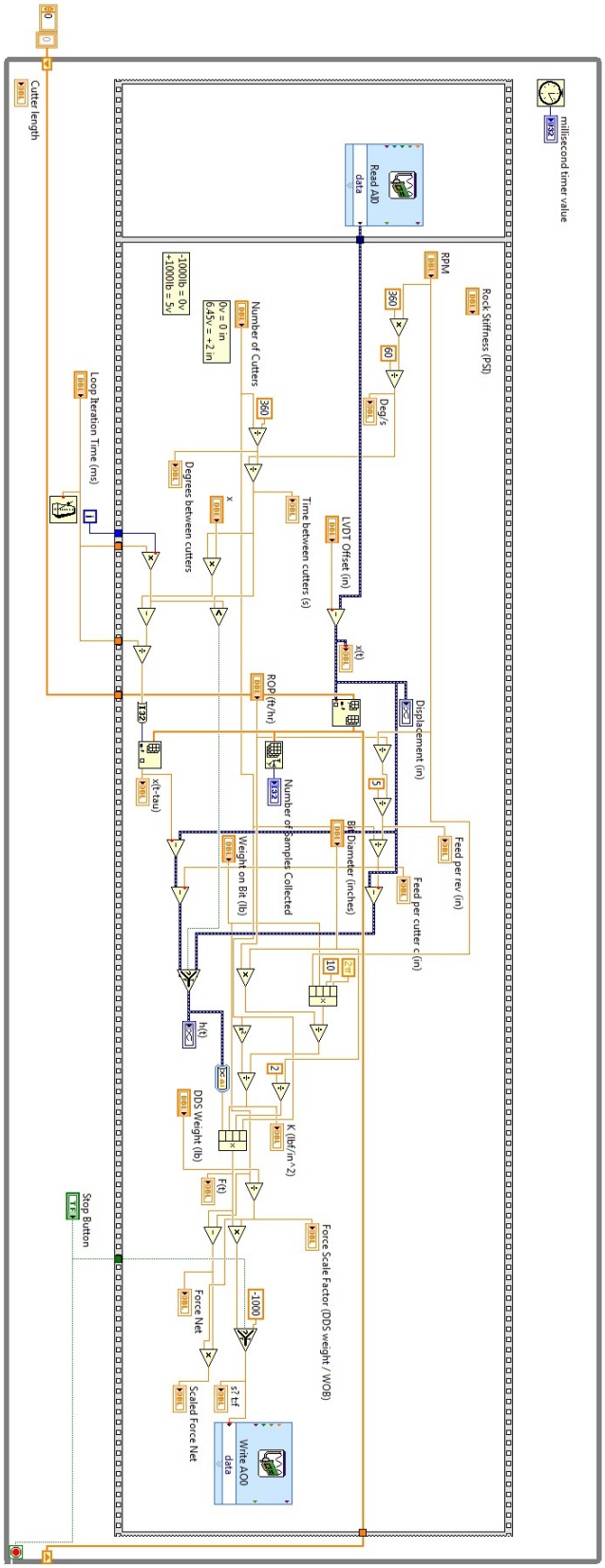

Figure 4-25. LabView Block Diagram of DDS Implementation of Tlusty Instability Model.

The operator can select parameters such as weight on bit, bit diameter, blade count on the bit, and RPM. Depending on the input parameters, the vibration amplitudes may maintain a steady state (stable) or grow to a point where the system is no longer stable and the simulated bit loses contact with the rock. The instability simulation was performed in the DDS configured with the VRS. Figure 4-26 depicts an example front panel setting with the VRS in the stiffest state. The plot at the bottom of the panel shows the bit vibration amplitude rising to a point of instability and then resetting and repeating until the simulation was stopped. A shift in the VRS stiffness can introduce stability with all other parameters maintained constant.

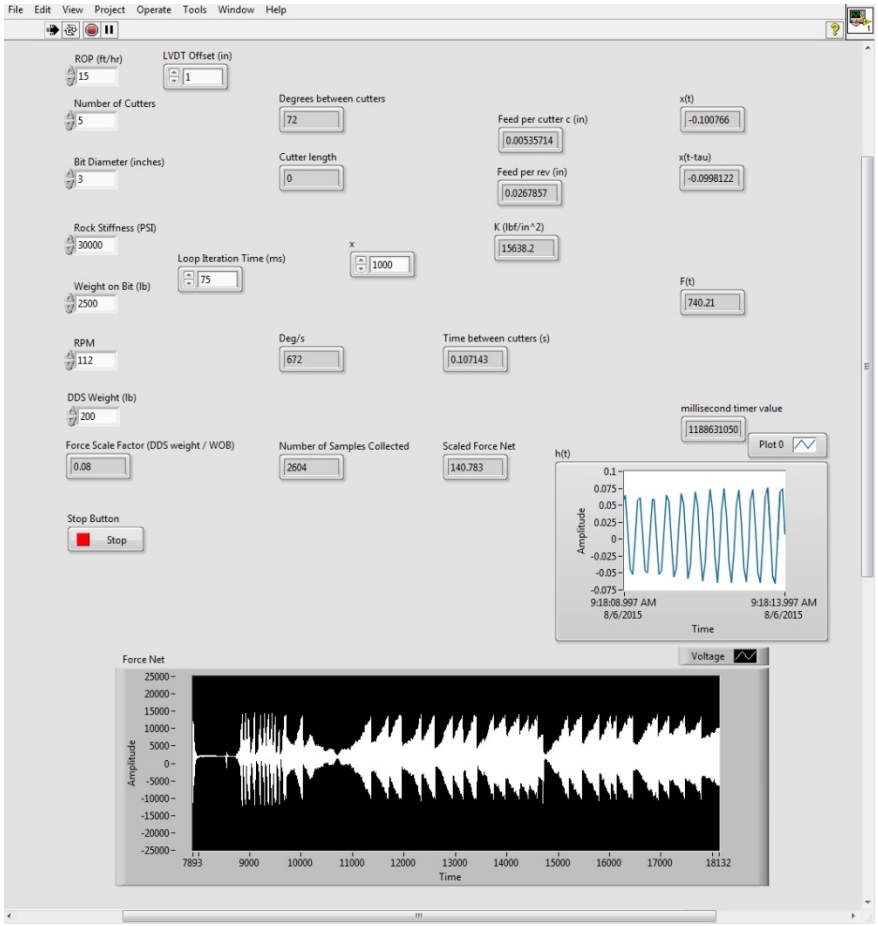

Figure 4-26. Front Panel of DDS Instability Model with VRS in the stiffest state.

4.5. Inertial Exciter Testing (Year 2 – DDS Integration & Testing)

4.5.1. Inertial Exciter Description

Xcite Systems, Batavia OH, also provides inertial exciters for excitation of large structures for modal characterization testing. The exciter consists of the previously described force/displacement actuator, mounted in a housing with guide shafts that displaces a 55 lb. (25 kg) mass to provide an inertial force. The force capability of the device as a function of

frequency is shown in Figure 4-28. A mechanical drawing of the purchased inertial exciter is shown in Figure 4-27. The inertial exciter can be mounted in any orientation to structures and can be digitally controlled for prescribed force excitation.

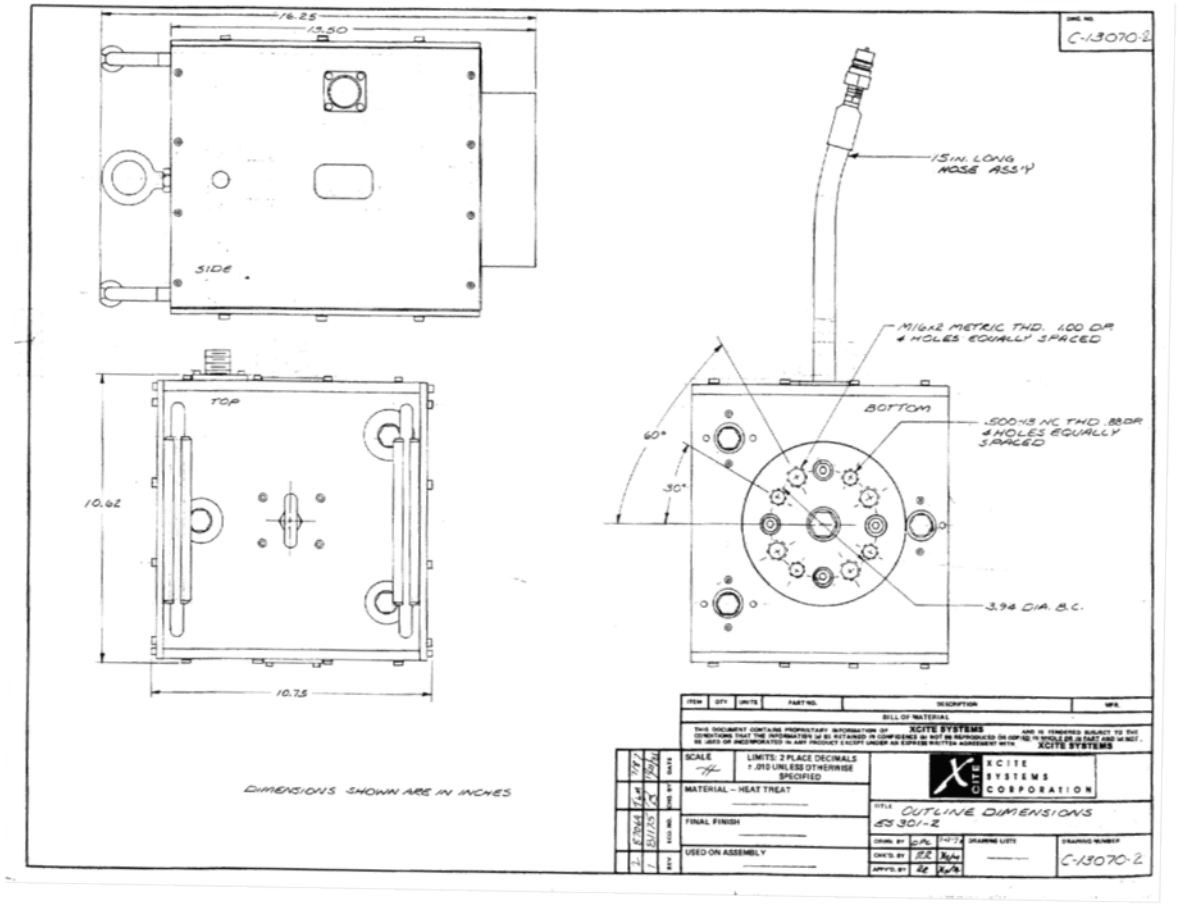

Figure 4-27. Xcite Systems Inertial Exciter.

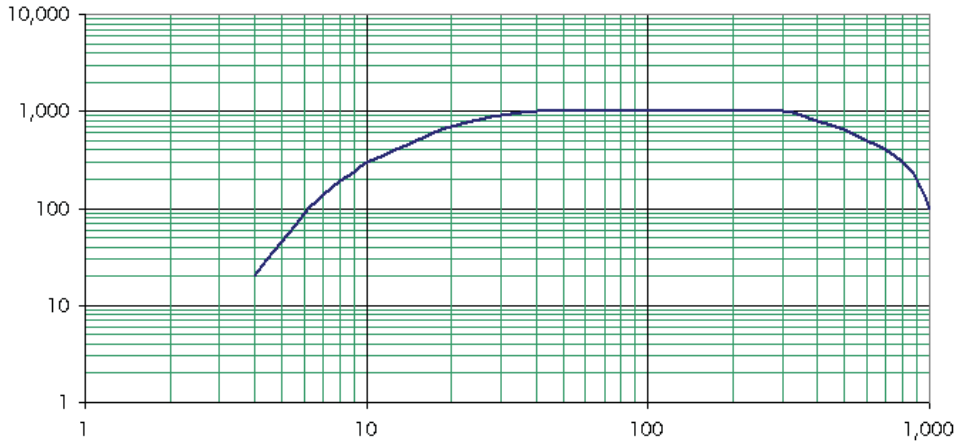

Figure 4-28. Inertial Exciter Force Capability.

4.5.2. DDS Integration

The inertial exciter was integrated into the DDS to evaluate the suitability of using an inertial exciter to suppress typical drillstring-like vibrations. The inertial exciter is shown mounted in the DDS in Figure 4-29. The springs to the left and right of the inertial exciter were installed to provide compliance between the exciter and the Xcite actuator at the bottom.

The bottom actuator simulates axial bit vibration and the inertial exciter is placed between the vibration source and a region of modal excitation. This implementation is analogous to potential operation within a drillstring because acceleration data at the inertial exciter location is used to produce opposing inertial forces in the correct phase to attenuate vibration transmission to the rest of the drillstring. In this way it may be possible to use inertial excitation to produce vibration attenuation nodes throughout a drillstring which may lead to smart systems for active suppression of aggregate drilling vibrations.

Figure 4-29. Inertial Exciter integrated with the DDS system.

4.5.3. Results from IE testing in the DDS

The viability of using an inertial exciter for active vibration reduction in a laboratory scale drill string was demonstrated on the DDS. Vibrations developed at resonant modes in the system are attenuated using dynamic forces generated by the hydraulically actuated reciprocating mass. Mass displacement is controllable by waveform, frequency and amplitude. A Matlab algorithm was developed to execute automated closed-loop minimization of drill string vibration at specific system modes using accelerometer feedback from the DDS system at the location of the inertial

exciter. The hardware of the control loop is implemented through a National Instruments PCI-6229 data acquisition card.

Tests were conducted on the DDS to demonstrate the ability of the inertial exciter to selectively remove specific modal excitation in the system. The bottom actuator was used to stimulate the system with prescribed input signals. Acceleration at the inertial exciter was monitored and used to characterize the response of the system as seen at that location. The signal from this accelerometer was then used to generate a cancellation signal that drove the inertial exciter. The cancellation signal varied in both phase and magnitude to hone in on the settings that minimized acceleration at the inertial exciter location. This procedure was executed for four different signal types: single sinusoid, sin + noise, superimposed sinusoids of different frequencies, multiple sines + noise. Results from testing the inertial exciter within the DDS are shown in the following figures.

A sin sweep was used to characterize the frequency response of the DDS configured with the inertial exciter. (Explain how this relates to system id discussed above). The results are shown below.

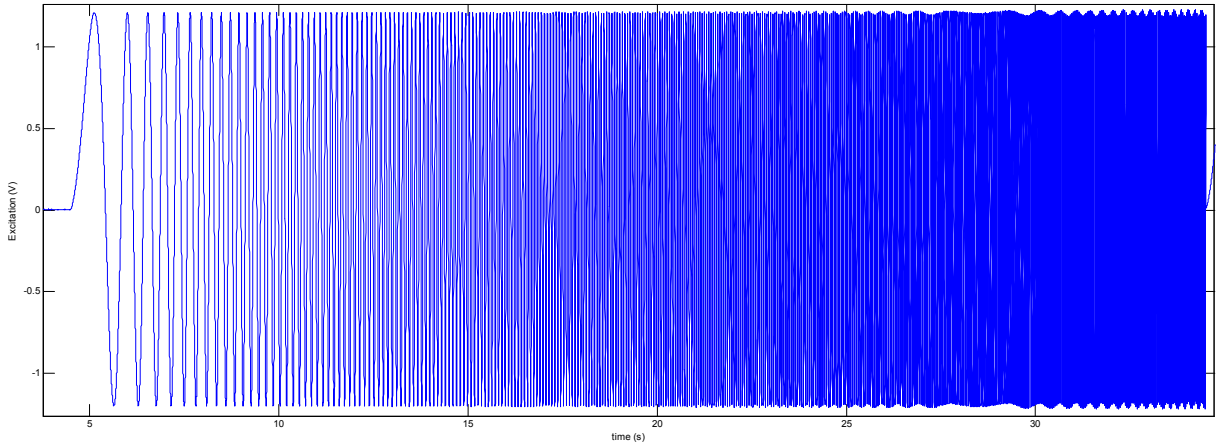

Figure 4-30. Sine sweep excitation signal time history (0.1-30 Hz over 30 seconds).

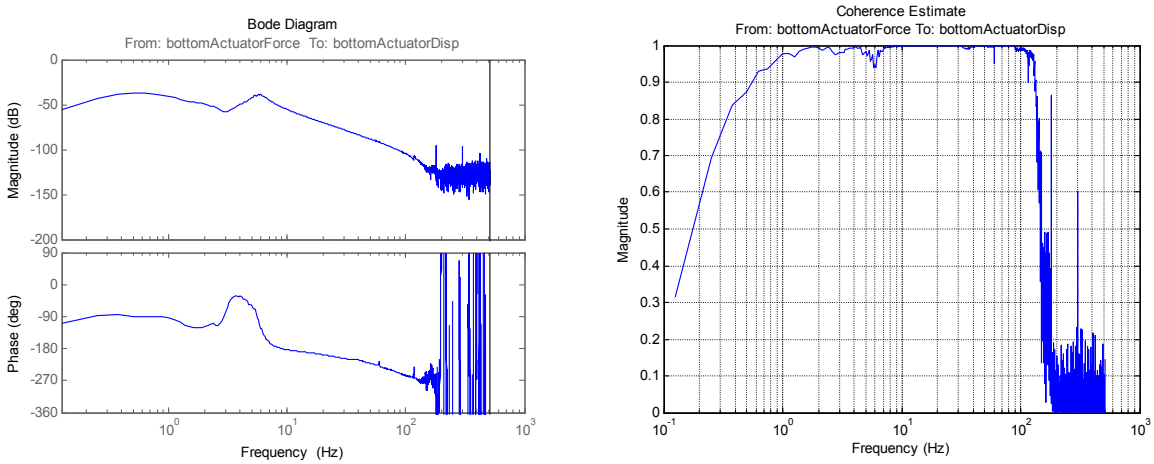

Figure 4-31. System transfer function in inertial exciter configuration.

Figure 4-32 depicts a waveform consisting of three sinusoids, each at a known DDS modal frequency with superimposed noise (3Hz, 6Hz, 15Hz). This signal was used as the driving signal for the bottom actuator. For demonstration purposes, attenuation of the 6Hz signal with the inertial exciter is shown. The closed loop Matlab algorithm was set for 6Hz sinusoid and it automatically determined the correct phase for maximum 6Hz signal attenuation. Figure 4-33. shows the effect of this configuration of the inertial exciter on the dynamic response of the system. The FFT plot shows the inertial exciter in phase and out of phase with the bottom actuator signal and cancelling out the driving signal at 6Hz.

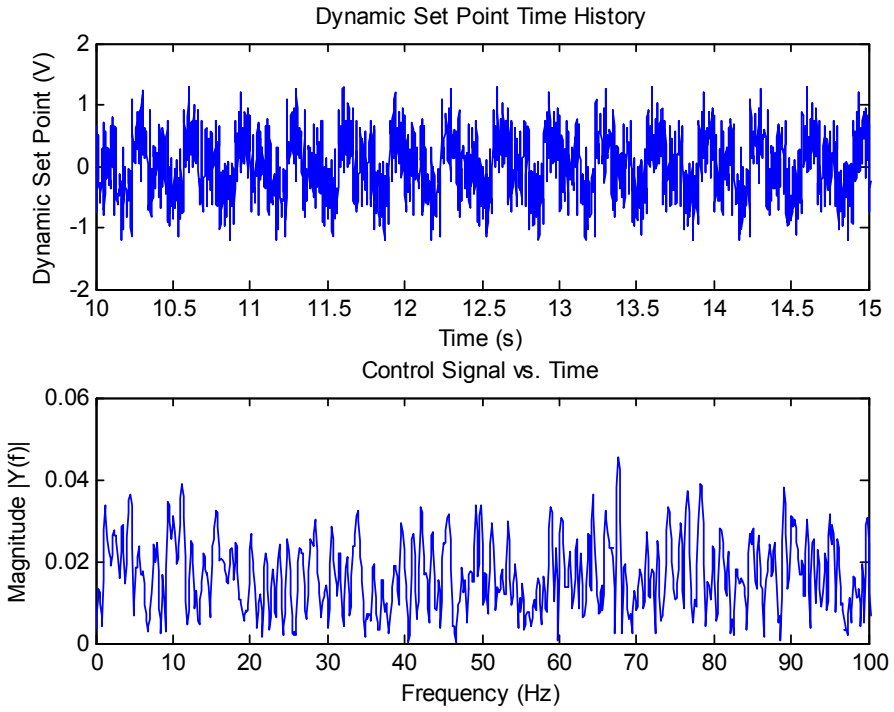

Figure 4-32. Control signal with 3Hz, 6Hz, and 15Hz overlaid with "noise".

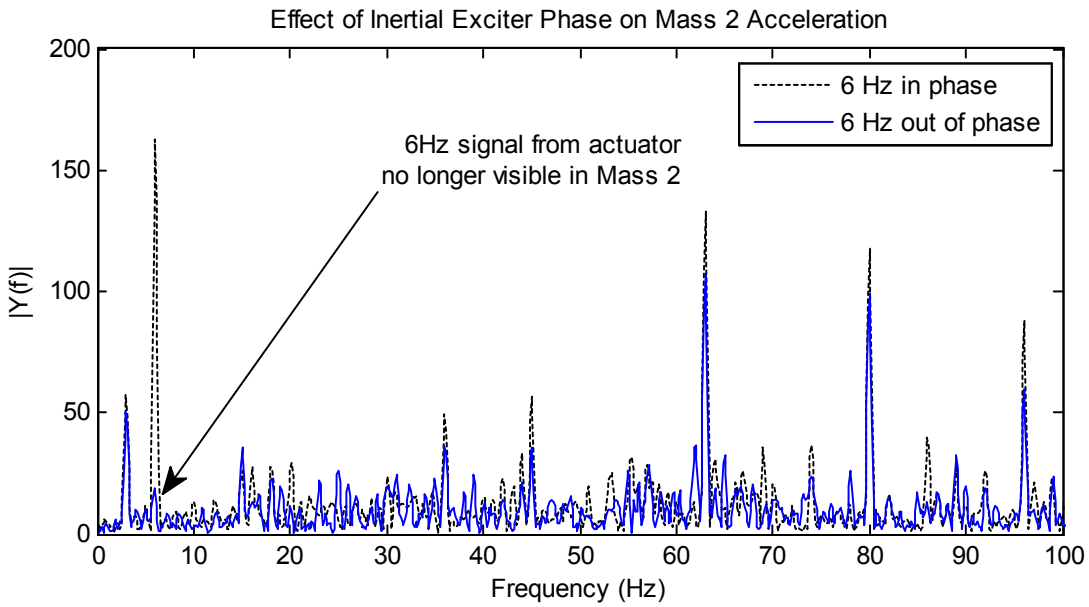

Figure 4-33. Effect of inertial exciter phase on FFT amplitude.

Figure 4-34 shows a time history of the FFT magnitude of the accelerometer data at the inertial exciter location for the 6 Hz cancellation configuration described above. As the signals sync in phase, the amplitude increases to the maximum value around 12 s into the test. The amplitude begins to decrease as the signals get out of phase and reaches a minimum approximately 50 s into the test.

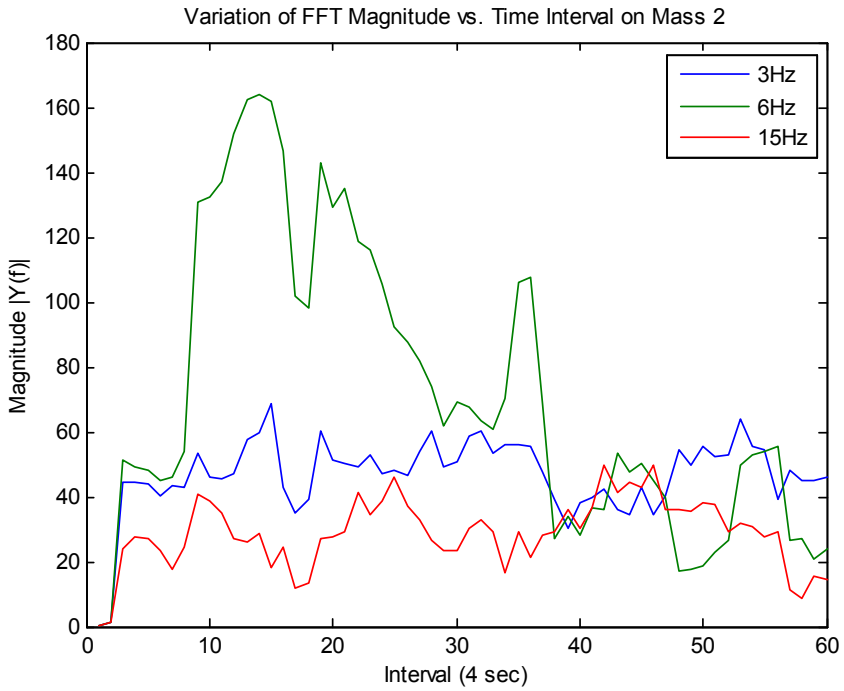

Figure 4-34. Variation of FFT magnitude due to phase shift.

Similar tests were conducted to cancel the 3 Hz and the 15 Hz portions of the driving signal. The 3Hz results are shown in Figure 4-35.

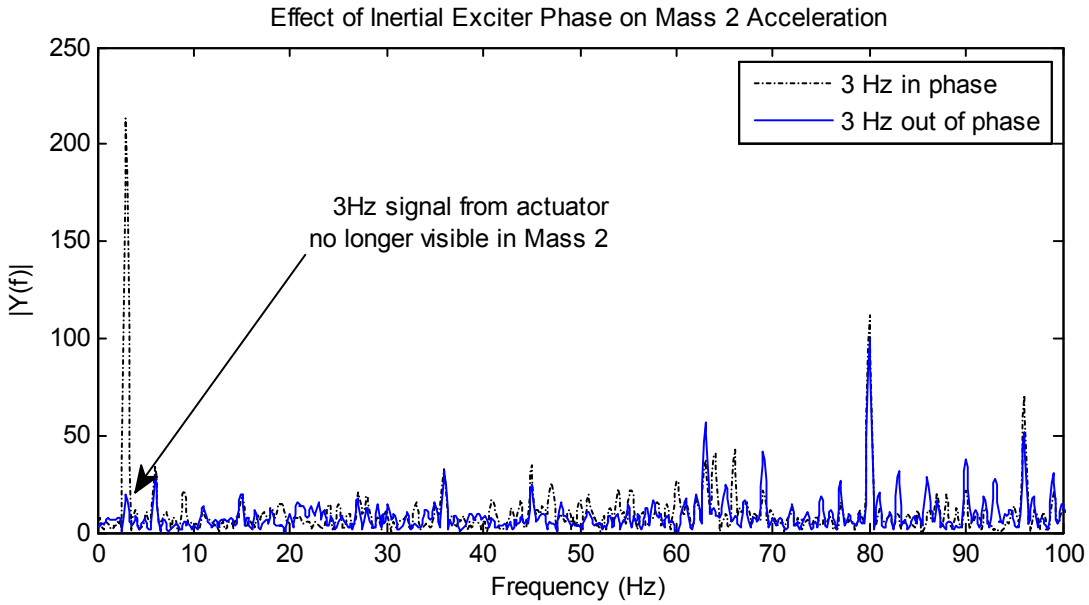

Figure 4-35. Effect of inertial exciter phase on FFT amplitude.

The results from these tests show that an inertial exciter can be used to cancel modes of vibration in a dynamic system. Part of the challenge to making it functional in the laboratory is getting the phase shift and magnitude correct. One can imagine implementations with algorithms analogous to those employed in noise cancelling head phones. The technical advance necessary for application of this technology to a real drill string is to develop an inertial exciter system in the form, fit and function necessary for downhole deployment. Sandia has conceived a prototype concept for a hydraulically-activated inertial exciter that is powered by pressurized drilling fluid flow from the surface.

This page intentionally left blank.

5. LABORATORY DRILLING SIMULATIONS (YEAR 3 - DRILLING APPLICABILITY DEMONSTRATION)

In the third year of the LDRD project, Sandia conducted a Drilling Applicability Demonstration to show the benefit of a variable rate spring in an actual drilling configuration. The Sandia Hard Rock Drilling Facility (HRDF) was used for these demonstrations with a Drilling Dynamic Simulator that reproduces the dynamic properties of a deep drillstring in the laboratory. Sandia contracted with Ulterra Drilling Technologies to obtain actual PDC bits for this testing. Two bits were manufactured to Sandia's specifications with four and five blades to allow the influence of the blade profile on instability to be addressed.

5.1. Drilling Facility Description

The Hard Rock Drilling Facility (HRDF) is a laboratory-based drilling facility as shown in the photograph below. The setup consists of a 3 in. (7.6 cm) diameter drillstring driven by a top drive supported by a stiffened beam within a structural steel frame. The drillstring is restricted to vertical movement by guide shafts. A fixed-displacement hydraulic motor rotates the drillstring and hydraulic cylinders draw down on the load head to apply drilling thrust. Proportional valves control the motion of the hydraulic cylinders. A three-foot rock cube is positioned on the base plate of the frame, clamped-down during drilling tests using an independent hydraulic system, and indexed with respect to the bit by an air caster that allows multiple holes to be drilled in a single rock sample. Water is used as a drilling fluid and is circulated through the bit.

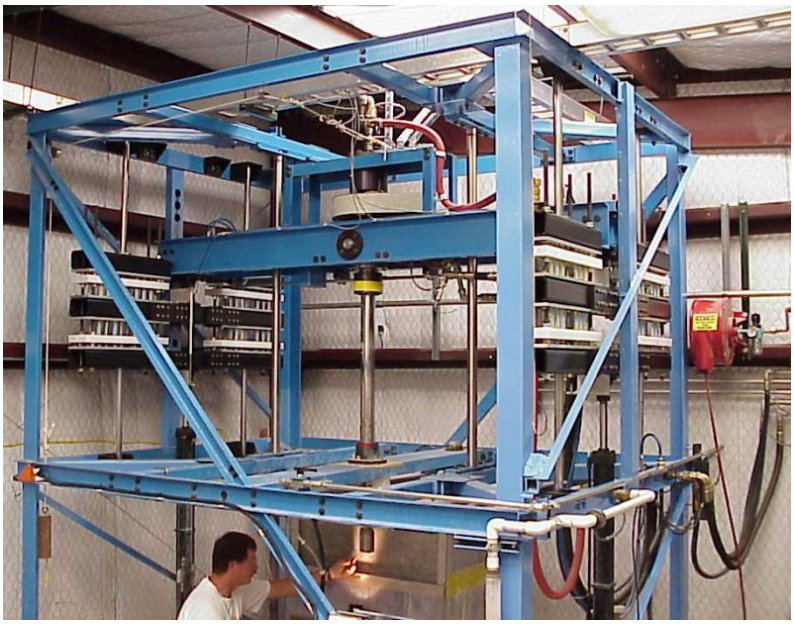

Figure 5-1. Sandia Hard Rock Drilling Facility.

The HRDF is controlled through a central computer, which also records pertinent data. Recorded data include Weight on Bit (WOB), torque, rotary speed, drillstring position and acceleration, and left and right cylinder positions. Weight on bit is measured by monitoring the differential pressure across the hydraulic cylinders. Torque is measured by monitoring the input pressure to

the fixed-displacement hydraulic drive motor; rotary speed is monitored using a rotary pulse generator on the hydraulic motor. Displacement transducers monitor rod positions of the hydraulic cylinders and a linear potentiometer is also used to monitor the drillstring's position with respect to the frame. Data from each test run was collected at a sampling rate of 512 samples per second.

5.2. Bit Development

Through a contractual agreement between Sandia National Laboratories and Ulterra Drilling Technologies, Ulterra has designed, fabricated and delivered industry-standard bits for testing by Sandia under laboratory-controlled conditions. Ulterra designed two 3.75" (9.5 cm) diameter PDC bits, with both four and five blades, and geometrically similar cutting structures to support these evaluations. The bits were tested in the Sandia Hard Rock Drilling Facility under rigid drillstring conditions to evaluate their baseline performance. Sandia is interested in follow-on testing with the subject drill bits to evaluate the phenomenon of self-induced vibrations. The four and five bladed bit designs are shown in face and side views in Figure 5-2 through Figure 5-5.

Figure 5-2. Four bladed bit designs – face view.

Figure 5-3. Five bladed bit designs – face view.

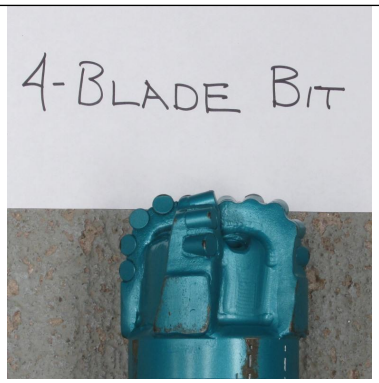

Figure 5-4. Four bladed bit designs – side view.

Figure 5-5. Five bladed bit designs – side view.

5.3. Rigid Drillstring Drilling Tests

The purpose of the rigid drillstring drilling tests is to measure the performance of the four and five bladed bit with a rigid drillstring. This will provide a baseline performance upon which to assess the severity of drillstring vibrations wSen the drillstring is compliant (section 5.4) and the ability of a variable rate spring fixture (section 5.6) to mitigate harmful vibrations.

5.3.1. Test Setup

Testing is conducted in two rock types: Sierra White Granite & Berea Sandstone. The bits are tested at constant rotary speed with the WOB increased incrementally from minimum to maximum values appropriate for the penetration rate response of the bit to evaluate a range of conditions within a single drill hole. For each bit/rock combination, tests are performed at three prescribed, constant rotational speeds: 100, 150, and 200 rpm. Weight on bit is increased in steps of 250 lb. (1112 N) throughout the range of approximately 2000 – 4000 lb. (8897 – 17794 N) for Sierra White Granite and approximately 1000 – 3000 lb. (4445 – 13345 N) for Berea Sandstone. WOB is increased by increments of approximately 250 lb. (1112 N) and the penetration rate and torque response are measured for each condition. Testing at constant WOB is conducted by controlling the source pressure delivered to the hydraulic cylinders using a cartridge valve within the hydraulic power unit.

5.3.2. Bit Characterization Testing

Raw and processed data are included in Appendix I. Figure I-1 through Figure I-3, Figure I-10 through Figure I-12, Figure I-19 through Figure I-24, and Figure I-31 through Figure I-34 display time histories for the Ulterra 4-blade/SWG, Ulterra 5-blade/SWG, Ulterra 4-blade/Berea, and Ulterra 5-blade/Berea test runs, respectively. For each bit/rock combination, Rate-of-Penetration (*ROP*), depth-of-cut, torque, torsional power, and specific energy are plotted as functions of Weight-on-Bit (*WOB*) over a continuous interval from each time history. The specific energy is also plotted against drilling strength after the method developed by Detournay et al. [Ref. 10, Ref. 11]. The lines plotted in each of the processed data figures (i.e., ROP vs. WOB) connect data averaged over intervals ranging from 10-25 seconds (and not over one second intervals, as explained in Data Processing). Each interval corresponds to the duration with which a unique WOB step was held in the respective test run.

With respect to the Berea Sandstone tests, the unusually high compliance of the Berea sample resulted in proportionally high ROPs. Because of the elevated ROPs—and in light of the limited sample depth to drill through— at times, multiple tests using the same bit/prescribed rotational speed were overlaid in order to present a proper sweep of WOB values. This was necessary for the 4-blade/100 RPM, 4-blade/150 RPM, 4-blade/200 RPM, and 5-blade/150 RPM tests. It also explains why, for instance, six time histories are reported for the 4-blade bit/Berea Sandstone tests (two separate tests were overlaid for each of the three bit/prescribed rotational speeds).

Processed data is presented in Appendix I. Data obtained from tests using the Ulterra 4-bladed bit are shown in Table I-1 through Table I-3 and Table I-7 though Table I-9, with the former table set corresponding to tests in Sierra White Granite (SWG) and the latter table set

corresponding to tests in Berea Sandstone (BSS). Similarly, results from tests using the Ulterra 5-bladed bit can be found in Table I-4 through Table I-6 and Table I-10 through Table I-12, again, with the former table set representing tests in Sierra White Granite and the latter set in Berea Sandstone. Note that data shown in Table I-1 through Table I-12 represent the line connected data points in the processed data figures (see previous paragraph).

Table I-13 through Table I-16 summarize the comparative performance of each bit in each rock drilled through. Table I-13 contains averaged parameters extracted using the Detournay method, in which ($\mu\gamma$) denotes the product of the rock's coefficient of friction (μ) and the bit coefficient (γ). Parameters extracted from tests in Sierra White Granite are denoted by ($SWG\ \mu\gamma$) while parameters deriving from Berea Sandstone tests runs are represented by ($BSS\ \mu\gamma$). Note that some of the parameters reported for the Berea tests are averaged over multiple test runs—as explained above, multiple tests were overlaid for certain bit/rotational speed tests.

Table I-14 shows the range in the torque and rotational speed of the drill string at the highest WOB step for each bit/prescribed rotational speed combination. The ranges given are not the absolute ranges observed during each test at the highest WOB step, but rather the maximum ranges observed between successive data points during the corresponding WOB step in each test. Table I-15 and Table I-16 summarize the percent difference in ROP achieved with the 5-blade bit versus the 4-blade bit at approximately the same WOB. The reported values are determined by first normalizing each bit's ROP to the WOB in which the particular ROP was achieved. Percent differences are then calculated between the normalized ROPs for each bit at approximately the same WOB.

Photographs of the bits following testing are shown in Figure 5-6 and Figure 5-7.

Figure 5-6. Face view photograph of four bladed bit following baseline testing.

Figure 5-7. Face view photograph of five bladed bit following baseline testing.

5.3.3. Data Processing

To smooth out fluctuations in the data due to inherent instrumentation variability, data points are averaged over one-second intervals before any calculations (i.e., ROP) are performed. Data corresponding to states of non-drilling (negative ROP, negative Torque, etc.) are then removed from each set.

Additionally, for each test run, a value equal to the "running torque" was subtracted from the resulting Torque data. The "running torque" represents the frictional torque produced by the drilling system (bearings, drive belt, etc.) when operating at a given rotational speed but NOT engaged with a rock sample.

5.3.4. Rigid Test Results Discussion

Data obtained from the 4 and 5-bladed Ulterra bits in both the Sierra White Granite and the Berea Sandstone demonstrate much the same patterns, with some slight variation. Of immediate interest is the comparative "aggressiveness" of each of the two bits in terms of Rate of Penetration, which can be seen in Figure I-36 and Figure I-39. From Table I-15, the 5-bladed bit is seen to achieve an ROP that was on average 10% higher in tests performed in the Sierra White Granite. In the WOB range of 3000 –4000 lb. (13345 – 171794 N), the difference is even greater, in which the improvement in ROP was on average 14% higher for the 5-bladed bit. For tests performed in the Berea Sandstone (see Table I-16), the 5-bladed bit achieved an average ROP that was nearly 30% higher than the 4-bladed bit.

Figure I-37 and Figure I-40 show the comparative depth-of-cut responses for each bit. Similar to the trend in ROP, the 5-bladed bit showed a greater DOC at nearly all WOBs seen during each of the rotational speed tests. Surprisingly, Figure I-38 shows that at rotational speeds of 150 and 200 rpm, the 4-bladed bit produced a greater torque response than the 5-bladed bit in the SWG, despite achieving a lower ROP. Figure I-41 shows results for the Berea tests, in which the comparative torques are seen to be roughly the same.

Interestingly, for the tests performed in SWG, increasing rotational speed of the drill bit resulted in an increase in the ROP between 100 and 150 rpm and a decrease between 150 and 200 rpm (see Figure I-4 and Figure I-13). For tests in the Berea, increasing rotational speed resulted in increased ROP at the same WOBs, as shown in Figure I-22 and Figure I-31. In terms of the SWG tests, it is clear that the maximum ROP achievable for a given rock hardness and WOB occurs at a specific rotational speed. It is also evident that this optimal rotational speed increases as WOB is increased, as evidenced by Figure I-13. The Berea results presumably do not show all the same trends as the SWG for several reasons. Firstly, the hardness of the rock proved to be significantly lower than anticipated—with an unconfined compressive strength (UCS) of roughly 7.5 ksi versus an anticipated value of 11.5 ksi. At such low rock strengths, ROP values increased significantly such that WOB steps could not be held for the time periods desired for drilling to stabilize. The low UCS also prevented tests from proceeding past the 2000 lb. (8897 N) WOB step, given the limited depth of the rock sample. In tandem, these limitations were dealt with by combining the results of two subsequent tests to cover the spectrum of WOB steps. This method is not ideal but allows more data points to be compared than can be captured in a single drill hole with the high rates of penetration obtained in Berea Sandstone.

For each rock, the depth-of-cut versus WOB responses showed the same general trend (see Figure I-5, Figure I-14, Figure I-23, and Figure I-32). That is, for the same WOB, depth-of-cut decreased as rotational speed increased. Physically, such a result is expected. Increasing depth-of-cut invokes an increase in the cutting action of the bit—while at low depths-of-cut, frictional forces tend to dominate. Rotating the drill bit at faster speeds, then, limits the depth at which cutters on each blade penetrate the rock surface each revolution and draws the force balance on the bit away from pure cutting and up the friction line. This observation is expected to hold as long as the rock is sufficiently hard. With the Berea tested, it can be seen that the depth-of-cut for each of the rotational speeds was roughly the same. Consequently, ROP is seen to be roughly proportional to RPM.

The trends seen for depth-of-cut versus rotational speed agree with the Detournay model. In the context of the Detournay model, it would appear that the friction mobilization point occurs at higher WOBs for higher angular speeds. Thus, for the WOBs seen in the test runs shown in Figure I-5 and Figure I-14, the bit being rotated at 200 rpm was just beginning along its Phase 2 curve (in which increased WOB translates into pure cutting, as frictional forces have reached limiting values) while the bit rotating at 100 rpm was at or nearly approaching the transition to Phase 3 drilling (where material build-up tends to occur because of inadequate hole cleaning). The bit rotating at 150 rpm represents the intermediate case. This explanation also makes sense within the context of the trends seen in bit efficiency.

Inherently, bit efficiency (as measured by the ratio of specific energy to the intrinsic specific energy of the rock being drilled) shows a decrease with an increase in rotational speed for the same WOB. Figure I-8 and Figure I-17 demonstrate this well, as the faster rotating bits required greater specific energy to drill at the same WOB. Possible explanations for this decrease in efficiency are bit break-in (tests run at higher rotational speeds were performed after tests at lower rotational speeds), poor hole cleaning, a shift in the drilling regime, or an increase in the contact stress transmitted between the bit's chamfers and the rock. Poor hole cleaning would have presumably been manifested by an increase in torque/decrease in ROP over a period of several seconds, but no such occurrence can be seen in the data. It has been suggested that in systems where stick-slip is known to occur, increasing the rotational speed of the drill bit may promote a decrease in the intensity of axial vibrations, effectually resulting in an increase in the average contact stress between bit and rock [Ref. 12]. While this may have some influence on the tests performed here, it is unlikely to be significant given the relative rigidity of the HRDF and the lack of severe axial vibrations observed in the test. As can be seen from Table I-13, for the much harder SWG medium, the value of parameter ($\mu\gamma$) decreased 13.2% between tests at 100 rpm and 200 rpm using the 4-bladed bit and 38.9% between tests at 100 rpm and 200 rpm using the 5-bladed bit. Additionally, each subsequent test with each bit in the granite resulted in a decreased ($\mu\gamma$) value. The Berea sandstone is thought to be insufficiently hard to generate any significant wear during the course of testing, so it is not considered in this context. In any case, the Berea data does not show as stark a trend in efficiency as the SWG data does.

It is possible also that the coefficient of friction (μ) could change slightly when operating at different rotational speeds. However, as discussed above, application of the Detournay model predicts that for the WOBs seen during the tests performed, the force balance between cutting and frictional forces shifted toward friction as rotational speed increased (and depth-of-cut

decreased). As the force balance between friction and cutting dictates efficiency (friction decreases efficiency), the Detournay model would explain the trend between efficiency and rotational speed. Presumably, this trend would reverse were higher WOBs applied during the tests.

It is important to point out that although increased rotational speeds led to greater inefficiency at a steady WOB, it promoted greater drilling stability. This can be seen by comparing the oscillations in torque and RPM in Figure I-1 through Figure I-3 and Figure I-10 through Figure I-12. Numerically, Table I-14 shows that the torque and RPM ranges seen at the highest WOB step in each of the tests decreased dramatically as rotational speed was increased (38.1% decrease in torque range per 50 rpm for the 4-bladed bit and 19.8% decrease in torque range per 50 rpm with the 5-bladed bit). Mention should be made as to why the specific energy appears to asymptotically approach a value greater than the intrinsic specific energy of the rock samples tested. In actuality, the explanation is probably rather simple. As the drill bit proceeds through the rock, lateral forces are produced that act to push the drill string against the guide bushings. This generates an excess of Torque not related to the actual drilling mechanics but rather the test setup. Since the excess torque also was not directly measurable, it could not be subtracted from the Torque readings and is thought to have increased the Torque (and consequently the specific energy) observed. This may also partially account for the differences in Torque observed between the 4 and 5-blade bits at the same rotational speeds if the lateral force signatures of the bits varied significantly.

From the testing performed in the HRDF facility at Sandia National Laboratories, the 5-bladed bit proved to be superior to the 4-bladed bit. The 5-bladed bit is seen to be slightly more aggressive in terms of ROP as compared to the 4-bladed bit—on the order of 10% greater ROP on average while drilling in Sierra White Granite and just shy of 30% increase in ROP in the Berea Sandstone. In terms of torque response, the 5-bladed bit experienced slightly lower torque at rotational speeds of 150 and 200 rpm than the 4-bladed bit at the same speeds and WOB. The 5-bladed bit did produce slightly higher torsional oscillations, but this is likely a result of the greater ROP achieved. This demonstrates the typical tradeoff between bit efficiency and torsional stability. Of particular interest for future testing is whether adding more blades to a bit without altering the radial location and height of cutters produces superior performance.

5.4. Simulation of Compliant Drillstrings in the Drilling Facility

In the next phase of drilling tests, compliance was added to the drillstring to simulate drilling depth and the drilling tests were repeated and compared to the rigid drillstring performance. The work described in this section was not developed with LDRD funding but the previously developed capability was used for testing the LDRD test bits.

5.4.1. Laboratory Simulation Objectives

The purpose of the dynamic drillstring simulation is to represent the dynamic characteristics of the drillstring in a controlled laboratory setting accurately reflecting field drilling conditions so that the bit response may be observed and correlated with bit design, operating conditions, and rock parameters. Ideally, one desires to simulate the properties of any drillstring in the laboratory and evaluate the response of a candidate bit in a representative rock sample. This approach, illustrated in Figure 5-8, would allow a bit to drill the formation and respond as if it is drilling at depth. Sandia has already developed and demonstrated this capability [Ref. 4]. There are several motivations for development of this capability.

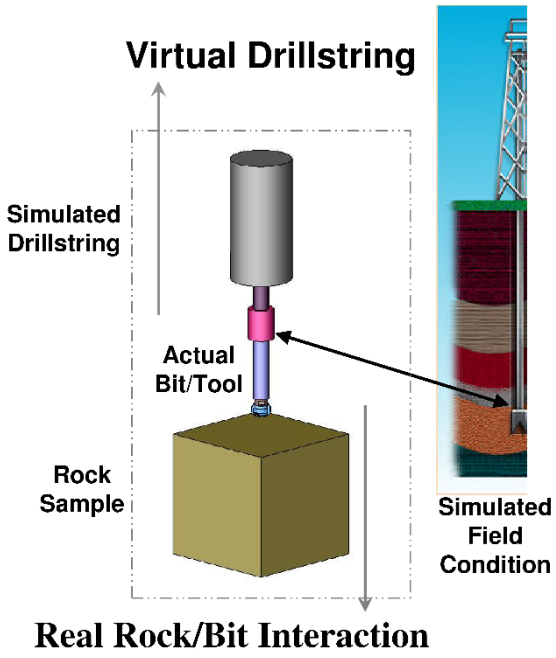

Figure 5-8. Laboratory simulation of drilling dynamics.

The dynamic range where the complications occur must be identified for these drillstring representations to be meaningful. Drillstrings vary dramatically in their properties depending upon their geometry, depth, well profile, and surface support. Consequently, drillstring modes of vibration exist in broad ranges. Zamudio [Ref. 28] shows fundamental modes of vibration in the sub-hertz level to tens of Hz for a 7200 ft. (2200 m) model of a drillstring. Jogi [Ref. 29] measured vibrations below 100 Hz for a relatively shallow depth. Wise [Ref. 30] measured

similar vibrations using a downhole diagnostics tool. These vibrations are observed at the bit in the longitudinal, rotational, and lateral axes. The present work addresses modes of vibration up to 100 Hz. The larger frequency modes will typically have smaller amplitudes and accordingly less energy. To accurately reflect reality, vibration modes should be included in all axes. However, for the purposes of this paper, the scope is limited to the representation of the axial mode of the drillstring. If a realistic simulation can be accomplished in the laboratory, obtaining these objectives will be of significant benefit to the drilling industry.

5.4.2. Mechanical Analog versus Model-Based Control

To understand how a drill bit specified for a given drillstring application will respond in a particular formation requires a capability to reproduce a broad range of drillstring attributes. The properties of a field drillstring can be simulated in the laboratory using either a mechanical analog or model-based control. These two approaches are illustrated schematically in Figure 5-9. In the mechanical analog approach, drillstring vibration is introduced using a mechanical system that has a dynamic response simulating simplistic models of a drillstring. For example, a single degree of freedom spring-mass-damper, or a system of spring-mass-dampers, that replicates the dynamic response of the desired system in narrow frequency bands.

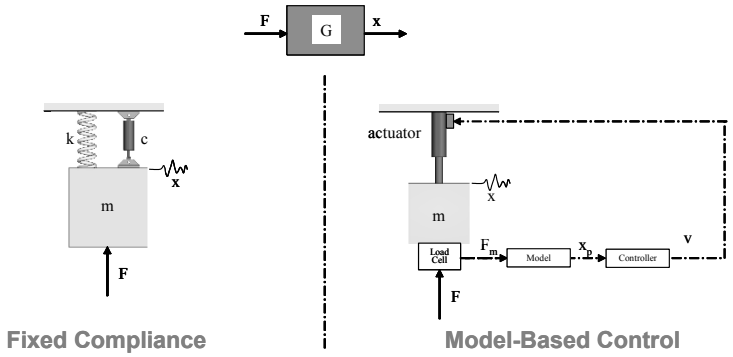

Figure 5-9. Mechanical Analog versus Model-Based Control.

In the model-based control approach, motion of the drillstring corresponding to a bit force is predicted using a computational model and replicated using a system of actuators. The model could represent a simple mechanical analog, an advanced representation based upon a complex model, or even reproduce measured data taken in the field. The model used to control the response is not limited to computational models but more generally a prescribed relationship between the input force and the resulting response. Research using these two approaches is summarized in this paper. If a system can be produced that models a drillstring in the laboratory, then real rock-bit interaction can be used to observe how drillstring vibration affects the response of the bit. Such a system can be used to address the influence of various effects characteristic of complex drillstring behavior that are observed in the field.

5.4.3. Simulation by Mechanical Analog

The dynamics of a field drillstring have been simulated in this facility by using a spring suspension system to support the vertically traversing beam, or load head, which consists of heavy structural steel channel that sits on the bit. The Hard Rock Drilling Facility, described

previously, has been used for these simulations. The long-stroke hydraulic cylinders are used to support this spring-mass system and regulate the weight on bit. The system is likened to field drilling in that as a driller pulls up on the drillstring to regulate WOB, pushing up on the spring suspension system with the long-stroke cylinders allows WOB to be regulated in the laboratory drilling facility. The load head is constrained to axial motion by guide shafts within the frame. The axial compliance for this laboratory representation is determined by the spring-suite comprising the suspension system, consisting of 96 compression springs with individual spring constants of 27 lb./in. (4729 N/m). The weight of the load head with the top drive is approximately 1610 lb. (730 kg). Hence, the system has a fundamental mode of vibration of approximately 4 Hz. (Rotational, or torsional, compliance has also been added to this system using two counter-wound power springs inside the shell of the belt-driven pulley. However, the rotational compliance is removed for the present testing.)

5.4.4. Drilling Tests with a Mechanical Analog

Drilling tests were conducted by rotating the bit at constant speed and easing the bit into the rock until an average WOB was obtained. Drilling parameters were controlled and the bit response was monitored. The drilling test in Figure 5-10 was conducted using a Sierra White Granite rock sample, a nominal WOB of 800 lb. (nominally 800/3 lb. per cutter) and rotational speed of 140 RPM. This figure shows the bit motion plotted with respect to the local rock surface. When the bit motion becomes positive, indicating that the bit is above the rock surface, the bit force (WOB) is released, rendering it equal to zero. The bit bounces above the local rock surface and, as it returns into the rock, high impact loads are applied to the cutters. The WOB in this plot was measured using a strain-gage based measurement sensor located just above the bit. It is apparent from this figure that this condition resulted in severe bit bounce, with impact loading at the bit exceeding 5000 lb. (2300 kg), more than six times the applied WOB.

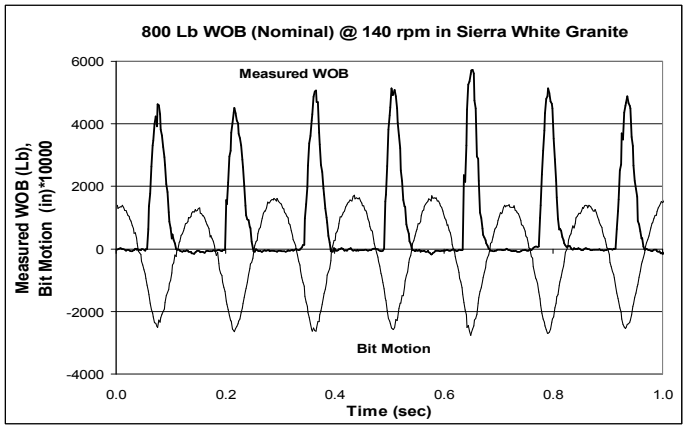

Figure 5-10. Bit motion and measured WOB from drilling tests with a mechanical analog.

Testing was repeated using a variety of operating conditions. The results show there are combinations of WOB and rotary speed that are preferred to reduce the severity of bit bounce. Figure 5-10 shows the peak bit motion measured as the rotary speed is varied from 140-260 RPM. This figure also superimposes the rate of penetration over the bit displacement using a semi-log scale. One sees that increased bit vibration at 200 RPM leads to a tremendous loss in

the ROP, i.e., practically no drilling is taking place. The importance of this condition to loss of penetration rate and likelihood of cutter bit damage is apparent. This work with fixed-compliance has been described in greater detail in Elsayed & Raymond [Ref. 8, Ref. 9] wherein the effect of coupling between axial and rotational vibrations due to the presence of rotational compliance is also addressed.

Although the potential for adverse behavior due to the influence of operating conditions, drillstring characteristics and bit characteristics is generally acknowledged within the industry, the aforementioned research quantitatively demonstrates the impact of vibration on drilling performance. It also provides the opportunity to quantify the effect of the interaction between the different drilling parameters. There are, however, numerous limitations to laboratory simulation using a mechanical analog. The mechanical analog is a single point representation that is not amenable to emulating the varying properties of the drillstring over time, such as the increase in length and compliance as more pipe is inserted into the hole. Mechanical analogs also tend to be very time consuming to exchange in the setup and have obvious cost implications with respect to maintaining the hardware necessary for a large range of compliance conditions Furthermore, since the damping is inherent in the type of analog used, it is difficult to precisely control the level of damping present in the system. For these reasons, simulation of the drillstring properties using model-based control is desired.

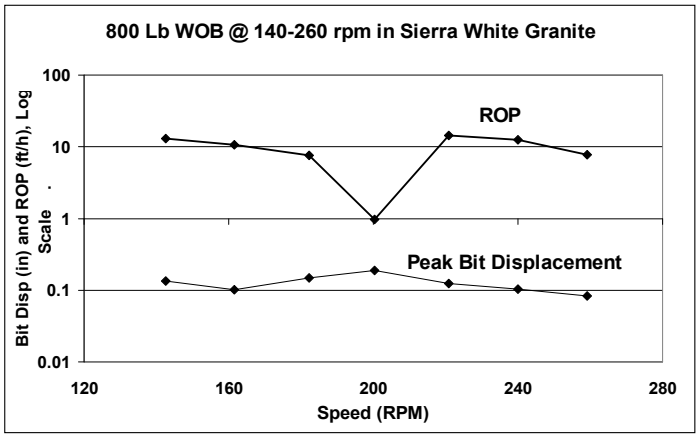

Figure 5-11. Effect of drillstring dynamics on bit response and resulting rate of penetration.

5.4.5. Simulation by Model-Based Control

The intent of simulation using model-based control is to reproduce the dynamic properties of potentially any drillstring without the limitations of a mechanical fixture, as described above. The approach is to computationally model the drillstring and allow real-rock bit interaction to generate the forces to be used as input to this model and then predict, or prescribe, how the system should respond to these forces. It then becomes a matter of enforcing the correct displacement at the interface between the bit and BHA using fast-acting actuators such that the bit "feels" as if it's in the hole at depth. The drilling function is performed by an actual bit in a representative rock sample, yet the bit will behave as though it were attached to a long, flexible drillstring specified at the user's discretion. A schematic of the approach is shown in Figure 5-12.

The former drilling facility was modified and used to demonstrate a prototype system using this approach. As in the mechanical analog, model-based control comprises two primary equipment subsystems: a drilling simulator and a dynamics simulator. The drilling simulator consists of the drill rig gantry with the vertically traversing frame. The dynamics simulator supports the drill bit (and possibly a BHA tool in future implementations) and produces the dynamic compliance of the drillstring at the bit using fast-acting actuators that are controlled by a model of the drillstring. The vertically traversing frame is used to support the dynamics simulator, analogous to how fixed-compliance was accommodated in the mechanical analog.

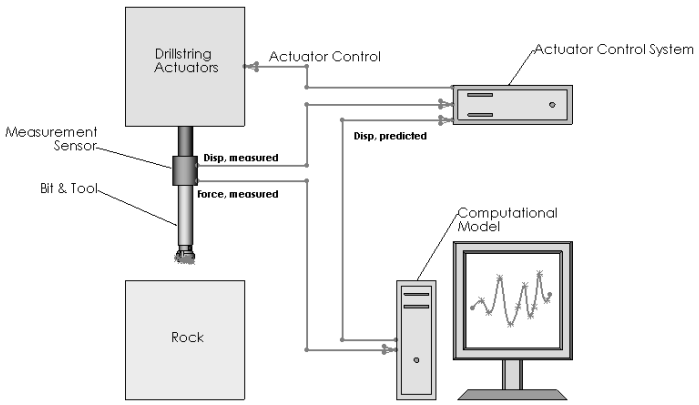

Figure 5-12. Model-Based Control Approach.

System Development a competent simulation using model-based control requires attention to several areas. These include Simulation Requirements Definition, Predictor Development, Dynamics Simulator Development, Servo-Hydraulic System Selection, and Controller Development. The reader is referred to an ASME Journal Article on this subject for further detail wherein each of these items are addressed separately along with the approach to implementation of these in a prototype system. These topics are coupled and their appropriate integration results in a system that meets the performance objectives. They are addressed summarily in the following.

5.4.6. Simulation Requirements Definition

The relationship between the forces applied to a particular drillstring and its displacement response must be understood to define performance requirements for the system. In the context of Figure 5-8, the Frequency Response Function, 'G', of the drillstring must be known, so its response can be predicted when it is subject to an arbitrary bit force. The relationship could be determined from a computational model consisting of simple formulations or a complex representation of a drillstring, depending upon the fidelity of response required. Field data of representative configurations can also be evaluated to understand these requirements. The displacement response should be characterized as a function of the bandwidth of the system. The initial objective for a prototype system was to reproduce the response seen in the mechanical analog fixture. This required a peak displacement of approximately 0.5 inch from static to 5 Hz.

5.4.7. Predictor Development

The drillstring model is the driver in the drilling dynamics simulator. When the bit encounters a reactive force from contact with the formation, the model predicts how the drillstring would respond to that force. It can be a computational model or any rule-based method that specifies the response based upon input parameters.

Some available computational modeling approaches for a predictor include transfer function representations, finite element analysis methods, wave propagation formulations, and normal modes analysis. With selection of a reasonable time increment for numerical integration in these models, desktop computers can predict future displacements very quickly enabling real-time updating of the actuator controllers. The complexity of the model utilized is primarily limited by the computational ability to provide a solution in time to update the controller. The appropriate level of spatial discretization necessary to reasonably reflect the vibrational behavior of the drillstring can be determined through sensitivity analysis which can also be utilized to optimize time discretization for control purposes. Preliminary work in this area indicates that fairly simplistic representations can be used to capture the dominant modes of vibration. A normal modes solution has been incorporated for a predictor and is presented in further detail later in this paper.

Field data can also be used as a predictive driver. This would allow vibrations encountered in production drilling operations to be reproduced. Using measurements of bit forces and the resulting response, the Systems Identification method could be used to develop frequency response functions for the drillstring. Systems Identification is a linear regression technique used in controls theory. It allows a representative model of the system to be developed by assuming a model order and using regression analysis to solve for the algebraic coefficients in the model. The order of the system is verified by reducing the least squares error between fit and actual data in the regression analysis.

In a real drillstring, the relationship between input and output variables can easily manifest itself as a non-linear relationship. The versatility of the model-based control approach is that it allows the predictor to be chosen to represent any user-specified drillstring and then addresses the ensuing response using the physical simulation.

5.4.8. Dynamics Simulator Development

To simulate the dynamic response on a particular axis of a drillstring requires that the laboratory system be configured with actuators that can produce dynamic displacements on that axis with amplitudes mandated by the predictor. The development of the dynamics simulator must address the mechanical design of the drilling equipment, the configuration of the actuators to produce the required dynamic response, the rock containment system, and the sensors used to monitor the mechanical response of the system. The mechanical design of the prototype system was a modification to the drilling system described above with the fixed-compliance system removed. To achieve the required system response, the dynamic mass of the top drive system had to be reduced by decoupling it from the load head. The top drive sits on a 12” wide structural steel channel and is supported by two 8” channels. The 8” wide channels were slotted to allow for

relative motion of the top drive system. This reduced the effective mass of the system and allowed axial motion of a lighter mass to be introduced. The system could have been configured with a lighter top drive to extend the frequency response, but the complexity of the system would have required a large system rebuild. As shown in Figure 5-13, the actuators are configured within the load path between the top drive beam and the vertically traversing beams to enforce the required displacement of the bit relative to the rock.

Figure 5-12 shows a measurement sensor at the interface between the bit and the dynamics simulator. It measures both the reaction force transmitted from the bit and the displacement response. The force measurements are input to the predictor to determine the required response of the drilling system to the drilling load. In the prototype system, the measurement sensor is integral to the actuators (described below). The actuators feature an integral strain-gage based load cell and an embedded displacement sensor (LVDT). The measured displacement can be used as input to the controller to assess the accuracy of the response relative to predictor requirements.

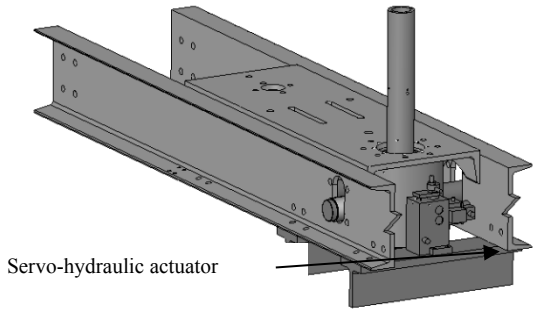

Figure 5-13. Dynamics simulator for model-based control.

The rock sample must be properly restrained so that is does not have any additional compliance that feeds back into the response of the bit. In the drilling facility, the rock is clamped at its base on a structural steel pallet that is clamped in place against an overhead plate. If pressurized containment is used, then the seal friction on the drillstring must be accounted for in the dynamic response of the simulator.

5.4.9. Servo-Hydraulic System Selection

The appropriate motive force technology must be identified to motivate the dynamics simulator with a bandwidth consistent with the output of the predictor. Servo-hydraulic actuators are the only motive-force technology available to accommodate the forces and displacement bandwidth applicable to this problem [Ref. 32]. However, these motions are subject to the additional overhead in mass and friction imposed by the mechanical system that supports the bit and top drive. Hence, the actuators must be selected to be an integral part of the overall system. The actuators have both static and dynamic force requirements since they operate in series with the load path.

Servo-hydraulic actuators powered by a 30 hp. hydraulic power unit were chosen for the prototype system. They are typically used for modal excitation analysis on large structures. They are compact and easily integrated into the drilling fixture, as shown in Figure 5-13, to

accomplish the dynamics simulation. These specific actuators produce 1000 lb. (453 kg) across a dynamic range of static to 100 Hz. The actuators force and displacement capability versus bandwidth is shown in Figure 5-14. The actuators are able to reproduce any transient signal that lies beneath these envelopes.

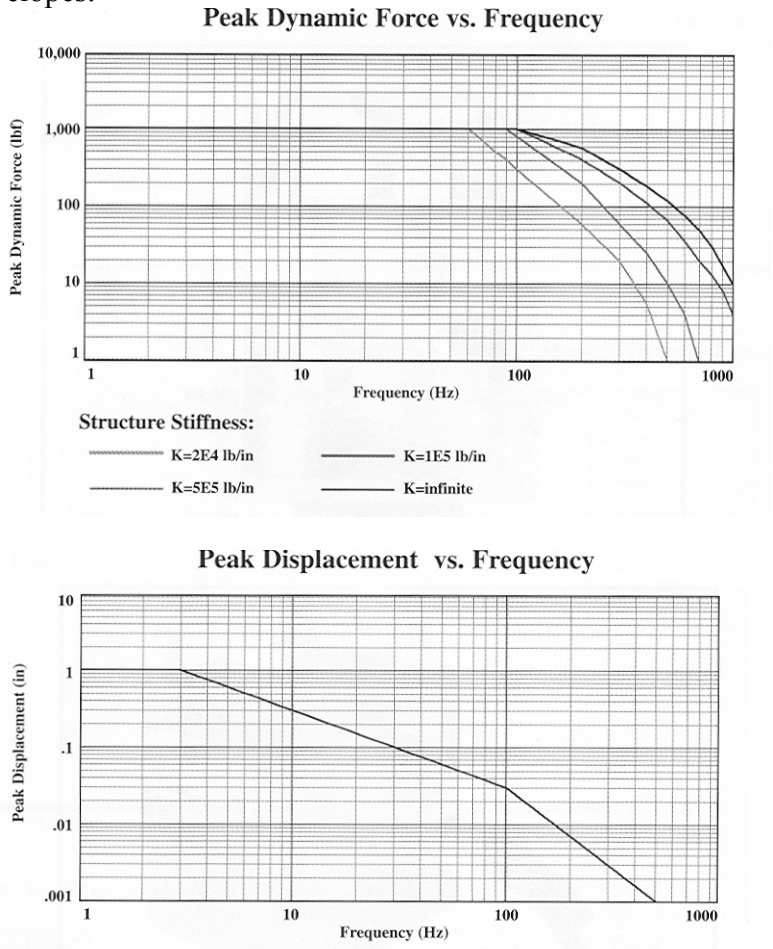

Figure 5-14. Force capacity and displacement response for servo-hydraulic actuators used in simulation (Xcite Systems 2000).
(Note these are the same exciters used in the DDS described in Section 4.)

5.4.10. Controller Development

The development of the overall system must also address the development of the controllers that drive the actuators in the dynamics simulator to produce the response mandated by the predictor. The actuators must accelerate the mass of the top drive and also drive the bit against the rock in response to the required model dynamics. The actuators are operated in stroke control mode, since a displacement is enforced based upon the output from the predictor. The approach to integrate the controller that drives the dynamic simulator was to have a system run in parallel completely autonomous from the drilling function performed by the drilling simulator. This is synonymous with how drilling takes place in the field, i.e., the drillstring responds based upon its dynamics properties regardless of how the drilling system is controlled. This autonomous system samples the force measurements from the measurement sensor, sends them to the predictor,

transmits the predicted command to the controller, and the controller sends a command signal to the actuators.

5.4.11. System Configuration

The basic system configuration consists of the servo-hydraulic actuators with the companion analog controller that drives the spool valve on the actuator, and the desktop computer equipped with software that is used for data acquisition and control. A data acquisition card is used to monitor the force and displacement measurements from the embedded sensors on the actuators. The software application monitors the forces from the load cell, inputs these to the predictor model, and then uses the predicted displacement values to output a voltage to drive the displacement of the actuators in stroke control mode. A sampling rate of 5000 Hz is used resulting in a solution time average of 200 microseconds per step. The output signal is sent to the analog controllers which in turn control the response of the actuators. The voltage to drive the actuators to get the required displacement must be specified. Hence, a transfer function is required for the actuators so they can be input the proper control signal to achieve the desired response. Testing was conducted to characterize the frequency response of the actuators when they are used to drive inertial masses that represent the dynamic mass of the top drive.

Some dynamic mass must be moved to accomplish the simulation. This mass includes the top drive, rotating drillstring, bit, and other components comprising the dynamics simulator. The displacement-bandwidth relationship for the overall system is a function of this mass. Too much dynamic mass in the system will limit the ability to meet the requirements for the simulation.

Testing was also conducted to characterize the frequency response of the actuators when they act against an elastic foundation. As the bit enters the rock, it is decelerated by the rock penetration reaction. The bit is driven by the actuators which are in stroke control mode, so the actuator force must be large enough to allow the bit to penetrate the rock in accordance with model predictions.

5.4.12. Overall System Transfer Function

Shake testing was conducted on weights representing the dynamics simulator to develop a transfer function for the overall system that can be used to control the actuators. A typical displacement-time history response is shown in Figure 5-15. A chirp input signal was provided to the actuator controller and the response of the system was observed. This information was used to develop a transfer function for the dynamic simulator when motivated by the servo-hydraulic system. For a 212 lb. (96 kg) mass, the response of the system starts to fall off after about 8 Hz.

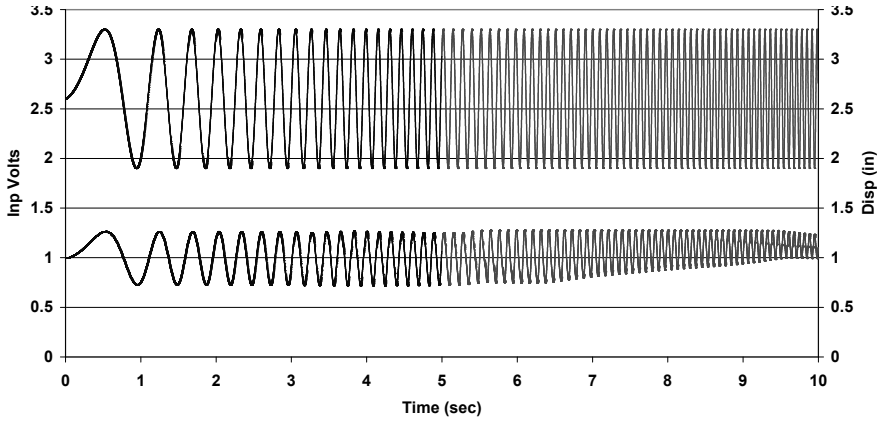

Figure 5-15. Input voltage (top) to actuator controller and actuator displacement response (bottom).

A transfer function for the displacement of the servo-hydraulic actuators as a function of driving voltage was derived using System Identification. The resulting function is shown in Figure 5-16. This was derived from the data in Figure 5-15 for 0-4 seconds (before the system response starts to drop off) corresponding to a frequency range of 0-10 Hz.

However, the inverse of this transfer function is needed to get the actual driving voltage applied to the actuator to enforce the correct displacement response. The block diagram shown in Figure 5-17 is used to produce the inverse of the transfer function in Figure 5-16. This system is input into the controller software to control the actuators in stroke-control mode.

$$H(s) = K\left[\frac{1 + T_z s}{1 + 2\zeta T_w s + (T_w s)^2}\right] \text{[in/v]}$$

with $K = 0.38376$,
$T_w = 0.01038$,
$\zeta = 0.7301$, and
$T_z = 0.0044012$

Figure 5-16. Transfer function for the servo-hydraulic actuator derived using System Identification.

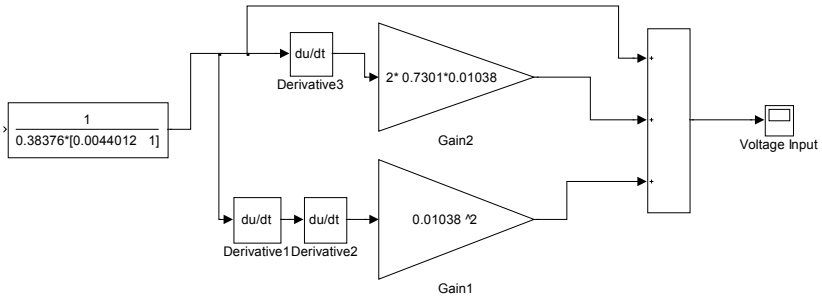

Figure 5-17. Block diagram to determine control voltage for a given displacement.

5.4.13. Proof-of-Concept Demonstration

With the exception of the predictor, the other components of the system have been prepared for a simulation. A transfer function for the drilling facility equipped with the mechanical analog can be characterized to develop a predictor, or drillstring driver, for a proof-of-concept demonstration using the model-based control approach.

5.4.14. Predictor for the Mechanical Analog

A model for this system (i.e., a frequency response function) was derived by impacting the end of the drillstring (when the mechanical analog was in place) with an instrumented hammer. Time histories of the impact force on the hammer and the resulting displacement of the bit are measured. A frequency response function (FRF) is derived by taking the ratio of these two quantities in the frequency domain. This is shown by the solid lines in Figure 5-18.

The drilling system with fixed-compliance acts like a simple harmonic oscillator. Accordingly, system-specific values of stiffness, mass, and damping can be expected to form a reasonable characterization (damping was derived by logarithmic decrement). However, when this is done, there is poor agreement between the predicted and measured frequency response functions. The system has extra apparent stiffness in the response of the drillstring due to stiction between the bearings and guide shafts throughout the system. Using an artificially higher stiffness (e.g., 5500 lb./in) results in a better fit, as shown in Figure 5-18. This frequency response function [1/5500/ $(0.0007562s^2 + 0.01s + 1)$] will be used to generate results for comparison to the mechanical analog system.\

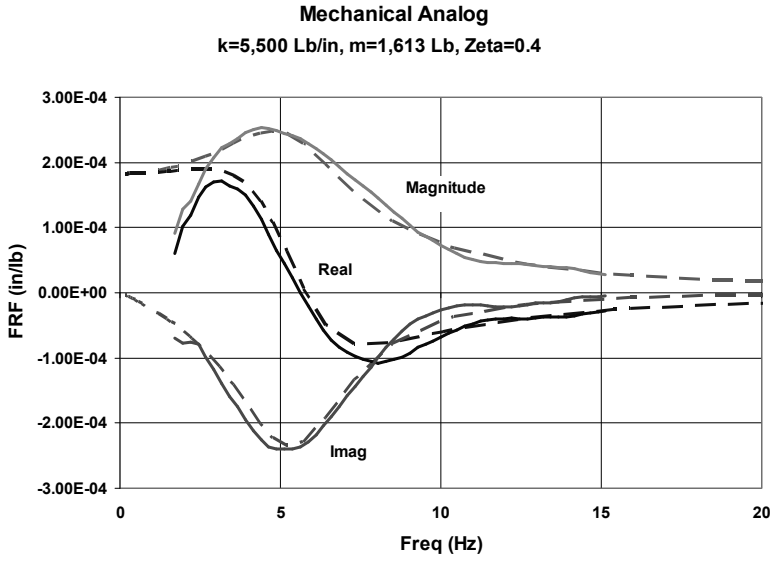

Figure 5-18. Transfer function for the mechanical analog (Bold lines represent measured data; dashed lines are fit).

5.4.15. *Implementation*

The foregoing developments are used to conduct a "model-based control simulation" using the frequency response function shown in Figure 5-18 as a predictive driver. To demonstrate that a model-based control simulation approach can be used to reproduce drill bit dynamics, a proof-of-concept demonstration was conducted in a static load frame prior to integrating it into the drilling function. This required that the actuators be re-configured. One of the actuators was used to generate a WOB force profile by loading it against a rigid frame. This force was measured, the FRF was used to predict the response of the drillstring, the voltage to produce this response was determined and sent to the actuator, the response of that actuator was monitored, and a comparison made to the predicted value from the model. This was done using the controller software and incorporated the previous control system characterizations. The approach is shown in Figure 5-19. The only difference from an actual drilling simulation is that the bit force was generated using a secondary actuator as opposed to actually drilling and using bit forces. This allowed the response of the system to be evaluated against a known input.

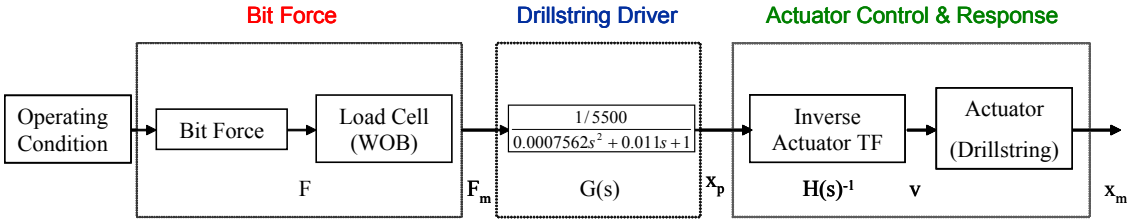

Figure 5-19. Implementation of the simulator to produce a given response for a drillstring.

The predicted response and the error in the measured response of the actuators are compared for a bit force in the form of a chirp in Figure 5-20. Favorable results are obtained with the measured response following the driver with an error of less than 0.010 inch (0.0254 cm) over the response range. This is for an open loop control algorithm, i.e., there is no real-time comparison between the displacement results from the servo-hydraulic actuator and the predictor to correct the input to the dynamics simulator. More accurate results could be obtained with feedback control.

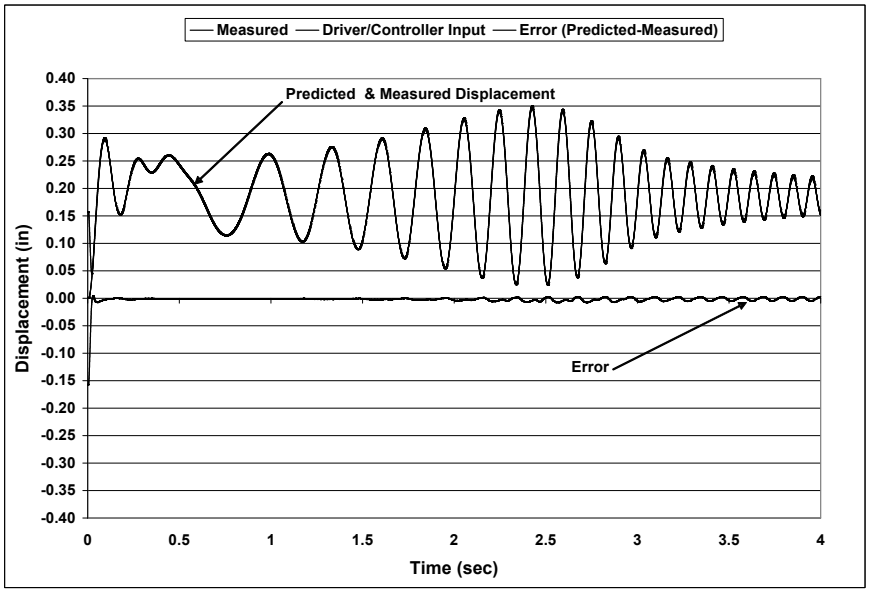

Figure 5-20. Agreement between predicted and measured displacements for the Proof-of-Concept demonstration.

5.5. Drilling Tests with Drillstring Compliance

5.5.1. SDOF (Simple Harmonic Oscillator of HRDF Axial Compliance Fixture)

Drilling tests with drillstring compliance follows the same approach used in Figure 5-19 only instead of forcing the system with another actuator, actual drilling tests are conducted. Drilling is conducted in Berea Sandstone (BSS) with both the 4 & 5 blade bits using the Simple Harmonic Oscillator introduced by the drilling simulator. A drilling condition of 1250 lb. WOB is selected to allow the range of rotary speeds of 100 to 200 RPM to be tested. Like the bit testing described in Appendix I, the testing with the SDOF or Simple Harmonic Oscillator described in Appendix J includes an overview of each drilling test. The dynamic response of the drillstring is seen in the oscillatory response of the WOB time history (e.g., Figure J-1). For each test, the WOB was constant and the rotary speed was increased incrementally throughout the drilling test. Also plotted is a representative time history for the left and right exciter and the corresponding forces measured at the exciter. A Fast Fourier Transform (FFT) of each of these signals is also plotted for representative drilling conditions and shows the drillstring compliance is responding at the dominant frequency of the simple harmonic oscillator. The shift to a higher frequency is presumed to be due to the increased stiffness at the bit/rock interface that increases the effective stiffness of the drillstring. The axial displacement responses of the four and five blade bits with respect to rotary speed are compared in Figure 5-21. This plot was prepared by computing the root mean square (rms) value of the displacement time history at each rotary speed. The variation in the response is indicative of how bit design influences drilling vibration conditions. This testing has established the viability of using model-based control as an advanced means of studying drill bit dynamics.

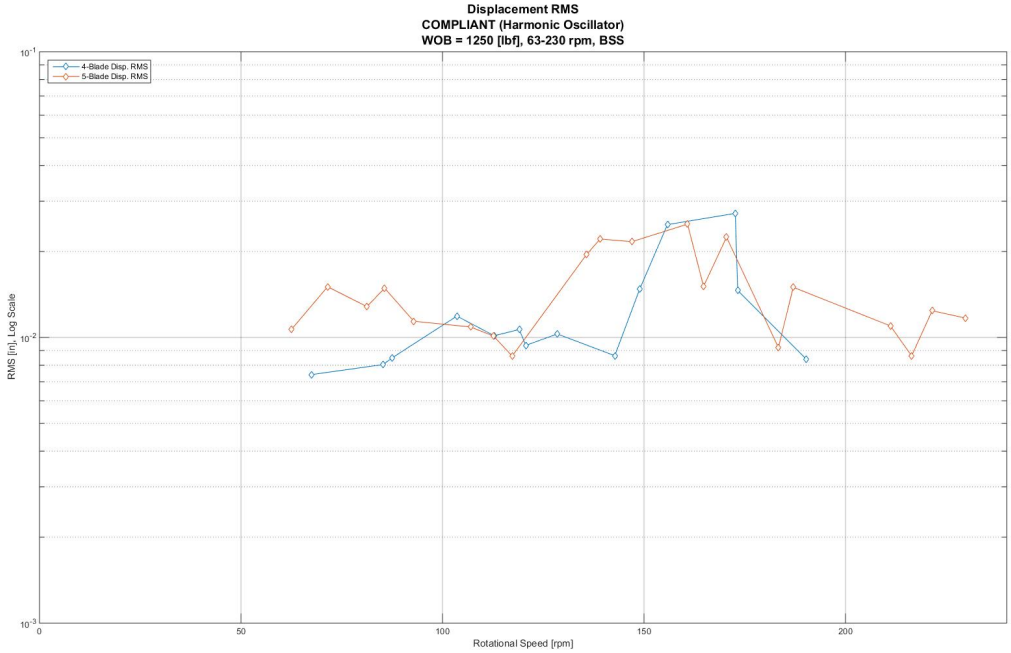

Figure 5-21. Bit response for the Proof-of-Concept drilling test in the time and frequency domain.

5.5.2. Drilling Tests with an Advanced Drillstring Representation MDOF (Tlusty Drillstring Model)

Unlike the previous approach, model-based control is not limited to simple modes of vibration, damping inherent in the mechanical analog, or single point design constraints. This approach can be used to more thoroughly evaluate bit, drillstring, and rock interactions. The method can also be applied to more advanced representations of a drillstring.

As described in Section 2, a drillstring model that is common in the literature [Ref. 28] is a normal modes characterization of a drillstring comprised of 7200 ft. (2200 m) of 4-1/2 inch (11.4 cm) diameter drill pipe and 780 ft. (240 m) of 6-1/2 inch (16.5 cm) diameter drill collar. The properties of the rig supporting this drillstring are also modeled at the top of the drillstring. The normal modes model was prepared by discretizing this system into a series of spring mass elements. The traveling block, swivel, and kelly are represented by a mass of 22600 lb. (10250 kg), and the draw works cable with spring stiffness of 52500 lb./in. (9.1 E6 N/m). The 7200 ft. (2200 m) drill pipe section is modeled using 19 lumped mass components with a mass of 5600 lb. (2540 kg) and stiffness of 28000 lb./in. (4.9 E6 N/m). The interface between the drill pipe and drill collar is modeled using a mass of 7720 lb. (3500 kg/cm) and stiffness of 28000 lb./in. (4.9 E6 N/m). The drill collar section is modeled using 7 lumped mass components with a mass of 9800 lb. (4400 kg) each and stiffness of 700000 lb./in. (122 E6 N/m).

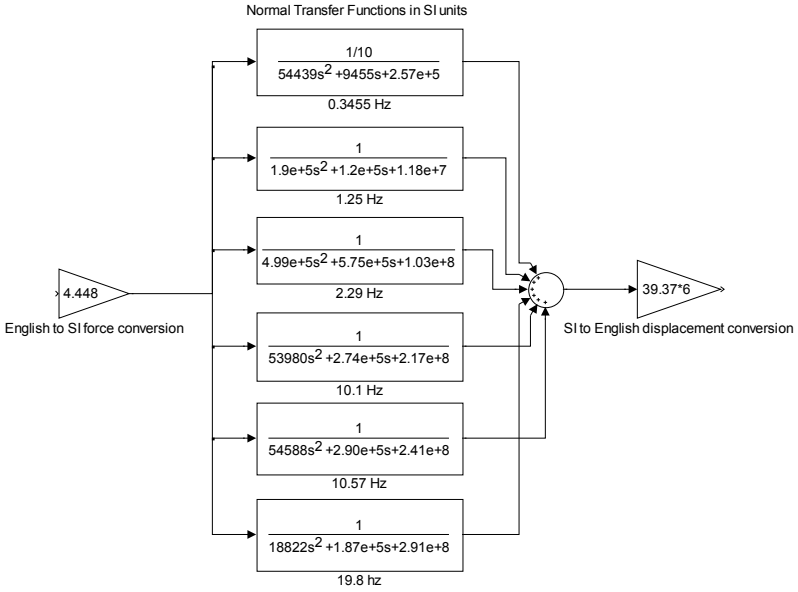

Figure 5-22. Dominant modes from the normal modes model used in predictor.

Rayleigh damping is used to apply uniform damping throughout the model. The assumption of proportional damping is commonly used in structural applications and facilitates diagonalization of the system of equations. It is also standard in many commercial finite element modal analysis software programs. This normal modes model has been implemented into the model-based control system as a predictive driver. Zamudio indicates the response of the system is dominated by the six most compliant modes in the system. This reduced system, shown in Figure 5-22, is used as a drillstring model to reproduce the Tlusty drillstring in the HRDF.

5.6. Variable Rate Spring Fixture Design and Development

In the final phase of testing, a variable rate spring was developed and integrated into the drilling facility with the deep drillstring compliance simulation.

Sandia subcontracted mechanical design services to Radigan Engineering for design, analysis, development, manufacturing, and delivery services in support of development of laboratory test fixtures and prototype components for evaluation in this application. The work accomplished in FY15 addresses development and demonstration of prototype hardware in a laboratory drilling facility that simulates the dynamic response of a drillstring. This specification defines requirements for development of a Variable Rate Spring Fixture (VRSF) that can be emplaced in the Sandia Hard Rock Drilling Facility (HRDF) in support of this research. Radigan Engineering worked with Sandia to specify, design, analyze, develop, manufacture and deliver test fixture assemblies for evaluation in the HRDF at Sandia – a unique facility that simulates drillstring dynamics in the laboratory using high-speed servo-hydraulic systems controlled by fast-acting computer models of a drillstring.

5.6.1. VRSF Requirements

Requirements were developed for the VRSF and include functional specifications, interface requirements, operating conditions and performance requirements. The VRSF was designed to conform to the following functional specification:

- perform as an axial load shock sub by absorbing shock and vibration during drilling tests while continuously transmitting torque via a spline from the Power Head to the drillstring.
- the design basis will assume rigid plate assemblies that distribute axial loads between parallel spring modules.
- have the capability of preloading integral spring assemblies to ensure they remain in compression during drilling conditions and shock & vibration events encountered during testing.
- include a modular approach to allow spring sets (helical or Belleville stacks) to be interchanged in accordance with laboratory drilling test requirements.
- include provision for thru-conveyance of drilling fluid using an Inner Shaft Coupling (per drawing HRDF-IDF-P1.)

The VRSF was specified to interface with the HRDF as follows:

- Serve as the mechanical interface between the HRDF Power Head (Top Drive) and the drillstring supporting the drill bit.
- Dimensions will be constrained to 24.0 in. (61 cm) diameter by 15.0 in. (38 cm) nominal overall length.
- The top of the assembly will attach to the HRDF Power Head via a 3.0 in. (7.6 cm) outer diameter cylindrical tube connection to a Speith Clamping Sleeve, Type DSK 3.00 x 4.25.
- The bottom of the assembly will attach to the drillstring via a 3.0 in. (nominal) diameter hole bored to a nominal depth of 5.831 in. (14.8 cm) with four (4) equally spaced 0.50 in.

(1.3 cm) diameter set screws to secure the drillstring to the VRSF for rotary torque transmittal.
- Mass will be prescribed to allow conformance with dynamic performance requirements specified below.

The VRSF must operate in accordance with the following:
- React the drilling thrust load applied to the drill bit (WOB 4000 lbs. max).
- Transmit rotary torque from the HRDF Power Head to the drillstring/drill bit (Torque 3600 in-lb. max).
- Support a drillstring and drill bit mass of approximately 60 lb. (27 kg) total.
- Provide a user-selectable spring rate as per specified operating conditions and performance requirements.

The VRSF will perform in accordance with the following:
- Provide a minimum of 32 spring states selectable between a minimum of five (5) spring modules.
- User-selectable spring rates via manual control of each spring module.
- Provide an overall spring rate of 300 – 9300 lb./in. (52540 – 1629000 N/m) in 300 lb./in. (52540 N/m) increments.
- Operate across a natural frequency range of 4 to 22 Hz when supporting the drillstring and bit assembly in addition to mass integral to the VRSF assembly (180 lb. total dynamic mass assumed).
- Allow 2.0 in. (5.1 cm) of axial compression in response to spring preload plus static and dynamic drilling conditions.
- Accommodate controllable damping of constituent vibrations (via mechanical/electrical integration of Sandia-provided Lord Magneto-Rheological (MR) fluid dampers).
- Be reconfigurable to allow other spring configurations (other rates, non-linear response, variable materials, etc.) in accordance with this specification.

Finally, the VRSF has Control, Automation & Instrumentation requirements:
- capable of being upgraded to demonstrate automated control using SMA actuators.
- have provision for a displacement transducer to monitor load deflection during drilling operations.

Stress analysis on critical components was used to validate the VRSF design prior to manufacture.

The resulting design developed by Radigan Engineering, and accepted by Sandia, is shown in Figure 5-23; the effective spring rates achievable with the VRSF are shown in Figure 5-24. The VRSF includes structural rigidity from an immovable frame (Figure 5-25) that acts like the housing of a drilling tool; a moving mass (Figure 5-26) housed within this structure compresses the active spring modules. The Variable Rate Spring Fixture (VRSF) is documented in detail in Appendix H. The VRSF is equipped with a rotary spline mechanism that allows each spring module to be selectively actuated – in comparable form to what was accomplished using the Variable Rate Spring (VRS). The VRSF is equipped with rigid tube assemblies that allow the spring modules to be removed from the load path so comparative testing can be accomplished in

the HRDF with the VRSF spring modules active and with the system in a rigid state. The VRSF also includes interfaces for installing MR dampers in parallel with the spring modules to allow the effectiveness of controllable damping to be evaluated as well. The design detail of the VRSF is documented in Appendix H including the Sandia-developed instrumentation integrated into the assembly to allow diagnostics while in operation.

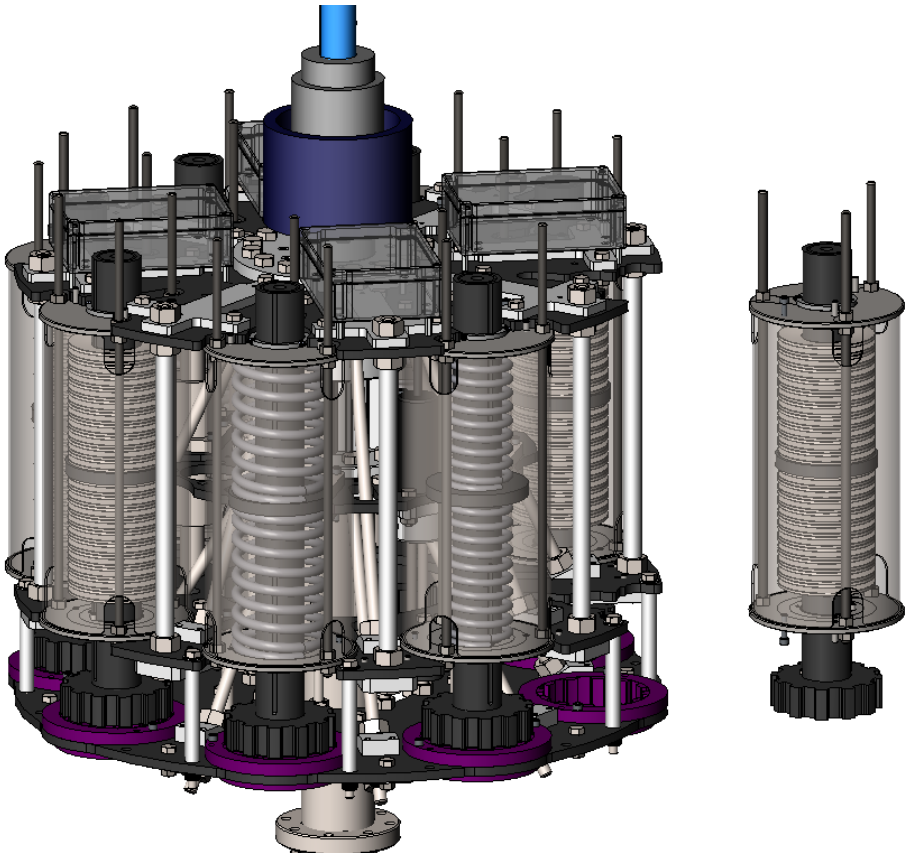

Figure 5-23. Variable Rate Spring Fixture (VRSF) with removable spring modules.

Module #	Module Spring Rate (lbf/in)	Individual Spring Rate k_{1 of 4} (lbf/in)
1	300	75
2	600	150
3	1200	300
4	2400	600
5	4800	1200
5b	6000	1500
All (a)	9000	
All (b)	14400	

Figure 5-24. Effective spring rates achievable by the VRSF with selective activation of individual spring modules.

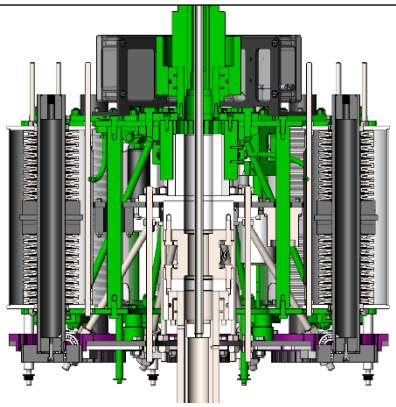

Figure 5-25. Variable Rate Spring Fixture – Rigid Assembly highlighted in green.

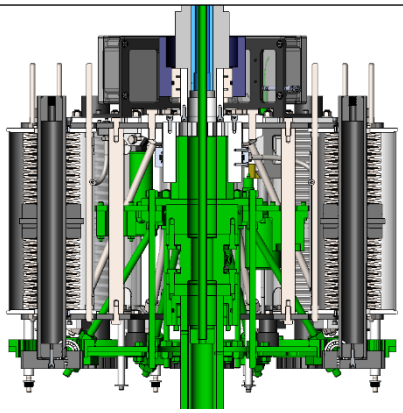

Figure 5-26. Variable Rate Spring Fixture – Dynamic Assembly highlighted in green.

5.7. Compliant Drillstring Drilling Tests with a Variable Rate Spring

The Variable Rate Spring Fixture (VRSF) was integrated into the HRDF to accommodate a drilling applicability demonstration of the significance of controllable stiffness in introducing stability. Drilling tests were conducted with the simple harmonic oscillator compliant drillstring described in Section 5.5.

Figure 5-27. VRSF installed in HRDF for Drilling Applicability Demonstration.

Initial testing was conducted to repeat the instability testing with the SDOF/SHO using the 5-blade bit in Berea Sandstone with an operating condition at 1250 lbf WOB and 100 RPM. Test results are included in Appendix K and include an overview of each test – as was done in Appendix I and Appendix J. Testing was first conducted with the VRSF rigid (i.e., no spring modules active) by installing rigid links within the VRSF load path that prevent the dynamic mass within the VRSF from moving. This was done to determine the peak bit deflections due to the presence of the increased mass of the VRSF before activating the spring modules. Figure K-1 shown a test overview, Figure K-2 shows the time history of the left and right exciter

displacement time history and Figure K-7 shows the frequency domain response of the exciter along with the frequency domain response of the force measured at the exciter; the increased mass of the VRSF decreases the primary mode of vibration for the simple harmonic oscillator. These test conditions were repeated by activating only spring module 4 (Figure K-3) during a drilling test, followed by activating only spring module 3 (Figure K-5). The variation in the response of the system is seen in the time and frequency domain in Appendix K. The acceleration on the HRDF top drive that supports the drillstring is measured during each of these tests. Figure 5-28, Figure 5-29 and Figure 5-30 show the acceleration measured on the HRDF top drive during these tests. The reduction in peak bit vibration acceleration due to the introduction of the module 4 spring stiffness is clearly seen by comparing Figure 5-29 and Figure 5-28; the vibration due to the target mode at approximately 8 Hz is significantly reduced. Conversely, further reductions in the VRSF spring stiffness by activating spring module 3 (Figure 5-30 compared to Figure 5-28) do not provide as much benefit. This compares favorably with drilling instability models results shown in Figure 3-20 that suggest there are preferential values of spring stiffness for a given drillstring. Further, Figure 5-31 provides a relative comparison of the displacement time histories of each of these tests. Spring module 4 provides a preferred response over the rigid VRSF and spring module 3 active responses.

Additional testing is required to further examine the preferred spring rates for a given drillstring. Future work will also address the benefit available from a controllable spring on a multi-degree of freedom drillstring, such as the Tlusty drillstring model simulation in the HRDF. These preliminary results demonstrate the benefit of a controllable stiffness actuator within the bottom hole assembly of a drillstring.

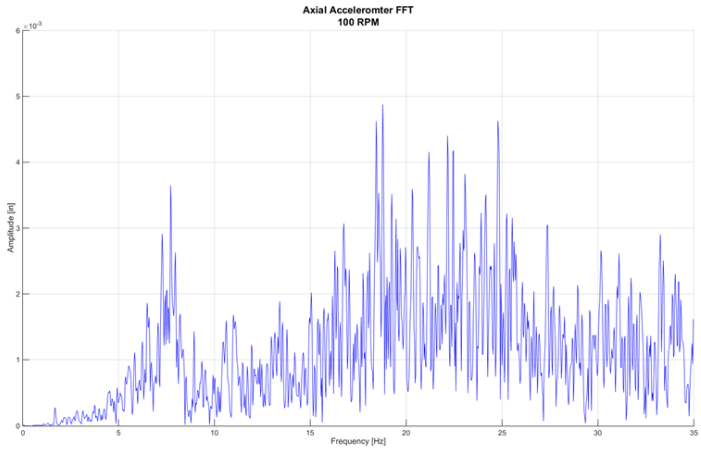

Figure 5-28. FFT of Acceleration on HRDF Power Head during drilling tests at 1250 lb WOB & 100 RPM with VRSF installed in Rigid Mode (all spring modules inactive).

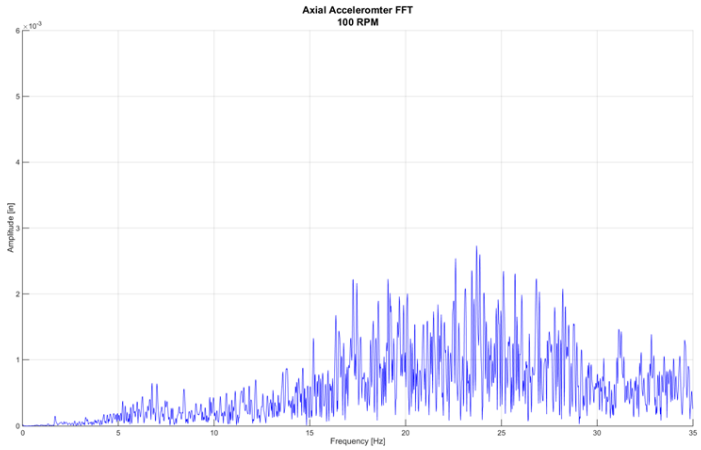

Figure 5-29. FFT of Acceleration on HRDF Power Head during drilling tests at 1250 lb WOB & 100 RPM with VRSF installed and spring module 4 active.

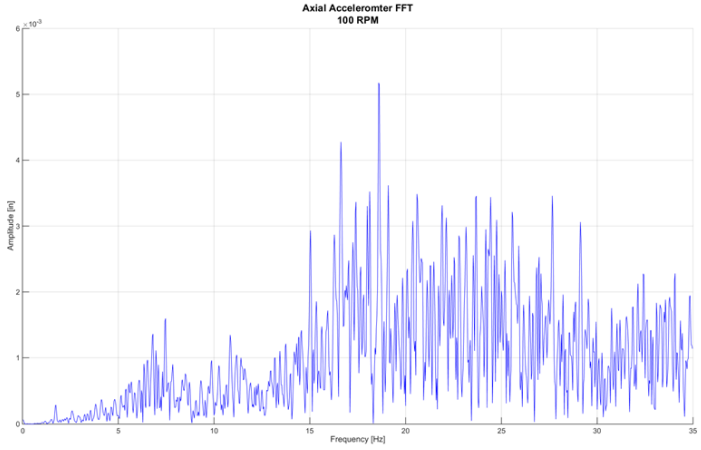

Figure 5-30. FFT of Acceleration on HRDF Power Head during drilling tests at 1250 lb WOB & 100 RPM with VRSF installed and spring module 3 active.

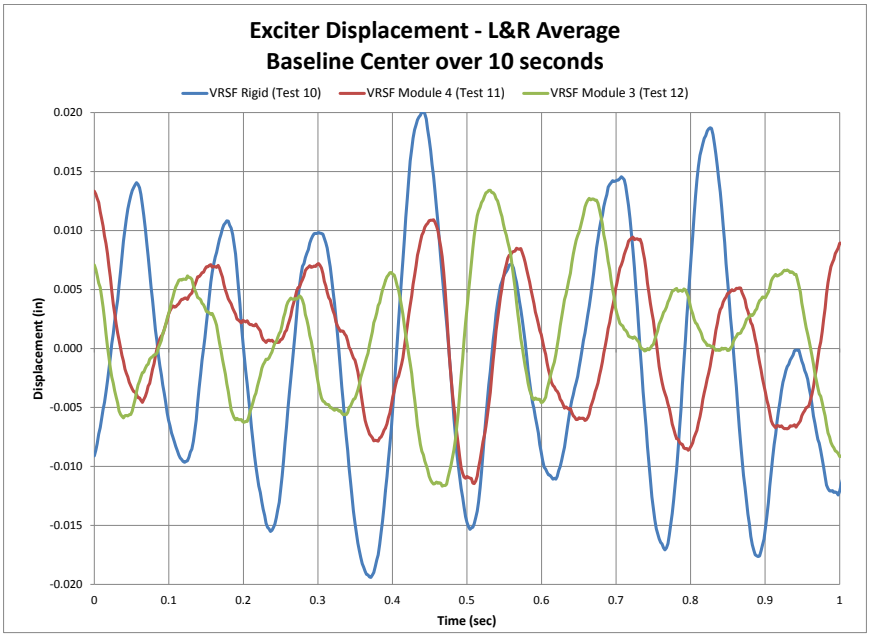

Figure 5-31. Results from drilling tests with VRSF installed in rigid condition and also with spring module 3 & 4 active.

6. PROTOTYPE CONCEPT DEVELOPMENT

A variety of concepts have been evaluated in this study that could be practically applied to reducing damaging drillstring vibrations. The primary focus is upon development of a variable rate spring downhole tool yet tuned mass dampers and inertial excitation concepts have been evaluated as well. It has been shown that a variable rate spring can be conceived to modify the dynamic properties of a drillstring to prevent instability arising from self-excitations. Such a downhole tool must be capable of being autonomously controlled in response to conditions encountered by the host drillstring. A variety of actively-controlled spring rate technologies have been considered including the companion technologies that enable self-activation to the preferred state.

6.1. Variable Rate Spring Downhole Tool

A concept has been developed for a prototype Variable Rate Spring tool that meets the requirements for the concepts outlined in this study. This concept uses the Sandia - proprietary design concepts consisting of a linear solid state spring, onboard sensors for host drillstring monitoring, on–board processors for system property identification, control logic, and shape memory alloys for low power, high force activation. The prototype concept is shown in Figure 6-1.

6.1.1. Spring Rate

Active spring control concepts considered include Shape Memory Alloys (SMA) (summarized in Appendix D), liquid springs (summarized in Appendix E), and Selective Fixed Rate Spring Module Activation (summarized in 0). While a shape memory alloy based spring is innovative and a pathway to application has been conceived, substantial power would be required downhole to convert a large cross-section of SMA material from martensitic to austenite condition. Furthermore, if the interstitial structures of large load bearing solid sections comprising the spring are not adequately transformed then the material would not perform as intended. Additional work is required to investigate overall feasibility. However, the high cost of SMA material and the large volumes that would be required suggests alternate solutions be explored.

A liquid spring was considered by Taylor Devices for this application. The limitation of a liquid spring for a downhole application is its temperature exposure, as temperature fluctuations are manifested as internal pressure changes within the liquid spring. While used for a variety of applications, a liquid spring for downhole applications may prove to be problematic. Taylor Devices proposes use of a machined spring, manufactured from high strength material, which could be used in place of Belleville springs typically used in high force, downhole applications.

The concept with immediate application relies upon selective activation of passive spring modules comprised of Belleville spring stacks. The concept outlined in 0 was used for the variable rate spring concept deployed within the DDS described in this study. It appears to hold great promise for this application, as a compact, high force, low power actuator can be used to allow conventional load bearing spring stacks to move in and out of the load path in response to operational requirements. Sandia has developed a concept that relies upon SMA wire to develop

high force with low power to introduce this functionality to the downhole tool. The variable rate spring comprising the downhole tool would be similar to the concept described in 0. The load bearing components would be housed within a drilling tool case with the operational loads transmitted through component springs reacting against the case and presenting the preferred spring rate to the drill bit. A main drive spline would allow translational motion of the bit for the necessary deflection while transmitting operational torque to the drill bit.

Figure 6-1. Sandia Prototype Variable Rate Spring Tool.

6.1.2. SMA for spring state activation

Work has been completed to demonstrate an SMA actuator could produce the functionality required to activate and deactivate the spring modules. An SMA test fixture was developed that allowed investigation of various SMA wire sizes for the application (see Appendix G). A series of tests was conducted to evaluate the suitability of using SMA wires for a down-hole rotary actuator.

An SMA desktop model was also developed that demonstrates that a rotary spline could be rotationally indexed to allow the spring modules to be activated and deactivated. A mechanical latch mechanism was also demonstrated to allow the system to power-off and yet still retain the entire spring state desired. The system would be integrated into the downhole tool using the general approach shown in Figure 6-2. Sandia has filed a patent application on the concept.

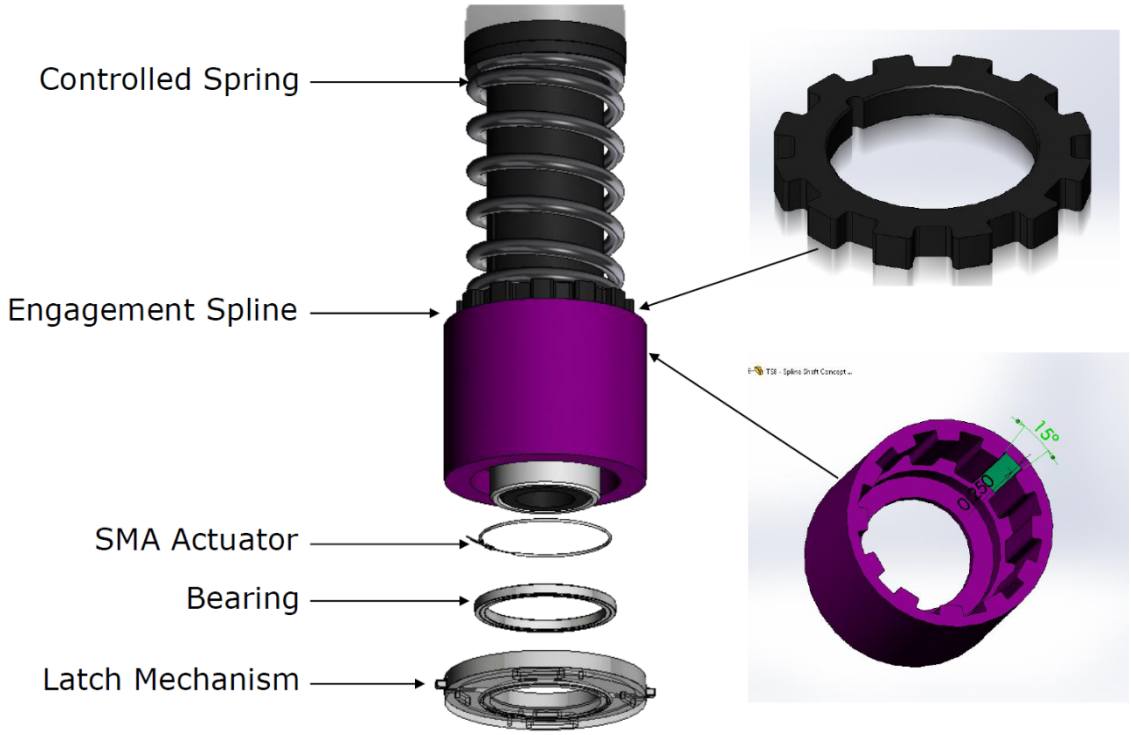

Figure 6-2. Smart Spring Module.

6.1.3. Damping

Although not shown in the above concept, the implementation of a variable rate spring would include some type of controllable damping to ensure the mode of vibration introduced by the compliance is appropriately damped. The VRSF fixture described in Appendix H includes capability for adding Magneto-Rheological (MR) fluid dampers in parallel with the active spring modules. An actual downhole tool would include an MR damper implementation as previously developed and licensed by Sandia (and described in [Ref. 7]). The damping functionality could be combined into a single tool or provided by a separate tool in the BHA.

6.1.4. Tool Sensors

The tool would include on-board sensors to measure both the operational load and displacement response so a frequency response function could be predicted by the on-board processor. This would consist of a strain gage section within the case to measure weight on bit and a linear variable differential transducer to measure bit displacement. An accelerometer would also be included to monitor the response on potentially both the tool support case as well as the dynamic mass.

6.1.5. Embedded Processing for System Identification

An embedded controller would be included in the downhole tool. Feasibility has been demonstrated by a processor identified in this study that is compatible with Matlab processing

algorithms for conducting spectral analysis on downhole data to determine control states. This processor would invoke the controls approach described below.

6.1.6. Controls Approach

To suppress vibrations, the variable elements (stiffness and damping) must be automatically controlled. Because of the difficulty of communicating reliably from down hole to the surface, and because the conditions observed at the surface often differ dramatically from those observed down hole, the active suppression system requires a local automatic control system that can be implemented on a simple embedded processor and can achieve desired outcomes using only data available from sensors located at or near the variable element. Several different classes of available control approaches are well-suited to this application.

6.1.7. Model-based gain-scheduling

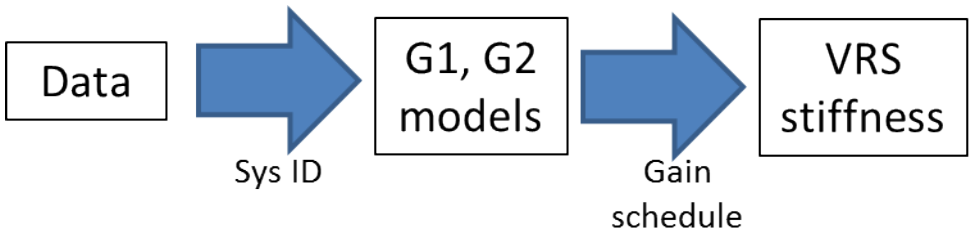

Figure 6-3. Schematic depiction of model-based gain-scheduling control approach.

Model-based gain-scheduling would take full advantage of the extensive modeling and simulation element of this work. In general, this method, shown schematically in Figure 6-3 would use real-time data to develop models of the drillstring dynamics above and below the variable element(s), and use either simple heuristic algorithms or lookup tables to select control parameters (e.g. stiffness). Multiple variations of this approach could be used. For example, in one variant, system identification methods could be used to fully generate a dynamic model of the relevant drillstring elements, which could then be analyzed to determine the optimal stiffness parameters (which act as control gains in this formulation). Alternatively, data could be used simply to identify resonant peaks, and these could be combined with prior model information to populate a stored dynamic model, which would subsequently be analyzed to select gains indirectly. This approach could draw on elements of adaptive control, in which dynamic model structure is known, but certain parameters are adapted continuously based on measured data.

To address instability conditions, the model must have adequate fidelity to identify the negative real portions of the frequency response transfer function. This is a potential challenge when attempting to fully identify the dynamics, and for this reason adaptive approaches may be preferred.

6.1.8. Model-based feedback

A second set of approaches would still use a model of the system but would use feedback control algorithms to directly modify the variable parameters based on measured system outputs. The main distinction between this and model-based gain scheduling is that the model would simply be used in the control law, rather than used as a reference. Because the control output is actually a stiffness parameter, the controller could take the form of an impedance (or "Z") controller. No information from prior simulations would be contained in the controller. The controller could take one of several forms, for example using adaptive control methods to adjust the control system model dynamics in response to measured data as the system changes over time, as sketched in Figure 6-4.

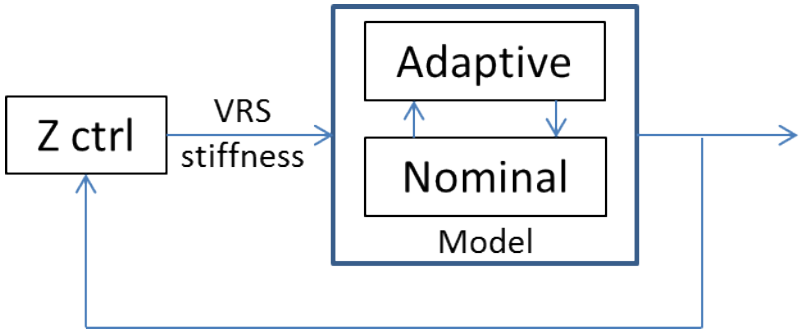

Figure 6-4. A simplified schematic of a model-based adaptive feedback control method.

6.1.9. Robust control

A final control approach would use only a fixed model of the system for controller design, while using robust control methods to accommodate the variations in the system dynamics with changing depth and drilling conditions. This approach would have the benefit of not requiring any model of the system to be estimated or computed in real time. The same controller (e.g., an impedance controller) would run at all times, and would respond directly to measured signals, as sketched in Figure 6-5. Such a controller would be entirely responsive to directly measured vibrations, with no additional intelligence to infer anything about the system from these signals. The main drawback of this approach is that it is unclear whether robustness terms alone could accommodate the required variations in the system dynamics without sacrificing control performance (e.g. response time, stiffness optimization) so much as to render the system ineffective.

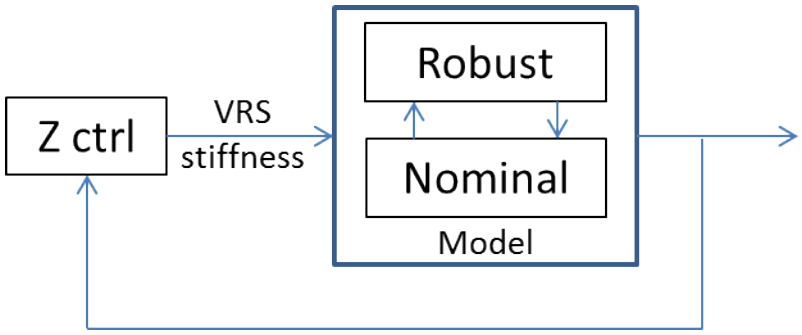

Figure 6-5. Schematic of robust impedance controller.

6.2. Tuned Mass Damper Concept

A tuned mass damper requires a variable rate spring be made available to adjust the response of the component mass to target the frequency of interest. Concepts employed in the development of the variable rate spring are also applicable to development of a tuned mass damper.

6.3. Inertial Exciter

The benefit of an inertial exciter has been demonstrated via computational modeling and laboratory hardware demonstrations. Sandia has developed a preliminary concept for a downhole inertial exciter. Although not the primary focus of this study it is worthy of additional consideration as well.

7. CONCLUSIONS

7.1. Technical Advance Summaries

Exceptional technical advances were made throughout the three year term of this LDRD project, including:

- Development of a drillstring computational model with sufficient fidelity to accommodate evaluation of active vibration suppression concepts;

- Application of dynamic substructuring modeling methods to drillstrings to enable rapid simulation of alternatives without repeated derivation of dynamics equations;

- Use of impedance and admittance based port-functions in substructured drillstrings to address actuator alternatives to enable modular modeling without concern for power loading effects;

- Integration of the Detournay and Defourny (DD) model for rock-bit interaction with a dynamic model of a drillstring and a dynamic model of bottom-hole geometry to enable real-time simulation of drilling instability;

- Development of a passive equivalent of a drillstring model in the Sandia Drilling Dynamics Simulator (DDS);

- Use of the DDS to simulate instability with and without a Variable Rate Spring (VRS);

- Evaluation of candidate technologies for use as variable rate springs in deep drillstrings to modify the physical response of the drillstring;

- Development of a prototype concept for a solid-state spring drilling assembly that achieves the form, fit, and function necessary to be considered a valid design concept for a downhole variable rate spring element within the bottom hole assembly;

- Laboratory hardware simulations demonstrating benefits available from deployment of variable rate springs in deep drillstrings;

- Laboratory simulations demonstrating benefits available from deployment of inertial exciters in drillstrings;

- Completion of a laboratory-based deep drilling applicability demonstration that demonstrates the prevalence of drilling vibrations, its dependence upon bit design, and further demonstrates the performance improvements available from a variable rate spring element in the bottom hole assembly;

- Development of a unique Shape Memory Alloy (SMA) system for high force, low power actuator applications (rotary drive & latching), including a unique application of teflon insulation on the actuator; and

- A patent application submission for use of smart materials, advanced sensing, processing, and control techniques for development in a downhole tool for mitigation of drilling vibrations.

These advances are relevant, unique and applicable to future prototype tool design, development, and field deployment.

7.2. Lessons Learned

Lessons have been learned that can be applied towards future development efforts in the art of drilling vibration suppression and management, including:

- Drillstring computational modeling is an effective tool to predict parameters for controllable elements in the BHA to effect stiffness modification, predict properties of tuned mass dampers for vibration absorption, and predict properties for inertial exciters for vibration cancellation.

- Dynamic substructuring can be combined with computational modeling and port-function based computational analysis tools to evaluate the influence of various actuator systems, such as variable compliance, on a drillstring frequency response function.

- Controllable stiffness concepts can be conceived that can be inserted into the BHA to influence the drillstring transfer function seen by the drill bit.

- Modeling & Simulation efforts have revealed that both resonance and instability can introduce potentially damaging vibrations to drilling processes. Both must be considered in designing systems to suppress vibrations. It is clear that shifting the frequency response function by adding a controllable stiffness element can dramatically reduce vibrations that originate from both resonance and from delay-based instability, and that ideal spring changes are non-trivial, i.e. problems can be introduced if the spring is either too soft or too stiff. However given the complexity of the drilling process, additional work is needed to *optimally* select spring stiffness to maximize drilling performance while minimizing damage.

Controls & System Identification work has revealed:

- System identification methods can be used to allow tools incorporating downhole measurements to derive representative transfer functions for host drillstrings to allow guidance in selecting preferred dynamic properties of the controllable BHA elements.

- Drilling stability may be predicted based on known properties of drillstring dynamics (e.g. determined from system identification) and complex rock-bit interaction models.

- The quality of system identification depends heavily on the details of the excitation signal, which is not directly controlled in a drilling process. Furthermore, it takes a long time (minutes) to develop a high-quality system ID model for these systems. Therefore, it is highly desirable, in the future, to develop alternative controls methods that do not require system identification.

Drilling dynamics Simulations have highlighted the importance of giving due consideration to the hardware configuration (damping, friction, etc.) to ensure a valid simulation is reproduced.

Drilling Simulations have shown the real value of the drillstring frequency response function can be shifted by a variable rate spring yet additional work is needed to understand the dynamics of rock cutter interaction. The static response of the bit response is reasonably well characterized; dynamics are not.

Shape Memory Alloy (SMA) development work has resulted in a unique demonstration of a rotary actuator based on Nitinol Shape Memory Alloy (TS7-014 - Nitinol Actuator Wire - Dynalloy control #: CS4853). Important SMA wire controllability issues were identified.

Embedded Control development for downhole deployment has revealed that Matlab and compatible processors are available that enable a practical solution. A viable platform has been identified that can accommodate deployment of necessary instrumentation and processors.

7.3. Recommendations

Recommendations emerging from the LDRD project team as a result of this work include the following:

Continue research and development (R&D) for modeling and simulation:

- Study optimization of drilling dynamics to balance drilling performance (e.g. rate of penetration) and protection of equipment. Additional work is required to understand which vibrations are the most damaging, how much vibration can be tolerated without damage, and how to target real-time dynamic changes most effectively to maximize overall system performance. This will require studies that tightly integrate the modeling process with very controlled experiments.

- Study the impact and benefits of multiple tunable compliant elements distributed throughout the drillstring, including the study of how controlling each element locally, with no communication between elements, impacts the overall system dynamics and stability properties.

Continue work on controls development:

- Pursue embedded control as a means to enable autonomous control of a downhole actuator in response to the dynamic properties of the host drillstring.

- Explore nonlinear control methods (e.g. sliding mode control) that specialize in rapid convergence to solutions from just a few samples of data from nonlinear systems, as a means of avoiding the challenges associated with down-hole system identification.

Continue work on Shape Memory Alloys (SMA) as a possible downhole actuator for engaging spring modules within a variable rate spring assembly. Give special consideration to high temperature SMA materials as the downhole environment will mandate it for general purpose drilling conditions. Continue research on behavior of thick sections and non-Nitinol material options as a potential solution for a downhole controllable spring.

Pursue development of a Variable Rate Spring downhole tool based upon these advances:

- Future work should include development and critical function evaluation of variable stiffness elements in controlled laboratory drilling demonstrations.

- Pursue licensing and commercialization with an industry partner from the drilling service industry.

- Develop advanced tool to work in collaboration with downhole MR damping technology previously developed and licensed by Sandia.

- Address viability of the downhole design concept with a full thermo-mechanical load analysis on representative sections that will necessarily comprise a variable rate spring.

R&D work should continue on the other vibration mitigation options peripherally addressed in this study. Both the Tuned Mass Damper concept and Inertial Exciter should be pursued on a theoretical basis with work performed to conceptualize pathways to realization of hardware that can be deployed downhole.

Finally, future work on the topic of drilling vibration mitigation and suppression must address other modes of vibration and other degrees of freedom (i.e., torsional vibrations, stick/slip, lateral, whirl) as well. A system-engineered solution is necessary and cannot be fully addressed without regard for how complex bit cutting structure designs interact with representative rock formations - as was addressed within this study for the case of longitudinal vibrations. The tools and methods applied herein are applicable to other vibration modes as well.

REFERENCES

1. de Klerk, D., Rixen, D.J., and Voormeeren, S.N., "General Framework for Dynamic Substructuring: History, Review, and Classification of Techniques," AIAA Journal, Vol. 46, 2008, 1169-81.
2. Hogan, N., "Impedance Control: An Approach to Manipulation," ASME Journal of Dynamic Systems, Measurement and Control, Vol. 107, 1985, 1-24.
3. Dareing, D., Tlusty, J., and Zamudio, C., "Self-Excited Vibrations Induced by Drag Bits", Journal of Energy Resource Technology, Vol. 112, 1990, 54-61.
4. Raymond, D.W, Elsayed, M.A., Polsky, Y., Kuszmaul, S.S., "Laboratory Simulation of Drill Bit Dynamics Using a Model-Based Servo-Hydraulic Controller," Journal of Energy Resource Technology, Vol. 130, 2008, 54-61.
5. Dynamic Substructuring of Drillstring Computational Models for Exploration of Actuator Alternatives, Raymond, D., Mesh, M., Buerger, S., Third International Colloquium on Nonlinear Dynamics and Control of Deep Drilling Systems, Minneapolis, May 29-30, 2014.
6. Liquid Spring for Drillstring Tool, Feasibility Report for Sandia National Laboratories, DP-19408-01, 8/30/2013.
7. Controllable Magneto-Rheological Fluid-Based Dampers for Drilling, US 7,036,612 B1, Raymond, D.W., & Elsayed, M.A., May 2, 2006.
8. Elsayed, M. A., Raymond, D. W., "Measurement and Analysis of Chatter in a Compliant Model of a Drillstring Equipped with a PDC Bit," *Proceedings, ASME ETCE Conference*, New Orleans, LA, Feb. 2000.
9. Elsayed, M. A., Raymond, D. W., "Analysis of Coupling Between Axial and Torsional Vibration in a Compliant Model of a Drillstring Equipped with a PDC Bit," *Proceedings, ASME ETCE Conference*, Houston, TX, Feb. 2002.
10. E. Detournay, P. Defourny, A phenomenological model of the drilling action of drag bits, International Journal of Rock Mechanics and Mining Sciences 29 (1) (1992) 13-23.
11. E. Detournay, T. Richard, M. Shepard, Drilling response of drag bits: theory and experiment, International Journal of Rock Mechanics and Mining Sciences 45 (8) (2008) 1347-1360.
12. T. Richard, C. Germay, E. Detournay, A simplified model to explore the root cause of stick-slip vibrations in drilling systems with drag bits, J. Sound Vib. 305 (3) (2007) 432-456.
13. Force-Deflection Characteristics of SMA-Based Belleville Springs, Furgiuele, Maletta, & Sgambitterra, SMASIS 2013-8203.
14. NiTi Belleville washers: Design, manufacturing and testing, Maletta, Filice, Furgiuele.
15. Changes in the Mechanical Behavior of Nitinol Following Variations of Heat Treatment Duration and Temperature, Heidi F. Khalil (Thesis).
16. J. Tlusty, Manufacturing Processes and Equipment, Prentice Hall, 2000.

17. J. Hale, Theory of Functional Differential Equations, Springer-Verlag, New York.

18. Kristian Albert Jakobsen, Damping of Structures, 2007.

19. Steen Krenk, Frequency Analysis of the Tuned Mass Damper, Journal of Applied Mechanics, 72, 2005, pp. 936-942.

20. Active Cancellation of Drill String Vibrations Using Inertial Exciters, Sandia Disclosure No. 12849, Raymond, D., Mesh, M., Buerger, S., 8/6/2013.

21. Solid State Spring Using Shape Memory Alloys (SMA), Sandia Disclosure No. 12869, Raymond, D., & Radigan, W., 10/01/2013.

22. Variable Rate Mechanical Spring for Suppression of Drilling Vibrations, Sandia Disclosure No. 12870, Raymond, D., Su, J.C., Radigan, W., 10/01/2013.

23. Variable Rate Liquid Spring for Suppression of Drilling Vibrations, Sandia Disclosure No. 12871, Raymond, D., Lee, D., 10/01/2013.

24. Variable Rate Compliance Module, Assembly and Tool for Suppression of Drilling Vibrations, Docket No. SD-12870/32467-0021.

25. Reference Design and Operations for Deep Borehole Disposal of High Level Radioactive Waste, Arnold, B.W., Brady, P.V., Bauer, S.J., and Pye, S., SAND2011-6749, October 2011.

26. Development of a Method for Predicting the Performance and Wear of PDC Drill Bits, Glowka, D.A., SAND86-1745, June 1987.

27. http://tomax.no/

28. Zamudio, C. A., Tlusty, J.L., and Dareing, D.W., 1987, "Self-Excited Vibrations in Drillstrings," SPE Tech. Paper, paper 16661, 62nd Annual Conf., Dallas, TX, pp. 117-123.

29. Jogi, P.N., Macpherson, J.D., and Neubert, M., "Field Verification of Model-Derived Natural Frequencies of a Drill String", *Journal of Energy Resources Technology,* Vol. 124, September, 2002, 154 – 162.

30. Wise, J. L., et al, "Hard-Rock Drilling Performance of a Conventional PDC Drag Bit Operated With, and Without, Benefit of Real-Time Downhole Diagnostics," *Transactions, Geothermal Resources Council Annual Meeting*, Morelia, Mexico, October 2003.

31. PDC Bits Demonstrate Benefit Over Conventional Hard-Rock Drill Bits, Raymond, D. W., *Geothermal Resources Council Transactions*, Sept. 2001.

32. Richard C. Dorf and Robert H. Bishop, Modern Control Systems, 8th Ed., Addison Wesley, Menlo Park, CA, 1998, p.56, Fig 2.19.

APPENDIX A. NORMAL MODES FORMULATION

A.1 Normal Modes

The global mass and stiffness matrices from the bar element model are used in a normal modes solution. Consider a mechanical system described by the equations of motion

$$M\ddot{u} + C\dot{u} + Ku = F \quad \text{(Eq. A-1)}$$

where u are nodal displacements, M and K are stiffness and mass matrices, C is the damping matrix, and F – is a vector of forces. Dimension of M and K are $n \times n$, where n is the number of degrees -of-freedom of the the system. Vector $F^T = [F_1, F_2, \ldots F_n]$ is of length n.
The homogeneous system without damping corresponding to (Eq. A-1) is (it is possible to use complex modes and apply them directly to original system instead):

$$M\ddot{u} + Ku = 0 \quad \text{(Eq. A-2)}$$

Performing the usual coordinate transformation using normal modes Φ of the system (Eq. A-2)

$$u = \Phi\theta \quad \text{(Eq. A-3)}$$
$$\dot{u} = \Phi\dot{\theta} \quad \text{(Eq. A-4)}$$
$$\ddot{u} = \Phi\ddot{\theta} \quad \text{(Eq. A-5)}$$

Substituting modal transformation into (Eq. A-1) one can obtain following equation in modal coordinates

$$[\Phi^T M\Phi]\ddot{\theta} + [\Phi^T C\Phi]\dot{\theta} + [\Phi^T K\Phi]\theta = \Phi^T F \quad \text{(Eq. A-6)}$$

We need to assume some kind of normalization along with modal damping

$$\Phi^T M\Phi = diag(\{m_l\}) \quad \text{(Eq. A-7)}$$
$$\Phi^T M\Phi = diag(\{m_l\}) \quad \text{(Eq. A-8)}$$

we arrive at the following equation

$$diag\{m_l\}\ddot{\theta} + diag(\{c_l\})\dot{\theta} + diag(\{k_l\})\theta = \Phi^T F \quad \text{(Eq. A-9)}$$

Expanding the right-hand side of the equation (assuming that r modes are sufficient to describe the system)

$$f = \Phi^T F = \begin{bmatrix} \phi_{11} & \phi_{12} & \cdots & \phi_{1r} \\ \phi_{21} & \phi_{22} & \cdots & \phi_{2r} \\ \vdots & \cdots & \cdots & \vdots \\ \phi_{n1} & \phi_{n2} & \cdots & \phi_{nr} \end{bmatrix}^T \begin{bmatrix} F_1 \\ F_2 \\ \vdots \\ F_n \end{bmatrix} \quad \text{(Eq. A-10)}$$

In the application to the G1/G2 problem we count grid points from the ground down. So for G2, $F_{n,G2} = 1, F_{1:n-1,G2} = 0$ and for G1 $F_{1,G1} = -1, F_{2:n-1,G1} = 0$. As a result, equation (Eq. A-10) can be greatly simplified and result in the following:

For G2,

$$f_{G2} = \begin{bmatrix} \phi_{n1} \\ \phi_{n2} \\ \vdots \\ \phi_{nr} \end{bmatrix} \quad \text{(Eq. A-11)}$$

For G1,

$$f_{G1} = -\begin{bmatrix} \phi_{11} \\ \phi_{12} \\ \vdots \\ \phi_{1r} \end{bmatrix} \quad \text{(Eq. A-12)}$$

Equation (Eq. A-9) can now be solved for the each of the modal coordiantes θ. Since all equations are uncoupled, the solution looks exactly like the solution for a single degree-of-freedom:

$$\theta_l = \frac{f_l}{-m_l\omega^2 + jc_l\omega + k_l} = \frac{f_l(-m_l\omega^2 - jc_l\omega + k_l)}{(-m_l\omega^2 + jc_l\omega + k_l)(-m_l\omega^2 - jc_l\omega + k_l)} = \\ = \frac{f_l(-m_l\omega^2 - jc_l\omega + k_l)}{(k_l - m_l\omega^2)^2 + c_l^2\omega^2} \quad \text{(Eq. A-13)}$$

where $\omega = 2\pi\nu$ is excitation frequency and k_l is the l-th generalized stiffness. Modal velocity can be calculated as $\dot{\theta}_l = j\omega\theta_l$.

We assume that the system can be accurately described with only r modes, so that only r equations (Eq. A-9) have to be solved.

Physical coordinates u can be found using modal transformation (Eq. A-3)

$$\begin{bmatrix} u_1 \\ u_2 \\ \vdots \\ u_n \end{bmatrix} = \begin{bmatrix} \phi_{11} & \cdots & \phi_{1r} \\ \phi_{21} & \cdots & \phi_{2r} \\ \vdots & \vdots & \vdots \\ \phi_{n1} & \cdots & \phi_{nr} \end{bmatrix} \begin{bmatrix} \theta_1 \\ \vdots \\ \theta_r \end{bmatrix} \quad \text{(Eq. A-14)}$$

A.2 Port Transfer Functions from Normal Modes

Transfer functions can be obtained in a similiar manner by converting equation (Eq. A-9) into the Laplace domain which leads to the following in terms of the Laplace parameter *s*:

$$m_l s^2 \bar{\theta}_l + c_l s \bar{\theta}_l + k_l \bar{\theta}_l = f_l \mathfrak{L}(F(t)) \quad \text{(Eq. A-15)}$$

or

$$\bar{\theta}_l = \frac{f_l \mathfrak{L}(F(t))}{m_l s^2 + c_l s + k_l} \quad \text{(Eq. A-16)}$$

where $\mathfrak{L}(F(t))$ is the Laplace transform of the applied force. Now the Laplace transform of the displacement in physical coordinates is calculated according to (Eq. A-14)
for the interface point on the G2 side:

$$\bar{u}_{n,G2} = \mathfrak{L}(F(t)) \sum_{l=1}^{r} \frac{\phi_{nl}\phi_{nl}}{m_l s^2 + c_l s + k_l} \quad \text{(Eq. A-17)}$$

for the interface point on the G1 side:

$$\bar{u}_{1,G1} = -\mathfrak{L}(F(t)) \sum_{l=1}^{r} \frac{\phi_{1l}\phi_{1l}}{m_l s^2 + c_l s + k_l} \quad \text{(Eq. A-18)}$$

and for the drill bit:

$$\bar{u}_{n,G1} = -\mathfrak{L}(F(t)) \sum_{l=1}^{r} \frac{\phi_{1l}\phi_{nl}}{m_l s^2 + c_l s + k_l} \quad \text{(Eq. A-19)}$$

Finally, for the impedance we have

$$\mathfrak{L}(Z_{1,G1}) = \frac{\mathfrak{L}(F(t))}{s\bar{u}_{1,G1}} = -\frac{1}{s\sum_{l=1}^{r} \frac{\phi_{1l}\phi_{nl}}{m_l s^2 + c_l s + k_l}} \quad \text{(Eq. A-20)}$$

$$\mathfrak{L}(Z_{n,G2}) = \frac{\mathfrak{L}(F(t))}{s\bar{u}_{n,G2}} = \frac{1}{s\sum_{l=1}^{r} \frac{\phi_{nl}\phi_{nl}}{m_l s^2 + c_l s + k_l}} \quad \text{(Eq. A-21)}$$

These terms may be inverted to obtain the admittance as in equations (Eq. A-10) and (Eq. A-11).

A.3 Tuned Dynamic Absorber – Modal Formulation

We would like to use tuned dynamic damper (TMD) to reduce vibration of the MDOF system. To achieve that we design TMD such that it controls vibration of the particular strongly participating natural mode. If several modes play important role then several TMDs are required, each tuned to a specific mode. What follows is expansion of the classic TMD theory for the MDOF system based on modal description of the system. Analysis utilizes important simplification that response at the damped eigenfrequency frequency is driven mostly by

respective mode and other modes can be ignored. System with TMD can be represented as an original system where TMD is replace by equivalent force. So for the point j where TMD is attached on the structure and mode l which is being damped we can modify (Eq. A-9) to

$$m_l\ddot{\theta}_l + c_l\dot{\theta}_l + k_l\theta_l = \Phi^T F + \Phi^T H \qquad \text{(Eq. A-22)}$$

where G is the internal force of the interaction between TMD and the system and $H = \{H_i\}$, where all $H_i = 0$, except H_j. Physical coordinate of the TMD attachment can be expressed as

$$u_j = \sum_{i=1}^{r} \phi_{ji}\theta_i \approx \phi_{jl}\theta_l \qquad \text{(Eq. A-23)}$$

Substituting ?? into the ?? and considring ?? for active mode only, we arrive to following

$$\frac{m_l}{\phi_{jl}^2}\ddot{u}_j + \frac{c_l}{\phi_{jl}^2}\dot{u}_j + \frac{k_l}{\phi_{jl}^2}u_j = \frac{\phi_{nj}}{\phi_{jl}}F_n + H_j$$

or using notation $\mathcal{M} = \frac{m_l}{\phi_{jl}^2}$, $\mathcal{C} = \frac{c_l}{\phi_{jl}^2}$ and $\mathcal{K} = \frac{k_l}{\phi_{jl}^2}$

$$\mathcal{M}\ddot{u}_j + \mathcal{C}\dot{u}_j + \mathcal{K}u_j = \frac{\phi_{nj}}{\phi_{jl}}F_n + H_j \qquad \text{(Eq. A-24)}$$

TMD itself is described by following equation of motion:

$$\begin{aligned} m_d\ddot{u}_d &= -H_j \\ H_j &= k_d(u_d - u_j) + c_d(\dot{u}_d - \dot{u}_j) \end{aligned} \qquad \text{(Eq. A-25)}$$

Equations A-24 and A-25 form system which needs to be solved in order to determine optimal parameters for the TMD. We proceed by eliminating internal force from the equations:

$$\begin{aligned} \mathcal{M}\ddot{u}_j + \mathcal{C}\dot{u}_j + \mathcal{K}u_j - k_d(u_d - u_j) - c_d(\dot{u}_d - \dot{u}_j) &= \frac{\phi_{nj}}{\phi_{jl}}F_n \\ m_d\ddot{u}_d + k_d(u_d - u_j) + c_d(\dot{u}_d - \dot{u}_j) &= 0 \end{aligned} \qquad \text{(Eq. A-26)}$$

$$\begin{bmatrix} \mathcal{M} & 0 \\ 0 & m_d \end{bmatrix}\begin{bmatrix} \ddot{u}_j \\ \ddot{u}_d \end{bmatrix} + \begin{bmatrix} \mathcal{C} + c_d & -c_d \\ -c_d & c_d \end{bmatrix}\begin{bmatrix} \dot{u}_j \\ \dot{u}_d \end{bmatrix} + \begin{bmatrix} \mathcal{K} + k_d & -k_d \\ -k_d & k_d \end{bmatrix}\begin{bmatrix} u_j \\ u_d \end{bmatrix} = \begin{bmatrix} \frac{\phi_{nj}}{\phi_{jl}}F_n \\ 0 \end{bmatrix} \qquad \text{(Eq. A-27)}$$

Steady state solution of this system is sought in the form

$$U = Re\left(\begin{bmatrix} U_j e^{i\omega t} \\ U_d e^{i\omega t} \end{bmatrix}\right)$$

so that (considering $\frac{\phi_{nj}}{\phi_{jl}}F_n = \mathcal{F}e^{i\omega t}$) Equaition ?? is transformed to:

$$\begin{bmatrix} -\omega^2\mathcal{M} + \mathcal{K} + k_d + i\omega(\mathcal{C} + c_d) & -k_d - i\omega c_d \\ -k_d - i\omega c_d & -\omega^2 m_d + k_d + i\omega c_d \end{bmatrix} \begin{bmatrix} U_j \\ U_d \end{bmatrix} = \begin{bmatrix} \mathcal{F} \\ 0 \end{bmatrix} \quad \text{(Eq. A-28)}$$

Solution of this system is

$$\begin{aligned} \frac{U_j}{\mathcal{F}} &= \frac{-\omega^2 m_d + k_d + i\omega c_d}{D} \\ \frac{U_d}{\mathcal{F}} &= \frac{k_d + i\omega c_d}{D} \end{aligned} \quad \text{(Eq. A-29)}$$

where D is determinant of the system.

$$D = (-\omega^2\mathcal{M} + \mathcal{K} + k_d + i\omega(\mathcal{C} + c_d))(-\omega^2 m_d + k_d + i\omega c_d) - (k_d + i\omega c_d)^2 \quad \text{(Eq.A-30)}$$

Selection of TMD parameters must be done so that U_j is minimized, thus minimizing modal response θ_l and as a results, response dominated by that mode at any location on the structure. Following (Eq. A-18) we introduce following notation:

$$\mu = \frac{m_d}{\mathcal{M}}$$

$$\omega_d^2 = \frac{k_d}{m_d}$$

$$\omega_j^2 = \frac{\mathcal{K}}{\mathcal{M}}$$

$$\zeta_j = \frac{\mathcal{C}}{2\sqrt{\mathcal{K}\mathcal{M}}} = \frac{\mathcal{C}}{2\omega_j\mathcal{M}}$$

$$\zeta_d = \frac{c_d}{2\sqrt{k_d m_d}} = \frac{c_d}{2\omega_d m_d}$$

Using these new parameters D takes form

$$D = \mathcal{M}m_d\left(-\omega^2 + \frac{\mathcal{K}}{\mathcal{M}} + \frac{k_d}{\mathcal{M}} + i\omega\frac{(\mathcal{C}+c_d)}{\mathcal{M}}\right)\left(-\omega^2 + \frac{k_d}{m_d} + i\omega\frac{c_d}{m_d}\right) - m_d\left(\frac{k_d}{m_d} + i\omega\frac{c_d}{m_d}\right)^2 =$$

$$\mathcal{M}m_d\left(-\omega^2 + \omega_j^2 + \frac{\mu k_d}{m_d} + i\omega(2\omega_j\zeta_j + 2\omega_d\mu\zeta_d)\right)(-\omega^2 + \omega_d^2 + i\omega 2\omega_d\zeta_d) - m_d^2(\omega_d^2 + i\omega 2\omega_d\zeta_d)^2$$

or

$$D = \mathcal{M}m_d\left[(-\omega^2 + \omega_j^2 + \mu\omega_d^2 + i\omega(2\omega_j\zeta_j + 2\omega_d\mu\zeta_d))(-\omega^2 + \omega_d^2 + i\omega 2\omega_d\zeta_d) - \mu(\omega_d^2 + i\omega 2\omega_d\zeta_d)^2\right] =$$

$$\mathcal{M}m_d\left[\left(\omega_j^2-\omega^2\right)+\mu\omega_d^2+i\omega\left(2\omega_j\zeta_j+2\omega_d\mu\zeta_d\right)\right)\left(\left(\omega_d^2-\omega^2\right)+i\omega 2\omega_d\zeta_d\right)-\mu(\omega_d^2+ i\omega 2\omega_d\zeta_d)^2\Big]$$

$$\frac{D}{\mathcal{M}m_d}=\left(\omega_j^2-\omega^2\right)+\mu\omega_d^2+i\omega\left(2\omega_j\zeta_j+2\omega_d\mu\zeta_d\right)\left(\left(\omega_d^2-\omega^2\right)+i\omega 2\omega_d\zeta_d\right) - \mu(\omega_d^2+i\omega 2\omega_d\zeta_d)^2 =$$

$$(\omega_j^2-\omega^2)(\omega_d^2-\omega^2)+\mu\omega_d^2(\omega_d^2-\omega^2)-2\omega^2\omega_d\zeta_d(2\omega_j\zeta_j+2\omega_d\mu\zeta_d)-\mu\omega_d^4+4\mu\omega^2\omega_d^2\zeta_d^2+ i\omega(2\omega_j\zeta_j+2\omega_d\mu\zeta_d)(\omega_d^2-\omega^2)+i\omega 2\omega_d\zeta_d(\omega_j^2-\omega^2)+\mu\omega_d^3 i\omega 2\zeta_d-\mu i\omega 4\zeta_d\omega_d^3$$

$$=(\omega_j^2-\omega^2)(\omega_d^2-\omega^2)-\mu\omega_d^2\omega^2+4\omega^2\omega_d\omega_j\zeta_d\zeta_j+i\omega(2\omega_j\zeta_j+2\omega_d\mu\zeta_d)(\omega_d^2-\omega^2)+$$

$$2\omega_d\zeta_d(\omega_j^2-\omega^2)+2\zeta_d\mu\omega_d^3-\mu 4\zeta_d\omega_d^3]=(\omega_j^2-\omega^2)(\omega_d^2-\omega^2)-\mu\omega_d^2\omega^2+4\omega^2\omega_d\omega_j\zeta_d\zeta_j+ i\omega 2\omega_d\zeta_d(\omega_j^2-(1+\mu)\omega^2)+2\omega_j\zeta_j(\omega_d^2-\omega^2)]$$

(Eq. A-29) now takes form

$$\frac{U_j}{\mathcal{F}}=\frac{-\omega^2m_d+k_d+i\omega c_d}{D}$$
$$\frac{U_d}{\mathcal{F}}=\frac{k_d+i\omega c_d}{D} \qquad \text{(Eq. A-31)}$$

$$\frac{U_j}{(\mathcal{F}\mathcal{K})}=\frac{\mathcal{K}(-\omega^2m_d+k_d+i\omega c_d)}{\mathcal{M}m_d(D\mathcal{M}m_d)}=\frac{(-\omega^2+\frac{k_d}{m_d}+\frac{i\omega c_d}{m_d})\omega_j^2}{(D\mathcal{M}m_d)}=\frac{(-\omega^2+\omega_d^2+2i\omega\omega_d\zeta_d)\omega_j^2}{(D\mathcal{M}m_d)}$$

(Eq A-32)

$$=\frac{(-\omega^2+\omega_d^2+2i\omega\omega_d\zeta_d)\omega_j^2}{(\omega_j^2-\omega^2)(\omega_d^2-\omega^2)-\mu\omega_d^2\omega^2+4\omega^2\omega_d\omega_j\zeta_d\zeta_j+i\omega 2\omega_d\zeta_d(\omega_j^2-(1+\mu)\omega^2)+2\omega_j\zeta_j(\omega_d^2-\omega^2)]}$$

$$\frac{U_d}{(\mathcal{F}\mathcal{K})}=\frac{\mathcal{K}(k_d+i\omega c_d)}{\mathcal{M}m_d(D\mathcal{M}m_d)}=\frac{\omega_j^2(\omega_d^2+2\omega_d\mu\zeta_d)}{(D\mathcal{M}m_d)}=$$

(Eq A-33)

$$\frac{(-\omega^2+\omega_d^2+2i\omega\omega_d\zeta_d)\omega_j^2}{(\omega_j^2-\omega^2)(\omega_d^2-\omega^2)-\mu\omega_d^2\omega^2+4\omega^2\omega_d\omega_j\zeta_d\zeta_j+i\omega 2\omega_d\zeta_d(\omega_j^2-(1+\mu)\omega^2)+2\omega_j\zeta_j(\omega_d^2-\omega^2)]}$$

It is interesting to note that quantity $\mathcal{F}\mathcal{K}$ has meaning of the equivalent static displacement. (Eq. A-32) is used for tuning TMD by minimizing U_j through optimal selection of the ω_d and ζ_d. Classical results presnted in (Eq. A-18), (Eq. A-19), and (Eq. A-20) are based on some simplifications, including ignoring damping in the system. Those simplifications lead to the following tuning of the TMD:

$$\omega_d=\frac{\omega_j}{1+\mu}$$

$$\zeta_d = \sqrt{\frac{\mu}{2(1+\mu)}}$$

More accurate analysis usually requires numerical optimization procedure to find TMD parameters.

A.4 Inertial Exciter for Vibration Reduction

Inertial exciter (IEx) can be approximated by oscillating force applied at certain point on the structure. Theoretical treatment of the inertial exciter is simpler than that of the TMD because there is no need to consider coupled dynamics of the TMD and system itself. Problems of selecting parameters of the IEx is reduced to determining force which needs to be applied to the structure to supress excitation of the particular mode. As in case of the TMD (Eq. A-22) and (Eq. A-23) form basis for the analysis with the distingtion that H is now force produced by IEx. We again assume that motion at the resonance of a particular normal mode is dominated by that mode and other modes can be ignored. Under these assumptions (Eq. A-22) for the modal coordinate of the mode which needs to be surpressed takes form:

$$m_l\ddot{\theta}_l + c_l\dot{\theta}_l + k_l\theta_l = \phi_{nl}F_n + \phi_{jl}H_j \qquad \text{(Eq. A-34)}$$

In order for the RHS of this equation to be equal to zero it is necessary for IEx force to satisfy condition:

$$H_j = -\frac{\phi_{nl}}{\phi_{jl}}F_n \qquad \text{(Eq. A-35)}$$

If this condition is satisfied than mode of concern won't be excited and resonance can be avoided.

A.5 Identifying Important Modes

Application of the TMD requires identification of the modes significantly contributing to the response. Since we mostly interested in the response of one particular point on the drill string (e.g. drill bit) measure based on the peak response at the point seems to be more suitable than measures based on energy associated with particular mode. To develop necessary equation we again can assume that peak response is reached at the resonance of a particular mode and dominated by that mode just like we did earlier in the TMD discussion. As such, displacement of the point is described by (Eq. A-23) and for the response of drill bit (nth point in the drill) string due to the harmonic force applied at the same location

$$u_n = \frac{\phi_{nl}^2}{(k_l - m_l\omega^2) - jc_l\omega} \qquad \text{(Eq. A-36)}$$

At the resonance frequency $k_l - m_l\omega^2 = 0$ and for the magnitude of the displacement

$$|u_n| = \frac{\phi_{nl}^2}{c_l\omega_l} \quad \text{(Eq. A-37)}$$

We can also obtain expressions for amplitude of the velocity and acceleration by multiplying displacement by $j\omega$ and $(j\omega)^2$ respectively.

$$|\dot{u}_n| = \frac{\phi_{nl}^2}{c_l} \quad \text{(Eq. A-38)}$$

$$|\ddot{u}_n| = \frac{\phi_{nl}^2\omega_l}{c_l} \quad \text{(Eq. A-39)}$$

or using modal damping instead of the equivalent viscous

$$|u_n| = \frac{\phi_{nl}^2}{2m_l\zeta_l\omega_l^2} \quad \text{(Eq. A-40)}$$

$$|\dot{u}_n| = \frac{\phi_{nl}^2}{2m_l\zeta_l\omega_l} \quad \text{(Eq. A-41)}$$

$$|\ddot{u}_n| = \frac{\phi_{nl}^2}{2m_l\zeta_l} \quad \text{(Eq. A-42)}$$

The only thing required for computitation of the resonance peak of the displacement, force and acceleration is knowledge of the respective modal parameters. Peak values can be sorted to determine most important modes of the system.

APPENDIX B. MATLAB SCRIPT FOR BAR ELEMENT MODEL

Listing of the Matlab Code Used for Normal Modes and Frequency Response Analysis (7200ft. Drill String, with substructuring)

```
Normal Mode Analysis of multiple degree of freedom axial vibration problem
%with lumped mass elements
%parameters of the drillstring and collar pipe
%this set of numbers is defined based on matching numbers in Dareing's
%paper
clear all
G1_length=10;
drawworks_stiffness=9.2e+6;
kelly_block_mass=10288;
collar_string_interface_mass=3511;
collar_string_interface_stiffness=4.94e6;
%drill bit support equivalent stiffness
DK=1.66878e6;
%string properties
string_youngs=2.05e11;
string_poisson=0.3;
string_dens=7890.5;
string_length=2200;
string_id=0.09714;
string_od=0.114;
%collar properties
collar_youngs=2.23e11;
collar_poisson=0.3;
collar_dens=6833.71;
collar_length=240;
collar_id=0.0543;
collar_od=0.165;
%
%discretizing drill collar and drill string
%number of elements and their length
n_string_el=300;
n_collar_el=200;
total_elements=2+n_string_el+n_collar_el;
string_el_length=string_length/n_string_el;
collar_el_length=collar_length/n_collar_el;
% Now we need to decide how it can be split
% One way of doing it is by specifying length of the bit - side
% portion of the string or G1 side
% Now we determine what constitutes G1 and G2
   if G1_length < collar_length
      collar_length_G1=G1_length;
```

```
        string_length_G1=0;
        collar_length_G2=collar_length-collar_length_G1;
        string_length_G2=string_length-string_length_G1;
        n_collar_el_G1=2*n_collar_el*round(collar_length_G1/collar_length+1);
        n_string_el_G1=0;
        n_collar_el_G2=2*n_collar_el*round(collar_length_G2/collar_length+1);
        n_string_el_G2=2*n_string_el;
% Compute total number of elements in each section. There is always a drawworks
% and kelly mass in G2 and interface stiffness and mass could be either in
% G1 or G2 depending on G1_length
        total_elements_G1=n_collar_el_G1+n_string_el_G1+1;
        total_elements_G2=n_collar_el_G2+n_string_el_G2+2;
    elseif G1_length == collar_length;
        collar_length_G1=G1_length;
        string_length_G1=0;
        collar_length_G2=0;
        string_length_G2=string_length;
        n_collar_el_G1=2*n_collar_el;
        n_string_el_G1=0;
        n_collar_el_G2=0;
        n_string_el_G2=2*n_string_el;
        total_elements_G1=n_collar_el_G1+n_string_el_G1+1;
        total_elements_G2=n_string_el_G2+2;  %interface always belongs to string

    else
        collar_length_G1=collar_length;
        string_length_G1=G1_length-collar_length_G1;
        collar_length_G2=0;
        string_length_G2=string_length-string_length_G1;
        n_collar_el_G1=2*n_collar_el;
        n_string_el_G1=n_string_el*round(string_length_G1/string_length+1);
        n_collar_el_G2=0;
        n_string_el_G2=2*n_string_el*round(string_length_G2/string_length+1);
        total_elements_G1=n_collar_el_G1+n_string_el_G1+1;
        total_elements_G2=n_collar_el_G2+n_string_el_G2+1;
    end
%discretizing drill collar and drill string
%number of elements and their length
%
%
% calculating mass and stiffness of collar and string elements
%crosssection area
string_area=pi*(string_od^2-string_id^2)/4;
collar_area=pi*(collar_od^2-collar_id^2)/4;
%for G1 and G2 - element length
if G1_length < collar_length
```

```
   string_el_length_G1=0;
   collar_el_length_G2=collar_length_G2/n_collar_el_G2;
elseif G1_length == collar_length;
  string_el_length_G1=0;
  collar_el_length_G2=0;
else
   string_el_length_G1=string_length_G1/n_string_el_G1;
   collar_el_length_G2=0;
end
%
string_el_length_G2=string_length_G2/n_string_el_G2;
collar_el_length_G1=collar_length_G1/n_collar_el_G1;


%mass - good for all permutations
string_el_mass_G1=string_el_length_G1*string_area*string_dens;
string_el_mass_G2=string_el_length_G2*string_area*string_dens;
collar_el_mass_G1=collar_el_length_G1*collar_area*collar_dens;
collar_el_mass_G2=collar_el_length_G2*collar_area*collar_dens;
%stiffness calculation is based on following formula area*youngs/length
%have to do it case by case
if G1_length < collar_length
   string_el_stiff_G1=0;
   collar_el_stiff_G2=collar_area*collar_youngs/collar_el_length_G2;
elseif G1_length == collar_length;
   string_el_stiff_G1=0;
   collar_el_stiff_G2=0;
else
   string_el_stiff_G1=string_area*string_youngs/string_el_length_G1;
   collar_el_stiff_G2=0;
end
%
collar_el_stiff_G1=collar_area*collar_youngs/collar_el_length_G1;
string_el_stiff_G2=string_area*string_youngs/string_el_length_G2;
%
%mass and stiffness of the collar elements
k_collar_G1=collar_el_stiff_G1;
k_collar_G2=collar_el_stiff_G2;
m_collar_G1=collar_el_mass_G1;
m_collar_G2=collar_el_mass_G2;
%mass and stiffness of the string elements
k_string_G1=string_el_stiff_G1;
k_string_G2=string_el_stiff_G2;
m_string_G1=string_el_mass_G1;
m_string_G2=string_el_mass_G2;
%
```

```
%Input stiffness and mass array in order of mass connections
k_G1=zeros(total_elements_G1,1);
m_G1=zeros(total_elements_G1,1);
k_G2=zeros(total_elements_G2,1);
m_G2=zeros(total_elements_G2,1);
k_G2(1)=drawworks_stiffness;   %drawworks stiffness              n
% kelly mass gets half of the next bar element
m_G2(1)=kelly_block_mass+m_string_G2/2;    %kelly and traveling block mass
%
%String portion of G2
   for i=2:n_string_el_G2+1
      k_G2(i)=k_string_G2;
      m_G2(i)=m_string_G2;
   end
%add interface mass and stiffness if interface is part of G2
if G1_length >= collar_length;
   m_G2(n_string_el_G2+1)=m_string_G2/2;
   m_G2(n_string_el_G2+2)=collar_string_interface_mass;
   k_G2(n_string_el+2)=collar_string_interface_stiffness;
end %done with string portion of G2
%++++++++++++++++++++++++++
%Collar portion of G2 if exists - loop to assign bulk of elements as well
%as interface and ends
if n_collar_el_G2 > 0
   for i=n_string_el_G2+2+1:n_string_el_G2+2+n_collar_el_G2
      k_G2(i)=k_collar_G2;
      m_G2(i)=m_collar_G2;
   end
   m_G2(n_string_el_G2+2)=m_collar_G2/2+collar_string_interface_mass;
   k_G2(n_string_el_G2+2)=collar_string_interface_stiffness;
   m_G2(n_string_el_G2+2+n_collar_el_G2)=m_collar_G2/2;
end
% G2 finished
%++++++++++++++++++++++++++++++++++++++++++++++
% Start G1
% If G1 has string portion
if n_string_el_G1 > 0;
 % form string portion of G1
     for i=1:n_string_el_G1;
        k_G1(i)=k_string_G1;
        m_G1(i)=m_string_G1;
     end
     m_G1(1)=m_string_G1/2;
%last mass in the string - half of the bar plus interface
m_G1(n_string_el_G1+1)=collar_string_interface_mass+m_string_G1/2;
%interface stiffness
```

```
k_G1(n_string_el_G1+1)=collar_string_interface_stiffness;
%starting from the first collar element of the collar
for i=n_string_el_G1+2:total_elements_G1
   k_G1(i)=k_collar_G1;
   m_G1(i)=m_collar_G1;
end
%first and last collar element is half bar
m_G1(n_string_el_G1+1)=m_collar_G1/2;
m_G1(total_elements_G1)=m_collar_G1/2;
end
% If G1 has only collar
if n_string_el_G1 == 0;
       for i=2:n_collar_el_G1;
         k_G1(i)=k_collar_G1;
         m_G1(i)=m_collar_G1;
       end
       k_G1(1)=k_collar_G1/2;
       m_G1(1)=m_collar_G1/2;
       k_G1(total_elements_G1)=k_collar_G1/2;
       m_G1(total_elements_G1)=m_collar_G1/2;
end

% Done with G1
%Setting up mass vector for G1
%
%Assemble mass matrix
n_k_G1=length(k_G1);
M_G1=zeros(length(k_G1),length(k_G1));
for i=1:n_k_G1
   M_G1(i,i)=m_G1(i);
end

%Assemble stiffness matrix
S_G1=zeros(n_k_G1,n_k_G1);
for i=1:n_k_G1-1
   S_G1(i,i)=k_G1(i)+k_G1(i+1);
   S_G1(i+1,i)=-k_G1(i+1);
   S_G1(i,i+1)=-k_G1(i+1);
end
S_G1(n_k_G1,n_k_G1)=k_G1(n_k_G1);
% m_G1
% k_G1
% m_G2
% k_G2
%length(m_G1)
%Reduce to standard eigenvalue problem
```

```
H_G1=M_G1\S_G1;
nmodesG1=50;
%Solve for eigenvalues and eigenvectors
[v_G1,w2_G1]=eigs(H_G1,nmodesG1,'sm');
%Calculate frequencies
w_G1=sqrt(w2_G1);

%Scale eigenvectors to normalize with respect to mass matrix
%for i=1:n
 %   C2(i)=v(:,i)'*M*v(:,i);
 %   C(i)=sqrt(C2(i));
 %   vn(:,i)=v(:,i)*1/C(i)
%end

%Scale eigenvectors to normalize with respect to bottom row
vn_G1=zeros(n_k_G1,nmodesG1);
for i=1:nmodesG1
   vn_G1(:,i)=v_G1(:,i)/v_G1(n_k_G1,i);
end

%Calculate normalized mass and stiffness matrices
Sn_G1=vn_G1'*S_G1*vn_G1;
Mn_G1=vn_G1'*M_G1*vn_G1;

%Assemble damping matrix
Cn_G1=diag(nmodesG1);
for i=1:nmodesG1
   Cn_G1(i,i)=2*0.04*sqrt(Sn_G1(i,i)*Mn_G1(i,i));
end
%++++++++++++++++++++++++++++++++++++++++++++
%
%Form matrices and solve system for G2
nmodesG2=50;
%Setting up mass vector for G2
%
%Assemble mass matrix
n_k_G2=length(k_G2);
M_G2=zeros(n_k_G2,n_k_G2);
for i=1:n_k_G2
   M_G2(i,i)=m_G2(i);
end

%Assemble stiffness matrix
S_G2=zeros(n_k_G2,n_k_G2);
for i=1:n_k_G2-1
   S_G2(i,i)=k_G2(i)+k_G2(i+1);
```

```
   S_G2(i+1,i)=-k_G2(i+1);
   S_G2(i,i+1)=-k_G2(i+1);
end
S_G2(n_k_G2,n_k_G2)=k_G2(n_k_G2);

%Reduce to standard eigenvalue problem
H_G2=M_G2\S_G2;

%Solve for eigenvalues and eigenvectors
[v_G2,w2_G2]=eigs(H_G2,nmodesG2,'sm');
%Calculate frequencies
w_G2=sqrt(w2_G2);

%Scale eigenvectors to normalize with respect to mass matrix
%for i=1:n
 %   C2(i)=v(:,i)'*M*v(:,i);
 %   C(i)=sqrt(C2(i));
 %   vn(:,i)=v(:,i)*1/C(i)
%end

%Scale eigenvectors to normalize with respect to bottom row
vn_G2=zeros(n_k_G2,nmodesG2);
for i=1:nmodesG2
   vn_G2(:,i)=v_G2(:,i)/v_G2(n_k_G2,i);
end

%Calculate normalized mass and stiffness matrices
Sn_G2=vn_G2'*S_G2*vn_G2;
Mn_G2=vn_G2'*M_G2*vn_G2;

%Assemble damping matrix
Cn_G2=diag(nmodesG2);
%sqtr(Sn_G2(i,i)*Mn_G2(i,i))= Sn_G2(i,i)*
for i=1:nmodesG2
   Cn_G2(i,i)=2*0.04*sqrt(Sn_G2(i,i)*Mn_G2(i,i));
end
%Cn(29,29)=2*0.04*sqrt(Sn(i,i)*Mn(i,i));
freq_G1=sort(diag(w_G1))/(2*pi);
freq_G2=sort(diag(w_G2))/(2*pi);
out_path='C:\Users\mmesh\Documents\SAND\2013SAND\DRILL_STRING\MODELING\AD
AMS_MODELS\7200Feet\RAymond_for_Paper';
file='convergence_study';
out=strcat(out_path,'/',file);
 %xlswrite(out,freq(1:100),2,'B1:B100')
 %freq_G1(1:10)
 %freq_G2(1:10)
```

```
 %xlswrite(out,freq)
%clear all
%Calculate transfer function response
%define modal force
% For G1 physical force is applied at the first node and drill bit is at
% the last node. For G2 force is applied at the last node
P_G1=zeros(total_elements_G1,1);
P_G2=zeros(total_elements_G2,1);
P_G1(1)=1.;
P_G2(total_elements_G2,1)=1.;
%modal force
P_G1_n=vn_G1'*P_G1;
%P_G1_n=vn_G1(1,:);
%modal force in this case is just first row of the modal matrix for the G1
%calculate
%FRFI stands for FRF at input point, FRFO - output
%
omega=.1:0.1:250;
%FRFI_G1=zeros(length(omega),1);
%FRFI_G2=zeros(length(omega),1);
onedof_frfG1=zeros(length(omega),nmodesG1);
onedof_frfG2=zeros(length(omega),nmodesG2);
for k=1:length(omega);
   for i=1:nmodesG1;
 [onedof_frfG1(k,i)]=(omega(k)*1i)^1*onedofmodal( Mn_G1(i,i),Sn_G1(i,i),Cn_G1(i,i),
omega(k) );
   end
   for i=1:nmodesG2;
 [onedof_frfG2(k,i)]=(omega(k)*1i)^1*onedofmodal( Mn_G2(i,i),Sn_G2(i,i),Cn_G2(i,i),
omega(k) );
    end
end
%onedof_frfG1 contains responses of modal coordinates for all freaquencies
%now calculate response of grids
grid_resp_G1_In=zeros(length(omega),1);
grid_resp_G1_Out=zeros(length(omega),1);
grid_resp_G2_In=zeros(length(omega),1);
for k=1:length(omega);
   for i=1:nmodesG1;
     grid_resp_G1_In(k)= grid_resp_G1_In(k)+onedof_frfG1(k,i)*vn_G1(1,i)^2;
    %grid_resp_G1_Out(k)=
grid_resp_G1_Out(k)+onedof_frfG1(k,i)*vn_G1(total_elements_G1,i)*vn_G1(i,total_elements_
G1);
   end
    for i=1:nmodesG2;
```

```
     grid_resp_G2_In(k)=
grid_resp_G2_In(k)+onedof_frfG2(k,i)*vn_G2(total_elements_G2,i)^2;
    end
end
%   figure
%   plot(omega/(2*pi),real(grid_resp_G1_In(:)),'b')
%   figure
%   plot(omega/(2*pi),angle(grid_resp_G1_Out(:)),'r')
figure
plot(omega/(2*pi),real(grid_resp_G2_In(:)),'g')
figure
plot(omega/(2*pi),angle(grid_resp_G2_In(:)),'r')
```

This page intentionally left blank.

APPENDIX C. SIMPLIFIED 4-MASS SYSTEM

In order to validate the process for simulating a drillstring using port functions in Simulink, representations of several different systems with varying levels of complexity were used and validated through several different solution methods. A simple four-mass chain of masses in series with a parallel spring-damper in between each mass (4DOF model) was used for initial validation In order to simplify the drillstring model for initial method validation. This model included a force input on the first mass and a terminating spring to a rigid boundary on the final mass as seen in Figure C-1. Here, *Fe* is the excitation force, and *Frig* is the terminating force applied by the drill rig, modeled by a spring. This model has basic dynamic characteristics similar to a drillstring, but is simple enough to allow solution by hand to validate the other solution approaches.

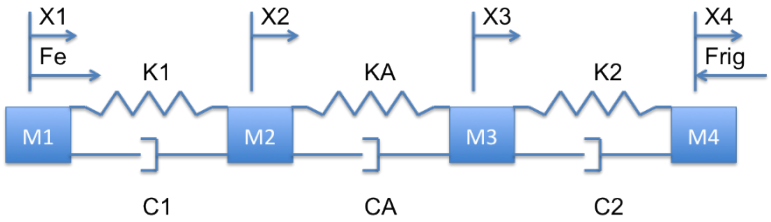

Figure C-1. Four mass model.

Three approaches to modeling the 4DOF system were used to cross-validate each other. The first approach was an ordinary differential equation model. Using standard equations of motion, a spring-mass-damper (SMD) system can be represented with the following ODE:

$$f = m\ddot{x} + c\dot{x} + kx \qquad \text{(Eq. C-1)}$$

Similarly, the 4DOF system can be represented by four, second order ODEs:

$$\ddot{x}_1 = \frac{c_1(\dot{x}_2 - \dot{x}_1) + k_1(x_2 - x_1)}{m_1} + F_e$$

$$\ddot{x}_2 = \frac{c_2(\dot{x}_3 - \dot{x}_2) + k_2(x_3 - x_2) - c_1(\dot{x}_2 - \dot{x}_1) - k_1(x_2 - x_1)}{m_2}$$

$$\ddot{x}_3 = \frac{c_3(\dot{x}_4 - \dot{x}_3) + k_3(x_4 - x_3) - c_2(\dot{x}_3 - \dot{x}_2) - k_2(x_3 - x_2)}{m_3} \qquad \text{(Eq. C-2)}$$

$$\ddot{x}_4 = \frac{-c_4\dot{x}_4 - k_4x_4 - c_3(\dot{x}_4 - \dot{x}_3) - k_3(x_4 - x_3)}{m_4}$$

This system was broken down into eight first order ODEs and solved using Matlab's ODE45 solver. This system's dynamics then were simulated using outputs at each node (mass) and a sinusoidal input force of 1N at 5 rad/s on mass, M1. The system's time response was plotted as seen in Figure C-2.

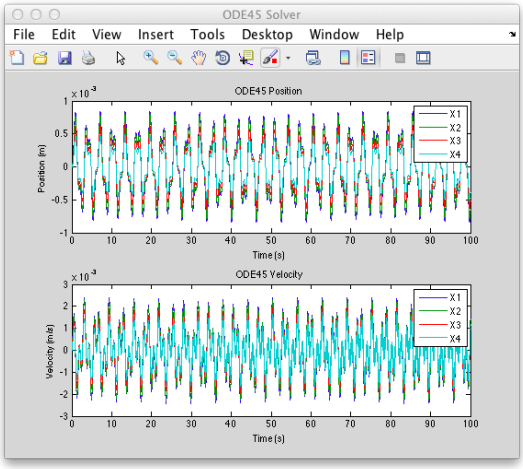

Figure C-2. ODE45 Position and Velocity Output.

For the second approach, the ODE model was translated into a Simulink block diagram in the time domain without using port functions, as seen in Figure C-3.

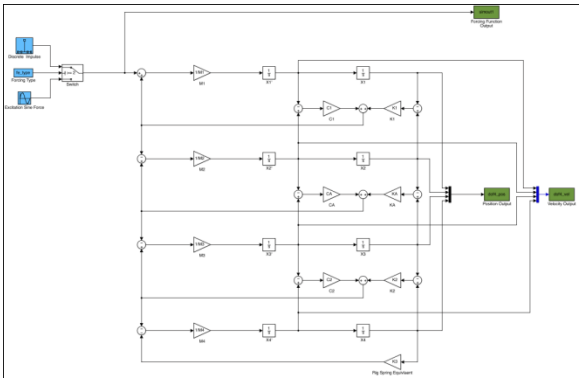

Figure C-3. 4DOF Simulink Model.

Again, similar time response plots using the same forcing function were generated as seen in Figure C-4.

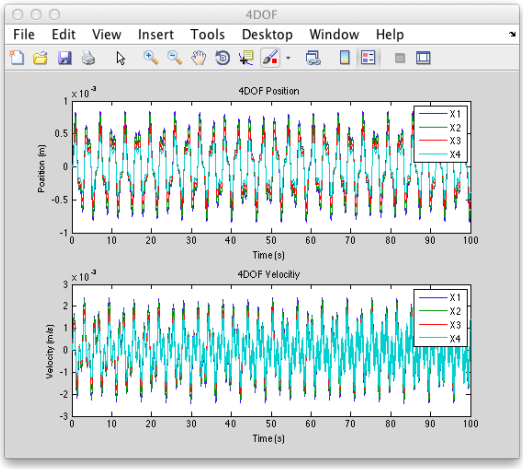

Figure C-4. 4DOF Position and Velocity Output.

For the third approach, the system model was split into three parts, G1, A, and G2 as seen in Figure C-5. The system was modeled using two-port impedance and admittance port functions, as described above. In order to use proper transfer functions for each element, G1 and G2 were represented with admittance functions while A was represented with impedance functions.

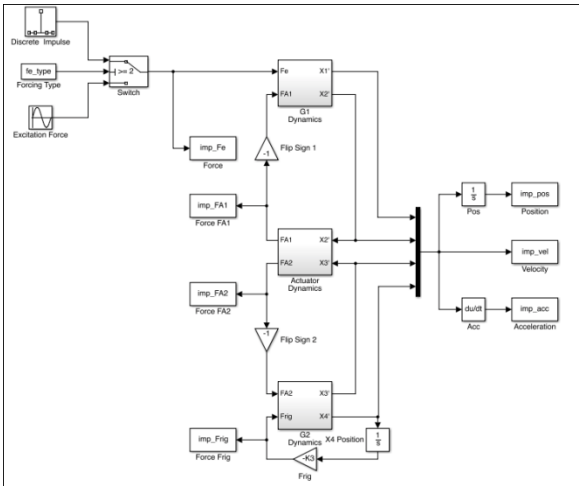

Figure C-5. 4DOF Impedance Model.

G1 and G2 each contain two masses and a joining spring and damper. The force input was applied at G1 and the terminating rig spring was applied at G2. The two-port admittances for G1 and G2 were calculated as seen below in the Laplace domain. (Eq. C-3) represents G1 and (Eq. C-4) represents G2.

$$\begin{bmatrix} sX_1 \\ sX_2 \end{bmatrix} = \begin{bmatrix} \dfrac{m_2 s^2 + c_1 s + k_1}{(m_1 m_2)s^3 + (m_1 c_1 + m_2 c_1)s^2 + (m_2 k_1 + m_1 k_1)s} & \dfrac{c_1 s + k_1}{(m_1 m_2)s^3 + (m_1 c_1 + m_2 c_1)s^2 + (m_2 k_1 + m_1 k_1)s} \\ \dfrac{c_1 s + k_1}{(m_1 m_2)s^3 + (m_1 c_1 + m_2 c_1)s^2 + (m_2 k_1 + m_1 k_1)s} & \dfrac{m_1 s^2 + c_1 s + k_1}{(m_1 m_2)s^3 + (m_1 c_1 + m_2 c_1)s^2 + (m_2 k_1 + m_1 k_1)s} \end{bmatrix} \begin{bmatrix} Fe \\ Fa_1 \end{bmatrix} \quad \text{(Eq. C-3)}$$

$$\begin{bmatrix} sX_2 \\ sX_4 \end{bmatrix} = \begin{bmatrix} \frac{m_4 s^2 + c_2 s + k_2}{(m_2 m_4)s^3 + (m_2 c_2 + m_4 c_2)s^2 + (m_4 k_2 + m_4 k_2)s} & \frac{c_2 s + k_2}{(m_2 m_4)s^3 + (m_2 c_2 + m_4 c_2)s^2 + (m_4 k_2 + m_2 k_2)s} \\ \frac{c_2 s + k_2}{(m_2 m_4)s^3 + (m_2 c_2 + m_4 c_2)s^2 + (m_4 k_2 + m_2 k_2)s} & \frac{m_2 s^2 + c_2 s + k_2}{(m_2 m_4)s^3 + (m_2 c_2 + m_4 c_2)s^2 + (m_4 k_2 + m_4 k_2)s} \end{bmatrix} \begin{bmatrix} Fa_2 \\ Frig \end{bmatrix} \quad \text{(Eq. C-4)}$$

An impedance model was used for the spring and damper that joins G1 and G2. This is shown in (Eq. 2-7).

This model was simulated and its output compared with the previous two methods. In Figure C-6, the impedance model time responses can be seen. The time responses between the three approaches matched exactly. This validated the method.

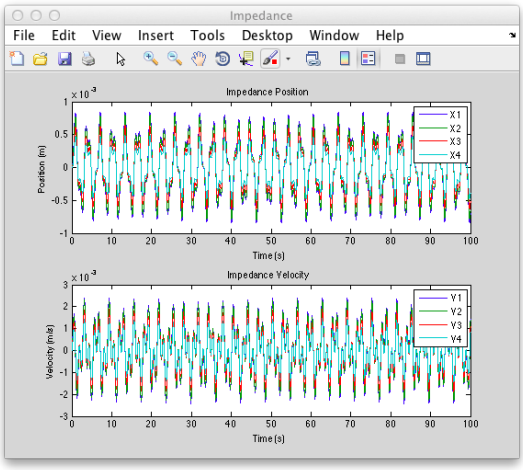

Figure C-6. Impedance Position and Velocity Output.

Normal Modes and Resonant Frequencies

The normal modes of the system were calculated from the mass and stiffness matrices. For the 4DOF system, the mass, *M*, and stiffness, *K*, matrices were derived as seen below.

$$M = \begin{bmatrix} m_1 & 0 & 0 & 0 \\ 0 & m_2 & 0 & 0 \\ 0 & 0 & m_3 & 0 \\ 0 & 0 & 0 & m_4 \end{bmatrix} \quad \text{(Eq. C-5)}$$

$$K = \begin{bmatrix} k_1 & -k_1 & 0 & 0 \\ -k_1 & k_1 + k_a & -k_a & 0 \\ 0 & -k_a & k_a + k_2 & -k_2 \\ 0 & 0 & -k_2 & k_2 + k_{rig} \end{bmatrix} \quad \text{(Eq. C-6)}$$

The characteristic polynomial of the 4DOF system can be found by taking the determinant of the following equation.

$$p_{4DOF} = |K - w^2 M| \quad \text{(Eq. C-7)}$$

The normal modes, or resonant frequencies, are the roots of p_{4DOF}.

4DOF Example

The 4DOF system was not a direct analog of the drill string. However, the methods involved in simulating the system were the same. To give an example of how the system was simulated, arbitrary mass, spring, and damper coefficients were picked as seen in Table C-1.

Table C-1. 4DOF Constants.

Mass		Spring		Damper	
M_1	25 kg	K_1	235 N/m	C_1	0.04
M_2	45 kg	K_a	100 N/m	C_a	0.04
M_3	15 kg	K_2	110 N/m	C_2	0.04
M_4	5 kg	K_{rig}	325 N/m		

Using these values, the resonant frequencies, which were found using the normal modes method, can be seen in Table C-2.

Table C-2. Resonant Frequencies for 4DOF System.

Normal Modes	
Mode: 1	0.736 rad/s
Mode: 2	3.3368 rad/s
Mode: 3	4.1035 rad/s
Mode: 4	9.2026 rad/s

To test the validity of the normal modes method on the 4DOF system, it was driven at the frequencies in Table C-2. The time responses at each frequency can be seen below. As can be seen, the system exhibits a resonant response at the normal mode frequencies as expected.

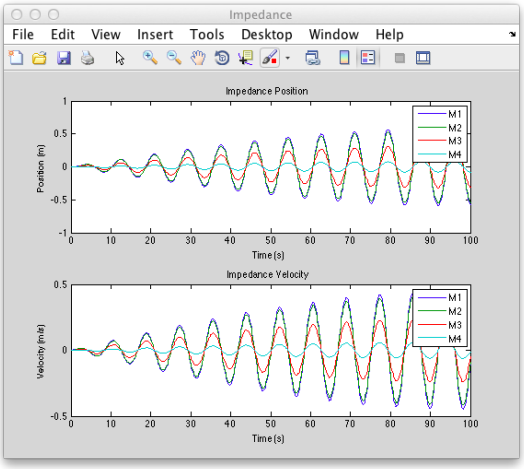

Figure C-7. 4DOF Response, Mode 1.

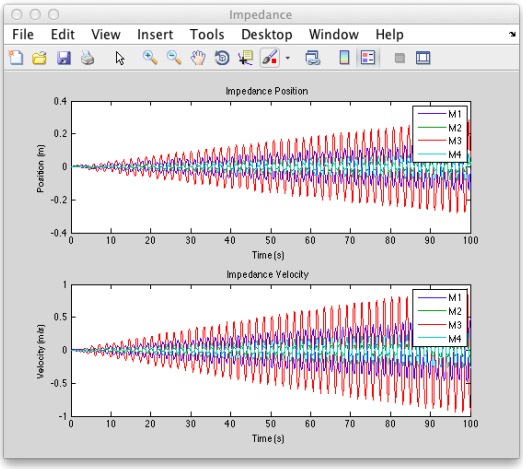

Figure C-8. 4DOF Response, Mode 2.

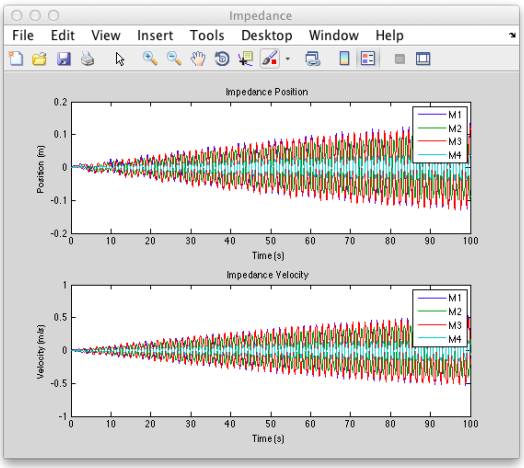

Figure C-9. 4DOF Response, Mode 3.

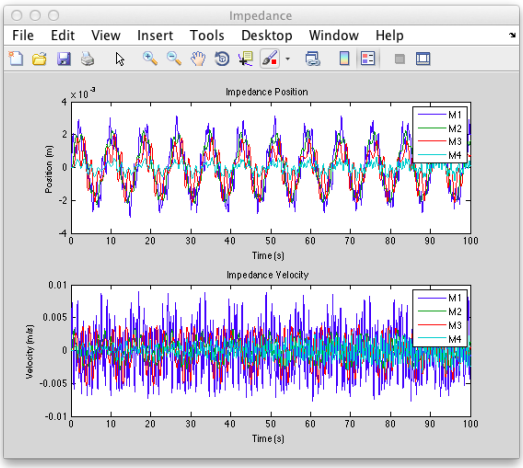

Figure C-10. 4DOF Response, Mode 4.

APPENDIX D. SMA VARIABLE RATE SPRING DESIGN

This page intentionally left blank.

SMA Variable Rate Belleville Spring System

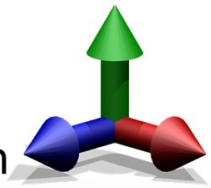

W. Radigan

Aug 27, 2013

SMA Stress-Strain Curve

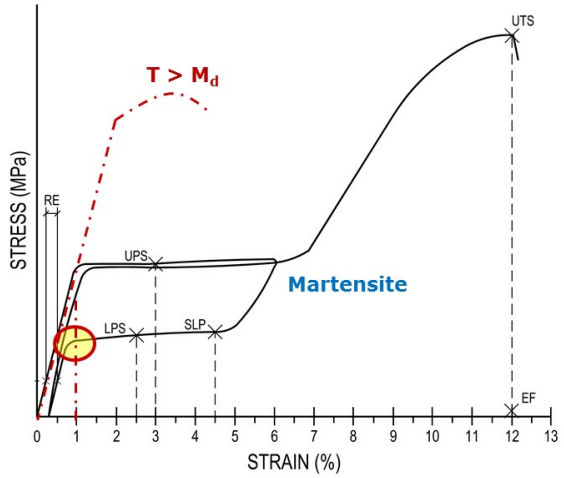

Nitinol Terminology

Table 2: Definitions of Properties extracted from stress-strain results, as defined by ASTM-F2516.

Property	Definition
Upper Plateau Strength (UPS)	Stress at 3% strain during the initial loading of the sample.
Lower Plateau Strength (LPS)	Stress at 2.5% strain during unloading of the sample after loading to 6% strain.
Start of Lower Plateau Strength (SLP)	Stress at 4.5% strain during unloading of the sample after loading to 6% strain.
Ultimate Tensile Strength (UTS)	Maximum resistance to fracture.
Strain to Failure (EF)	Maximum strain reached.
Residual Elongation (RE)	Difference between the strain at a stress of 7.0 MPa during unloading of the sample and the strain at a stress of 7.0 MPa during initial loading of the sample.

SMA Stress-Strain Curves vs. Temp.

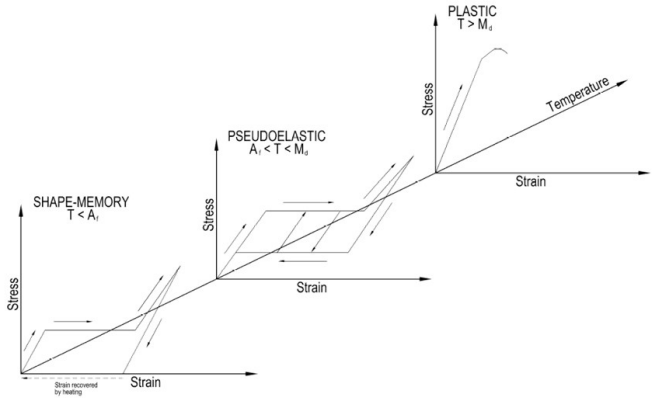

Figure 3: Schematic of the stress-strain curve during shape-memory, pseudoelastic and plastic deformation material responses due to an increase in testing temperature.

SMA Spring Actuators

Typical behaviour of a SMA compression spring

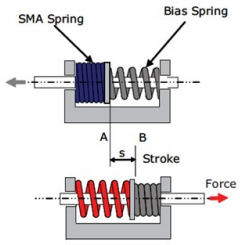

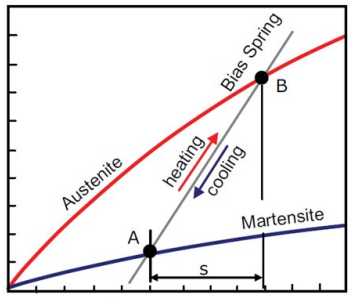

saes getters

2013-08-27 - Rev H

SMA Spring Module

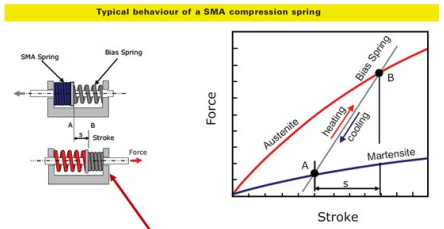

"More generally, two or more springs are **in series** when any external stress applied to the ensemble gets applied to each spring without change of magnitude, and the amount strain (deformation) of the ensemble is the sum of the strains of the individual springs. Conversely, they are said to be **in parallel** if the strain of the ensemble is their common strain, and the stress of the ensemble is the sum of their stresses."

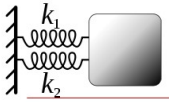

Since the outside ends of both springs are constrained, in operation these springs are in a **parallel** configuration, not **series**.

$$k_{eq} = k_1 + k_2$$

2013-08-27 - Rev H

Belleville Spring Dimensions & Terminology

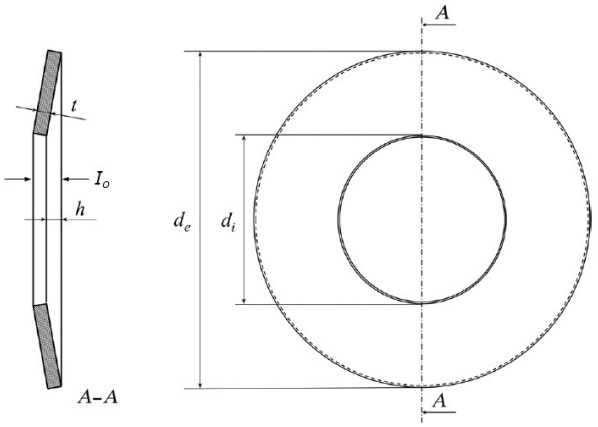

2013-08-27 - Rev H

Modeling SMA Belleville's in Excel

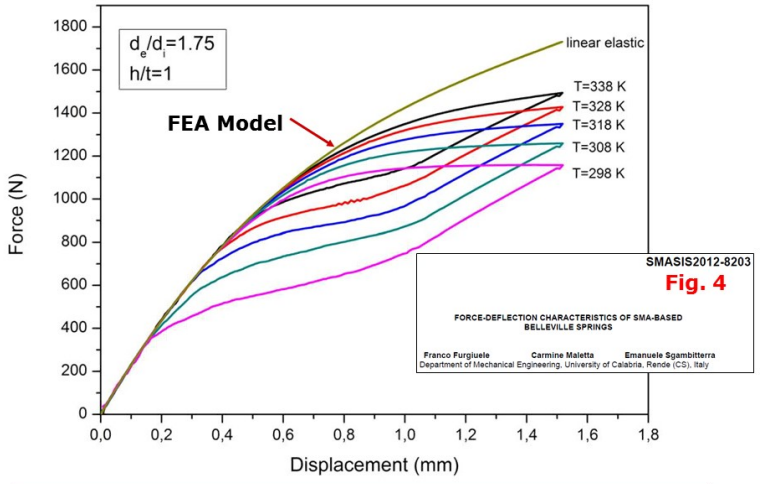

2013-08-27 - Rev H

Modeling SMA Belleville's in Excel

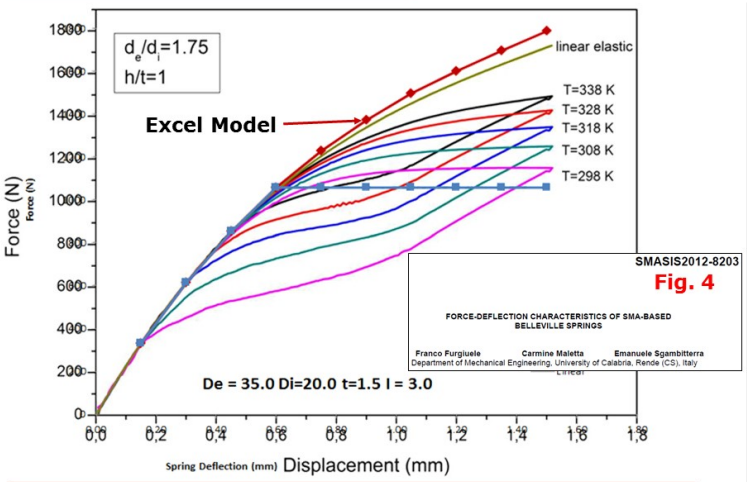

Modeling SMA Belleville's in Excel

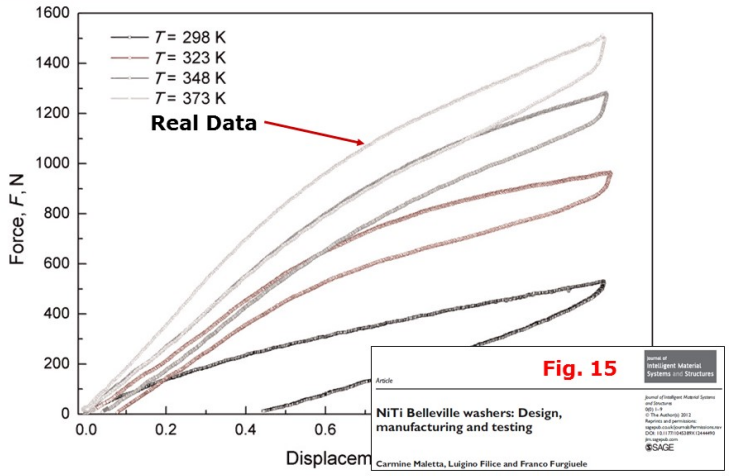

Modeling SMA Belleville's in Excel

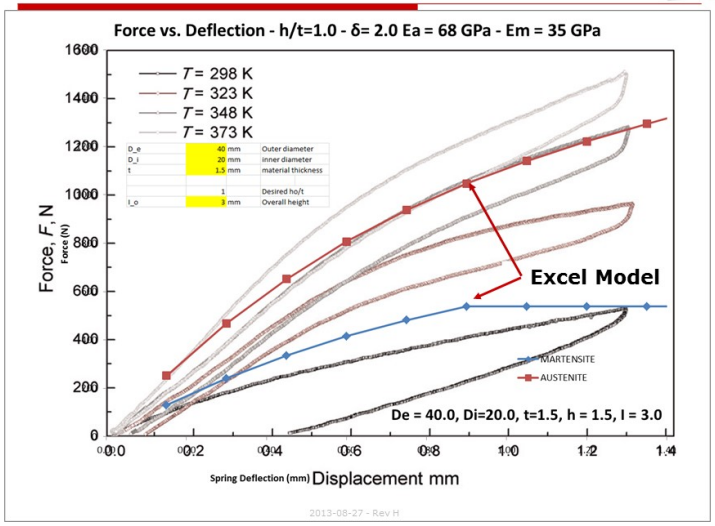

SMA Belleville Springs

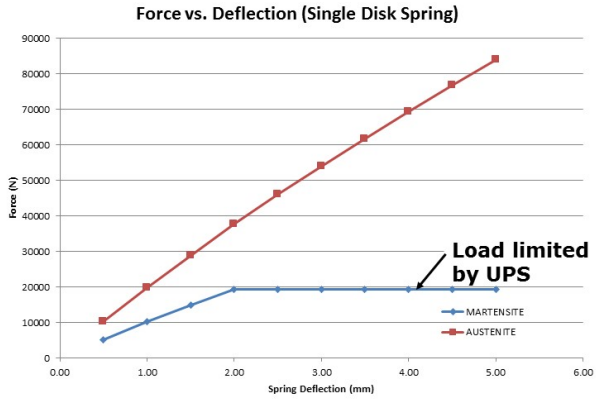

Free Body Diagram

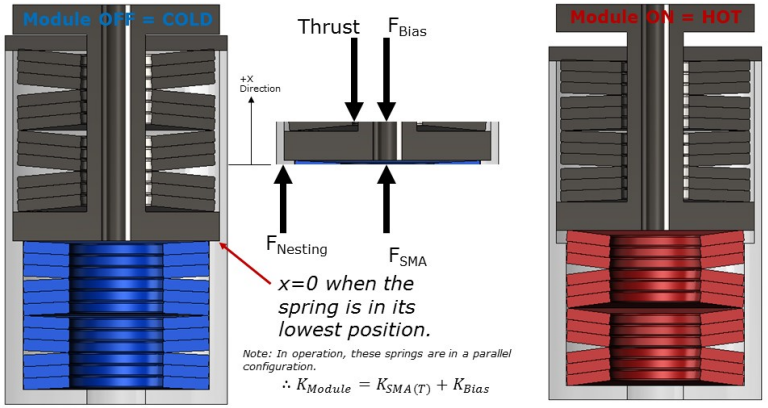

Note: In operation, these springs are in a parallel configuration.

$\therefore K_{Module} = K_{SMA(T)} + K_{Bias}$

Free Body Diagram

$F_{Bias}(x) = k_{Bias} * (\delta_{Bias} + x)$

$F_{SMA}(x) = k_{SMA} * (\delta_{SMA} - x)$

Spring preload deflections.

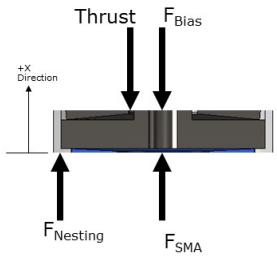

$@\ x = 0$

$F_{Bias} = k_{Bias} * \delta_{Bias} = P_{Bias}$ = Bias Preload

$F_{SMA} = k_{SMA} * \delta_{SMA} = P_{SMA}$ = SMA Preload

$@\ x = \delta_{SMA}$

$F_{Bias} = k_{Bias} * (\delta_{Bias} + \delta_{SMA})$

$F_{SMA} = k_{SMA} * (\delta_{SMA} - \delta_{SMA})$

$F_{SMA} = k_{SMA} * 0 = 0$

Free Body Diagram

When the module is "OFF" the plate is seated against the lower stop.

$\sum F_y = 0$

$\sum F_x = F_{SMA} + F_{Nesting} - F_{Bias} - Thrust = 0$

$F_{Nesting} = F_{Bias} + Thrust - F_{SMA\{Martensite\}}$

When the module is "ON" $\rightarrow F_{Nesting} = 0$

$\sum F_y = 0$

$\sum F_x = F_{SMA} - F_{Bias} - Thrust = 0 \rightarrow Thrust = F_{SMA} - F_{Bias}$

Bias Force is in the opposite direction of SMA and with the opposite slope.

$Thrust = k_{SMA} * (\delta_{SMA} - x) - k_{Bias} * (\delta_{Bias} + x)$

$Thrust = k_{SMA} * \delta_{SMA} - k_{SMA} * x - k_{Bias} * \delta_{Bias} - k_{Bias} * x$

$Thrust = (k_{SMA} * \delta_{SMA} - k_{Bias} * \delta_{Bias}) - x * (k_{SMA} + k_{Bias})$

SMA Preload Force — Bias Preload Force — System Slope

$Thrust = (P_{SMA} - P_{Bias}) - x * (k_{Module})$

Free Body Diagram

$Thrust = (k_{SMA} * \delta_{SMA} - k_{Bias} * \delta_{Bias}) - x * (k_{SMA} + k_{Bias})$

SMA Preload Force — Bias Preload Force

At $x=x_{max}$, the Thrust = 0 → and $F_{SMA}=F_{Bias}$

$0 = k_{SMA} * \delta_{SMA} - k_{Bias} * \delta_{Bias} - x_{max} * (k_{SMA} + k_{Bias})$

$k_{SMA} * \delta_{SMA} = k_{Bias} * \delta_{Bias} + x_{max} * (k_{SMA} + k_{Bias})$

$$\delta_{SMA} = \frac{k_{Bias} * \delta_{Bias} + x_{max} * (k_{SMA} + k_{Bias})}{k_{SMA}}$$

OR

$P_{Aus} = P_{Bias} + x_{max} * (k_{SMA} + k_{Bias})$

At x=0, the thrust should be $Thrust_{max}$.

$Thrust_{Max} = (k_{SMA} * \delta_{SMA} - k_{Bias} * \delta_{Bias}) - \cancel{x}^{0} * (k_{SMA} + k_{Bias})$

$Thrust_{Max} = P_{Aus} - P_{Bias}$ OR $P_{Bias} = P_{Aus} - Thrust_{Max}$

Module Design Diagram

$$k_{Module} = k_{Bias} + k_{SMA}$$

For this design we will choose $k_{Bias} = k_{SMA}$.

$$\therefore \frac{k_{Module}}{2} = k_{Bias} = k_{SMA}$$

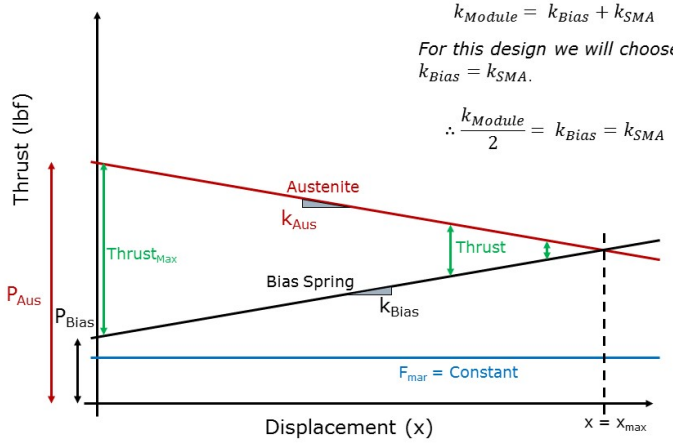

Desired SMA Drilling Tool Spring Rates

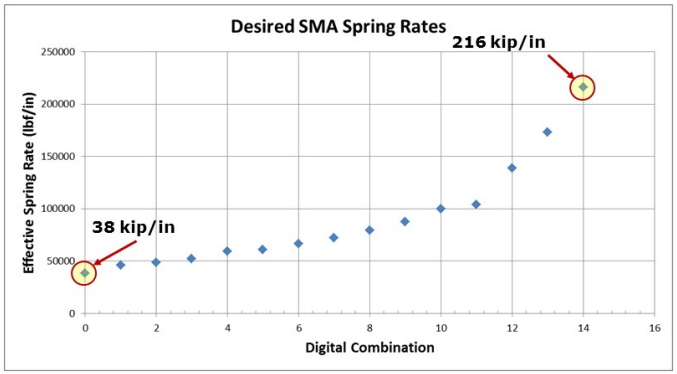

SMA Module Spring Rates

WOB_{min}	10,000	lbf				Desired Range	43	kip/in	Min			
WOB_{max}	60,000	lbf					215	kip/in	Max			
K_{stiff}	1.00E+07	lbf/in	= Spring Collapses --> Deflection Limiter Stiffness									

Module Spring Rates

Module Deflections

Single Module Spring Rate (lbf/in)	K1	K2	K3	K4
Multiplier	2.50	1.35	1.70	2.15
K_{Module}	107,500	145,125	182,750	231,125
k_{Aust}	53,750	72,563	91,375	115,563
k_{Bias}	53,750	72,563	91,375	115,563
\delta_{in}	0.56	0.41	0.33	0.26

	Min	38,474	lb/in
	Max	216,138	lb/in
	Range	177,664	lb/in

	Bit Number										
State	1	2	3	4				(lb/in)	K_s	\delta_{min}	\delta_{max}
0	0	0	0	0	107500	145125	182750	231125		38474	0.260	1.559
1	0	0	0	1	100	145125	182750	10000000		45946	0.218	1.306
2	0	0	1	0	100	145125	10000000	231125		48498	0.206	
3	0	0	1	1	100	145125	10000000	10000000		61002	0.164	
4	0	1	0	0	107500					52081	0.192	
5	0	1	0	1	107500				0	66781	0.150	0.898
6	0	1	1	0	107500					72312	0.138	
7	0	1	1	1	107500	10000000	10000000	10000000		104141	0.096	
8	1	0	0	0	10000000	145125	182750	231125		59562	0.168	
9	1	0	0	1	10000000	145125	182750	10000000		79602	0.126	0.754
10	1	0	1	0	10000000	145125	10000000	231125		87587	0.114	0.685
11	1	0	1	1	10000000	145125	10000000	10000000		139070	0.072	0.431
12	1	1	0	0	10000000	10000000	182750	231125		100014	0.100	0.600
13	1	1	0	1	10000000	10000000	182750	10000000		173251	0.058	0.346
14	1	1	1	0	10000000	10000000	10000000	231125		216138	0.046	0.278
15	1	1	1	1	10000000	10000000	10000000	10000000		2500000	0.004	0.024

$$n_1 = \frac{WOB_{max}}{K_{Module\ 1}}$$

$$K_{s_1} = \frac{1}{\frac{1}{K1_9} + \frac{1}{K2_9} + \frac{1}{K3_9} + \frac{1}{K4_9}}$$

$$max\ 1 = \frac{WOB_{max}}{K_{eff\ 1}}$$

$$min\ 1 = \frac{WOB_{min}}{K_{eff\ 1}}$$

K1 SMA Spring Module

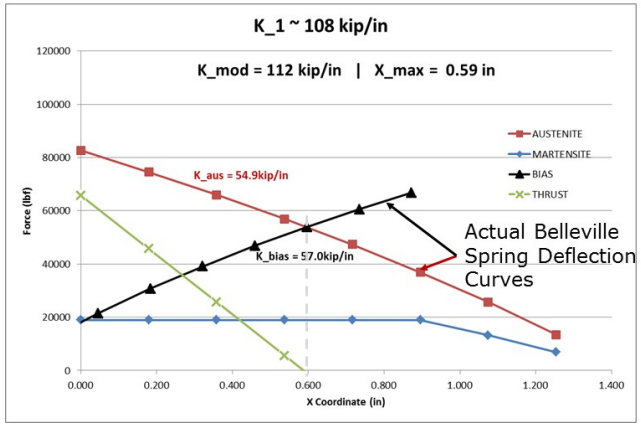

K1 SMA Spring Module

SMA SPRING

Disk Spring Geometry					
Label	Value	Units	Note		English Units
D_e	160	mm	Outer diameter		6.299 in
D_i	80	mm	inner diameter		3.150 in
t	10	mm	material thickness		0.394 in
	1		Desired ho/t		
l_o	16.5	mm	Overall height		0.650 in
h_o	6.5	mm	Available deflection		0.256 in
	1.25%		Strain Limit		
Martensite Material	SMASIS (E_M)	35000	MPa	$h_o = l_o - t$	
Austenite Material	SMASIS (E_A)	68000	MPa		

Disk Spring Stack Geometry				
Label	Value	Units	Note	English Units
	25.40	mm	Desired Total Stack defl.	1 in
	240204	N	Desired Load between 20% & 80% defl.	54000 lbf
	253461	N	Predicted Load between 20% & 80% defl.	56980 lbf
			Desired Spring Rate	54 kip/in
	5	%	Tolerance	
	7	6.513	Springs Required in series (multiplies STROKE)	
	4	3.791	Springs required in parallel (multiplies LOAD)	
	28		# of Springs in stack	
	77	mm	Single Series Stack Height	3.01 in
	306	mm	Total Stack Height	12.05 in
	300.8	mm	Grip length (20% Preload)	
	285.2	mm	Deflection Limiter (80% Travel)	

2013-08-27 - Rev H

K1 SMA Spring Module

BIAS SPRING

Disk Spring Geometry					
Label	Value	Units	Note		English Units
D_e	160	mm	Outer diameter		6.299 in
D_i	80	mm	inner diameter		3.150 in
t	7	mm	material thickness		0.276 in
	1		Desired ho/t		
l_o	12	mm	Overall height		0.472 in
h_o	5.0	mm	Available deflection		0.197 in
	1.13%		Strain Limit		
Spring Material	51 CrV 4	206000	MPa	$h_o = l_o - t$	

Disk Spring Stack Geometry					
Label	Value	Units	Note		English Units
	20.32	mm	Desired Total Stack defl.		0.8 in
	192163	N	Desired Load between 20% & 80% defl.		43200 lbf
	201120	N	Predicted Load between 20% & 80% defl.		45214 lbf
			Desired Spring Rate		54 kip/in
	8	%	Tolerance	Preload	0.23 in
	7	6.773	Springs Required in series (multiplies STROKE		5.842 mm
	4	3.822	Springs required in parallel (multiplies LOAD)		
	28		# of Springs in stack		
	54	mm	Single Series Stack Height		2.13 in
	216	mm	Total Stack Height		8.50 in
	212.0	mm	Grip length (20% Preload)		
	200.0	mm	Deflection Limiter (80% Travel)		

2013-08-27 - Rev H

SMA Module Stack

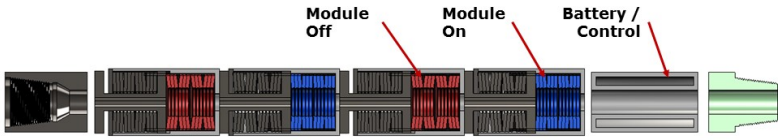

2013-08-27 - Rev H

Bibliography

- Force-Deflection Characteristics of SMA-Based Belleville Springs
  - Furgiuele, Maletta, & Sgambitterra
  - SMASIS 2013-8203
- NiTi Belleville washers: Design, manufacturing and testing
  - Maletta, Filice, Furgiuele
- Changes in the Mechanical Behavior of Nitinol Following Variations of Heat Treatment Duration and Temperature
  - Heidi F. Khalil (Thesis)

2013-08-27 - Rev H

APPENDIX E. TAYLOR LIQUID SPRING REPORT

This page intentionally left blank.

REVISIONS			
LTR	DESCRIPTION	DATE	APPROVED

Liquid Spring for Drill String Tool
Feasibility Report
For
Sandia National Laboratories

Taylor Devices Part Number: 67DP-19408-01

Reference: Sandia National Labs PO: 1329417,1

PREPARED	M.Czajka 8/26/2013	taylor devices inc. 90 Taylor Drive North Tonawanda, NY 14120 Phone (716) 694-0800		
CHECKED	A.K. 8/30/2013			
TEST ENGR.				
QUALITY				
ENGR. APVD.	A.K. 8/30/2013	Feasibility Report for Sandia National Laboratories		
SIZE: A	FSCM. NO. 06742	DRAWING NO. 67DP-19408-5000		REV. I/R

PAGE 1 OF 29

1. Contents

2. Scope

Taylor Devices, Inc. was tasked by Sandia National Laboratories to design a liquid based spring drilling tool. Per Sandia National Laboratories, the feasibility of a liquid spring with the following operating parameters is to be determined:

- The liquid spring drilling tool shall carry a 60,000 lbs maximum static load plus a 20,000 lbs maximum dynamic load with a nominal static operating range of 10,000 lbs to 60,000 lbs.
- The liquid spring shall have a nominal diameter of 7 inches and conform to packaging within a 30 ft drilling tool with API connections for drill pipe compatibility.
- The system shall be able to operate over a downhole temperature range of 68-392°F (20-200°C).
- The spring shall be adjustable to allow rates per Table 1. This variable rate system may be continuous or activated in discrete steps.

TABLE 1:

Force (lbs) (max)	Stiffness (lbs/in)	Displacement (in)
80,000	215,000	0.37
80,000	172,000	0.47
80,000	129,000	0.62
80,000	86,000	0.93
80,000	43,000	1.86

- The design shall incorporate a 2 inch internal bore for thru conveyance of drilling fluid.

There were several requirements that were added after the project started:
A minimum service life of 50-100 hours is desired. Expected frequency range is dc to 50 Hz.
An up-stop is needed in case the drill has to exert more force than usual.
Lock and unlock actions are to take place within 60 seconds maximum.
The lock and unlock mechanism shall have a life of at least 100 cycles, limited by battery life.
The temperature extremes as listed above were defined.

3. Applicable Documents

Sandia National Laboratories	1329417,1	Purchase Order
TDI	67DP-19408-01	Spring Top Level Part Number

4. Definition of Terms

- Preload - Taylor Devices liquid spring seals are pressure energized. A pressure of 1,000 psi or more is usually required to energize the seals correctly. This pressure acts over the rod area to generate a preload; the force which must be applied to begin to compress the unit.
- Endload - The force created by the pressure of the compressed fluid acting on the rod area, at the end of stroke.

5. Summary

A liquid spring works on the principal of fluid compressibility. As the piston rod enters the fluid cylinder, it displaces volume. This in turn compresses the unit and causes a pressure rise. This pressure acts over the area of the piston rod and results in a spring force. By altering the volume of the fluid and/or changing the size of the piston rod, different spring rates can be achieved.

This application is unique. Most conventional liquid springs use a solid piston rod and a single seal. For this application a 2" thru bore is required to transport the drilling fluid. This made it necessary to use a stepped rod configuration (rod entering unit is larger in diameter than the rod leaving the unit). The volume of displaced fluid is equal to the area difference between the large and small rod diameters multiplied by the stroke length. (See Figure 1). This can be illustrated through a simple free body diagram whereby the fluid pressure is acting on all piston rod surfaces within the fluid chamber.

The high temperature extreme specified also requires special accommodation. With a temperature range of 70°F-392°F fluid volume compensation and seal-ability become governing design issues. Liquid spring design must take this fluid expansion into account. For every degree Fahrenheit rise in fluid temperature the internal pressure will rise approx 60 to 90 psi (depending on pressure vessel geometry). Typically this pressure rise is acceptable and the endload pressure is limited to approximately 35,000 psi when the unit is at its hottest operating temperature. Note that the preload also increases with temperature. For this application allowing the preload pressure rise is not an option. For example, if the preload pressure were to rise such that the resulting preload was 20,000 lbs and only 15,000 lbs of drill pipe was loading the spring, the spring would not stroke. Rather, it would act as a rigid link.

TDI examined many different options for thermal fluid compensation. The only option that could be applied here was to allow the piston rod to extend from the unit to make up for the increase in fluid volume. For example, imagine a weight of 15,000 lbs resting on the spring which generates a static spring pressure of 7,500 psi over a rod area of 2 in^2. If the fluid volume increases by 2 in^3 the piston rod would extend 1 in.

The disadvantage of allowing the piston rod to extend with an increase in temperature is the effect it has on the spring rate. As the fluid expands and piston rod extends, the volume of fluid which can be compressed increases, thus lowering the spring rate. This decrease in rate can be as much as 20-30% and must be accounted for when determining system level performance.

Designing a spring that could accommodate all the requested spring rates of Table 1 was also challenging. The most efficient way to achieve the rates was to design a stack of liquid springs in series with the ability to "shut off" individual spring segments as needed. With liquid springs operating at the same loads, the lower the rate the longer the spring. Therefore, a "worst case length" spring segment was designed using the 43,000 lbs/in rate to see if it would be possible to fit a 30' drill section (refer to Figure 1). This spring segment proved excessively long.

The shortest length series stack of liquid springs occurs when the lowest target rate of 43,000 lbs/in is the rate of all 5 springs in series. This is the design that was selected.

$$\frac{1}{K_{eq}} = \frac{1}{K_1} + \frac{1}{K_2} + \frac{1}{K_3} + \frac{1}{K_4} + \frac{1}{K_5}$$

It is obvious that many different K values would yield 43,000 lbs/in. With 5 spring modules there are a total of 31 possible combinations of spring elements. TDI set out to optimize the K values such that a maximum number of different combinations of spring segments would correspond to the target rates.

The current design is 5 modular liquid springs. The modular design allows testing of each module individually. The optimized values for the spring rates are:

K1 = 360,600 lbs/in;

K2 = 213,000 lbs/in;

K3 = 360,600 lbs/in;

K4 = 213,000 lbs/in;

K5 = 134,200 lbs/in

(Refer to Appendix A for a detailed explanation).

Table 2 contains a list of all the possible combinations of springs and the resulting spring rates. Note that all segments need to be active to achieve the lowest spring rate in Table 1. There is built in redundancy in the selection of other rates, this redundancy is a benefit and adding another segment to achieve redundancy for the lowest rate may be beneficial to the system.

Table 2: Liquid Spring Module Rates

TEMPERATURE = 70°F K1=360,600 LBS/IN K2=213,000 LBS/IN K3=360,600 LBS/IN K4 = 213,000 LBS/IN K5=134,200 LBS/IN							TEMPERATURE = 400°F K1=287,200 LBS/IN K2=169,600 LBS/IN K3=287,200 LBS/IN K4 = 169,600 LBS/IN K5=106,900 LBS/IN						
SPRINGS USED:						COMBINED SPRING RATE (LBS/IN)	SPRINGS USED:						COMBINED SPRING RATE (LBS/IN)
K1	K2	K3	K4	K5		44,668	K1	K2	K3	K4	K5		35,574
K1	K2	K4	K5			50,983	K1	K2	K4	K5			40,603
K2	K3	K4	K5			50,983	K2	K3	K4	K5			40,603
K1	K2	K3	K5			56,520	K1	K2	K3	K5			45,016
K1	K3	K4	K5			56,520	K1	K3	K4	K5			45,016
K2	K4	K5				59,378	K2	K4	K5				47,288
K1	K2	K3	K4			66,952	K1	K2	K3	K4			53,316
K1	K2	K5				67,026	K1	K2	K5				53,383
K1	K4	K5				67,026	K1	K4	K5				53,383
K2	K3	K5				67,026	K2	K3	K5				53,383
K3	K4	K5				67,026	K3	K4	K5				53,383
K1	K3	K5				76,936	K1	K3	K5				61,281
K1	K2	K4				82,218	K1	K2	K4				65,469
K2	K3	K4				82,218	K2	K3	K4				65,469
K2	K5					82,329	K2	K5					65,570
K4	K5					82,329	K4	K5					65,570
K1	K2	K3				97,645	K1	K3	K4				77,760
K1	K3	K4				97,645	K1	K2	K3				77,760
K1	K5					97,802	K1	K5					77,903
K3	K5					97,802	K3	K5					77,903
K2	K4					106,500	K2	K4					84,800
K1	K2					133,905	K1	K2					106,631
K1	K4					133,905	K1	K4					106,631
K2	K3					133,905	K2	K3					106,631
K3	K4					133,905	K3	K4					106,631
K5						134,200	K5						106,900
K1	K3					180,300	K1	K3					143,600
K2						213,000	K2						169,600
K4						213,000	K4						169,600
K1						360,600	K1						287,200
K3						360,600	K3						287,200

Table 2 also contains a list of the resulting spring rates when the liquid spring stack is operating at 400°F. Notice that the rates drop approximately 20%. This drop is conservative as the drilling fluid will provide some cooling. To adjust for the drop in stiffness, different combinations of springs can be chosen.

During a telecon on 8/21/2013, Sandia expressed interest in decreasing the number of spring segments. Work to this effect is presented in Appendix A.

The ability to turn on/off spring segments is required to make the series spring stack feasible. Many locking mechanisms were examined and a simple straight forward method was settled upon (refer to the locking section for more information). A method of communicating when to lock and unlock could be through sonar, or through pressure pulses through the drilling fluid. Both of these could be built into the locking mechanism controller.

The liquid spring series spring stack is completely sealed to the elements. Sealed telescoping joints are between each spring module.

6. Operating Parameters

6.1 O.D. and Length Requirements

The maximum O.D. allowed is 7". The maximum length of the complete spring stack shall be less than 30' (drill section length). The O.D. restriction proved to be a large factor in designing the springs. Piston Rod O.D. was limited by the 7" OD max and seal/cap cross section.

6.2 Center Thru Hole

For conveyance of drilling fluid a continuous 2" ID thru hole is required thru the whole spring stack. The current design has a minimum thru hole of 2" with telescoping sealed sections that allow the spring to stroke while allowing fluid conveyance. The operating pressure of the drilling fluid was mentioned to be around 2-3 ksi, allowing the use of conventional rod wipers and seals.

6.3 Temperature Range

The operating temperature range was specified as 68-392°F (20-200°C). The drilling fluid pumped through the piston rod could act as a cooling source. Temperature /flow rate of the drilling fluid is unknown.

6.4 Static and Dynamic Loads

The spring stack shall support a static load which may vary from 10,000 lbs to 60,000 lbs. In addition to the static load a maximum dynamic load of 20,000 lbs may exist. The liquid spring stack is compression only, never taking tensile loads.

6.5 Range of Operating Frequencies

From email from Sandia (David Raymond, 6/11/2013) "Expected frequencies and response vary with drilling conditions; frequency content in the dc to 50 hz level can be anticipated."

6.6 Number of Cycles for Lock and Unlock

Per Telecon on 8/21/2013, the number of lock/unlock cycles required per battery charge is 100. Battery and torque motor design must be sized accordingly.

6.7 Time Allowed for Lock and Unlock

Per Telecon on 8/7/2013, an Unlocked to Locked time of 1 minute shall be used.

6.8 Lock and Unlock Signals

This is not specified at the present time. We have discussed using sonic pulses and electromagnetic signals.

6.9 Upstop

Per Telecon on 8/7/2013,the ability to limit the stroke of the spring in the event of a runaway drill condition (maximum load exceeds 80,000 lbs) was deemed necessary. The purpose of the Upstop is

to limit the allowable deflection of the spring module. The current design uses the locking mechanism to function as the Upstop.

7. Design Description - Liquid Spring

7.1 Materials / Safety Factors used

All major structural components will be designed with heat treated 17-4PH Stainless Steel per AMS 5643. All safety factors use the material properties at 392°F. Minimum safety factor is 1.5 on yield strength and 2.0 on ultimate strength.

7.2 Seal Design and Materials:

Taylor Devices, Inc. standard seal material for high pressure liquid springs is Teflon. The seal design itself is proprietary therefore no information on seal dimensions or sizing is supplied. Taylor Devices has historically used Teflon as a material for liquid spring seals in applications where the endload pressures have reached nearly 40,000 psi. However, a liquid spring with an operating temperature range of nearly 400°F has not been designed. This is a major design driver for this application and presents a high risk to feasibility of using a liquid spring for this component.

Teflon (polytetrafluorethylene) is a synthetic flouropolymer of tetrafluoroethylene, a fluorocarbon solid of high molecular weight. It is hydrophobic and has one of the lowest coefficients of frictions of any solids (0.05 - 0.10). The Taylor seal is pressure energized. The low coefficient of friction cuts down on friction forces on the piston rod. The low coefficient of friction also cuts down on seal wear.

The melting point of Teflon is 620°F. The pyrolysis of Teflon is detectable at 392°F. This is right at the upper temperature that this unit will be exposed to. The fact that a drilling fluid will be pumped continuously through the piston rod and thus cooling the seal and fluid might provide adequate temperature margin. This would need to be thoroughly evaluated during the hardware design phase with a thermal study. This high temperature could severely limit the life of the liquid spring seals. It is for this reason that the design concept of using a metallic machined spring design is presented in Section 8 of this report.

Seal life is also directly impacted by the number of expected cycles. With a maximum expected frequency of 50 Hz and a design life of 100 hours, a total of 18,000,000 cycles is possible.

7.3 Damping

Each liquid spring segment has the ability to produce damping force. A piston head is affixed to the piston rod (see Figure 2). The diametric clearance between the cylinder and the piston head, and length of the piston head are chosen to generate the required damping. Required damping values were unknown at the time of this report.

7.4 Locking Mechanism

Please refer to Figure 3 and Figure 4 for details on the Locking Mechanism.

Each individual spring element needs a locking mechanism to eliminate spring stroke thus creating a rigid link. A couple different designs were evaluated.

Two of the designs were similar in that they locked the piston rod in the exact position as when the mechanism was activated. This method has one large flaw. If the piston rod is not allowed to extend, the pressure buildup when the temperature increases might exceed 30,000 psi (depending on the position of the rod prior to engaging locking mechanism). This would lead to seal failure and thus spring failure.

The Locking Mechanism design chosen is simple in concept. A ring with a thread interface to the cylinder has a bevel gear on the I.D. which is driven by a hollow shaft torque motor. The ring advances until it comes in contact with a flange on the piston rod. The direction of contact is such that the unit is extended by the ring. If the weight on the liquid spring is temporarily removed, the ring can be threaded all the way to eliminate all ability to stroke from this module. To unlock the spring this process would be simply reversed.

The Locking Mechanism also functions in the Upstop role. The position of the threaded ring could be controlled via the torque motor and feedback from a non contact position transducer to always maintain the correct distance away from the flange on the piston rod.

7.5 Hollow Shaft Torque Motor/ Harmonic Drive

Please refer to Figure 2 and Figure 3 for location of the motor.

The necessity for a 2" thru hole for drilling fluid complicates the motor selection. A hollow shaft torque motor will drive a gear which in turn drives 2 spur gears which in turn drive the threaded ring. A rotary encoder is necessary for the Upstop feature. There are commercially available hollow shaft torque motors that come close to fitting the mounting envelope as currently laid out, however a custom designed torque motor is necessary.

A custom designed controller/battery pack also needs to be designed. The logic involved with the controller is relatively simple and straight forward. Batteries that operate at 200°C are available for downhole applications.

7.6 Center Thru Hole

A provision for conveying drill fluid thru the unit consists of a hole thru the center of each piston rod which is sealed to a telescoping tube to allow for spring stroke. One end of the telescoping tube is threaded into a piston rod and sealed with a static seal. The other enters the piston rod of the next spring module and is sealed with a wiper and dynamic seal. This creates a sealed pathway thru the entire liquid spring assembly.

Figure 1: 43,000 lbs/in Liquid Spring Module (not used in final design spring stack)

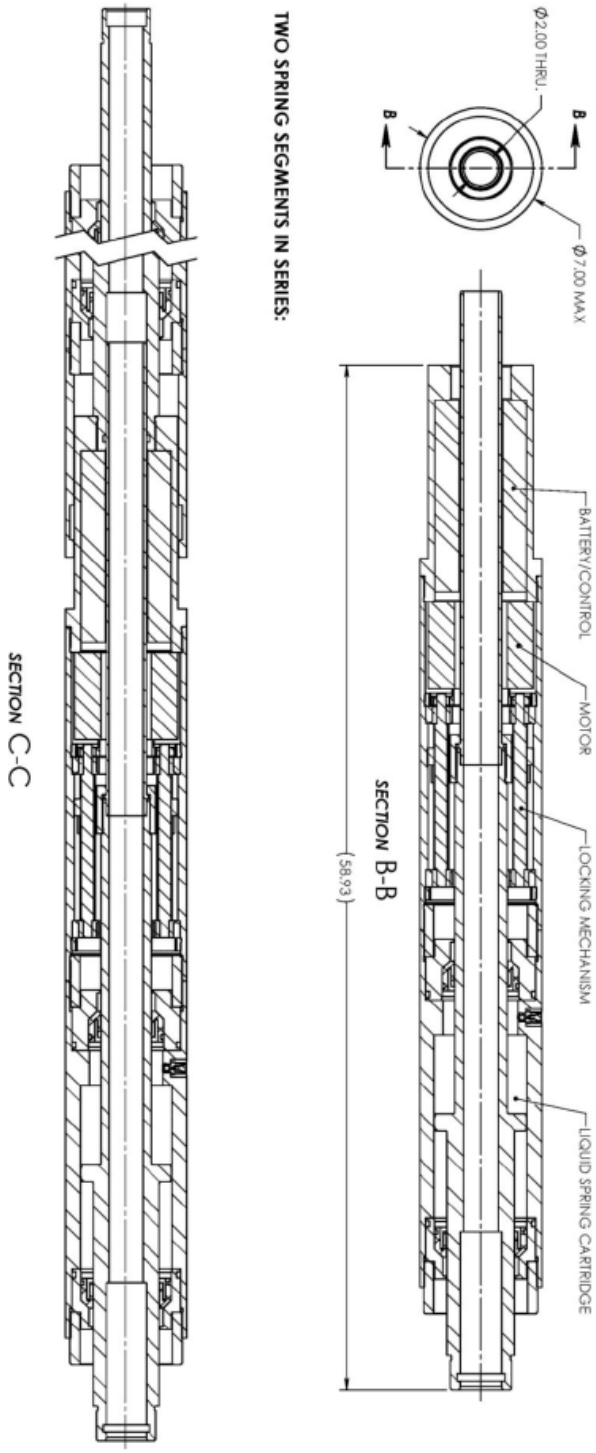

SIZE	FSCM. NO.	DRAWING NO.	REV.
A	06742	67DP-19408-5000	I/R

PAGE 10 OF 29

Figure 2: Five Segment Liquid Spring

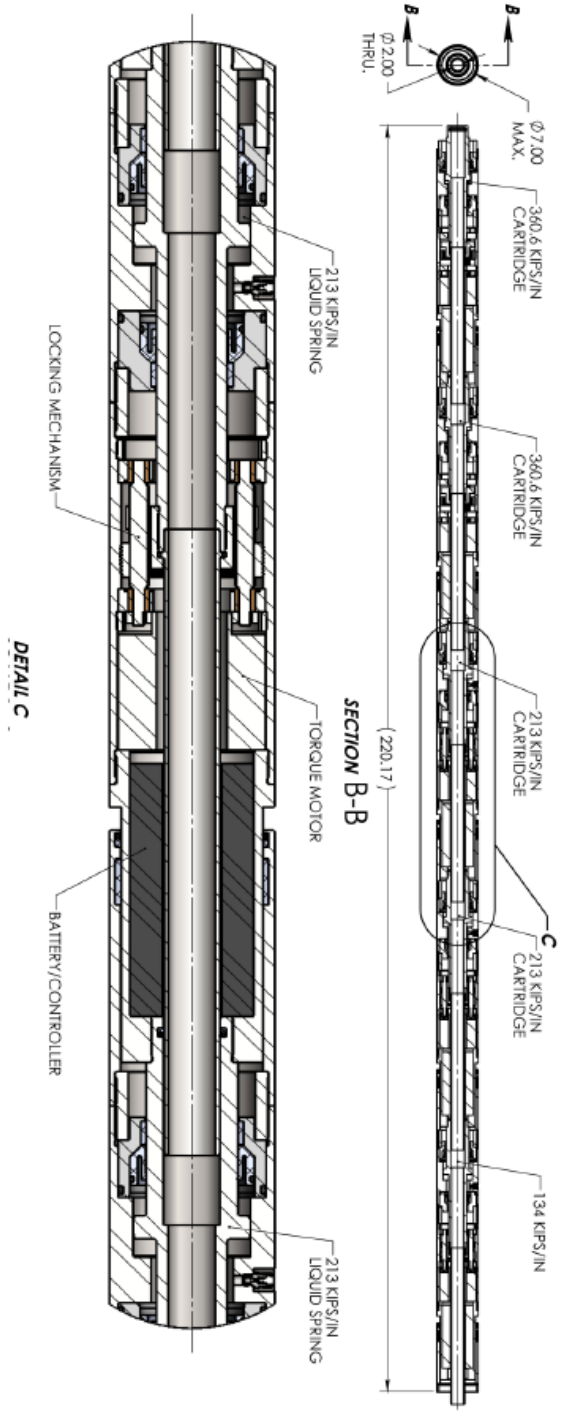

SIZE	FSCM. NO.	DRAWING NO.	REV.
A	06742	67DP-19408-5000	I/R

PAGE 11 OF 29

Figure 3: Caging (Lock/Unlock) Mechanism

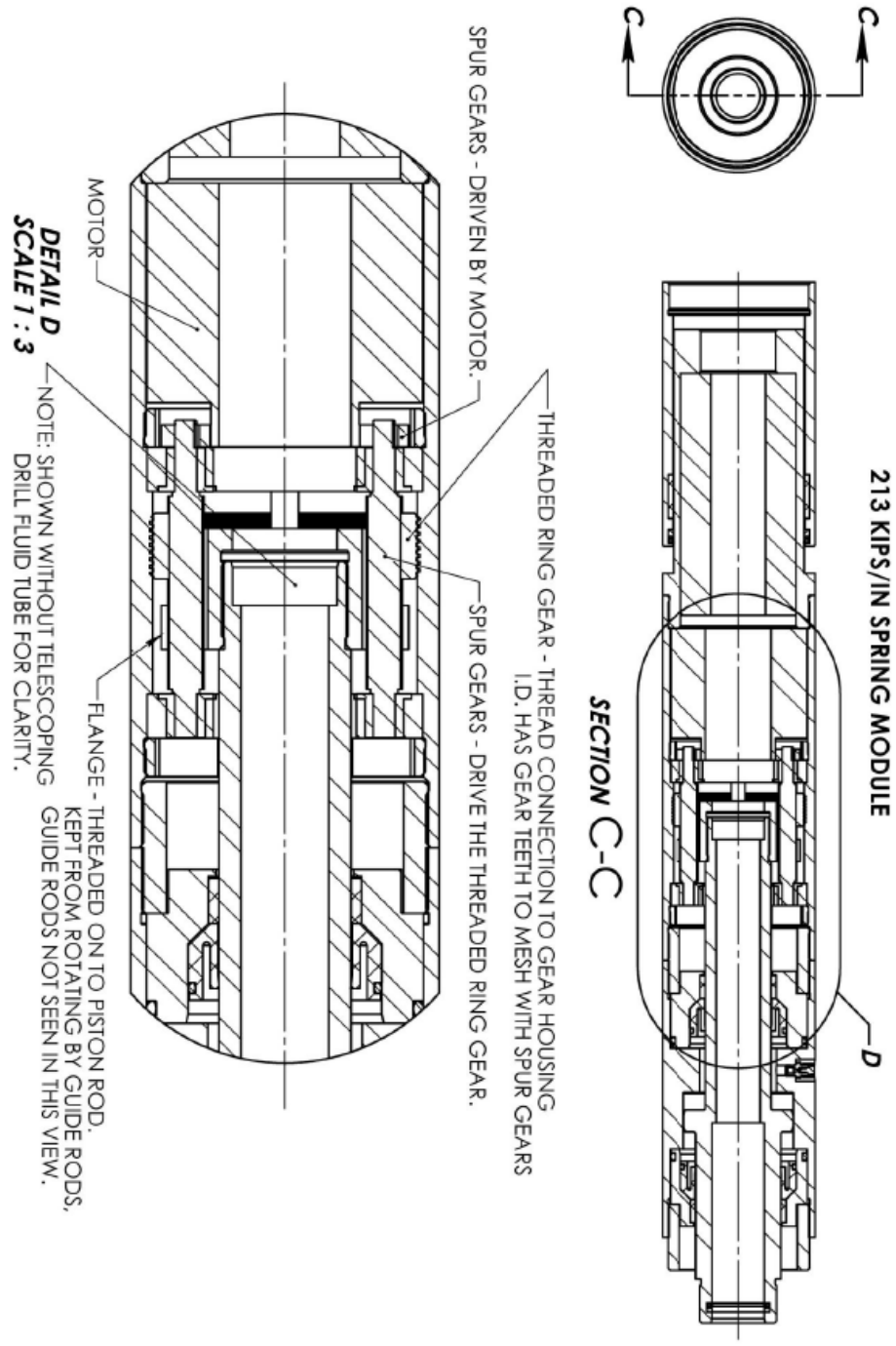

SIZE	FSCM. NO.	DRAWING NO.	REV.
A	06742	67DP-19408-5000	I/R

PAGE 12 OF 29

Figure 4: Caging (Lock/Unlock) Mechanism Alternate View

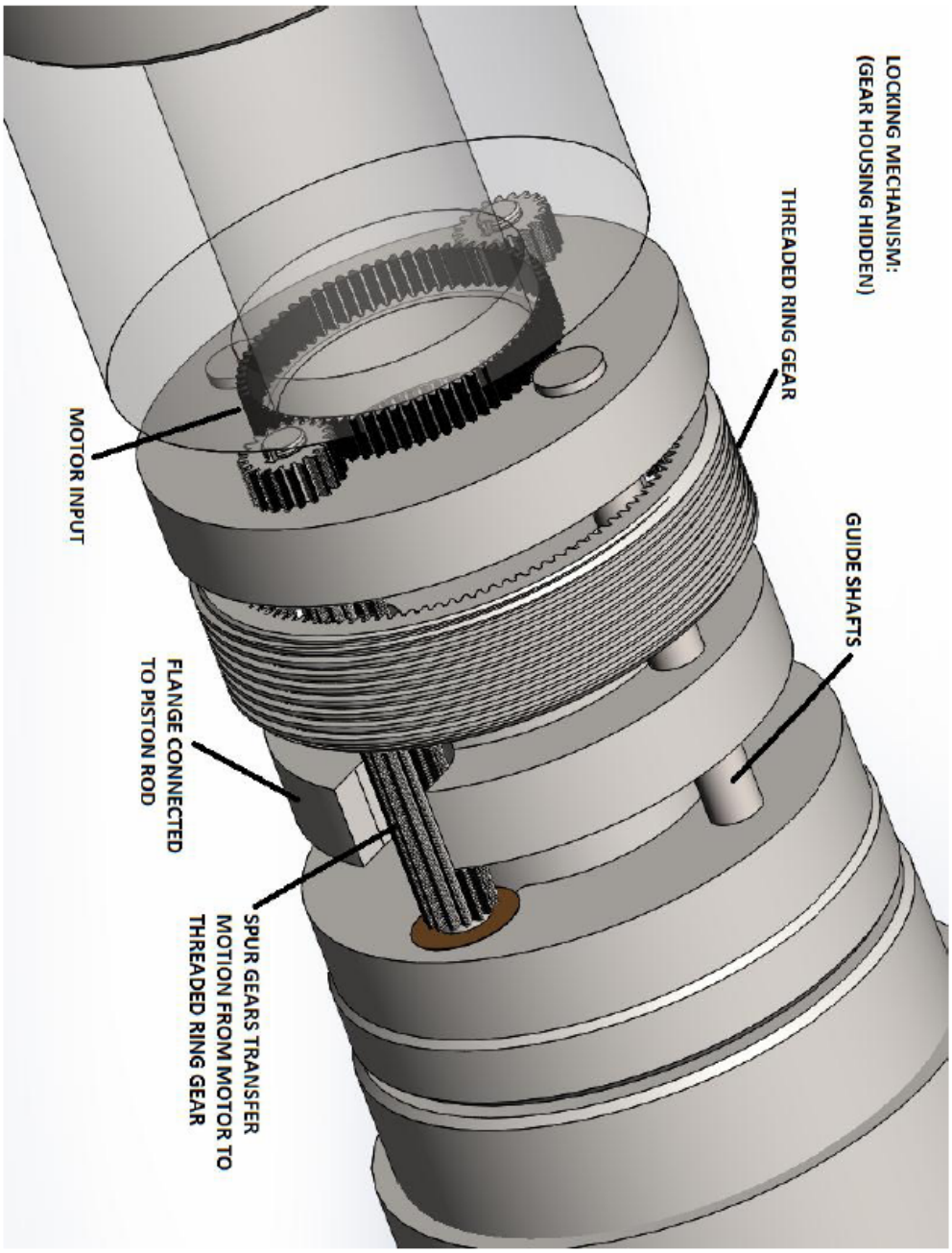

SIZE	FSCM. NO.	DRAWING NO.	REV.
A	06742	67DP-19408-5000	I/R

8. Design Description - Machined Spring

In addition to examining the feasibility of a liquid spring, TDI also examined the feasibility of a metallic machined spring design. TDI has experience in the design and manufacture of large (and small) machined springs.

The design concept for the machined spring stack is similar to the liquid spring stack. Five spring modules with the ability to be turned on and off to give a range of spring rates. The rates found for the liquid spring were used for the design of the machined springs.

8.1 Materials / Safety Factors Used

All major structural components were designed with heat treated 17-4PH Stainless Steel per AMS 5643. The machined spring was designed with VASCOMAX C-300 which is 18% nickel maraging steel. Vascomax C-300 was chosen for its tensile strength and high fatigue strength. Its yield strength is approx 278 ksi, ultimate strength is approx 284 ksi and its fatigue strength is approx. 125 ksi (rotating beam, 10^8 cycles). Minimum safety factor is 1.5 on yield strength and 2.0 on ultimate strength. Fatigue life was evaluated using a Goodman diagram for this material. See Appendix B.

8.2 Spring Design

The spring itself is designed thru the use of FEA (ANSYS). The number of coils, coil width, and coil thickness are chosen such that the optimal solution is found to fit the package. The longest spring will be the spring that has the most deflection, in this case when the rate equals 134.2 kips/in (refer to Table 2). This spring has a free length of 42.25 inches, which when packaged in the housing with a locking mechanism, etc, gives an overall module length of 77.25 inches. The length of the 213 kip/in spring is 72.75" and the length of the 360.6 kip/in spring is 65.75". The total length of all 5 modules is 77.25"+2*72.75"+2*65.75" = 354.25" or 29'-6.25", which fits within the 30' drill segment (additional work could be done to shorten the length of each module if needed).

8.3 Spring Damping

Sandia had requested damping for the liquid spring, so damping would be required on a machined spring. The spring itself would have practically no damping. Therefore TDI came up with a way to add damping to the modules. A damper would be added to each spring module (see Figure 6). The Damper has a built in coil spring pressurized accumulator to allow for thermal expansion of the fluid.

8.4 Locking Mechanism

The locking mechanism is the same mechanism that is used on the liquid spring (refer to Figure 4 and Figure 5)

Figure 5: 134.2 Kips/in Machined Spring Layout

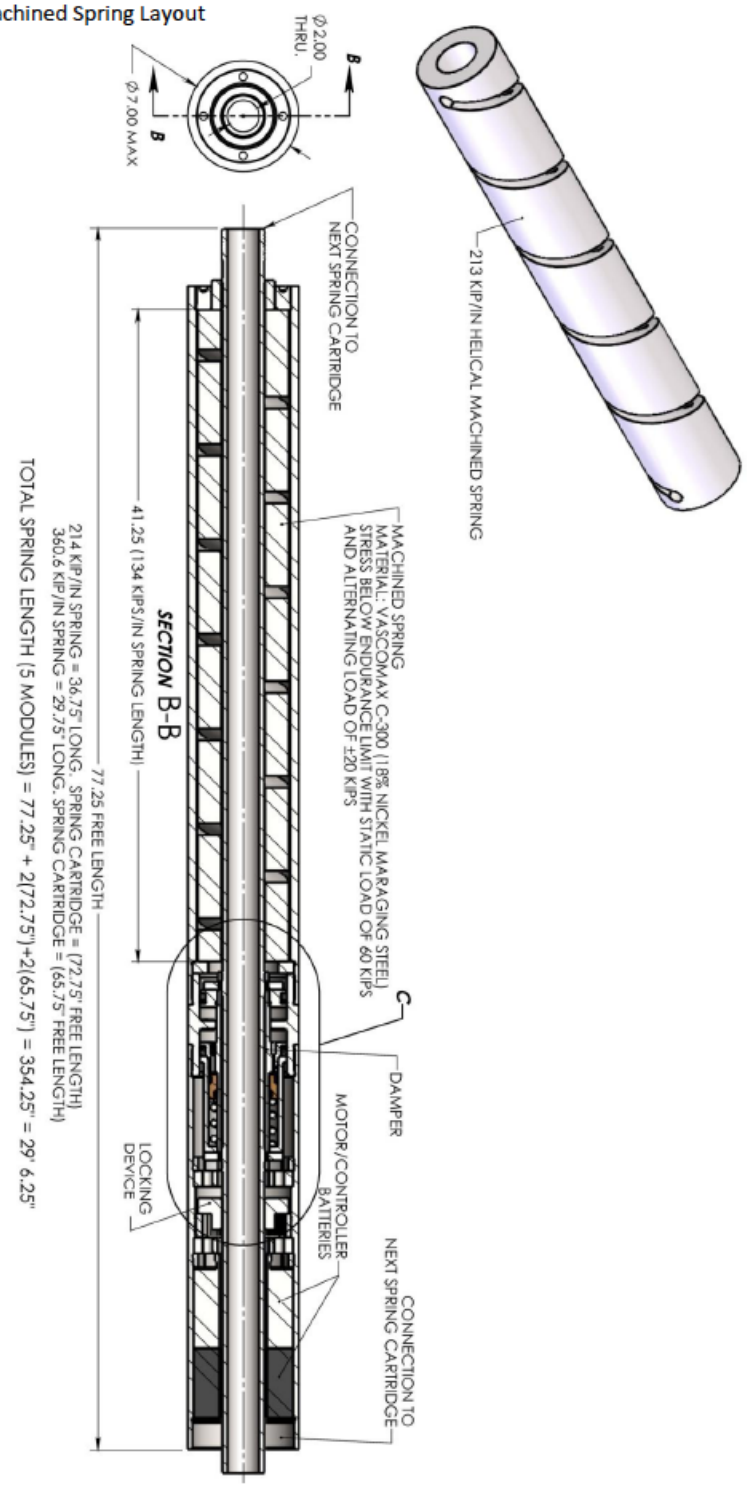

SIZE	FSCM. NO.	DRAWING NO.	REV.
A	06742	67DP-19408-5000	I/R

PAGE 15 OF 29

Figure 6: Detail View of Machined Spring Damper (Detail C from Figure 5)

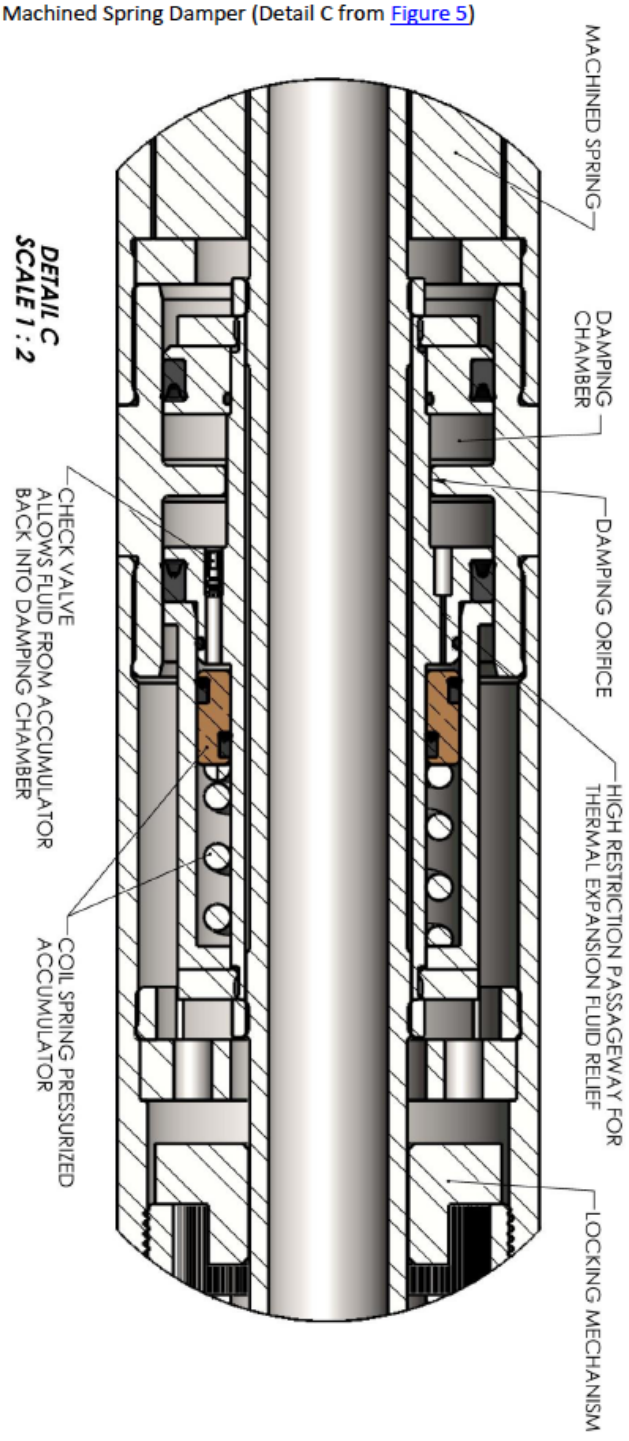

SIZE	FSCM. NO.	DRAWING NO.	REV.
A	06742	67DP-19408-5000	I/R

PAGE 16 OF 29

9. Comparison of a Liquid Spring with a Machined Spring

Machined springs have the following benefits over liquid springs:

- No seals to wear out.
- They can be designed for infinite life.
- A machined springs rate has only a slight temperature dependence due to decrease in modulus at elevated temperatures (~5% decrease)
- They have little risk at high temperature and high cyclic input.
- There is no risk of fluid leakage that would cause unexpected drilling delays or intermittent performance.

A machined spring also has advantages over other forms of springs such as belleville springs. With a machined helical spring there is no wear from galling/fretting from spring washers sliding past one another.

10. Conclusions and Recommendations

The most significant conclusion from this study is that a variable rate spring that meets all parameters is possible, although significant risk could exist depending on which design is selected. The design layouts and accompanying analyses in this study show that a spring with 7.0 inch outside diameter, a 2.0 inch diameter through hole, and a maximum length of 30 feet can theoretically supply the necessary load carrying capability and the desired frequency range.

The investigation included two separate designs; a liquid spring and a mechanical spring. Both concepts work in a theoretical sense. The liquid spring design will have a larger number of development risks than the mechanical machined spring. Here are some of them:

High Temperature

The 393 deg. F maximum temperature is near the operating limit of the Teflon material used for the seal. It might be necessary to depend upon the drilling mud for cooling.

Spring Rate Varies with Temperature

The silicone oil expands as temperature rises, which increases the fluid volume and lowers the spring rate. It may be necessary to switch various segments in and out to compensate for this change in spring rate.

Variable Position Up-Stop

As the position of the piston rod varies with temperature, it will be necessary for both the clamp mechanism and the up-stop to move accordingly, which complicates the control mechanism.

Finite Life

The Teflon seal has a life of over one million cycles at room temperature. Cyclic life may be severely limited due to the operating frequency range. Additionally, we do not know the expected life at 393°F. To our knowledge, a liquid spring has not been used at this elevated temperature in any application.

The mechanical machined spring concept is free from all of these development risks.

Recommendations

Our recommendation is that the mechanical spring concept using a machined spring for the resilient element should be used as the main design configuration for future efforts. It works well, meets all parameters, and fits within the required envelope. The single machined spring in each segment is free from friction and scrubbing, and is similar to springs produced in the based for other vibration isolators.

11. Appendices

11.1 Appendix A - Liquid Spring

Liquid Spring Design:

A program was written to evaluate all possible rod/cylinder bore combinations possible to achieve the target spring rate. The work sheet below contains the basic functions of that program.

K= 360,600 lbs/in worksheet:

Small Rod Diameter:	3	in	
Large Rod Diameter:	3.875	in	
Differential Rod Area:	4.72466	in^2	
Cylinder OD:	7	in	
Cylinder ID:	4.5	in	
Preload:	10000	lbs	
Endload:	80000	lbs	
Ambient 70°F spring rate:	360600	lbs/in	
stroke:	0.194	in	
Preload Pressure:	2,117	psi	
Endload Pressure:	16,932	psi	
d_p:	0.016		<= formulas to obtain delta variables are proprietary.
d_e:	0.09		<= formulas to obtain delta variables are proprietary.
d_D:	0.07078		<= formulas to obtain delta variables are proprietary.
VT:	12.9585	in^3	
VG:	12.76	in^3	
Z:	0.02		<= Correction factor for radial expansion
VGC:	12.502	in^3	<= volume of silicone required.
Fluid Column Length:	1.41	in	
Volume of Silicone fluid expansion:	2.187	in^3	<=Silicone thermal expansion coeff = 0.00053
Distance down bore to space rod:	0.463	in	<= Thermal expansion volume / diff rod area.

The empirical algorithms used to calculate some of the variables are proprietary to TDI.

Finding the optimal values for K1, K2, K3, K4, K5, and K6: First an Excel Spreadsheet was set up

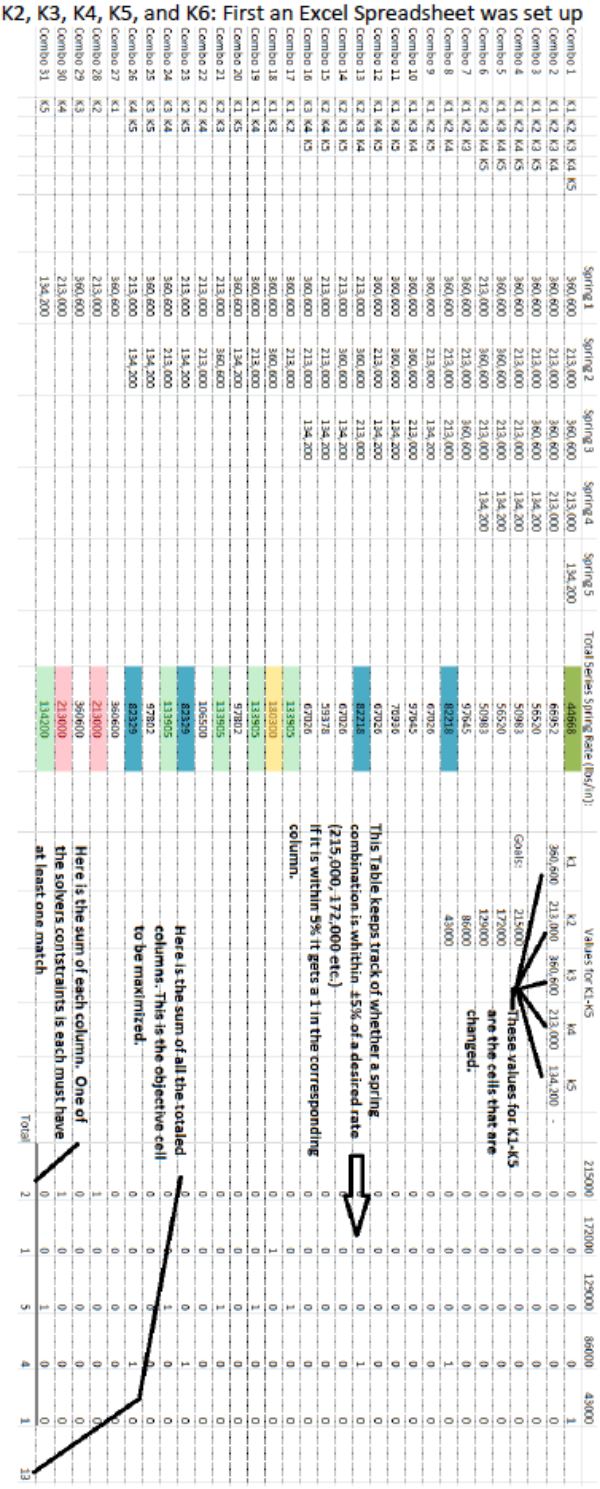

SIZE	FSCM. NO.	DRAWING NO.	REV.
A	06742	67DP-19408-5000	I/R

PAGE 20 OF 29

Then Excel Solver was used to obtain the values for K1-K5. Solver is an add-in that comes with Excel 2007 and 2010 (2010 version used here). You designate which cells to alter to maximize or equal a goal setting up constraints to the solution as well. For the springs the following constraints were used:

-Max and min values for K1-K5 (reasonable values for the spring rates)

-The series rate for all springs being activated has to equal the softest target rate of 43000 lbs/in

-There has to be at least one combination of springs for each target rate (±5% on the rate)

Maximizing the total number of combinations that exist is the goal.

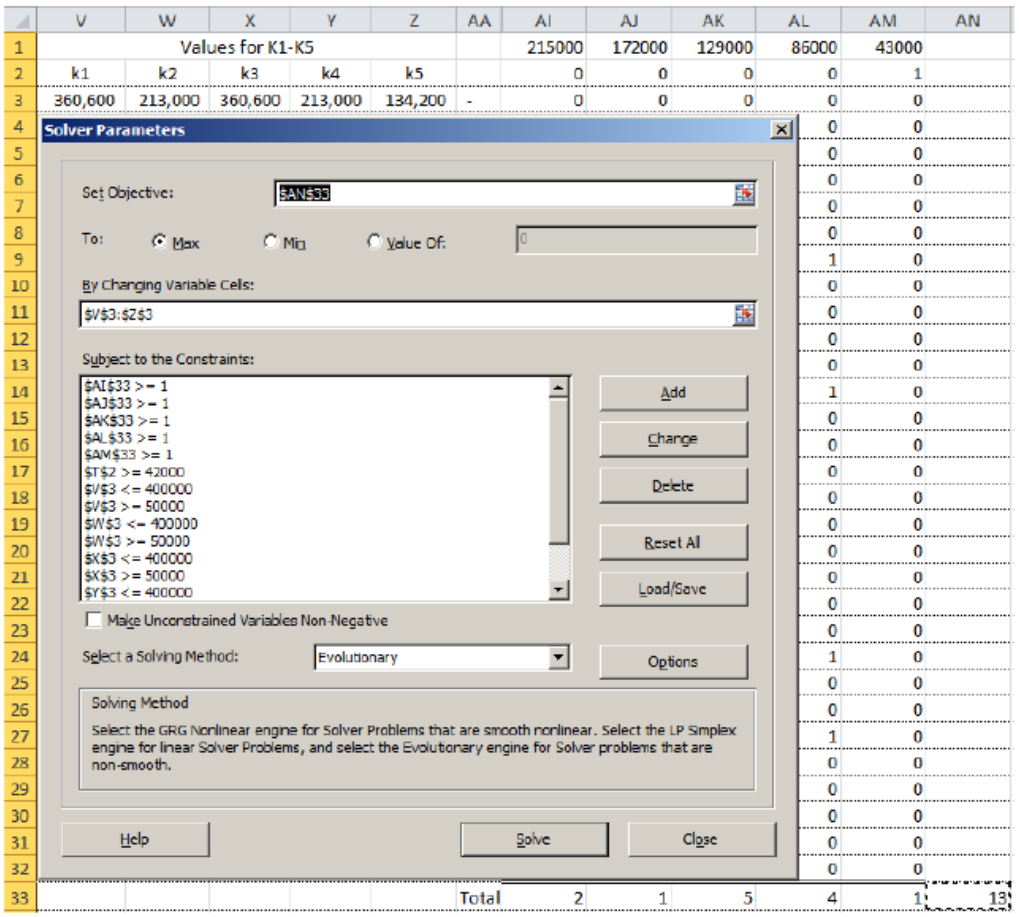

Using the evolutionary solver, rates of (2)360,600 lbs/in, (2)213,000 lbs/in , and 134,200 lbs/in were found.

SIZE	FSCM. NO.	DRAWING NO.	REV.
A	06742	67DP-19408-5000	I/R

PAGE 21 OF 29

These values for K1-K5 were then used in a program written to find the liquid spring parameters:

360.6 Kips/In Liquid Spring Parameters

large rod dia	cylinder id	preload pressure	endload pressure	VGC	fluid column length	thermal fluid expansion	hot rate	VGC hot	endload pressure hot	endload force hot	cylinder stress	cylinder stress when hot	Distance down bore to space head	small column length
3.875	4.5	2116.5491	16932.39279	12.502	1.41489537	2.18654064	287200	14.6882	13916.6248	65751.5	40784.981	33520.91356	0.462792062	1.199568505
3.875	4.505	2116.5491	16932.39279	12.502	1.40925521	2.18654064	287200	14.6882	13916.6248	65751.5	40875.513	33595.3214	0.462792062	1.19294189
3.875	4.51	2116.5491	16932.39279	12.502	1.40365366	2.18654064	287200	14.6882	13916.6248	65751.5	40966.481	33670.04605	0.462792062	1.186860624
3.875	4.515	2116.5491	16932.39279	12.502	1.39809032	2.18654064	287200	14.6882	13916.6248	65751.5	41057.736	33745.0894	0.462792062	1.179824257
3.875	4.52	2116.5491	16932.39279	12.502	1.39256482	2.18654064	287200	14.6882	13916.6248	65751.5	41149.432	33820.45335	0.462792062	1.173332341
3.875	4.525	2116.5491	16932.39279	12.502	1.38707677	2.18654064	287200	14.6882	13916.6248	65751.5	41241.52	33896.13982	0.462792062	1.166884437
3.875	4.53	2116.5491	16932.39279	12.502	1.38162582	2.18654064	287200	14.6882	13916.6248	65751.5	41334.002	33972.15075	0.462792062	1.160480111
3.875	4.535	2116.5491	16932.39279	12.502	1.37621159	2.18654064	287200	14.6882	13916.6248	65751.5	41426.882	34048.48809	0.462792062	1.154118933

The outputted table was filtered out until a spring was found which met all geometry constraints, hoop stress safety factor, and minimal spring rate change at hot temperatures.

The curve on the right illustrates the hot spring rate and fluid volume relationship.

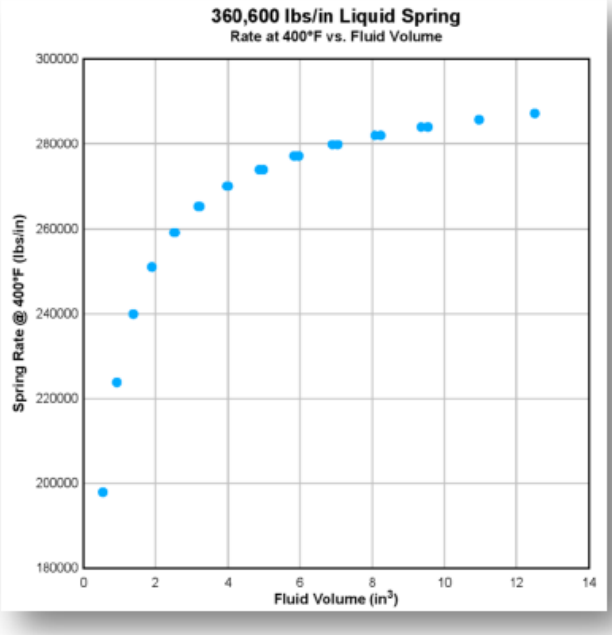

Once all liquid spring parameters were found a layout drawing of each spring module was created.

SIZE	FSCM. NO.	DRAWING NO.	REV.
A	06742	67DP-19408-5000	I/R

During a telecon on 8/21/2013 Sandia requested that a liquid spring with only 3 modules be examined. The 3 modules were examined in a similar manner as the 5 module spring presented above. Below are the results for 3 spring modules.

			Spring 1	Spring 2	Spring 3	Series Rate (lbs/in)				215000	172000	129000	86000	43000	
K1	K2	K3	134,000	85,500	219,000	42150	k1	k2	k3	0	0	0	0	1	
K1	K2		134,000	85,500	-	52196	134,000	85,500	219,000	0	0	0	0	0	
K1	K3		134,000	219,000	-	83133				0	0	0	1	0	
K2	K3		85,500	219,000	-	61493	Goals:	215000		0	0	0	0	0	
K1			134,000	-	-	134000		172000		0	0	1	0	0	
K2			85,500	-	-	85500		129000		0	0	0	1	0	
K3			219,000	-	-	219000		86000		1	0	0	0	0	
								43000							
										1	0	1	2	1	5

K1 is 134,000 lbs/in, K2 is 85,500 lbs/in, and K3 is 219,000 lbs/in.

The resulting spring rates achievable with these springs are:

42,150 lbs/in
52,196 lbs/in
83,133 lbs/in
61,493 lbs/in
134,000 lbs/in
85,500 lbs/in
219,000 lbs/in

Notice that there is no rate near the desired target rate of 172,000 lbs/in.

Liquid Spring Module Stress Calculations.

Calculations for the 134,200 lbs/in spring module are presented below. Other modules share similar operating pressures and loads.

Some of the stress calculations on the major components are presented below.

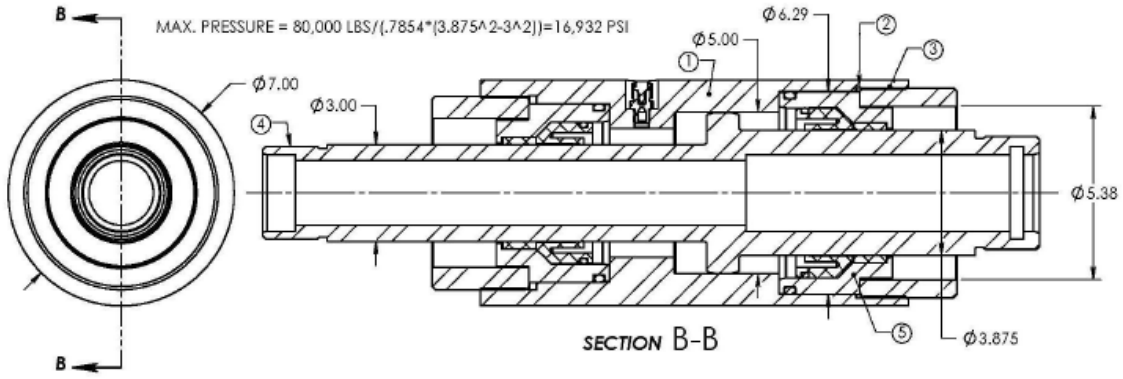

The calculations are for the following areas of concern. (refer to circled numbers in above figure)

1 - Hoop stress on the cylinder.

2 - Undercut tensile stress on the cylinder

3 - Thread shear stress on the cylinder.

4 - Thread shear stress where the locking mechanism flange attaches to the piston rod.

5 - Shear stress on the cylinder cap.

SIZE	FSCM. NO.	DRAWING NO.	REV.
A	06742	67DP-19408-5000	I/R

PAGE 24 OF 29

Cylinder:

Material: 17-4PH STAINLESS STEEL PER AMS 5643 (@ 400°F) COND. H-1025

Tensile Yield Strength:	130,500	psi		
Tensile Ultimate Strength:	139,500	psi		
Shear Strength:	85,500	psi	Max. Internal Pressure (P_{max}):	16,932 psi
Bearing Yield Strength:	225,000	psi	Max. Axial Load (F_{max}):	80,000 lb.
Bearing Ultimate Strength:	298,800	psi		

1.) Hoop Stress:

Outer Diameter (OD_{cyl}):	7.00	in.
Bore Diameter (ID_{cyl}):	5.00	in.

$\sigma = P_{max} * ((OD_{cyl}^2 + ID_{cyl}^2)/(OD_{cyl}^2 - ID_{cyl}^2))$

$\sigma =$ 52,207 psi

Safety Factor (Yield):	2.50
Safety Factor (Ultimate):	2.67

2.) Undercut Stress:

The force on the undercut is a result of the max pressure on the area of the cylinder cap

F= 16932 psi x .7854(6.29^2-3^2) = 326,455 lbs

Outer Diameter (OD_{cyl}):	7.00	in.
Cyl. Undercut Diameter (D_{uc}):	6.530	in.

$\sigma = (\text{Load on cap}) * 4/(\pi * (OD^2 - D_{uc}^2))$

$\sigma =$ 65,364 psi

Safety Factor (Yield):	2.0
Safety Factor (Ultimate):	2.1

3.) Thread Shear Stress:

Load on Cap (F):	326,455	lb.
Thread Pitch Diameter (D):	6.44	in.
Engaged Thread Length (L):	1.27	in.

$\tau = 2 * F / (\pi * D * L)$

$\tau =$ 25,411 psi

Safety Factor (Shear): 3.4

SIZE	FSCM. NO.	DRAWING NO.	REV.
A	06742	67DP-19408-5000	I/R

Piston Rod:

Material:	17-4PH STAINLESS STEEL PER AMS 5643 (@ 400°F) COND. H-925				
Tensile Yield Strength:	139,500	psi			
Tensile Ultimate Strength:	153,000	psi			
Shear Strength:	85,500	psi	Max. Axial Load (F_{ap}):	80,000	lb.
Bearing Yield Strength:	225,000	psi			
Bearing Ultimate Strength:	298,800	psi			

Since the column length is so short, and the load only 80,000 lbs, buckling is not a concern.

The most highly stressed area on the piston rod is the threads where the flange for the locking mechanism is mounted. These threads must react 80,000 lbs.

4.) Thread Shear Stress

Load on flange (F):	80,000	lb.
Thread Pitch Diameter (D):	2.81	in.
Engaged Thread Length (L):	1.50	in.
$\tau =$	$2* F / (\pi * D * L)$	
$\tau =$	12,070	psi
Safety Factor (Shear):	7.1	

Cylinder Cap:

Material:	17-4PH STAINLESS STEEL PER AMS 5643 (@ 400°F) COND. H-1025				
AllowableTensile Stress:	130,500	psi			
Tensile Ultimate Strength:	139,500	psi			
Allowable Shear Stress:	85,500	psi	Max. Internal Pressure (P_{max}):	16,932	psi
Bearing Yield Strength:	225,000	psi	Max. Axial Load (F_{max}):	80,000	lb.
Bearing Ultimate Strength:	298,800	psi			

The Cylinder Cap is loaded by the pressure acting on the unsupported area which is .7854*(5.38^2-3.875^2) = 10.94 in^2. This area multiplied by the max internal pressure yields the load on the Cylinder Cap 10.94 in^2 * 16,932 psi = 185,230 lbs.

5.) Shear Stress:

Shear Diameter (D):	5.27	in.	$\tau =$	F/(3.14*D*L)	
Shear Length (L):	0.71	in.	$\tau =$	15758	psi
			Safety Factor (Shear):	5.4	

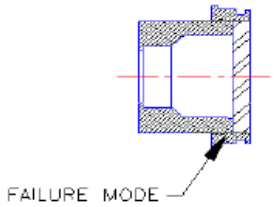

SIZE	FSCM. NO.	DRAWING NO.	REV.
A	06742	67DP-19408-5000	I/R

Also evaluated was the flange that reacts all the load when the locking mechanism is deployed.

This flange is loaded in plate bending so ANSYS was used to examine the stress.
A simple model consisting of the flange and the threaded ring gear was made.

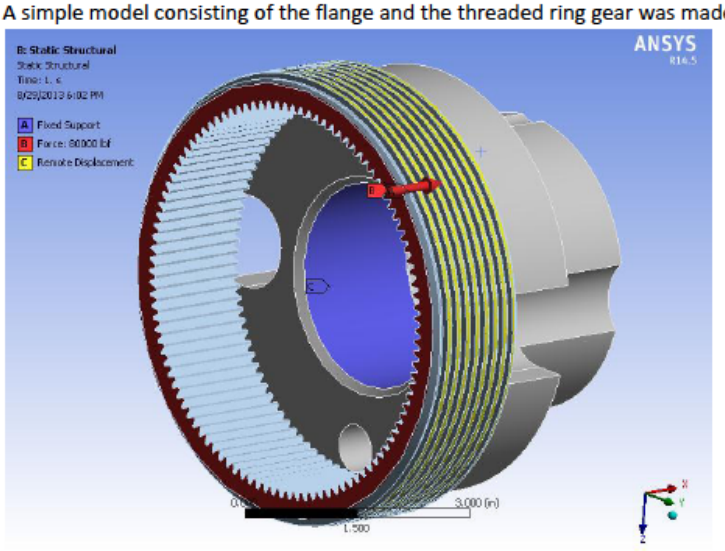

The contact between the ring gear and flange was set to no separation. A fixed support was placed on the threaded ID of the flange. A load of 80,000 lbs was applied to the threaded ring gear. The rotational DOF's of the ring gear were also fixed. Flange is made from 17-4PH Stainless steel per AMS 5643 H-1025

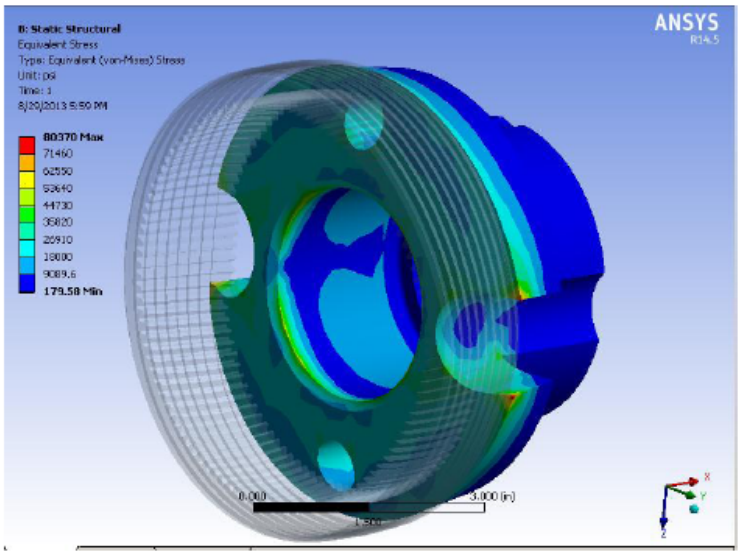

The stress near the ID is approx. 50 ksi. F.S. yield = 130.5 ksi/50 ksi = 2.61 F.S. ult = 139.5 ksi / 50 ksi = 2.79

SIZE	FSCM. NO.	DRAWING NO.	REV.
A	06742	67DP-19408-5000	I/R

PAGE 27 OF 29

11.2 Appendix B - Machined Spring

ANSYS (FEA software) was used to design each spring. The design goal was to design the spring for infinite life. Below is a sample stress of analysis of the 360.6 kips/in machined spring. All springs were stressed similarly. Material is VascoMax C-300. Its yield strength is approx 278 ksi, ultimate strength is approx 284 ksi and its fatigue strength is approx. 125 ksi (rotating beam, 10^8 cycles).

FEA model setup:

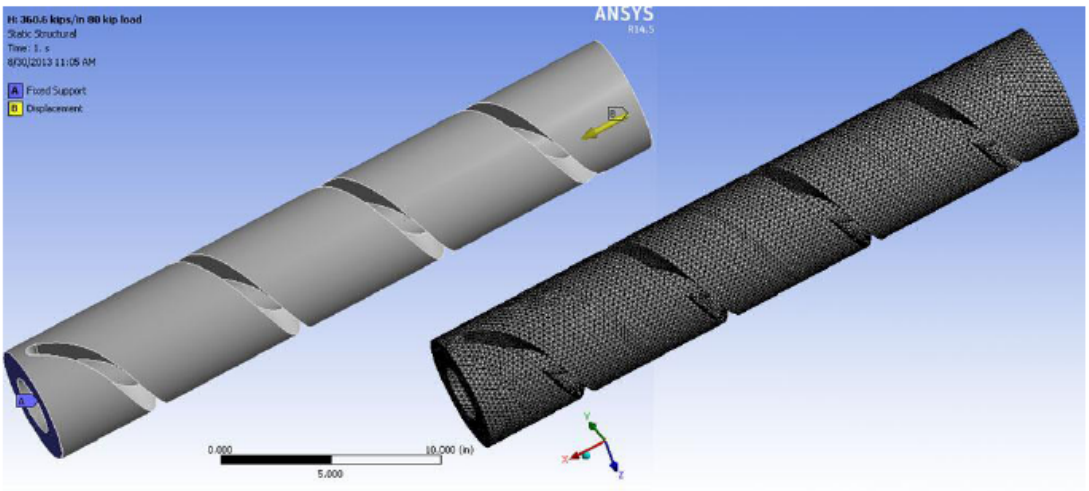

A fixed support on one end and a corresponding deflection at loads of 60 kip and 80 kip (max. mean load and max total load)

Stress at 60 kip load:

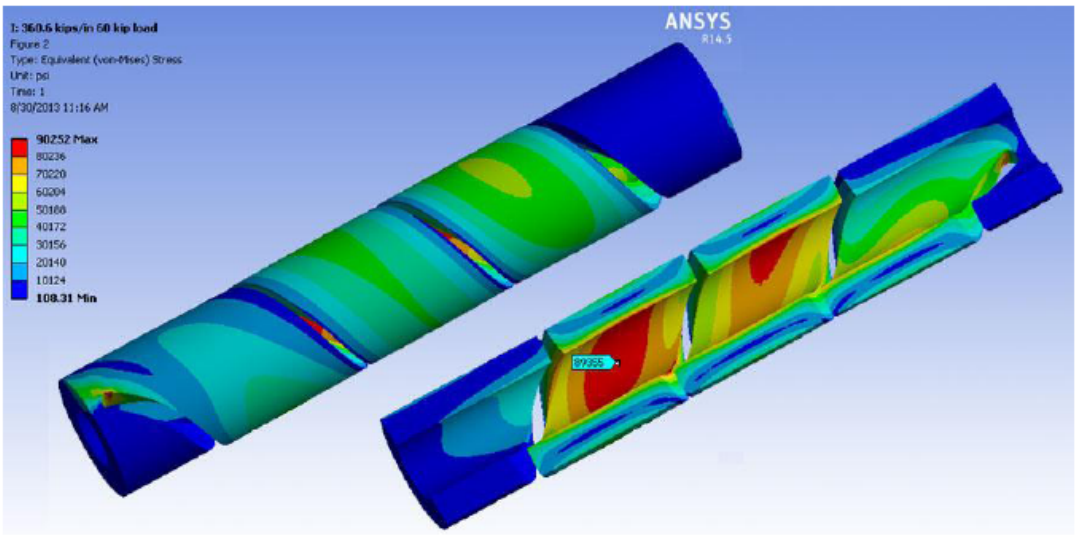

Max. equivalent stress is approx 90 ksi.

SIZE	FSCM. NO.	DRAWING NO.	REV.
A	06742	67DP-19408-5000	I/R

Stress at 80 kip load:

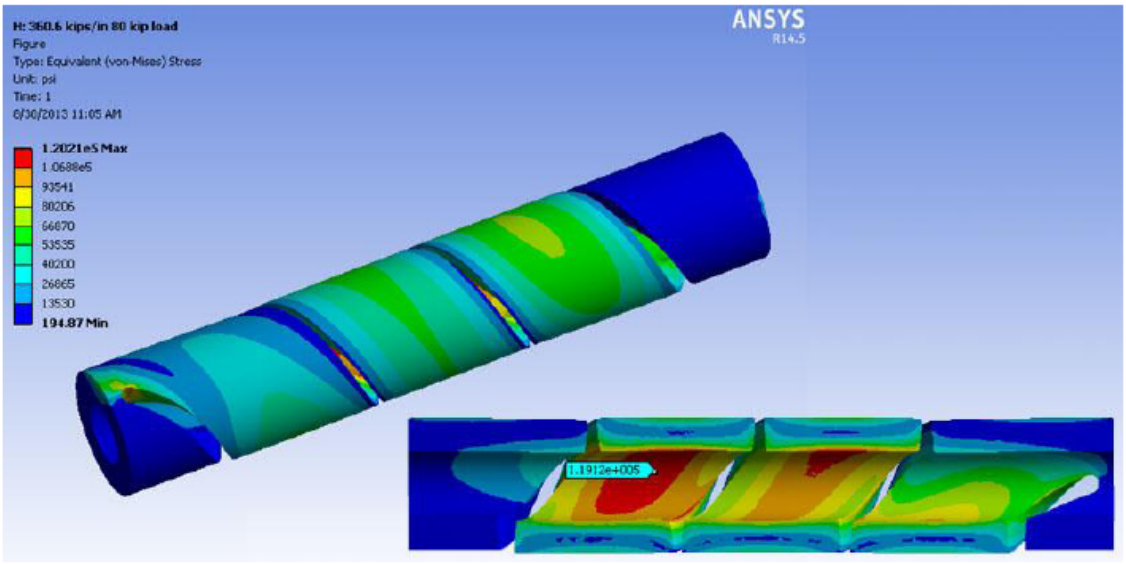

Max. equivalent stress is approx 120 ksi.

The endurance limit of VascoMax C-300 with correction factors for size and temperature is approx 80% of the listed value or 100 ksi. A Goodman diagram was constructed using a mean stress of 90 ksi and alternating stress of 30 ksi.

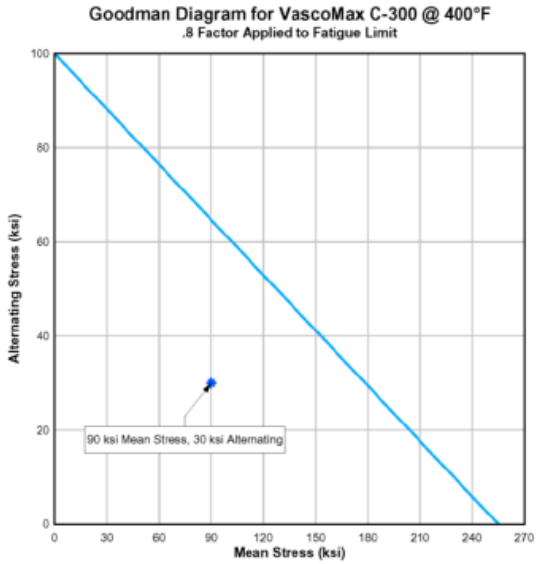

The design stress is below the Goodman curve.

SIZE	FSCM. NO.	DRAWING NO.	REV.
A	06742	67DP-19408-5000	I/R

This page intentionally left blank.

APPENDIX F. VARIABLE RATE SPRING (VRS) DESIGN DETAIL

This page intentionally left blank.

Selective Belleville Spring System

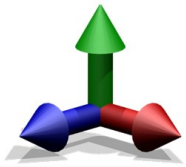

W. Radigan

May 7, 2013

Design Goals

- Design a variable spring with properties of:
  - Spring rates between 20 lbf/in and 600 lbf/in
  - Total weight less than 150 lb
  - Less than 50 lb moving mass
  - Minimum of 2 in available deflection
  - Attachment points for MTS load frames and DDS

Stack Load Selections

Displacement	2 in								Total Rate:	668 lbf/in	109 N/mm
	50.8 mm								Total Load:	1336 lbf	5516 N
	Desired				Actual (from CSC Spring Data)						
	Rate	Load	Rate	Load	Rate	Load	Rate	Load	On/Off	Max Load (lbf)	Max Load (N)
Stack 1	20 lbf/in	40 lbf	4 N/mm	178 N	22 lbf/in	44 lbf	4 N/mm	196 N	1	44	178
Stack 2	40 lbf/in	80 lbf	7 N/mm	356 N	50 lbf/in	100 lbf	9 N/mm	445 N	1	100	356
Stack 3	80 lbf/in	160 lbf	14 N/mm	712 N	96 lbf/in	192 lbf	17 N/mm	854 N	1	192	712
Stack 4	160 lbf/in	320 lbf	28 N/mm	1423 N	161 lbf/in	322 lbf	28 N/mm	1432 N	1	322	1423
Stack 5	320 lbf/in	640 lbf	56 N/mm	2847 N	339 lbf/in	678 lbf	59 N/mm	3016 N	1	678	2847

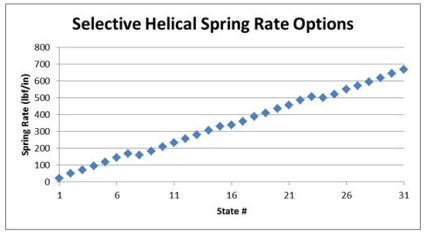

Binary Load Selections

Case 1	Case 2	Case 3	Case 4	Case 5	Case 6	Case 7	Case 8	Case 9	Case 10
22 lbf/in	50 lbf/in	72 lbf/in	96 lbf/in	118 lbf/in	146 lbf/in	168 lbf/in	161 lbf/in	183 lbf/in	211 lbf/in
44 lbf	100 lbf	144 lbf	192 lbf	236 lbf	292 lbf	336 lbf	322 lbf	366 lbf	422 lbf
1	2	3	4	5	6	7	8	9	10
1 44	0 0	1 44	0 0	1 44	0 0	1 44	0 0	1 44	0 0
0 0	1 100	1 100	0 0	0 0	1 100	1 100	0 0	0 0	1 100
0 0	0 0	0 0	1 192	1 192	1 192	1 192	0 0	0 0	0 0
0 0	0 0	0 0	0 0	0 0	0 0	0 0	1 322	1 322	1 322
0 0	0 0	0 0	0 0	0 0	0 0	0 0	0 0	0 0	0 0

Case 11	Case 12	Case 13	Case 14	Case 15	Case 16	Case 17	Case 18	Case 19	Case 20
233 lbf/in	257 lbf/in	279 lbf/in	307 lbf/in	329 lbf/in	339 lbf/in	361 lbf/in	389 lbf/in	411 lbf/in	435 lbf/in
466 lbf	514 lbf	558 lbf	614 lbf	658 lbf	678 lbf	722 lbf	778 lbf	822 lbf	870 lbf
11	12	13	14	15	16	17	18	19	20
1 44	0 0	1 44	0 0	1 44	0 0	1 44	0 0	1 44	0 0
1 100	0 0	0 0	1 100	1 100	0 0	0 0	1 100	1 100	0 0
0 0	1 192	1 192	1 192	1 192	0 0	0 0	0 0	0 0	1 192
1 322	1 322	1 322	1 322	1 322	0 0	0 0	0 0	0 0	0 0
0 0	0 0	0 0	0 0	0 0	1 678	1 678	1 678	1 678	1 678

Case 21	Case 22	Case 23	Case 24	Case 25	Case 26	Case 27	Case 28	Case 29	Case 30	Case 31
457 lbf/in	485 lbf/in	507 lbf/in	500 lbf/in	522 lbf/in	550 lbf/in	572 lbf/in	596 lbf/in	618 lbf/in	646 lbf/in	668 lbf/in
914 lbf	970 lbf	1014 lbf	1000 lbf	1044 lbf	1100 lbf	1144 lbf	1192 lbf	1236 lbf	1292 lbf	1336 lbf
21	22	23	24	25	26	27	28	29	30	31
1 44	0 0	1 44	0 0	1 44	0 0	1 44	0 0	1 44	0 0	1 44
0 0	1 100	1 100	0 0	0 0	1 100	1 100	0 0	0 0	1 100	1 100
1 192	1 192	1 192	0 0	0 0	0 0	0 0	1 192	1 192	1 192	1 192
0 0	0 0	0 0	1 322	1 322	1 322	1 322	1 322	1 322	1 322	1 322
1 678	1 678	1 678	1 678	1 678	1 678	1 678	1 678	1 678	1 678	1 678

Helical Spring Designs

- Off-the-shelf coil springs
- Spring Steel
- 2+ inches deflection

Select	CSC Stock #	OD (in)	ID (in)	Free Length (in)	Rate (lbs/in)	Sugg. Max Defl (in)	Sugg. Max Load (lbs)	Solid Length (in)	Wire Dia. (in)	Total Coils	Spring Weight (lb)	1st Natural Frequency (Hz)
Spring 1												
	4347	3.375	2.991	5.25	22	2.8	61	0.91	0.192	4.75	0.369	75.9
Spring 2												
	1879	3.421	2.921	3.84	50	2.5	124	1.38	0.25	5.5	0.722	81.8
Spring 3												
	4076	3.75	3.126	5.5	96	2.2	212	2.03	0.312	5.5	1.223	87.0
Spring 4												
	73369	3.656	2.906	6	161	2.6	411	2.62	0.375	7	2.159	84.8
Spring 5												
	73447	3.906	2.97	6	339	2.1	706	3.28	0.468	7.01	3.525	96.3

Belleville Stack #1 Properties (Light)

22 lbf/in 50 lbf/in 96 lbf/in 161 lbf/in 339 lbf/in

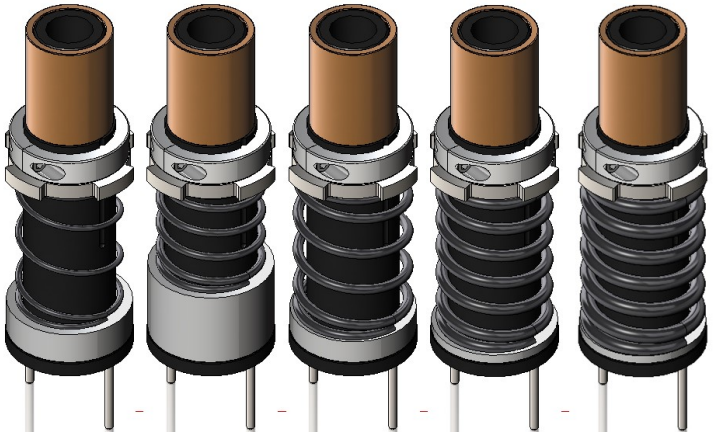

Full Assembly

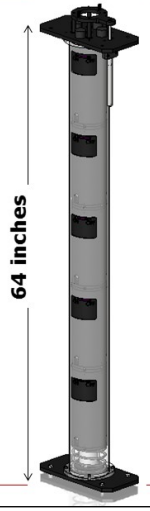

Bias Spring Assembly

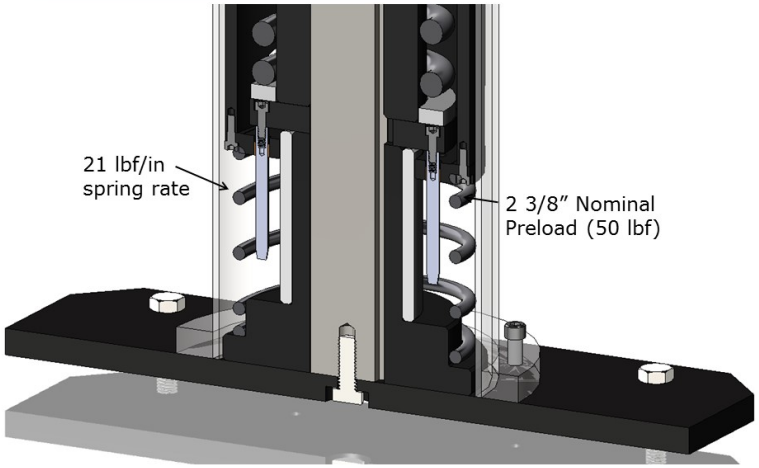

Stack Selection Mechanism

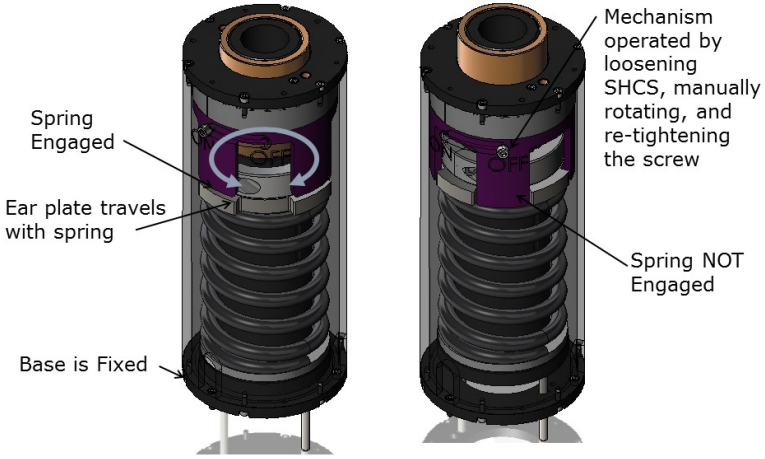

Stack Selection Mechanism

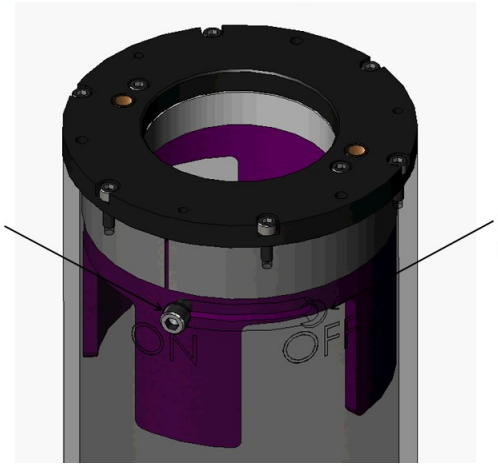

Stack Selection Mechanism

Moving Mass

5.7 lb EA x 5 = 29 lb Total Moving Mass

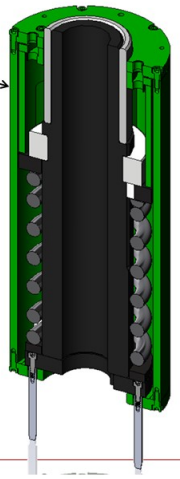

+ Contribution from moving portion of the springs.

Mass Distribution

Name	English Value	Unit	Metric Value	Unit	Note
Moving Mass	5.7	lbm	2.6	kg	Mass of a single "Spring Selection Assy"
Number of bits	5				Number of bits in the system
Total Moving Mass	28.7	lbm	13.0	kg	
System Weight	130.0	lbm	59.0	kg	SolidWorks calculation of the entire system weight.
Static Weight	101.3	lbm	45.9	kg	

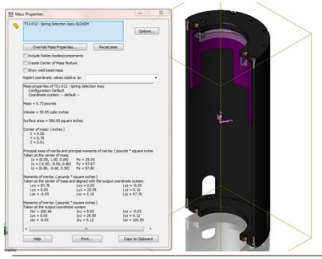

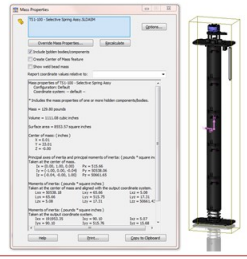

Spring Stack Bearing Surfaces

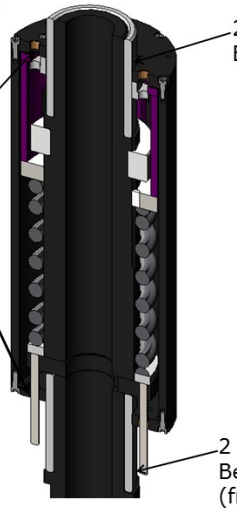

2 ¾" OD PTFE Bearing (#1)

¼" ID Oilite Bearings (anti-rotation)

2 ¾" OD PTFE Bearing (#2) (from assy below)

Stack Selector Bearing Surfaces

PSA Backed PTFE applied to flat surfaces

Delrin retaining cap

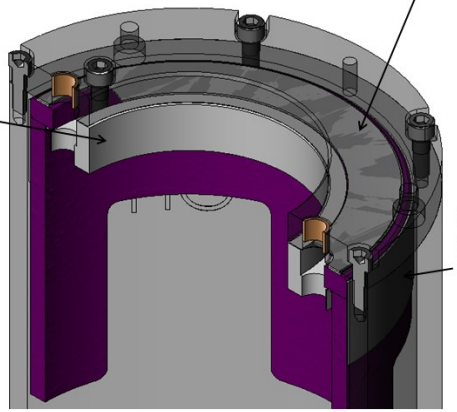

PSA Backed PTFE applied to OD of selector

DDS Installation

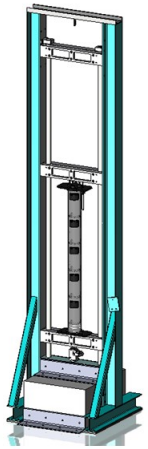

DDS Attachment Points (1)

4X 3/8-16 Fasteners
(10" x 5" Square Pattern)

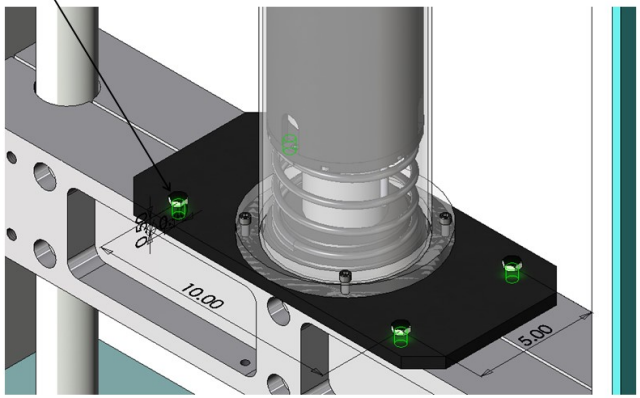

DDS Attachment Points (2)

2X 3/8-16 Fasteners
(4" Bolt Circle)

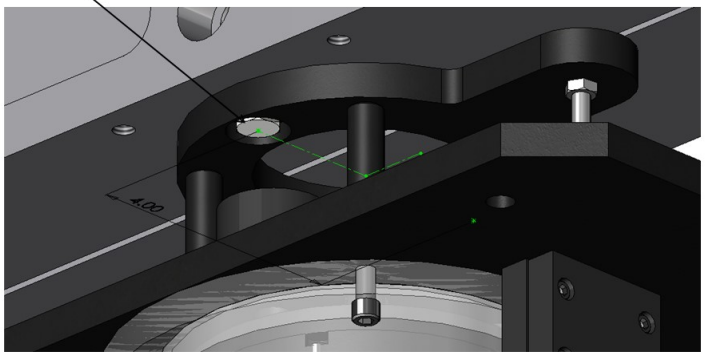

Displacement Monitoring

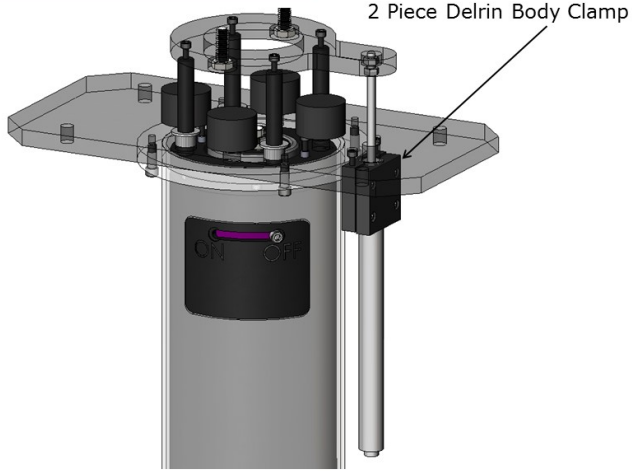

Acrylic Viewing Cover

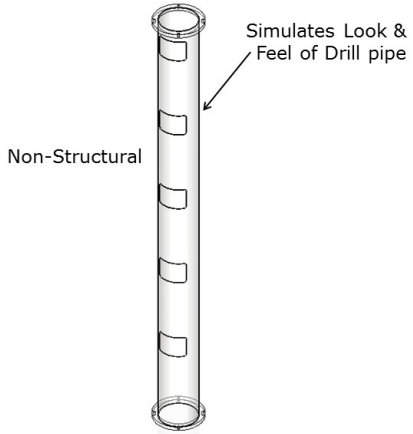

Spindle Assembly

Full Assembly (1)

Full Assembly (2)

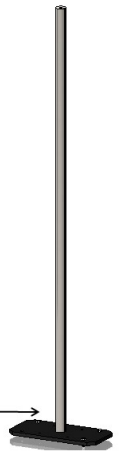

Full Assembly (3)

Full Assembly (4)

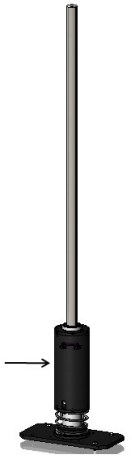

Full Assembly (5)

Full Assembly (6)

Full Assembly (7)

Full Assembly (8)

Full Assembly (9)

Full Assembly (10)

Full Assembly (11)

Cost

ITEM NO.	QTY.	Number	DESCRIPTION	Vendor	VendorNo	Cost
1	4		Rubber Bumper, 5/16-18 Thd	McMaster	8926T39	$7.05 EA
2	12		Pull-Out Dowel Pin, 1/4" OD, 2-1/2" Lg, 8-32 Thd	McMaster	97175A325	$2.46 EA
3	4		Flanged Sleeve Bearing, 1/2" ID X 5/8" OD	McMaster	2706T25	$4.69 EA
4	104		SCREW, SHCS, 8-32 X 1/2" LG			
5	20		SAE 863 Sleeve Bearing, 1/4" ID, 5/16" OD, 1/4" LG	McMaster	2686T42	$0.34 EA
6	5		SCREW, SHCS, 1/4-20 X 5/8" LG			
7	10		SCREW, SHCS, 8-32 X 3/4" LG			
8	5		PIN, DOWEL, 1/4" X 1/2"			
9	5		Shaft Collar, 2.5" bore	McMaster	6436K55	$34.07 EA
10	1		Helical Spring, 2.991 ID x 22 lbf/in	Century Spring	4347	$32.76 EA
11	1		Helical Spring, 2.921 ID x 50 lbf/in	Century Spring	1879	$20.35 EA
12	1		Helical Spring, 3.126 ID x 96 lbf/in	Century Spring	4076	$51.00 EA
13	1		Helical Spring, 2.906 ID x 161 lbf/in	Century Spring	73369	$34.21 EA
14	1		Helical Spring, 2.970 ID x 339 lbf/in	Century Spring	73447	$37.28 EA
15	1		SPRING, HELICAL, 4.187 ID x 21lb/in	Century Spring	4079	$55.74 EA
16	8		SCREW, SHCS, 1/4-20 X 3/4" LG			
17	8		Hex Bolt 3/8-16 x 1" LG	McMaster	92965A624	$13.53 / PK 50
18	2		Flat Washer 3/8" x .04" Thk	McMaster	95229A480	$3.72 / PK 100
19	1		Omega LVDT	Omega	LD621-100	$760

Machine shop quote still outstanding

Subcomponent Design

Spring Spindle

Material: 7075 Aluminum
Weight: ~ 5 lb

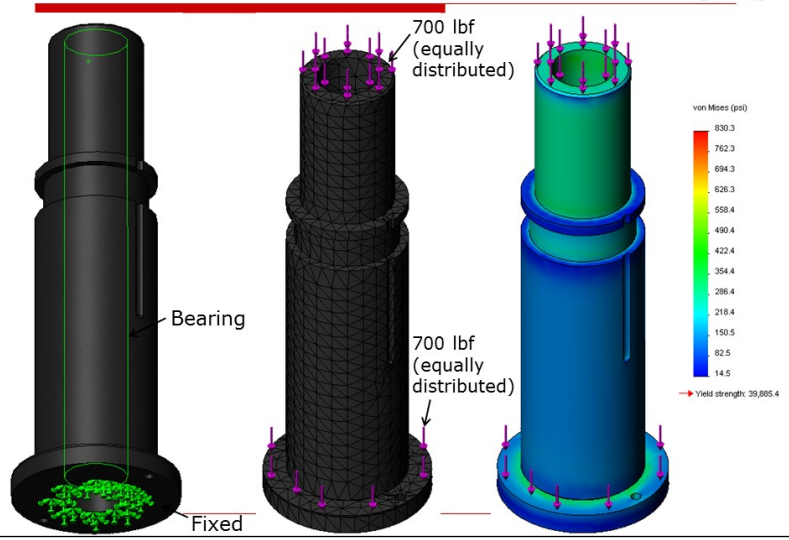

This page intentionally left blank.

APPENDIX G. SHAPE MEMORY ALLOY (SMA) ACTUATOR DETAIL

This page intentionally left blank.

SMA Testbed Data

W. Radigan
2014-04-28

Summary

- A series of tests was conducted using the "SMA Testbed" device to assess the suitability of using SMA (specifically "Flexinol") wires for a rotary actuator.
- The data presented here shows the measured temperature of the wire over the course of a 60sec test.
  - The wire temperature was measured using a micro-thermistor with a diameter of .023". This is relatively large compared with the wires that we are measuring and we expect to see a significant temperature lag.

Apparatus

- The micro-thermistors were calibrated using a handheld thermocouple meter and a hot-water bath.
- Thermistor coefficients were obtained from the manufacturer (Qti).

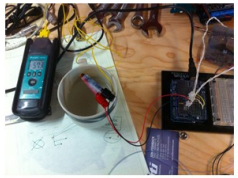

ENGINEERING INFORMATION

- Typical diameter 0.023 inches
- Typical wire size #38 AWG
- Leads: solid nickel, Polyesterimide insulation
- Material: epoxy, polyimide
- Typical Dissipation Constant: 0.2mW/°C in still air*
- Typical Time Constant in still air: 3 seconds max*
- E320 sensors RoHS compliant
- Available in point-matched and interchangeable tolerances

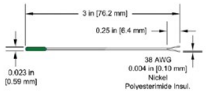

* Depends on mounting

Apparatus

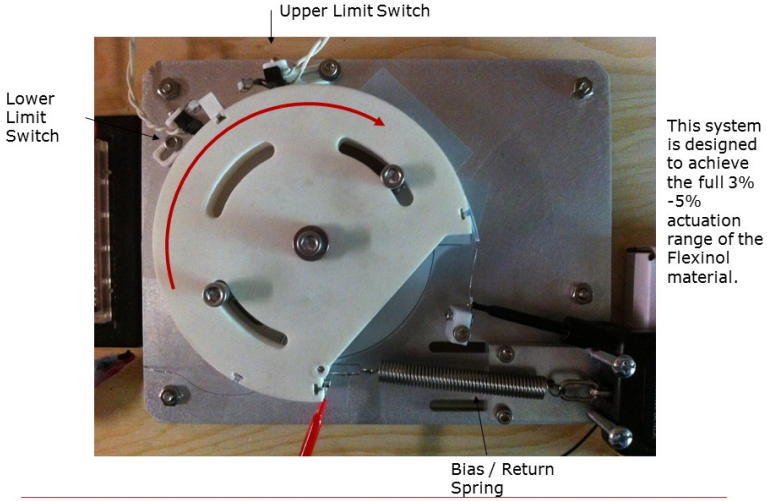

This system is designed to achieve the full 3% -5% actuation range of the Flexinol material.

Apparatus

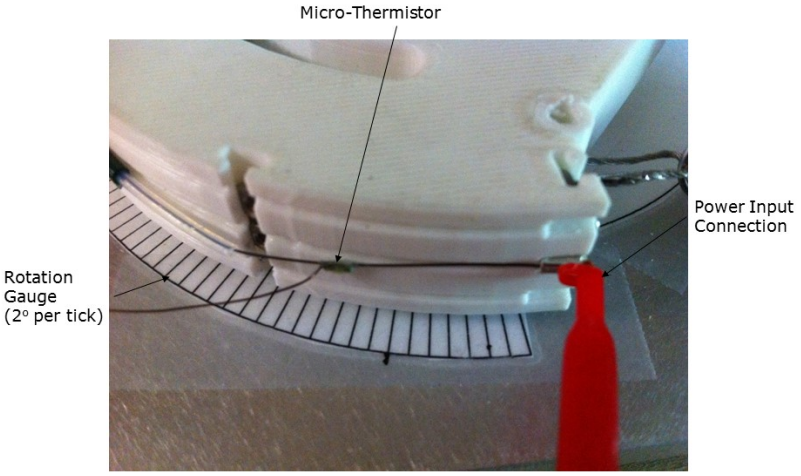

Test Summary

- Dynalloy provides a reference matrix of wire size, pull force, and drive current.
- The purpose of this testing was to assess the suitability of this information in a rotary actuator (the reference designs are all “straight pull”) and to assess the possible range of values that could be used.

Diameter Size inches (mm)	Resistance ohms/inch (ohms/meter)	Heating Pull Force* pounds (grams)	Cooling Deformation Force* pounds (grams)	Approximate** Current for 1 Second Contraction (mA)	Cooling Time 158° F, 70°C "LT" Wire*** (seconds)	Cooling Time 194° F, 90°C "HT" Wire*** (seconds)
0.001 (0.025)	36.2 (1425)	0.02 (8.9)	0.008 (3.6)	45	0.18	0.15
0.0015 (0.038)	22.6 (890)	0.04 (20)	0.016 (8)	55	0.24	0.20
0.002 (0.050)	12.7 (500)	0.08 (36)	0.032 (14)	85	0.4	0.3
0.003 (0.076)	5.9 (232)	0.18 (80)	0.07 (32)	150	0.8	0.7
0.004 (0.10)	3.2 (126)	0.31 (143)	0.12 (57)	200	1.1	0.9
0.005 (0.13)	1.9 (75)	0.49 (223)	0.20 (89)	320	1.6	1.4
0.006 (0.15)	1.4 (55)	0.71 (321)	0.28 (128)	410	2.0	1.7
0.008 (0.20)	0.74 (29)	1.26 (570)	0.50 (228)	660	3.2	2.7
0.010 (0.25)	0.47 (18.5)	1.96 (891)	0.78 (356)	1050	5.4	4.5
0.012 (0.31)	0.31 (12.2)	2.83 (1280)	1.13 (512)	1500	8.1	6.8
0.015 (0.38)	0.21 (8.3)	4.42 (2250)	1.77 (900)	2250	10.5	8.8
0.020 (0.51)	0.11 (4.3)	7.85 (3560)	3.14 (1424)	4000	16.8	14.0

Plot Format

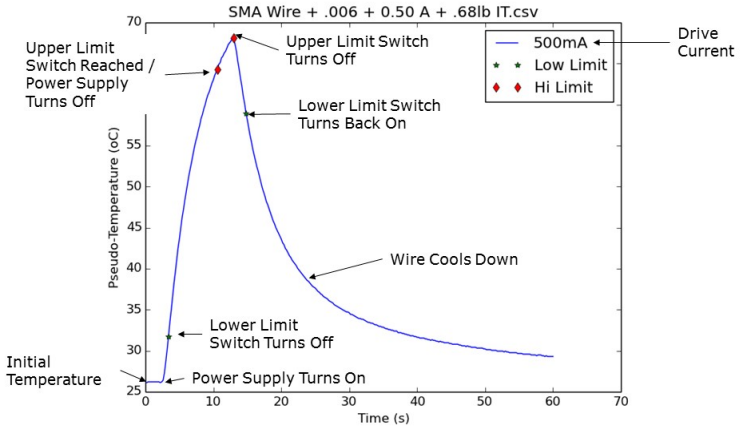

Data - .006” Wire

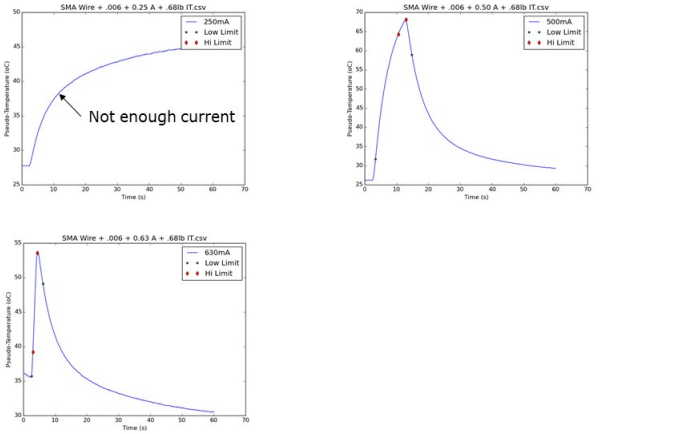

Data - .006” Wire

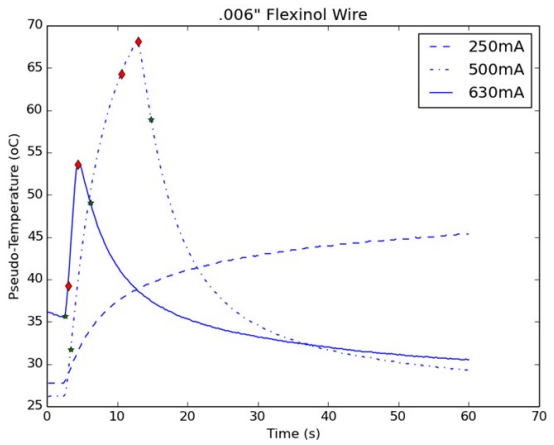

Data - .012” Wire

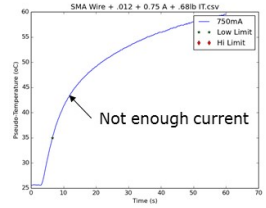

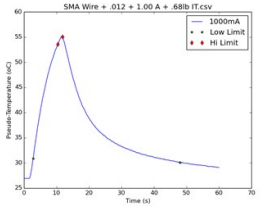

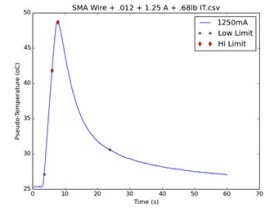

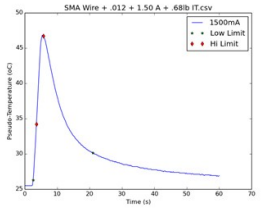

Data - .012” Wire

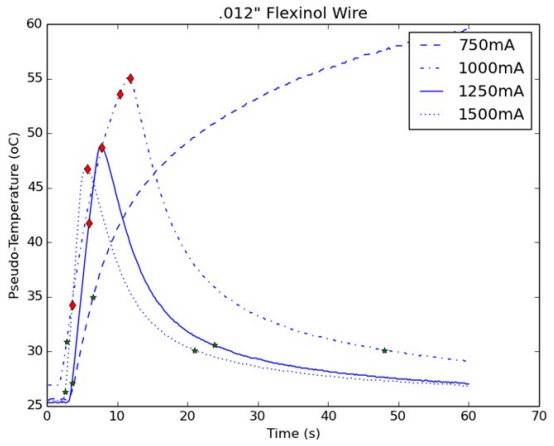

Data - .020” Wire

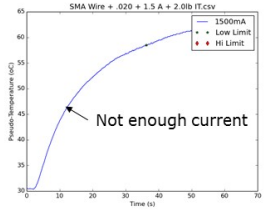

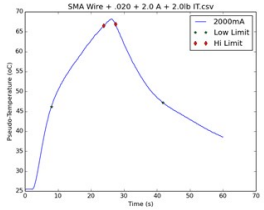

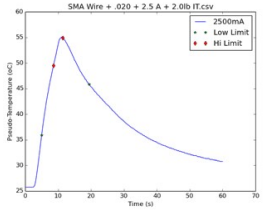

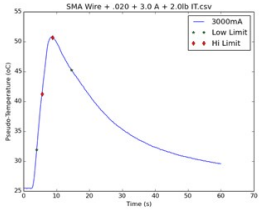

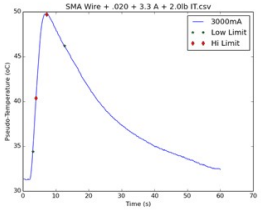

Data - .020” Wire

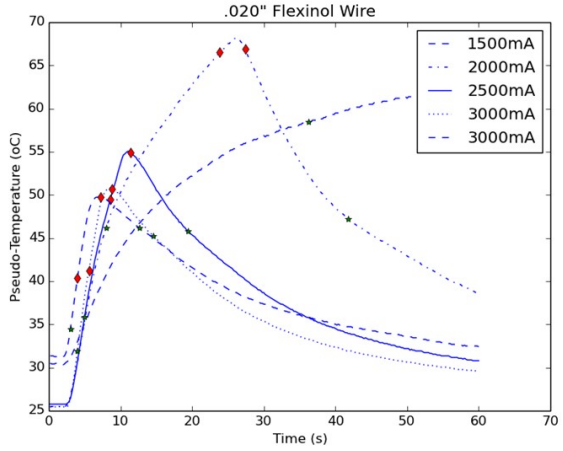

APPENDIX H. VARIABLE RATE SPRING FIXTURE (VRSF) DESIGN

VRSF Instrumentation Summary

The VRSF is instrumented with eight sensors, a battery pack and a system for wireless data collection. Figure H-1 depicts the sensor and instrumentation connection details in accordance with mount location on the VRSF Solidworks model. The fundamental measurements tracked are the spring displacement (LVDTs), accelerations of both the top and bottom sides of the VRSF (MEMS accelerometers), and the axial force and torque on the bit (Custom Load + Torque cell).

A 14.4V NiMH rechargeable battery pack (12H4/3AF4500R2WR) is used to power the data acquisition electronics and sensors. A National Instruments NI-9191 wireless chassis was used with an NI-9205 32-Ch +/- 10V CDAQ module for collecting the data from the rotating system wirelessly. Signal conditioners (DCA-Vehicle Signal Conditioner) by Interface Force were used with a custom ordered 5611 combination Load + Torque cell with a 1.5" through hole for water passage in the drill string. The battery and electronics are mounted to the VRSF with failsafe silicone vibration damping mounts to protect them from vibration.

This system serves as a wireless instrumentation platform for development of embedded control algorithms that will monitor drilling dynamics and select spring stiffness states accordingly. Control systems developed on the data acquisition computer using powerful programming tools such as Matlab can be formatted for downhole embedded electronics targets in the future.

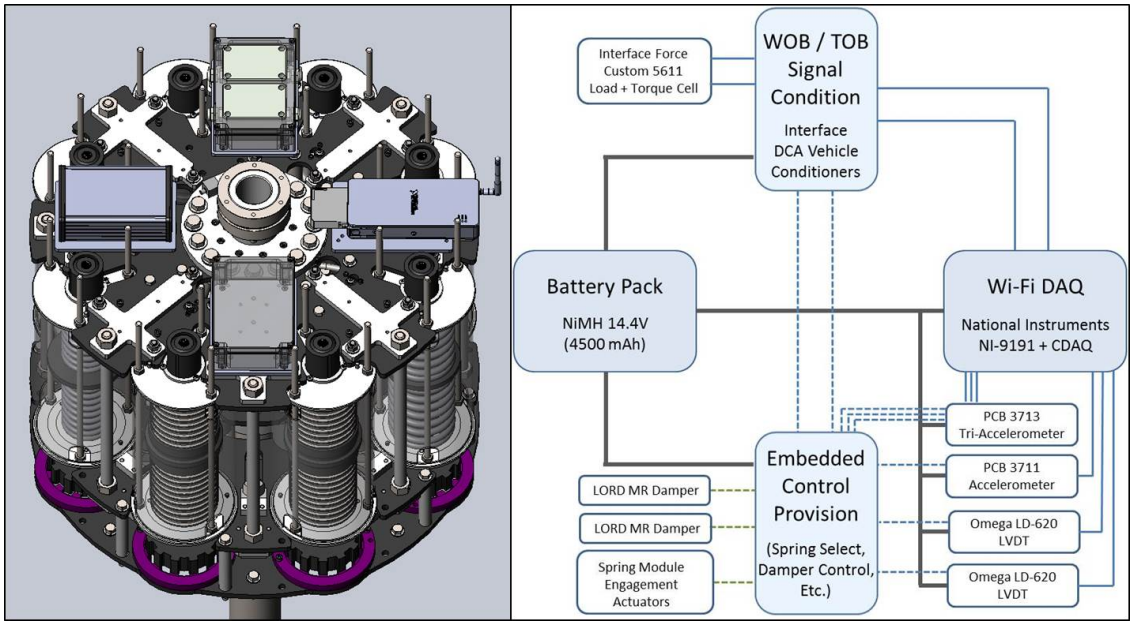

Figure H-1. FVRSF Sensors and Instrumentation description and Solidworks view.

This page intentionally left blank.

VRSF Preliminary Design Presentation

RADIGAN ENGINEERING

W. Radigan

2015-01-28

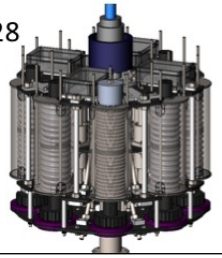

Design Goals

RADIGAN ENGINEERING

- ? 15” Overall Height
  - 20” Overall Height
- ? 24” Diameter
  - 27” Diameter
- ✓ 2” Axial Compression
- ✓ Mate to existing HRDF Systems
  - “Power Head” Above
  - “Drillstring” Below
- ✓ Moving Mass of 185lb
  - ~280lb
  - *Spring Rates have been adjusted to maintain target frequencies*
- ✓ Support a maximum WoB of 4,000lbf
- Provide a minimum of 32 selectable spring rates
  - 300 in-lb – 14,400 in-lb (@ 300 in-lb increments)
- ✓ Include provision for MR Fluid Dampers as used in FY2002 IDF

FY 2002 IDF (For Reference)

RADIGAN ENGINEERING

Rigid Assembly | Moving Assembly | Lower Plate (for preload)

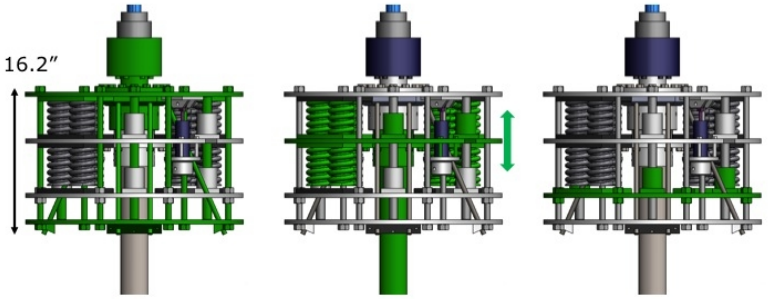

FY 2002 IDF (For Reference)

RADIGAN ENGINEERING

CSC Spring #	Individual Spring Rate	System Frequency
12152	27 lb/in	4 Hz
73192	145 lb/in	10 Hz
73203	255 lb/in	12.8 Hz
73237	1625 lb/in	32 Hz

CSC Stock #	73237	CSC Stock #	73192	CSC Stock #	73203	CSC Stock #	12152
OD (in)	2.906	OD (in)	2.906	OD (in)	2.906	OD (in)	1.500
ID (in)	1.844	ID (in)	2.220	ID (in)	2.156	ID (in)	1.156
Free Length (in)	5.000	Free Length (in)	7.000	Free Length (in)	6.000	Free Length (in)	8.630
Rate (lbs/in)	1625.000	Rate (lbs/in)	145.000	Rate (lbs/in)	255.000	Rate (lbs/in)	27.000
Sugg. Max Defl. (in)	0.790	Sugg. Max Defl. (in)	2.700	Sugg. Max Defl. (in)	2.000	Sugg. Max Defl. (in)	3.800
Sugg. Max Load (lbs)	1276.000	Sugg. Max Load (lbs)	392.000	Sugg. Max Load (lbs)	509.000	Sugg. Max Load (lbs)	101.000
Solid Length (in)	3.850	Solid Length (in)	3.480	Solid Length (in)	3.330	Solid Length (in)	3.780
Wire Dia. (in)	0.531	Wire Dia. (in)	0.343	Wire Dia. (in)	0.375	Wire Dia. (in)	0.172
Total Coils	7.250	Total Coils	10.200	Total Coils	8.880	Total Coils	22.000
Material	Oil Tempered	Material	Oil Tempered	Material	Oil Tempered	Material	Spring Steel
Ends	Closed Ground	Ends	Closed Ground	Ends	Closed Ground	Ends	Closed Ground
Finish	None	Finish	None	Finish	None	Finish	Zinc

FY 2002 IDF (For Reference)

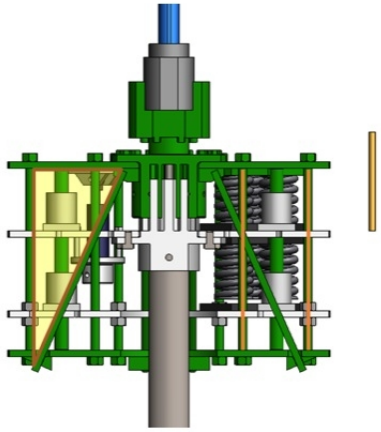

System Frequency Updates

- VRSF Design has a moving mass of 280lb [127kg]
- This results in a net decrease in the system natural frequencies.

Description	Symbol	Value	Unit	Note	Equation
Moving Mass	M_(Dynamic)=	215	lbm	Includes Dynamic Assy + 8 spindles	
	Module_1=	7.6	lbm	Total mass of 4 springs	
	Module_2=	13.2	lbm		
	Module_3=	17.6	lbm		
	Module_4=		lbm		
	Module_5=	35.6	lbm		
	Module_5b=	27.2	lbm		
	Spring_Mass=	93.6	lbm		
	M_(moving)=	278	lbm	Dynamic mass + 2/3 of Spring mass	
	M_(moving)=	126	kg		

Frequencies of Interest	f_i=		Angular Speed (rad/s)	Spring Rate (lbf/in)	<-- / 4
		12.83 Hz	80.6	4,671	1,168
		26.45 Hz	166.2	19,850	4,963
		32.39 Hz	203.5	29,767	7,442
		---			
		2 Hz	12.6	113	28
		4 Hz	25.1	454	113
		6 Hz	37.7	1,021	255
		8 Hz	50.3	1,816	454
		10 Hz	62.8	2,837	709
		12.8 Hz	80.4	4,649	1,162
		22.4 Hz	140.7	14,237	3,559
		100 Hz	628.3	283,738	70,934

2002 IDF

CSC Spring #	Individual Spring Rate	System Frequency
12152	27 lb/in	4 Hz
73192	145 lb/in	10 Hz
73203	255 lb/in	12.8 Hz
73237	1625 lb/in	32 Hz

System Frequency Updates

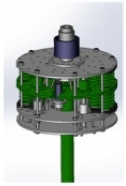

System Frequency		Angular Speed (rad/s)	ID @ 185 lbm Spring Rate (lbf/in)	VRSF @ 280 lbm Spring Rate (lbf/in)
12.83	Hz	80.6	3,061	4,709
26.45	Hz	166.2	13,009	20,014
32.39	Hz	203.5	19,508	30,013

2	Hz	12.6	74	114
4	Hz	25.1	298	458
6	Hz	37.7	669	1,030
8	Hz	50.3	1,190	1,831
10	Hz	62.8	1,859	2,861
12.8	Hz	80.4	3,047	4,687
22.4	Hz	140.7	9,330	14,354
100	Hz	628.3	185,949	286,075

System Frequency Updates

Module #	Module Spring Rate (lbf/in)	Individual Spring Rate k_(1 of 4) (lbf/in)	Max δ (in)	Requried Spring Defl.
1	300	75	2.00	4.00
2	600	150	2.00	4.00
3	1200	300	2.00	4.00
4	2400	600	1.67	3.33
5	4800	1200	0.83	1.67
5b	6000	1500	0.67	1.33
All (a)	9000		0.44	0.89
All (b)	14400		0.28	0.56

"Module 5b" provides the additional spring rate needed to reach the 22.4Hz natural frequency.

Simplified Model Analysis

- A grossly simplified model was constructed to double-check design assumptions and parameter values.
  - Center Disk has a mass of 280lb

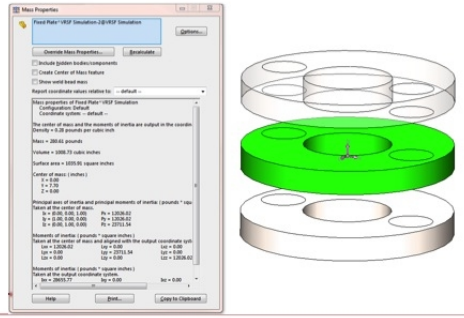

Simplified Model Analysis

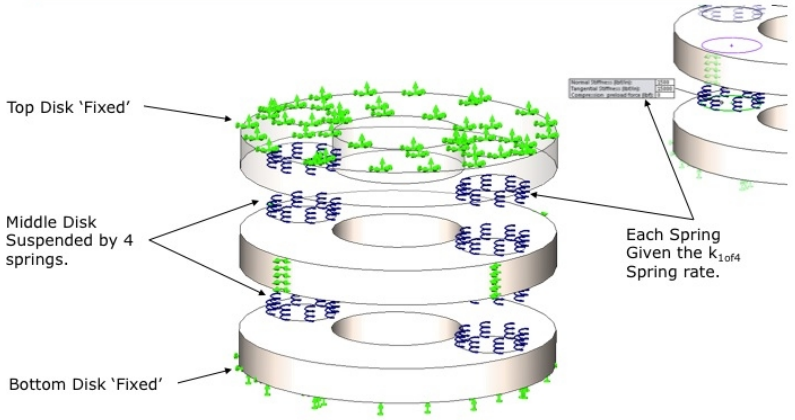

Simplified Model Analysis (Frequency)

- At k_{max} = 14,400 lbf/in (k_{1of4} = 3,600 lbf/in)
- Model predicts a 1st harmonic of 22.7Hz

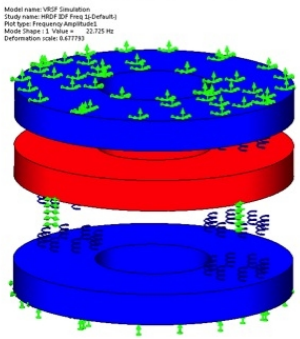

- At k_{min} = 300 lbf/in (k_{1of4} = 75 lbf/in)
- Model predicts a 1st harmonic of 3.2Hz

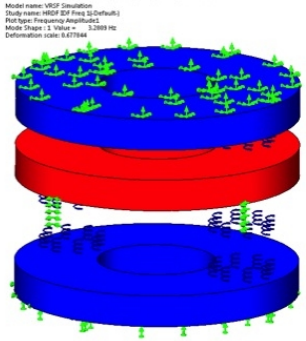

Simplified Model Analysis (Static)

- At k_{max} = 14,400 lbf/in (k_{1of4} = 3,600 lbf/in)
- Model predicts a static deflection of 0.28in

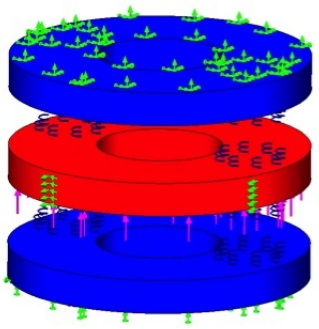

- At k_{mid} = 2,400 lbf/in (k_{1of4} = 600 lbf/in)
- Model predicts a static deflection of 1.67in

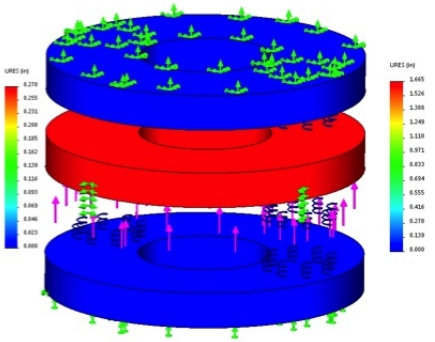

VRSF

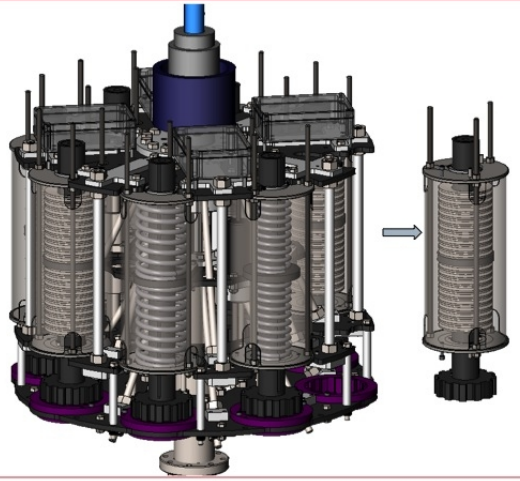

VRSF "Rigid Assembly"

Diagonal bracing similar to IDF

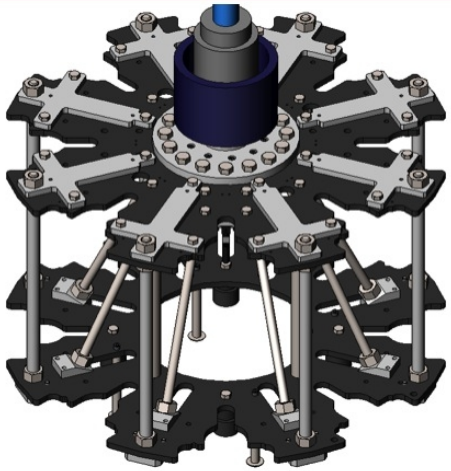

VRSF "Rigid Assembly"

Vertical rods have thin-walled steel sleeve to set overall height.

Double Nut Assembly sets definite position for angled all-thread.

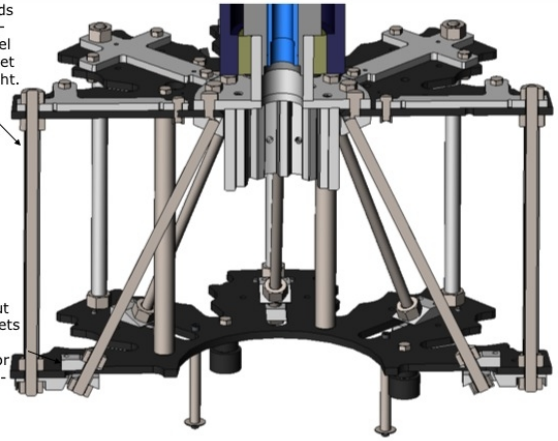

VRSF "Rigid Assembly"

Steel Supports stiffen top plate and bottom plate

Contoured OD allows for spring modules to be removed radially.

Plate material is 3/8" Thick 6061 Aluminum

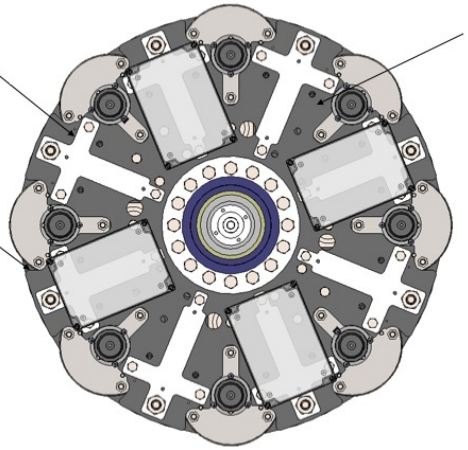

Rigid Assy FEA

45° Symmetrical Section

Symmetry Boundary Conditions

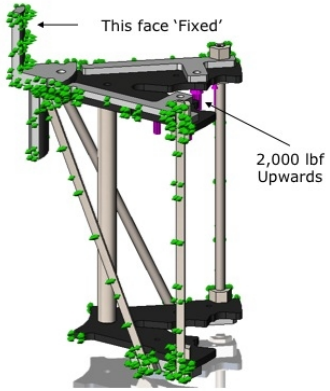

Rigid Assy FEA

All Hardware is Grade 5 or equivalent (90ksi Yield)

Spline & Stiffening Plates 4140/4340 (60ksi Yield)

Large Plates 6061-T6 Aluminum (40ksi Yield)

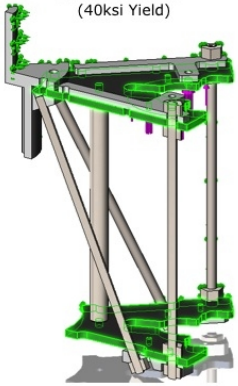

Rigid Assy FEA

.125" Tetrahedral Mesh

All Connections 'Bonded'
254k Total Elements

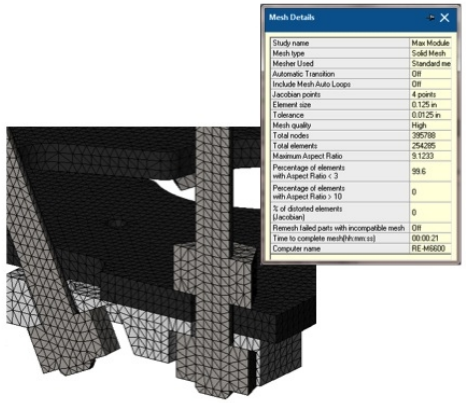

Mesh Details

Study name	Max Module
Mesh type	Solid Mesh
Mesher Used	Standard me
Automatic Transition	Off
Include Mesh Auto Loops	Off
Jacobian points	4 points
Element size	0.125 in
Tolerance	0.0125 in
Mesh quality	High
Total nodes	395788
Total elements	254295
Maximum Aspect Ratio	9.1233
Percentage of elements with Aspect Ratio < 3	99.6
Percentage of elements with Aspect Ratio > 10	0
% of distorted elements (Jacobian)	0
Remesh failed parts with incompatible mesh	Off
Time to complete mesh(hh:mm:ss)	00:00:21
Computer name	RE-M6600

Rigid Assy FEA

Von Mises Stress Distribution

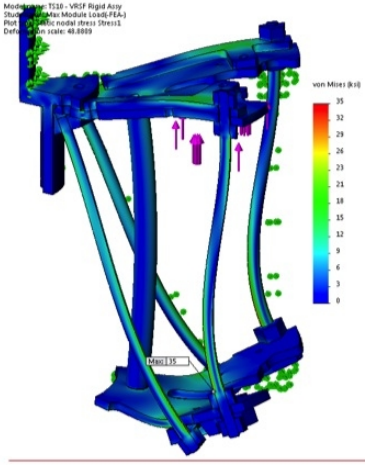

Factor of Safety Distribution (Yield)

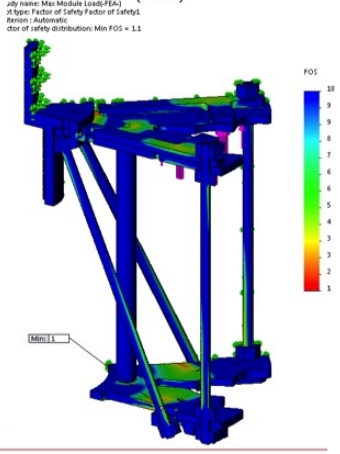

Rigid Assy FEA

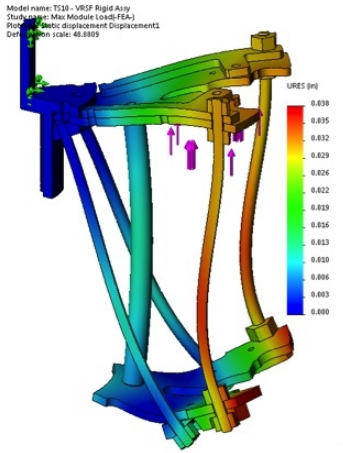

Rigid Assy FEA

Areas with Factor of Safety (FOS) > 3.0

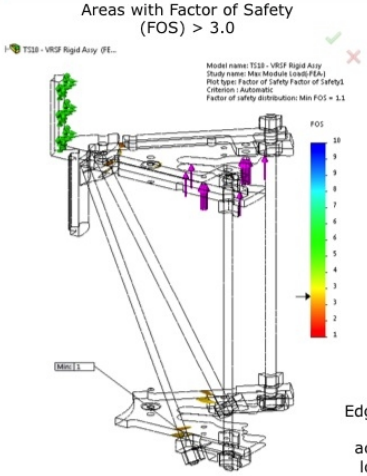

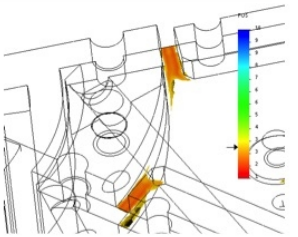

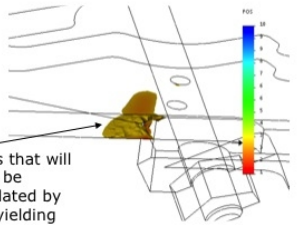

Edge effects that will likely be accommodated by localized yielding

Moving Plate

Revised hole pattern for male spline (12x → 16x)

Lower Mount for MR Dampers

4X 1" Linear Bearings

Diagonal bracing does not interfere with Rigid Assembly.

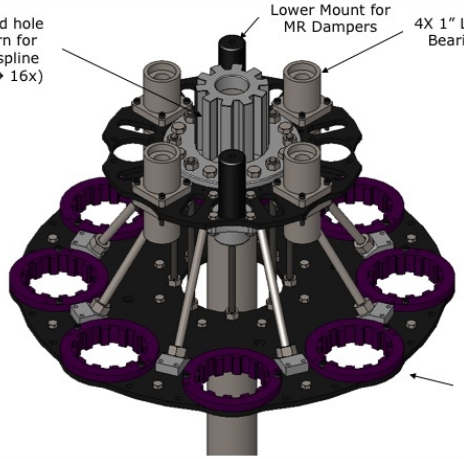

Module Selection Splines

Dynamic Assy FEA

45° Symmetrical Section

Symmetry Boundary Conditions

This face 'Fixed'

2,000 lbf Downwards

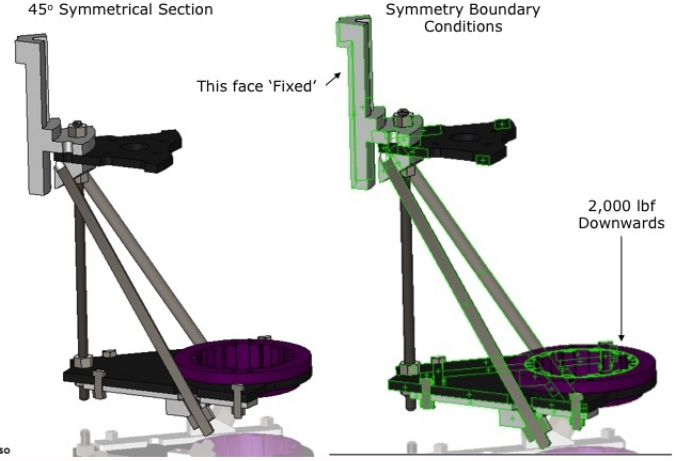

Dynamic Assy FEA

All Hardware is Grade 5 or equivalent (90ksi Yield)

Splines & Stiffening Plates 4140/4340 (60ksi Yield)

Large Plates 6061-T6 Aluminum (40ksi Yield)

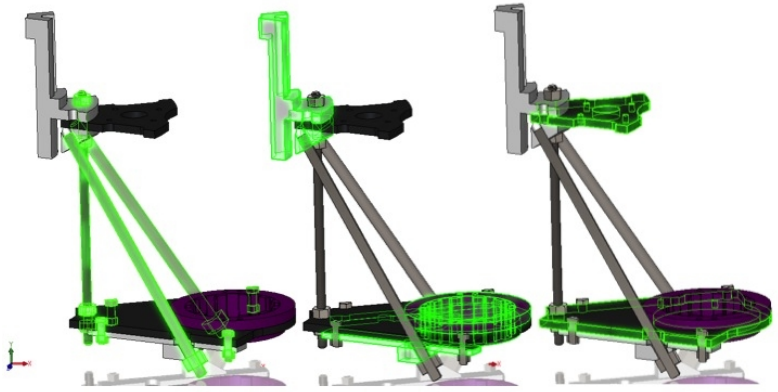

Dynamic Assy FEA

.125" Tetrahedral Mesh

All Connections 'Bonded'
206k Total Elements

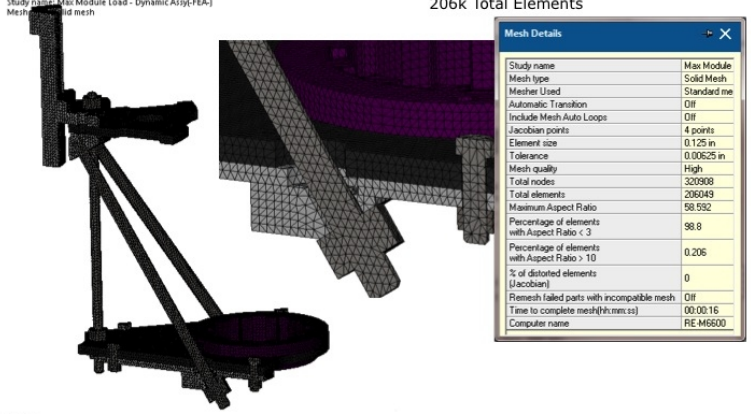

PPT ISO

Dynamic Assy FEA

Von Mises Stress Distribution

Factor of Safety Distribution (Yield)

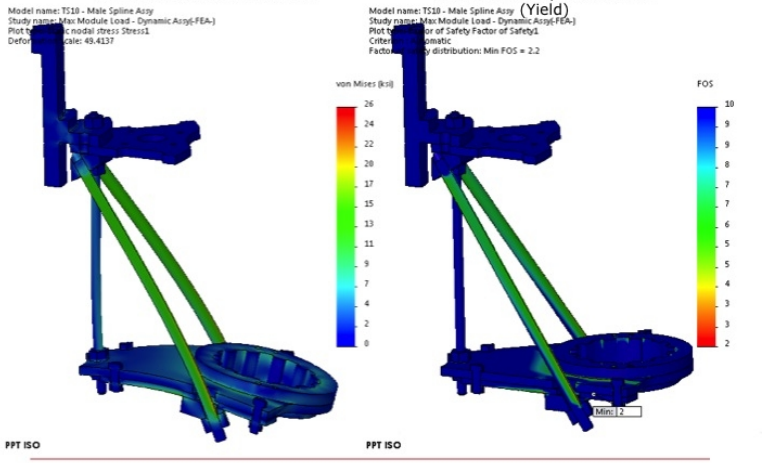

PPT ISO PPT ISO

Dynamic Assy FEA

Von Mises Stress Distribution

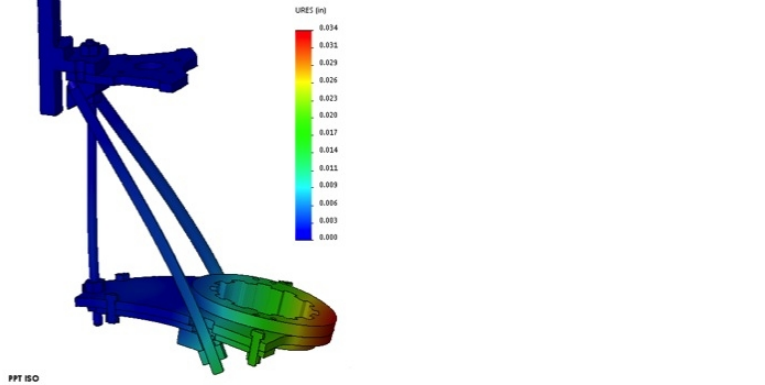

PPT ISO

Dynamic Assy FEA

Areas with Factor of Safety (FOS) > 3.0

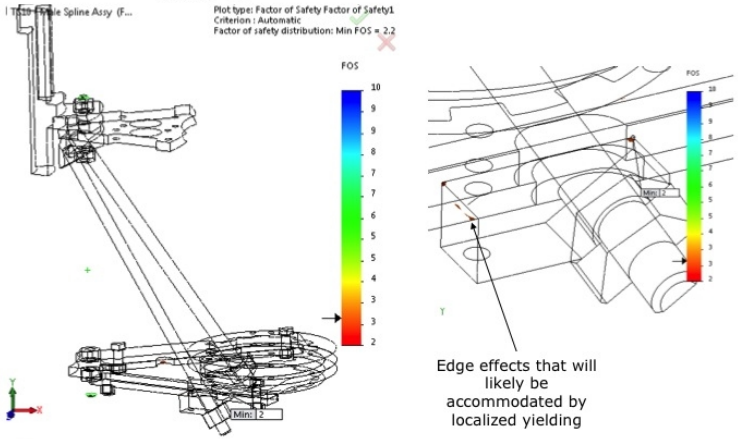

Bolted Spline Assembly Updates

- The male & female splines were revised to be bolted assembles to reduce cost and improve manufacturing lead-times.

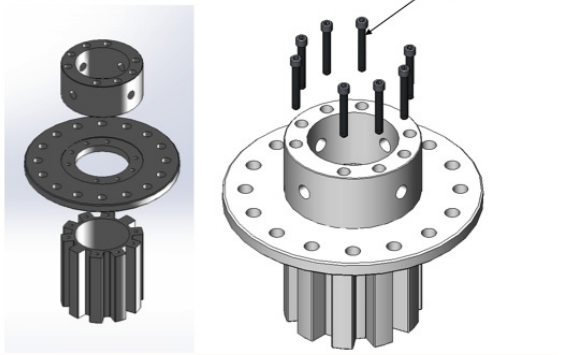

Bolted Spline Assembly Updates

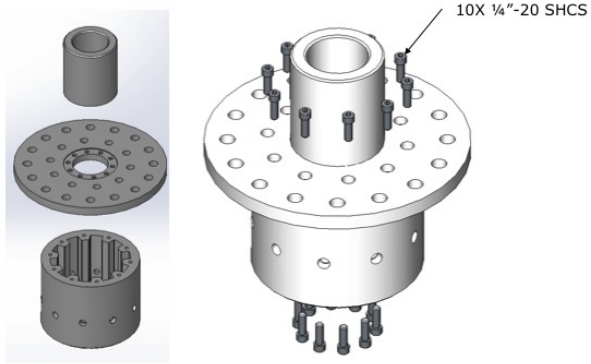

MR Damper Provision

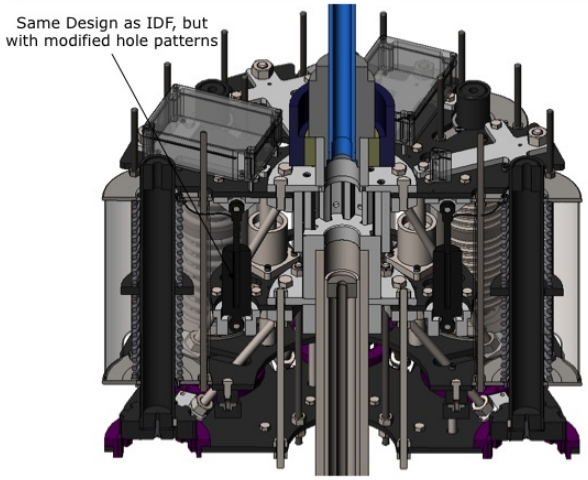

Electronics

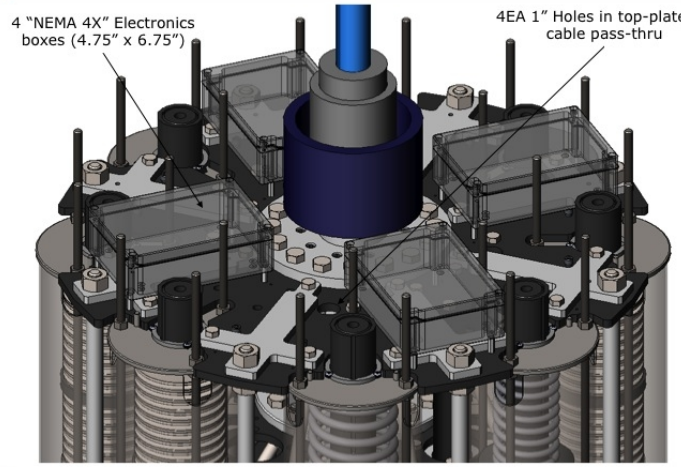

Electronics

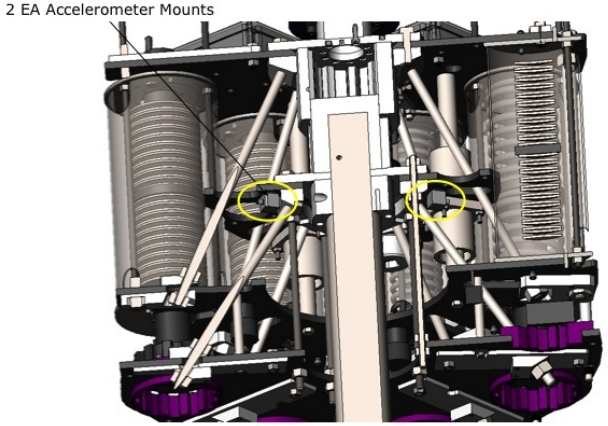

Travel Limiting System

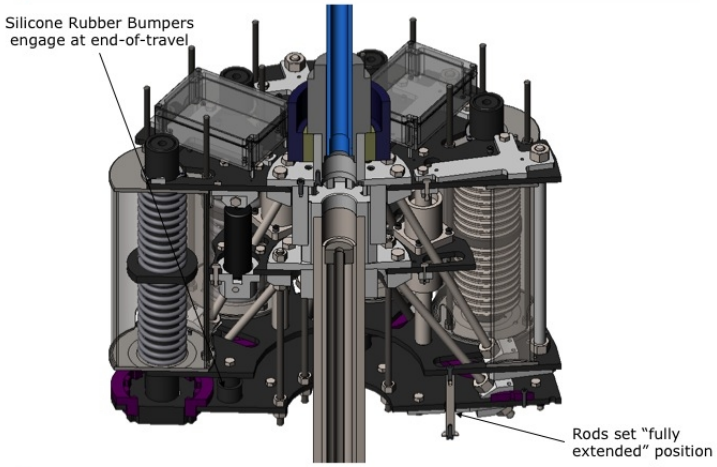

"Rigid Link"

A "Rigid Link" between the Rigid and Dynamic assemblies is formed by a steel sleeve of the appropriate length that is fastened by a 3/8" bolt. The assembly can accommodate 16 connections.

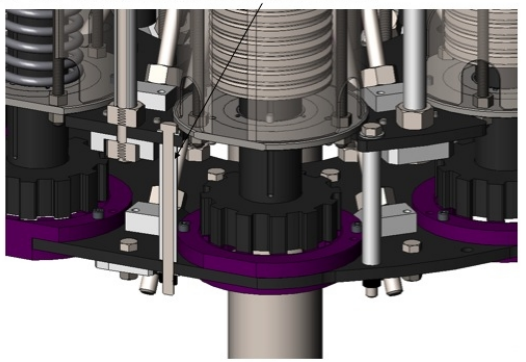

VRSF Section View

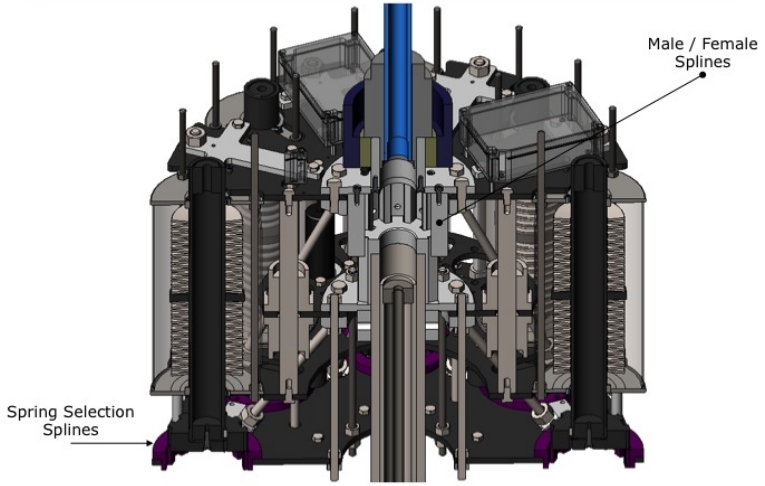

Preloaded Spring Module

Spring Envelope:	2" ID *(min)*	4" OD *(max)*	6.0" Pre-Loaded Length *(max)*

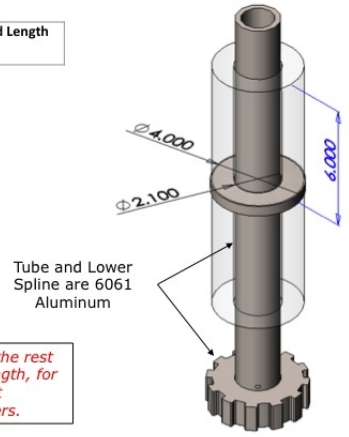

The Spring Envelope represents a constraint on the rest of the system. Allowing a greater pre-loaded length, for example, increases the overall system height but increases the options available for spring members.

Preloaded Spring Module

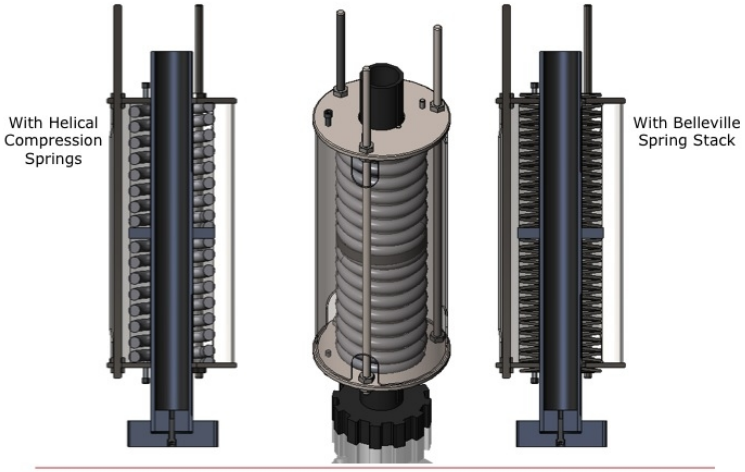

Preloaded Spring Module

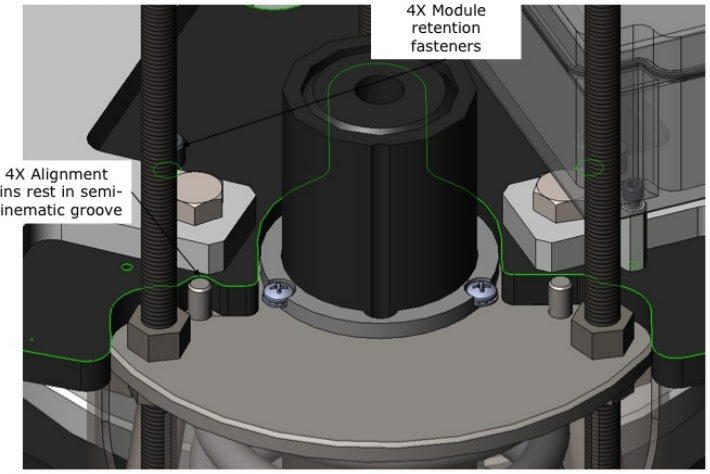

Preloaded Spring Module

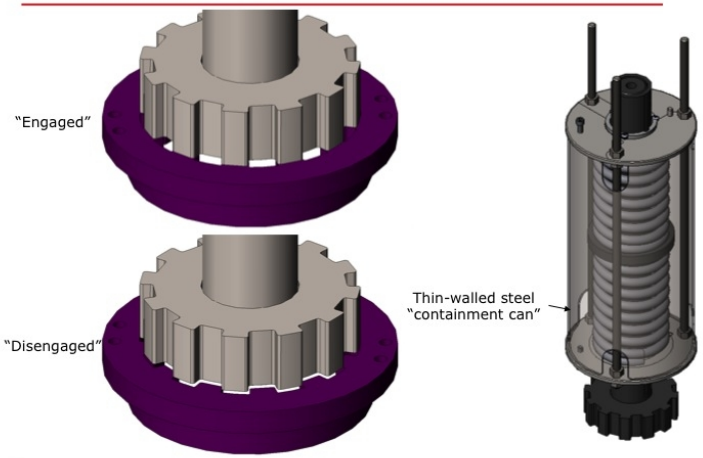

Preloaded Spring Module

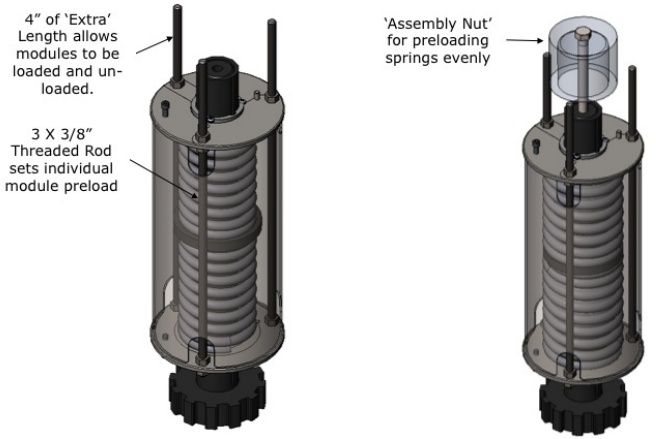

Preloaded Spring Module

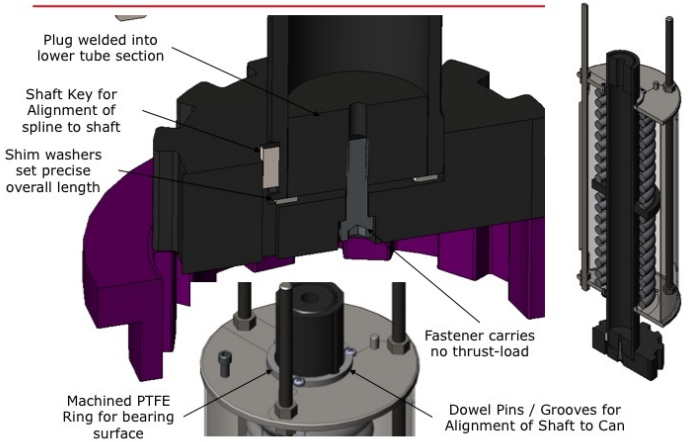

Spring Module FEA

- In Progress

Spring Module Top Plate FEA

Since the full analysis of the spring module is in-progress, an intermediate analysis was performed on just the top plate.

Material: 1020 Steel – 60 ksi Yield

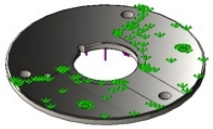

Nodes in contact with 3/8" Aluminum Plate set to 'Fixed'

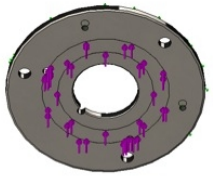

2,000 lbf Load Applied to Spring contact area.

*Isometric

Spring Module Top Plate FEA

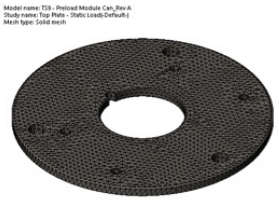

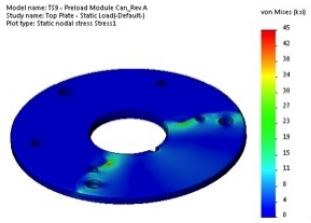

Mesh Details

Study name	Top Plate - Static Load (-Default-)
Mesh type	Solid Mesh
Mesher Used	Standard mesh
Automatic Transition	Off
Include Mesh Auto Loops	Off
Jacobian points	4 points
Element size	0.125 in
Tolerance	0.00625979 in
Mesh quality	High
Total nodes	43632
Total elements	26296
Maximum Aspect Ratio	8.238
Percentage of elements with Aspect Ratio < 3	99.2
Percentage of elements with Aspect Ratio > 10	0
% of distorted elements (Jacobian)	0
Time to complete mesh(hh:mm:ss)	00:00:02
Computer name	RE-M6600

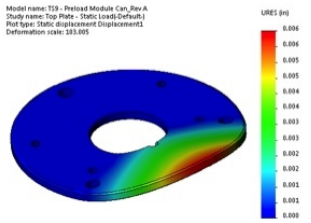

Spring Modules

Module #	Module Spring Rate (lbf/in)	Individual Spring Rate k_(1 of 4) (lbf/in)		Max δ (in)	Requried Spring Defl.
1	300	75		2.00	4.00
2	600	150		2.00	4.00
3	1200	300		2.00	4.00
4	2400	600		1.67	3.33
5	4800	1200		0.83	1.67
5b	6000	1500		0.67	1.33
All (a)	9000			0.44	0.89
All (b)	14400			0.28	0.56

Symbol	Value	Unit	Note	Equation
WoB_(Max)=	4000	lbf		
X_(Max)=	2	in		

Spring Modules

Module #1 Module #2 Module #3 Module #4 Module #5 Module #5b

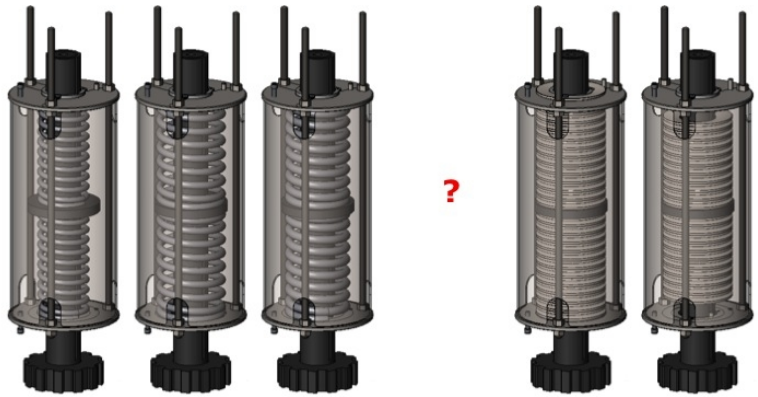

?

Module #1 – Coil Spring

Module #	if k_{min} = 300 lbf/in	k_{1 of 4} (lbf/in)
1	300	75
2	600	150
3	1200	300
4	2400	600
5	4800	1200
5b	6000	1500
All (a)	9000	
All (b)	14400	

Century Spring Stock#73187
$31.02 Each
(In stock as of Jan 28, 2015)

We slightly exceed the "suggested" maximum deflection, but don't exceed the "Solid Length"

Select	CAD	CSC Stock #	OD (in)	ID (in)	Free Length (in)	Rate (lbs/in)	Sugg. Max Defl (in)	Sugg. Max Load (lbs)	Solid Length (in)	Wire Dia. (in)	Total Coils	Material	Ends	Finish
		73180	2.906	2.344	7.000	62.000	3.700	230.000	2.810	0.281	9.990	Oil Tempered	Closed Ground	None
		73187	2.906	2.282	8.000	84.000	3.600	304.000	3.520	0.312	11.300	Oil Tempered	Closed Ground	None

Module #2 – Coil Spring

Module #	if k_{min} = 300 lbf/in	k_{1 of 4} (lbf/in)
1	300	75
2	600	150
3	1200	300
4	2400	600
5	4800	1200
5b	6000	1500
All (a)	9000	
All (b)	14400	

Century Spring Stock#73436
$35.73 Each
(In stock as of Jan 28, 2015)

We slightly exceed the "suggested" maximum deflection, but don't exceed the "Solid Length"

Select	CAD	CSC Stock #	OD (in)	ID (in)	Free Length (in)	Rate (lbs/in)	Sugg. Max Defl (in)	Sugg. Max Load (lbs)	Solid Length (in)	Wire Dia. (in)	Total Coils	Material	Ends	Finish
		73436	3.906	3.094	8.000	136.000	3.500	477.000	3.530	0.406	8.700	Oil Tempered	Closed Ground	None
		73206	2.906	2.156	10.000	143.000	3.600	509.000	5.350	0.375	14.300	Oil Tempered	Closed Ground	None

Module #3 – Coil Spring

Module #	if k_{min} = 300 lbf/in	k_{1 of 4} (lbf/in)
1	300	75
2	600	150
3	1200	300
4	2400	600
5	4800	1200
5b	6000	1500
All (a)	9000	
All (b)	14400	

Century Spring Stock#73436
$37.28 Each
(In stock as of Jan 28, 2015)

7 items found

Select	CAD	CSC Stock #	OD (in)	ID (in)	Free Length (in)	Rate (lbs/in)	Sugg. Max Defl (in)	Sugg. Max Load (lbs)	Solid Length (in)	Wire Dia. (in)	Total Coils	Material	Ends	Finish
		73206	2.906	2.156	10.000	92.000	2.600	266.000	5.350	0.375	14.300	Oil Tempered	Closed Ground	None
CALL		73454	3.906	2.906	8.000	325.000	2.500	824.000	4.500	0.500	9.000	Oil Tempered	Closed Ground	None

This spring doesn't provide the full 4" inches of required travel, but it does come close.

5 items found

Select	CAD	CSC Stock #	OD (in)	ID (in)	Free Length (in)	Rate (lbs/in)	Sugg. Max Defl (in)	Sugg. Max Load (lbs)	Solid Length (in)	Wire Dia. (in)	Total Coils	Material	Ends	Finish
CALL		73550	4.406	3.406	8.000	251.000	2.900	737.000	4.000 ?!?	0.500	8.010	Oil Tempered	Closed Ground	None
CALL		CUSTOM	~4.406	~3.406	8.000	300.00	2.900	737.000	3.75 ?	0.500	8.010	Oil Tempered	Closed Ground	None
CALL		73514	4.156	3.156	8.000	278.000	2.800	778.000	4.310	0.500	8.630	Oil Tempered	Closed Ground	None
		73556	4.406	3.344	8.000	327.000	2.700	879.000	4.250	0.531	8.010	Oil Tempered	Closed Ground	None
		73394	3.656	2.720	8.000	292.000	2.600	750.000	4.350	0.468	9.300	Oil Tempered	Closed Ground	None
CALL		73454	3.906	2.906	8.000	325.000	2.500	824.000	4.500	0.500	9.000	Oil Tempered	Closed Ground	None

Going up to 4.5" OD adds some other options that might be worth considering.

Module #4 – Coil Spring

Module #	if k_{min} = 300 lbf/in	k_{1 of 4} (lbf/in)
1	300	75
2	600	150
3	1200	300
4	2400	600
5	4800	1200
All	9300	

Currently working with Century Spring to identify a **custom spring** that will satisfy all of our requirements.

Belleville options for Stack #4 **are prohibited** by the requirement to have ~3.3in of travel.

NOTE:
- If ho/t is limited to ~ 1.0 and reasonable thicknesses are ~3.0mm
- Using only the 20%-80% deflection range gives us 2mm of travel per spring
- 3.3in [84.5mm] 85mm / 2mm = ~40 springs single-stacked.
- 30 Springs single stacked will be about 40*6mm = 240mm [9.45in]

Module #5 - Belleville

Disk Spring Geometry

Label	Value	Units	Note	English Units
D_e	100	mm	Outer diameter	3.937 in
D_i	51	mm	inner diameter	2.008 in
t	3.5	mm	material thickness	0.138 in
	1		Desired ho/t	
l_o	6.3	mm	Overall height	0.248 in
h_o	2.8	mm	Available deflection	0.110 in
	1.13%		Strain Limit	
Spring Material	51 CrV 4	206000	MPa	

$h_o = l_o - t$

Disk Spring Stack Geometry

Label	Value	Units	Note	English Units
	43.18	mm	Desired Total Stack defl.	1.7 in
	9074	N	Desired Load at 80% defl.	2040 lbf
	9019	N	Predicted Load @ 80% defl.	2028 lbf
			Desired Spring Rate	1.2 kip/in
	8	%	Tolerance Preload	0.83 in
	26	25.702	Springs Required in series (mu	21.16658 mm
	1	1.006	Springs required in parallel (multiplies LOAD)	
	26		# of Springs in stack	
	94	mm	Single Series Stack Height	3.69 in
	163.8	**mm**	**Total Stack Height**	**6.45 in**
	93.2	mm	Grip length (20% Preload)	
	91.6	mm	Deflection Limiter (80% Travel)	

Module #5 - Belleville

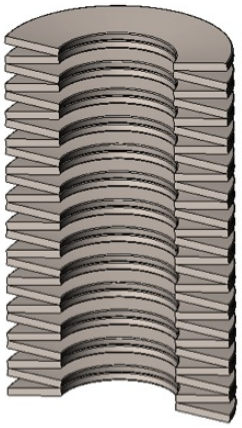

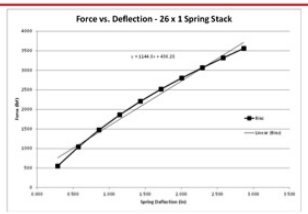

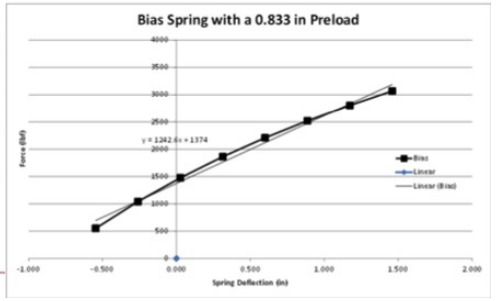

Module #5b - Belleville

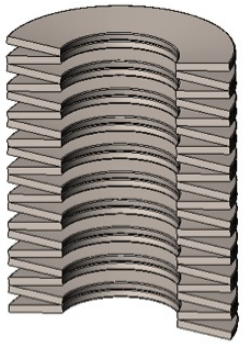

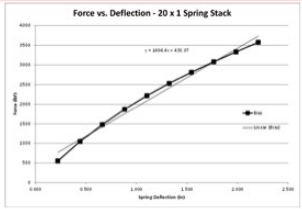

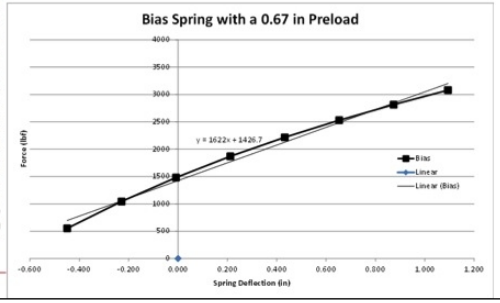

Module #5b - Belleville

Disk Spring Geometry

Label	Value	Units	Note	English Units
D_e	100	mm	Outer diameter	3.937 in
D_i	51	mm	inner diameter	2.008 in
t	3.5	mm	material thickness	0.138 in
	1		Desired ho/t	
l_o	6.3	mm	Overall height	0.248 in
h_o	2.8	mm	Available deflection	0.110 in
	1.13%		Strain Limit	
Spring Material	Key 6150	206842	MPa	

$h_o = l_o - t$

Disk Spring Stack Geometry

Label	Value	Units	Note	English Units
	33.73	mm	Desired Total Stack defl.	1.328 in
	9068	N	Desired Load at 80% defl.	2038 lbf
	9056	N	Predicted Load @ 80% defl.	2036 lbf
			Desired Spring Rate	1.535 kip/in
	8	%	Tolerance Preload	0.67 in
	20	20.078	Springs Required in series (mu	17.018 mm
	1	1.001	Springs required in parallel (multiplies LOAD)	
	20		# of Springs in stack	
	73	mm	Single Series Stack Height	2.87 in
	126.0	**mm**	**Total Stack Height**	**4.96 in**
	72.2	mm	Grip length (20% Preload)	
	70.6	mm	Deflection Limiter (80% Travel)	

This SAME Disk Spring Stack is a good fit for the #5b Module too:
The only difference is using 20 springs in a stack instead of 26

APPENDIX I. ULTERRA BIT RIGID DRILLSTRING TESTING

This page intentionally left blank.

Four-Blade Bit (Sierra White Granite)

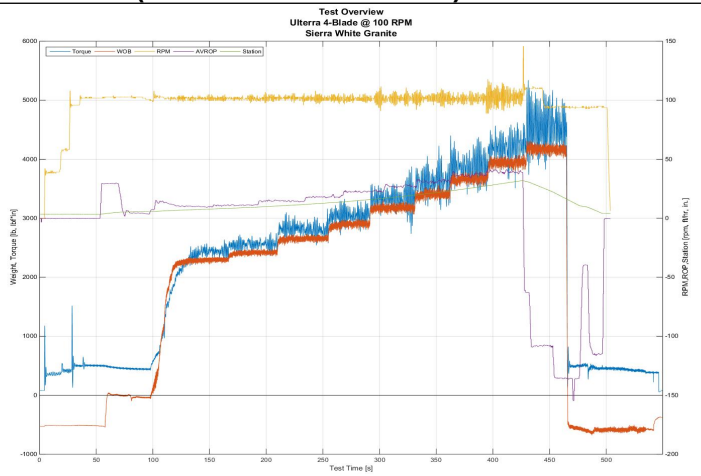

Figure I-1. Test overview for 4-blade bit in Sierra White Granite at 100 [rpm] (Test1_072215_1351_1).

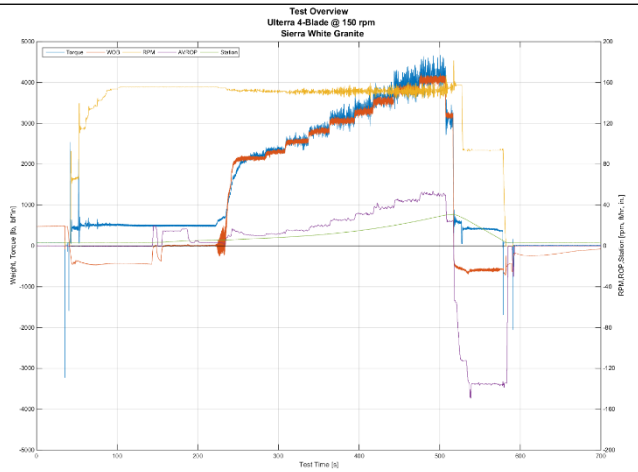

Figure I-2. Test overview for 4-blade bit in Sierra White Granite at 150 [rpm] (Test2_072215_1425_1).

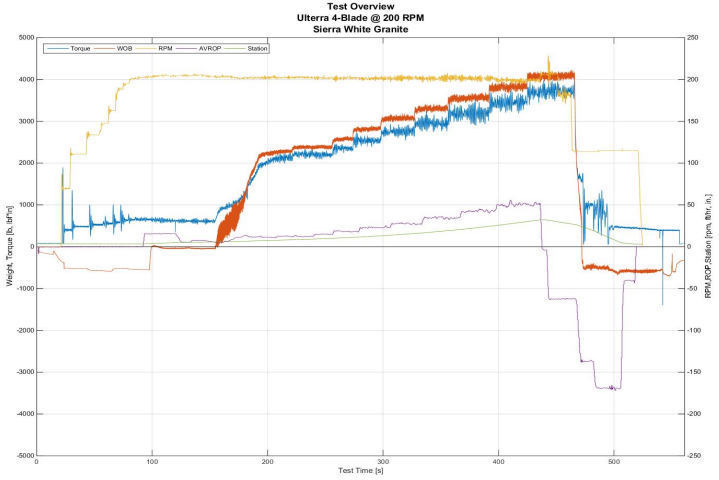

Figure I-3. Test overview for 4-blade bit in Sierra White Granite at 200 [rpm] (Test1_072315_1443_1).

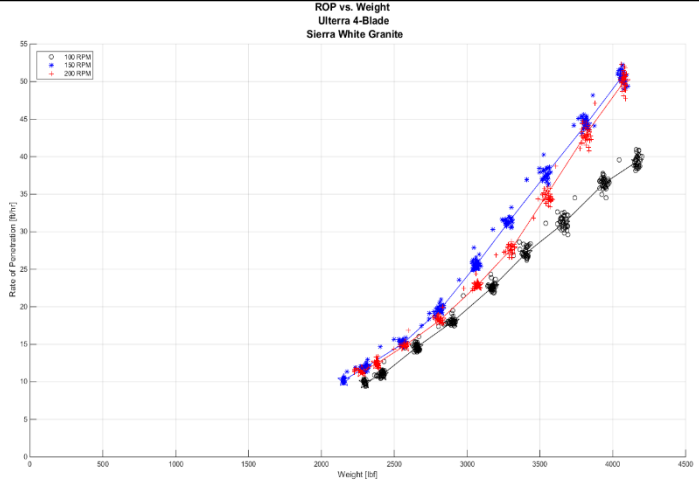

Figure I-4. ROP vs. WOB for 4-blade bit in Sierra White Granite.

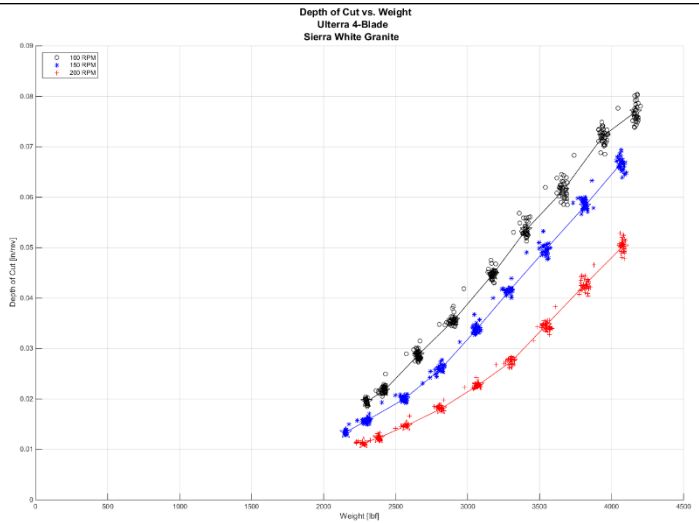

Figure I-5. Depth of cut vs. WOB for 4-blade bit in Sierra White Granite.

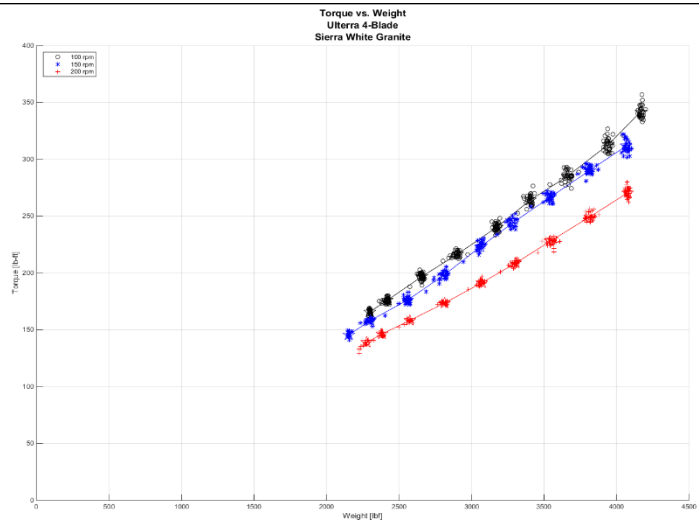

Figure I-6. Torque vs. WOB for 4-blade bit in Sierra White Granite.

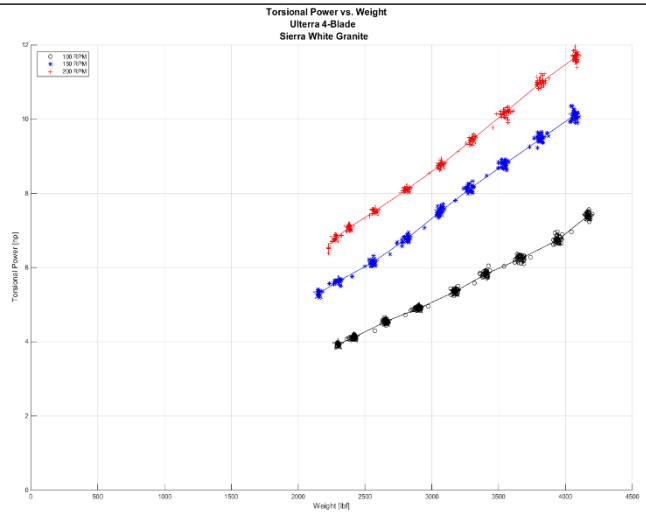

Figure I-7. Torsional power vs. WOB for 4-blade bit in Sierra White Granite.

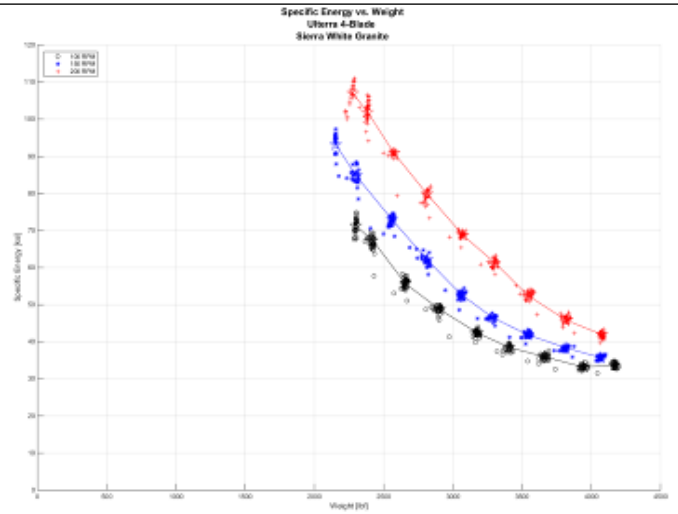

Figure I-8. Specific energy vs. WOB for 4-blade bit in Sierra White Granite.

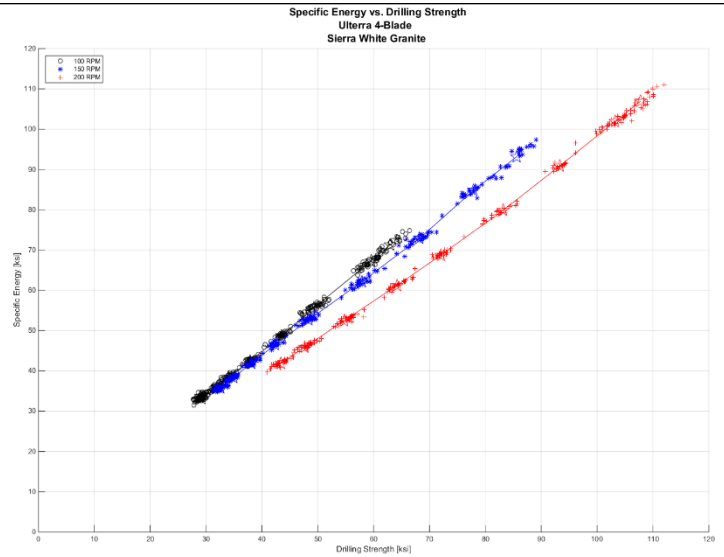

Figure I-9. Specific energy vs. drilling strength for 4-blade bit in Sierra White Granite.

Five-Blade Bit (Sierra White Granite)

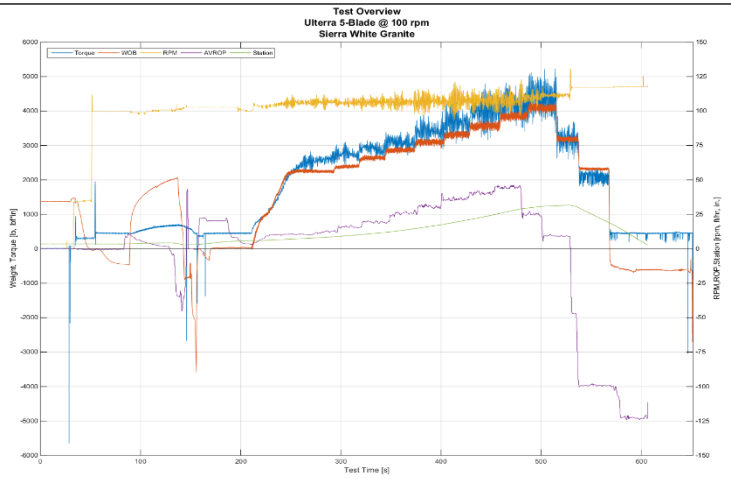

Figure I-10. Test overview for 5-blade bit in Sierra White Granite at 100 [rpm] (Test1_072415_1322_1).

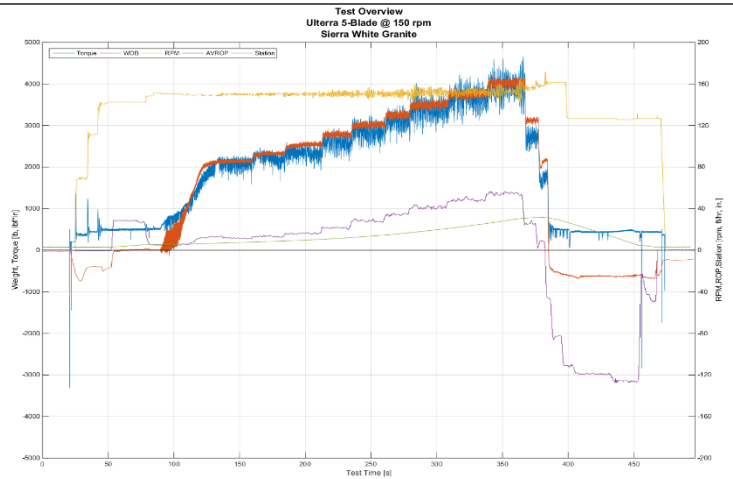

Figure I-11. Test overview for 5-blade bit in Sierra White Granite at 150 [rpm] (Test2_072415_1344_1).

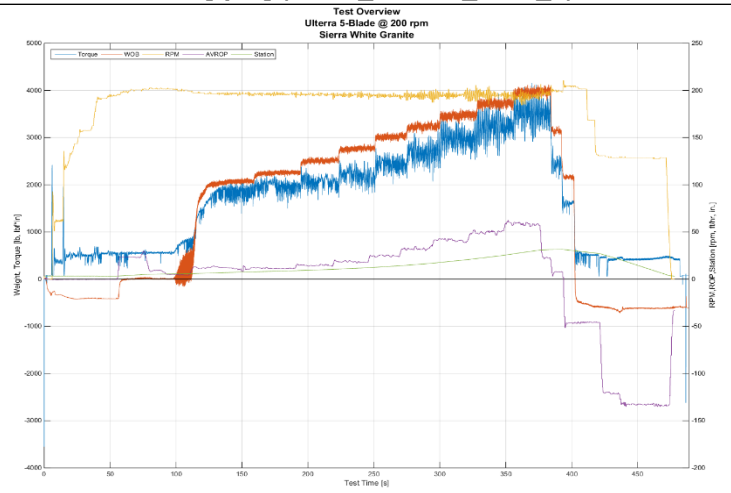

Figure I-12. Test overview for 5-blade bit in Sierra White Granite at 200 [rpm] (Test3_072415_1401_1).

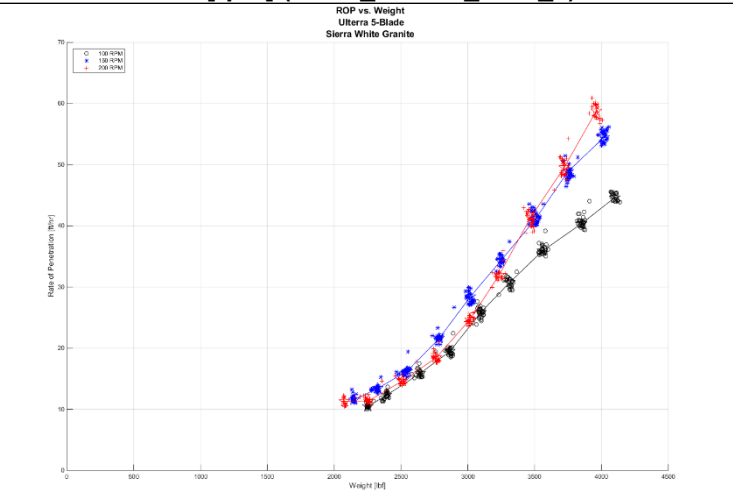

Figure I-13. ROP vs. WOB for 5-blade bit in Sierra White Granite.

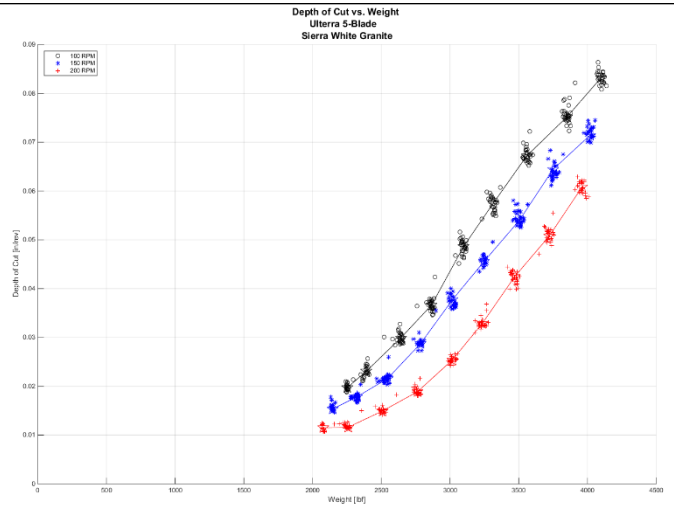

Figure I-14. Depth of cut vs. WOB for 5-blade bit in Sierra White Granite.

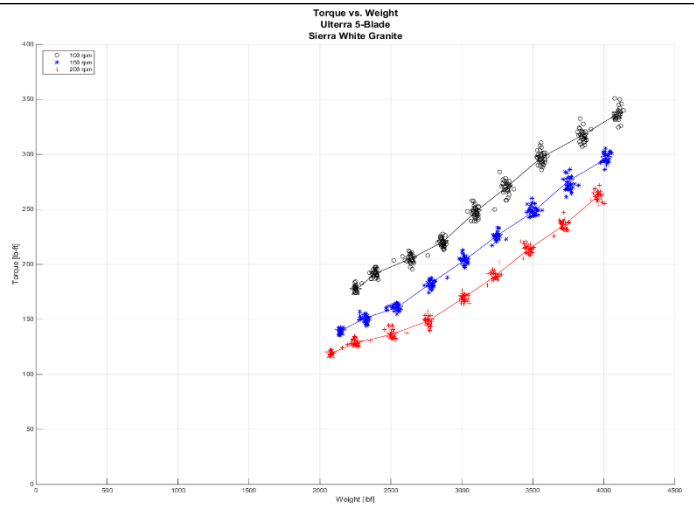

Figure I-15. Torque vs. WOB for 5-blade bit in Sierra White Granite.

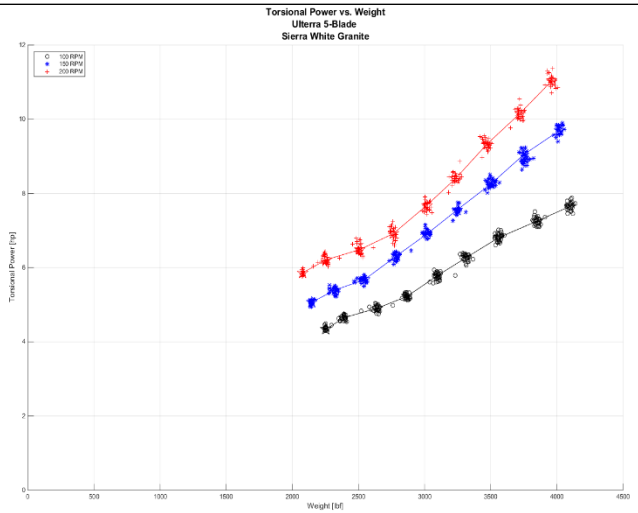

Figure I-16. Torsional power vs. WOB for 5-blade bit in Sierra White Granite.

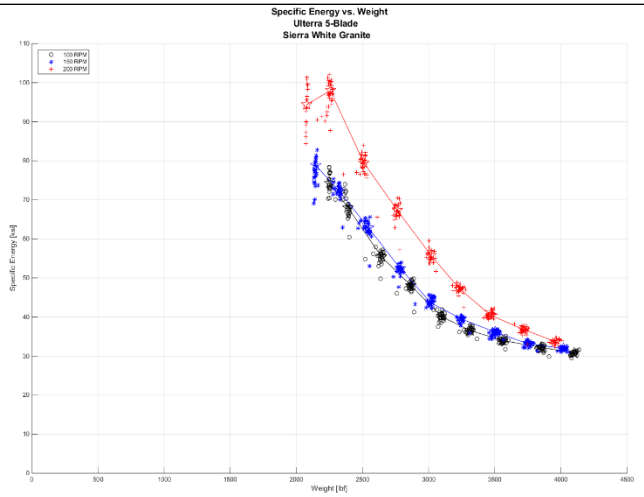

Figure I-17. Specific energy vs. WOB for 5-blade bit in Sierra White Granite.

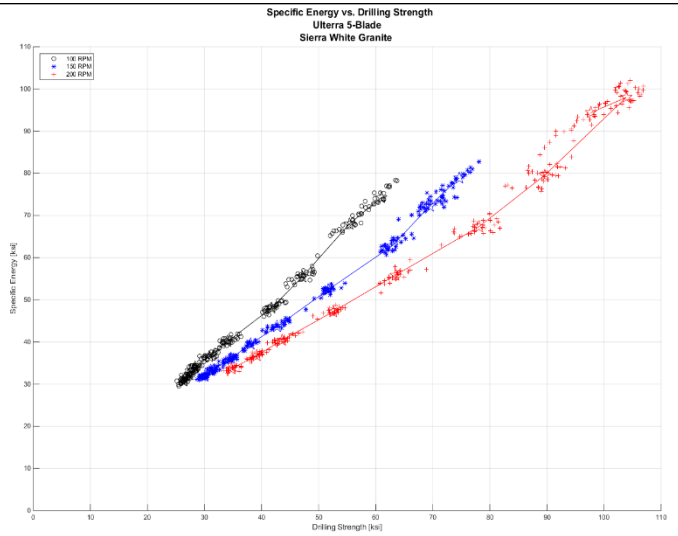

Figure I-18. Specific energy vs. drilling strength for 5-blade bit in Sierra White Granite.

Four-Blade Bit (Berea Sandstone)

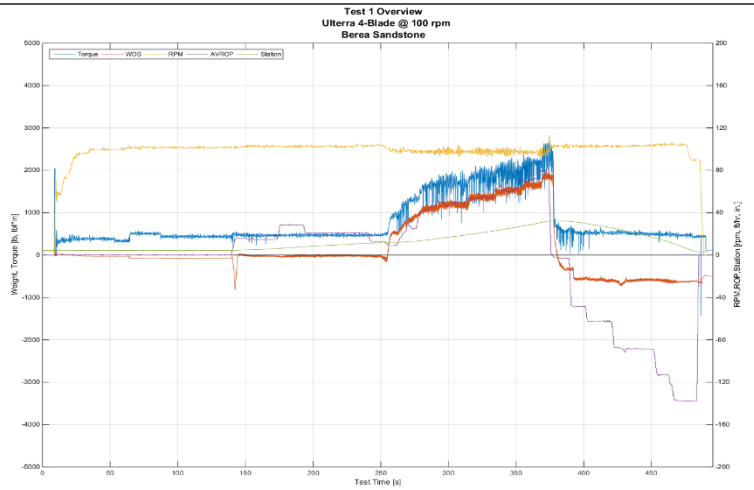

Figure I-19. Test 1 overview for 4-blade bit in Berea Sandstone at 100 [rpm] (Test1_080315_1329_1).

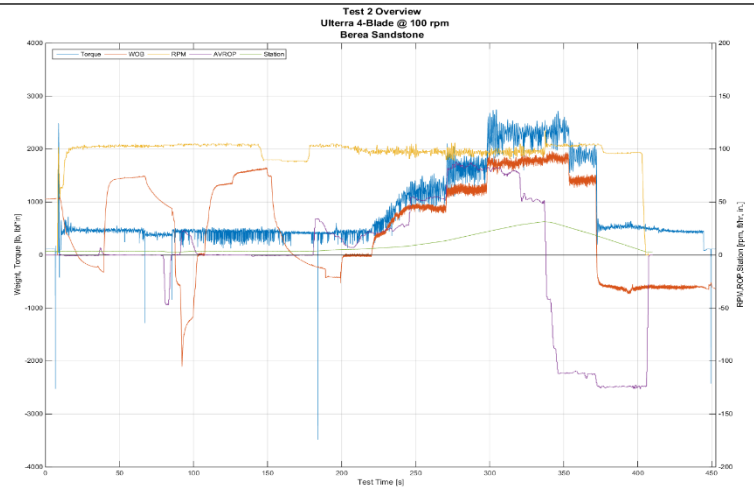

Figure I-20. Test 2 overview for 4-blade bit in Berea Sandstone at 100 [rpm] (Test3_080315_1423_1).

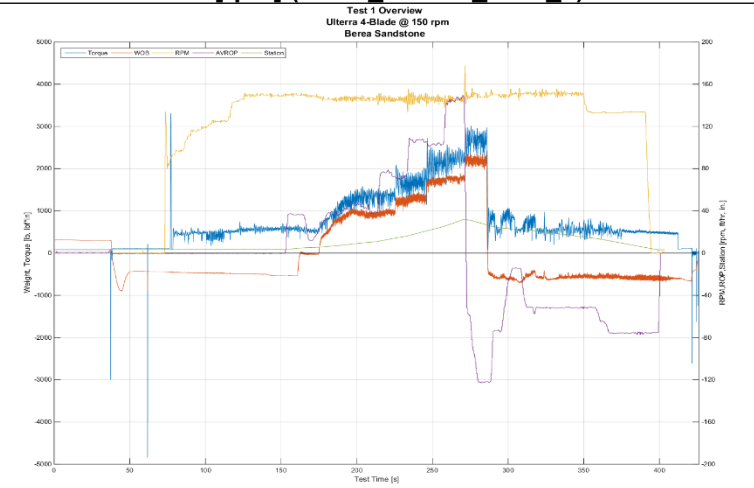

Figure I-21. Test 1 overview for 4-blade bit in Berea Sandstone at 150 [rpm] (Test5_080315_1447_1).

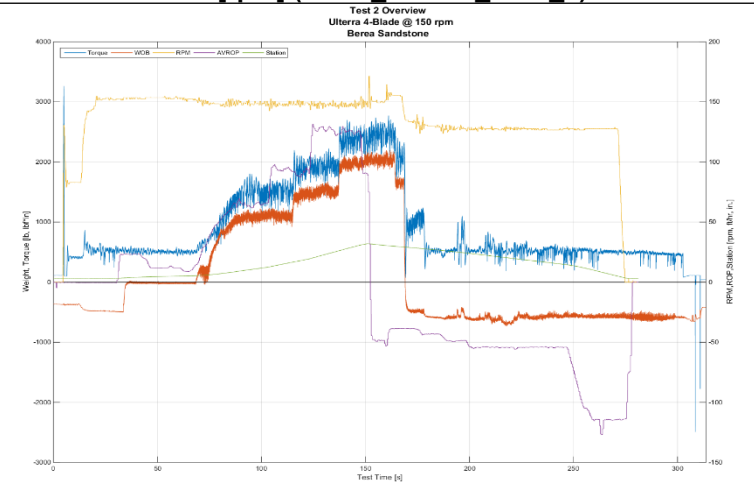

Figure I-22. Test 2 overview for 4-blade bit in Berea Sandstone at 150 [rpm] (Test6_080315_1503_1).

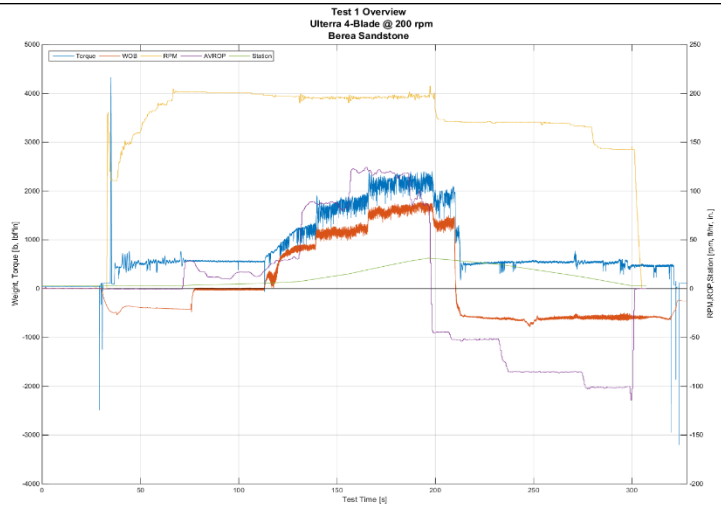

Figure I-23. Test 1 overview for 4-blade bit in Berea Sandstone at 200 [rpm] (Test7_080315_1514_1).

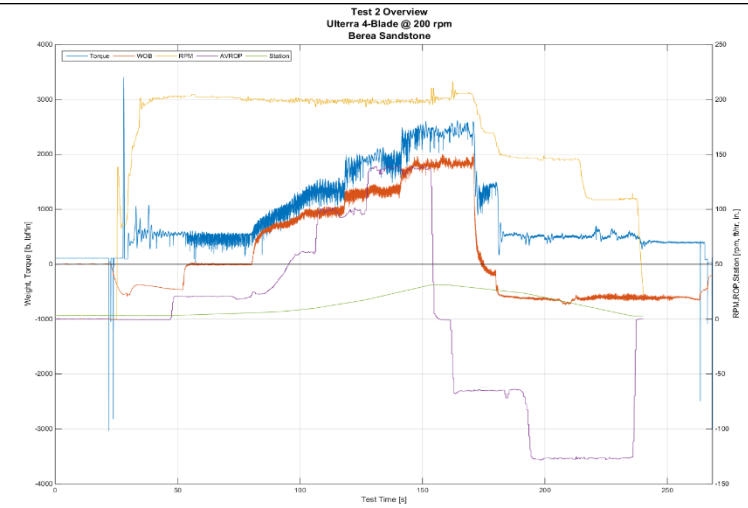

Figure I-24. Test 2 overview for 4-blade bit in Berea Sandstone at 200 [rpm] (Test8_080315_1525_1).

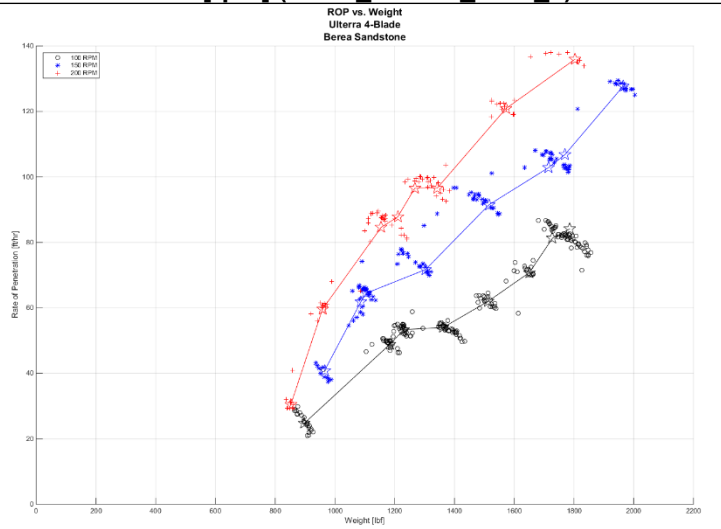

Figure I-25. ROP vs. WOB for 4-blade bit in Berea Sandstone.

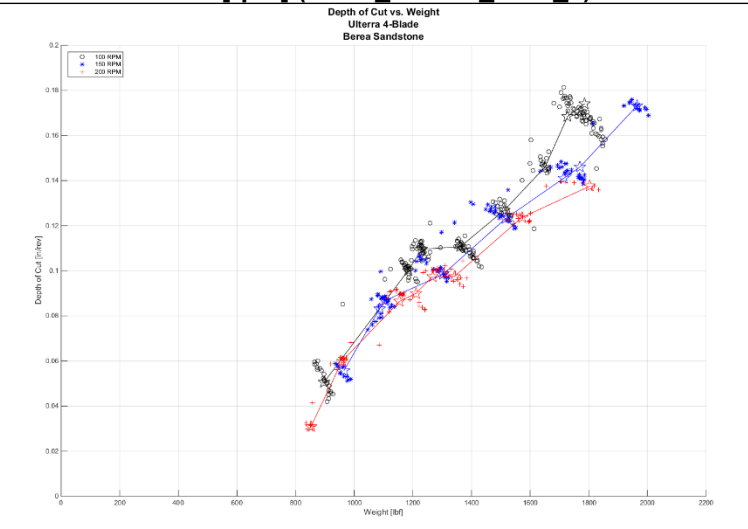

Figure I-26. Depth-of-cut vs. WOB for 4-blade bit in Berea Sandstone.

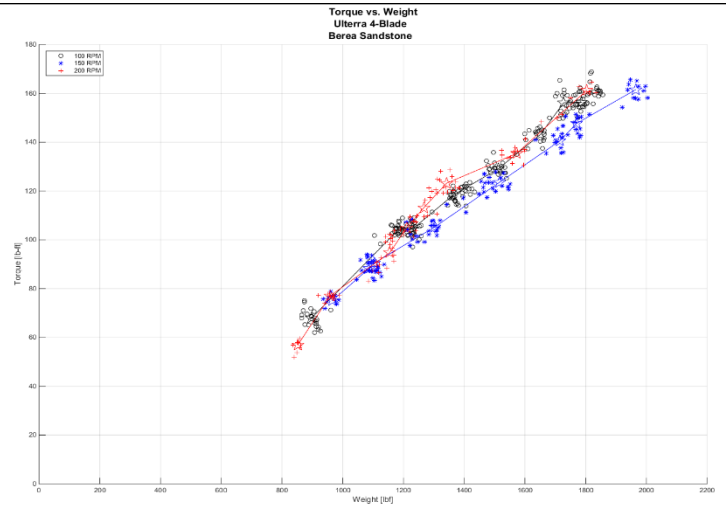

Figure I-27. Torque vs. WOB for 4-blade bit in Berea Sandstone.

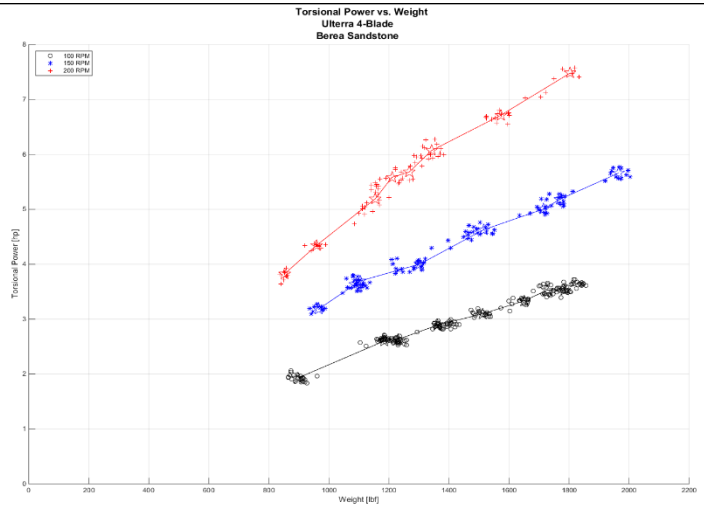

Figure I-28. Torsional power vs. WOB for 4-blade bit in Berea Sandstone.

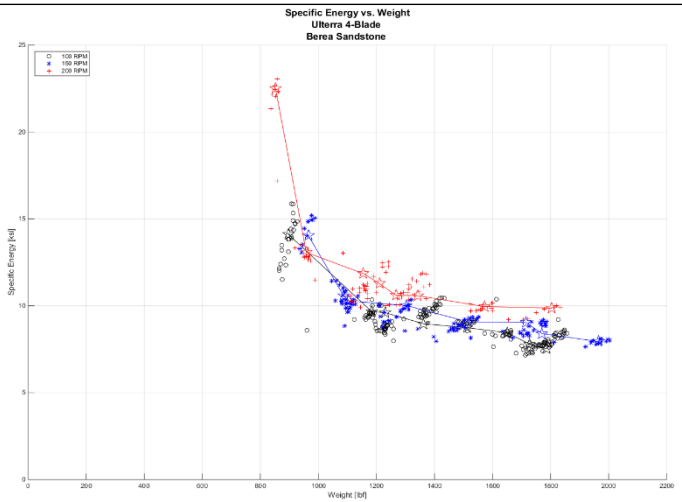

Figure I-29. Specific energy vs. WOB for 4-blade bit in Berea Sandstone.

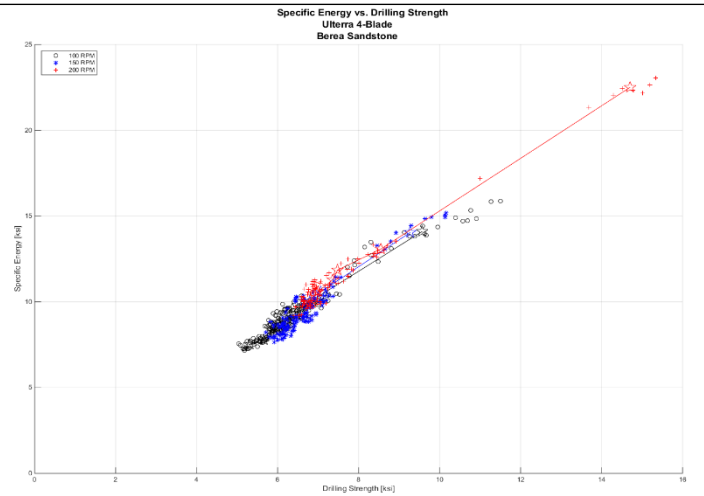

Figure I-30. Specific energy vs. drilling strength for 4-blade bit in Berea Sandstone.

Five-Blade Bit (Berea Sandstone)

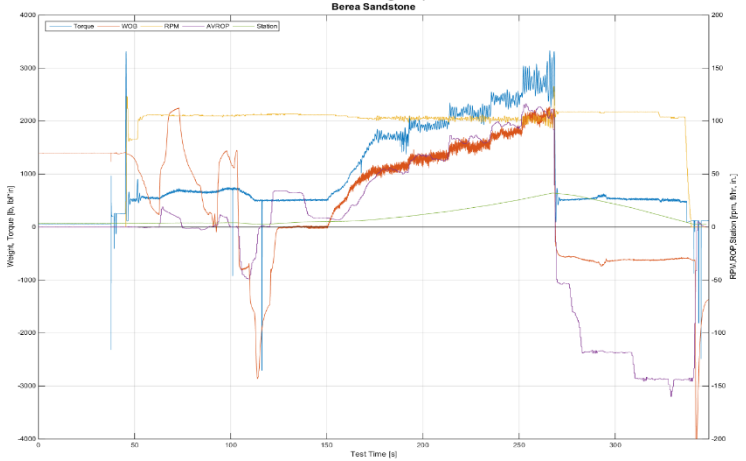

Figure I-31. Test overview for 5-blade bit in Berea Sandstone at 100 [rpm] (Test1_080415_1041_1).

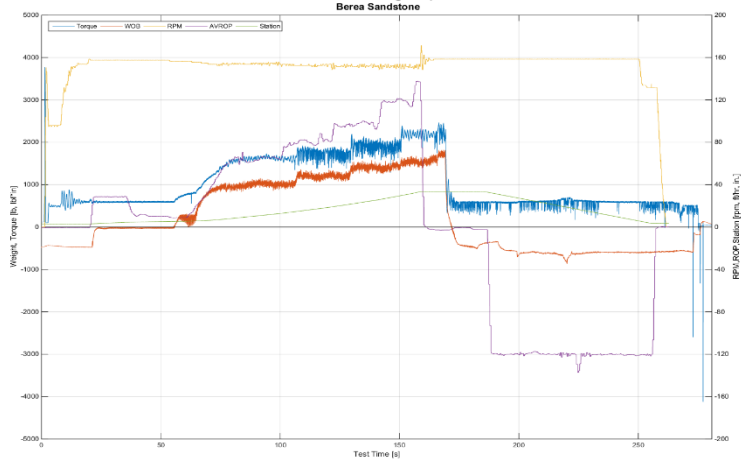

Figure I-32. Test 1 overview for 5-blade bit in Berea Sandstone at 150 [rpm] (Test2_080415_1102_1).

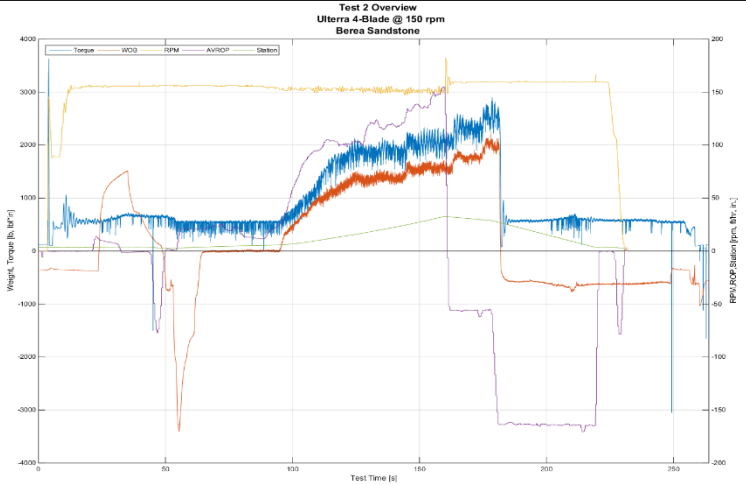

Figure I-33. Test 2 overview for 5-blade bit in Berea Sandstone at 150 [rpm] (Test3_080415_1114_1).

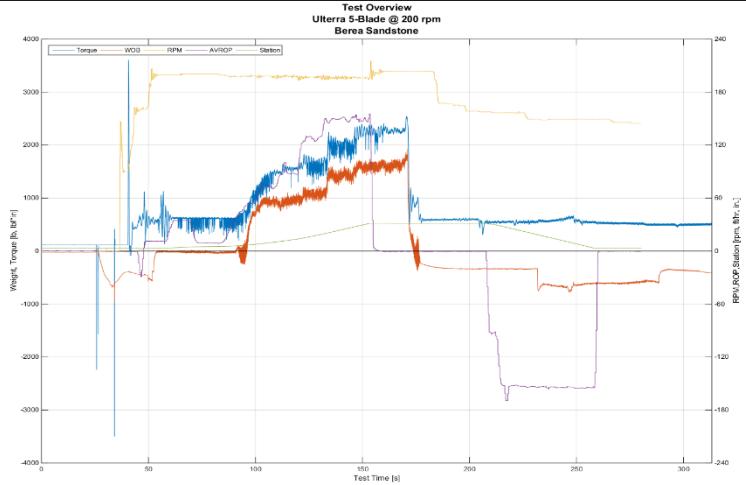

Figure I-34. Test overview for 5-blade bit in Berea Sandstone at 200 [rpm] (Test4_080415_1127_1).

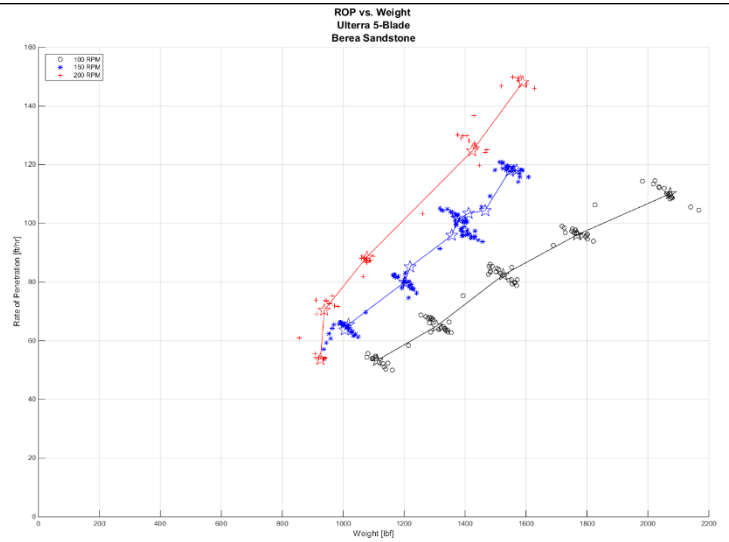

Figure I-35. ROP vs. WOB for 5-blade bit in Berea Sandstone.

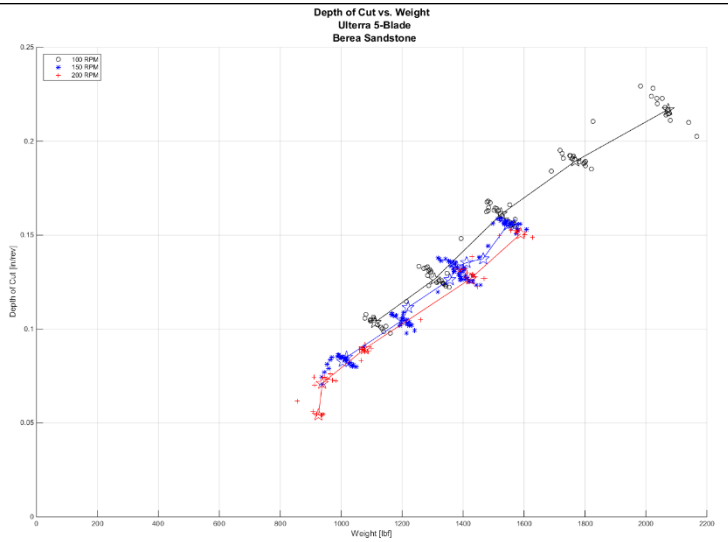

Figure I-36. Depth of cut vs. WOB for 5-blade bit in Berea Sandstone.

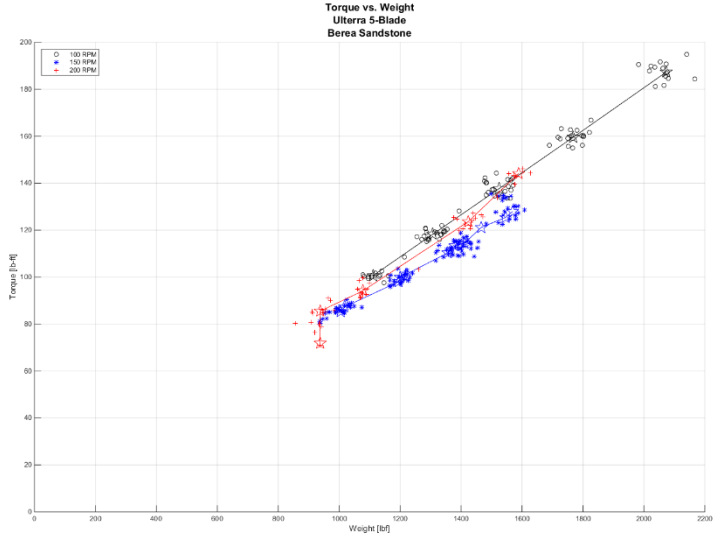

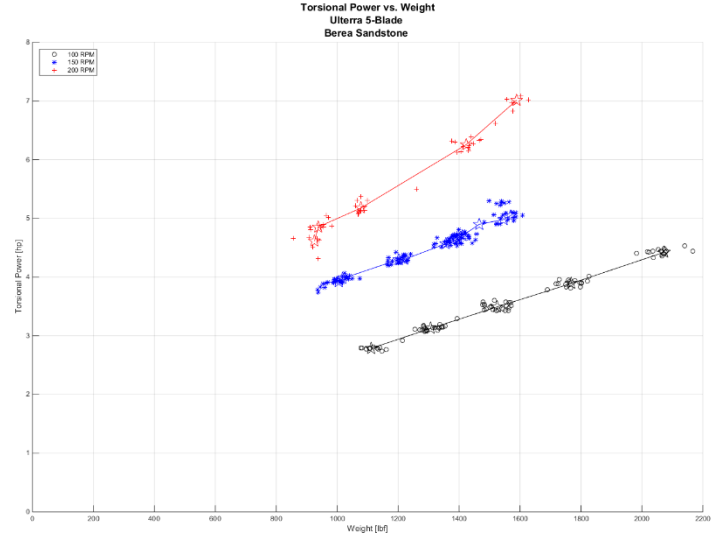

Figure I-37. Torque vs. WOB for 5-blade bit in Berea Sandstone.

Figure I-38. Torsional power vs. WOB for 5-blade bit in Berea Sandstone.

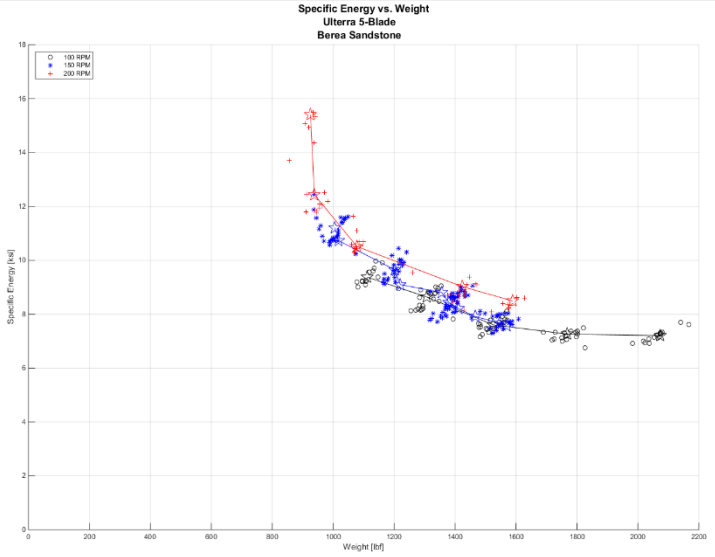

Figure I-39. Specific energy vs. WOB for 5-blade bit in Berea Sandstone.

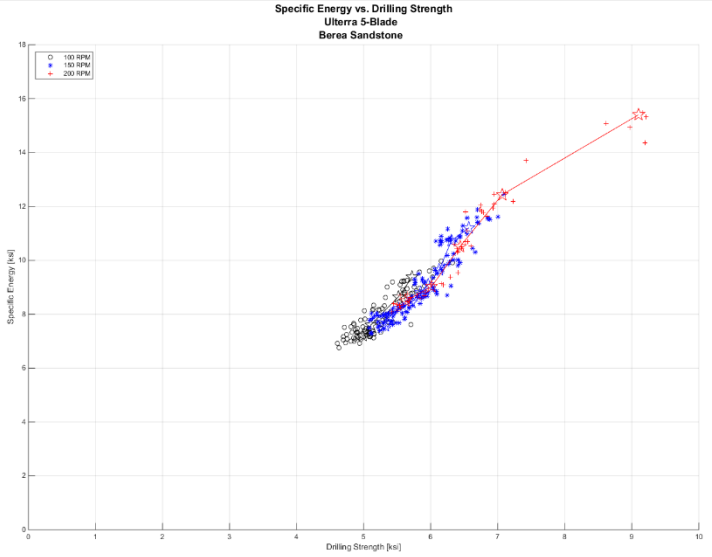

Figure I-40. Specific energy vs. drilling strength for 5-blade bit in Berea Sandstone.

Bit Comparison (Sierra White Granite)

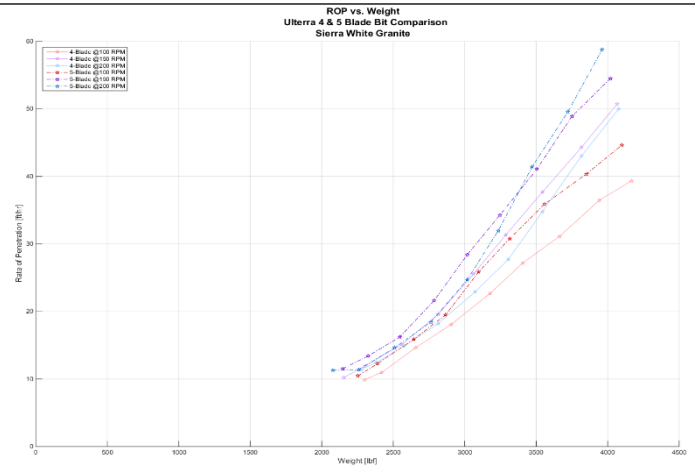

Figure I-41. ROP vs. WOB for 4 and 5 bladed bit tests in Sierra White Granite.

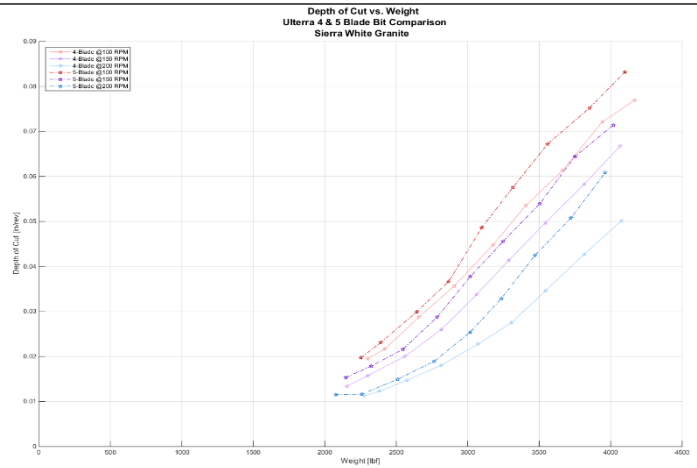

Figure I-42. Depth-of-cut vs. WOB for 4 and 5 bladed bit tests in Sierra White Granite.

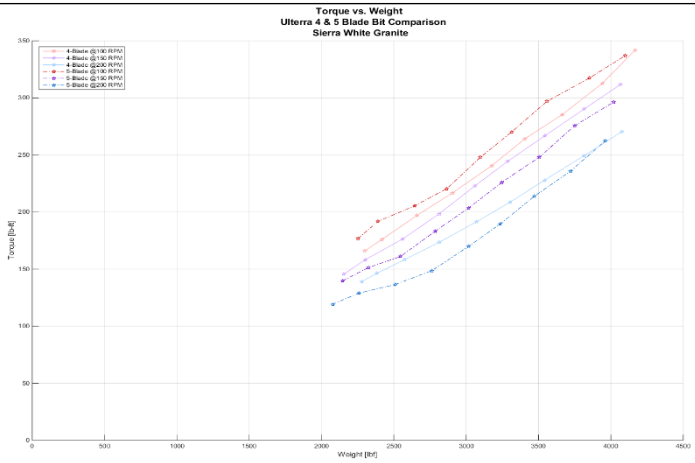

Figure I-43. Torque vs. WOB for 4 and 5 bladed bit tests in Sierra White Granite.

Bit Comparison (Berea Sandstone)

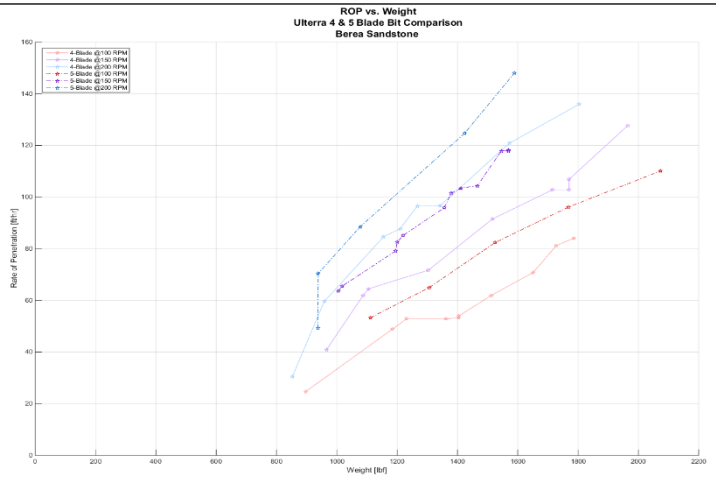

Figure I-44. ROP vs. WOB for 4 and 5 bladed bit tests in Berea Sandstone.

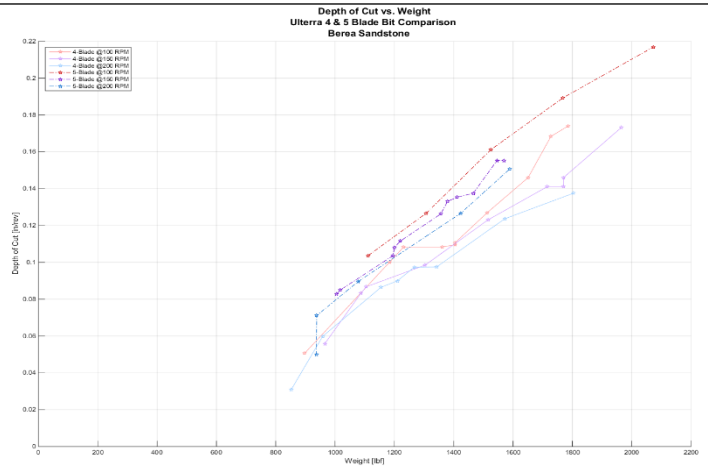

Figure I-45. Depth-of-cut vs. WOB for 4 and 5 bladed bit tests in Berea Sandstone.

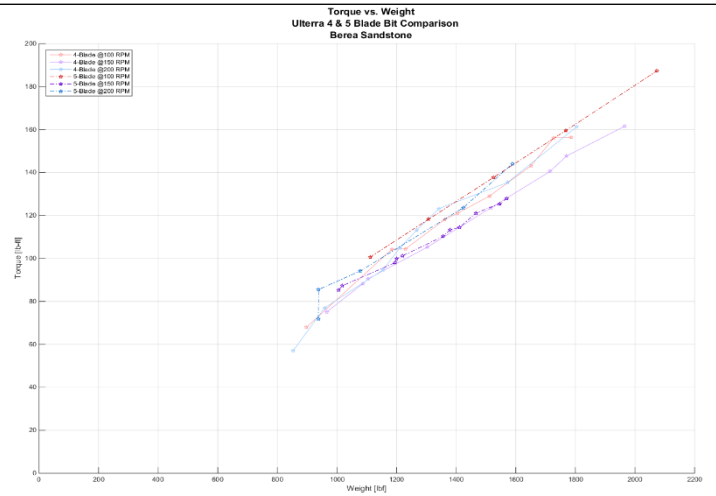

Figure I-46. Torque vs. WOB for 4 and 5 bladed bit tests in Berea Sandstone.

Four-Blade Bit (Sierra White Granite)

Table I-1. Four-blade bit results in Sierra White Granite at 100 rpm.

Data Pt. #	Penetration Interval [in]	R.O.P [ft/hr]	Depth of Cut [in/rev]	Weight on Bit [lbf]	Torque [ft×lb]	Rotary Speed [rpm]	Torsional Power [hp]
1	7.0- 7.8	9.9	.020	2300	166	102.	3.9
2	8.1 - 9.1	11.0	.022	2420	176	101.	4.1
3	10.2 - 11.4	14.7	.029	2660	197	102.	4.6
4	12.2 - 13.7	18.1	.036	2910	217	101.	4.9
5	14.5 - 16.4	22.6	.045	3180	241	101.	5.4
6	17.2 - 19.4	27.2	.054	3410	264	102.	5.8
7	19.9 - 22.5	31.1	.061	3660	285	102.	6.2
8	23.7 - 26.7	36.5	.072	3940	313	101.	6.7
9	28.0 - 31.3	39.4	.077	4170	342	103.	7.4

Table I-2. Four-blade bit results in Sierra White Granite at 150 rpm.

Data Pt. #	Penetration Interval [in]	R.O.P [ft/hr]	Depth of Cut [in/rev]	Weight on Bit [lbf]	Torque [ft×lb]	Rotary Speed [rpm]	Torsional Power [hp]
1	6.8 - 7.5	10.2	.013	2150	146	152.	5.3
2	7.7 - 8.5	11.9	.016	2300	158	151.	5.6
3	8.9 - 9.9	15.1	.020	2560	176	151.	6.1
4	10.3 -11.6	19.6	.026	2810	198	151.	6.8
5	12.3 – 14.0	25.6	.034	3060	223	151.	7.5
6	14.6 - 16.7	31.4	.041	3290	245	152.	8.1
7	17.1 - 19.6	37.7	.050	3540	267	152.	8.8
8	21.0 – 24.0	44.3	.058	3820	290	152.	9.5
9	25.6 – 29.0	50.8	.067	4070	312	152.	10.1

Table I-3. Four-blade bit results in Sierra White Granite at 200 rpm.

Data Pt. #	Penetration Interval [in]	R.O.P [ft/hr]	Depth of Cut [in/rev]	Weight on Bit [lbf]	Torque [ft×lb]	Rotary Speed [rpm]	Torsional Power [hp]
1	7.1 - 7.6	11.4	.011	2280	139	202.	6.8
2	8.0 - 8.6	12.5	.012	2380	146	202.	7.1
3	9.2 - 9.9	14.9	.015	2570	158	202.	7.5
4	10.4 - 11.3	18.2	.018	2810	174	202.	8.1
5	12.1 - 13.3	22.9	.023	3070	192	201.	8.8
6	14.4 - 15.8	27.7	.028	3310	209	202.	9.5
7	16.8 - 18.5	34.8	.035	3540	228	201.	10.2
8	21.6 - 23.8	43.0	.043	3820	250	201.	11.0
9	26.0 - 28.5	50.0	.050	4080	271	199.	11.7

Five-Blade Bit (Sierra White Granite)

Table I-4. Five-blade bit results in Sierra White Granite at 100 rpm.

Data Pt. #	Penetration Interval [in]	R.O.P [ft/hr]	Depth of Cut [in/rev]	Weight on Bit [lbf]	Torque [ft×lb]	Rotary Speed [rpm]	Torsional Power [hp]
1	7.1 - 7.8	10.5	.020	2250	177	106.	4.3
2	8.0 - 8.8	12.3	.023	2390	192	107.	4.6
3	9.1 - 10.2	15.9	.030	2620	205	106.	4.9
4	10.5 - 11.8	19.5	.037	2860	220	106.	5.2
5	12.7 - 14.4	25.9	.049	3100	248	107.	5.8
6	15.0 - 17.6	30.8	.058	3310	270	107.	6.3
7	17.7 - 20.1	35.9	.067	3560	297	107.	6.8
8	21.4 - 24.1	40.4	.075	3850	317	108.	7.3
9	25.2 - 28.2	44.6	.083	4100	337	108.	7.7

Table I-5. Five-blade bit results in Sierra White Granite at 150 rpm.

Data Pt. #	Penetration Interval [in]	R.O.P [ft/hr]	Depth of Cut [in/rev]	Weight on Bit [lbf]	Torque [ft×lb]	Rotary Speed [rpm]	Torsional Power [hp]
1	7.2 - 7.7	11.5	.015	2150	140	150.	5.1
2	8.0 - 8.7	13.4	.018	2320	151	150.	5.4
3	9.4 - 10.3	16.2	.022	2550	161	150.	5.7
4	10.6 - 11.7	21.6	.029	2790	183	150.	6.3
5	12.5 - 13.9	28.4	.038	3020	204	151.	6.9
6	14.7 - 16.4	34.3	.046	3260	226	151.	7.6
7	18.0 - 20.1	41.1	.054	3500	248	152.	8.3
8	21.6 - 24.1	48.9	.064	3790	276	152.	9.0
9	26.6 - 29.4	54.5	.071	4090	296	153.	9.7

Table I-6. Five-blade bit results in Sierra White Granite at 200 rpm.

Data Pt. #	Penetration Interval [in]	R.O.P [ft/hr]	Depth of Cut [in/rev]	Weight on Bit [lbf]	Torque [ft×lb]	Rotary Speed [rpm]	Torsional Power [hp]
1	6.8 - 7.6	11.3	.012	2080	119	196.	5.9
2	8.0 - 8.8	11.4	.012	2260	219	196.	6.2
3	9.2 - 10.2	14.6	.015	2510	137	196.	6.4
4	10.7 - 11.9	18.4	.019	2760	149	195.	6.9
5	12.3 - 13.9	24.7	.025	3020	170	194.	7.7
6	14.4 - 16.5	32.0	.033	3230	190	195.	8.4
7	17.6 - 20.3	41.4	.043	3470	214	195.	9.3
8	21.4 - 24.7	49.6	.051	3720	236	195.	10.2
9	25.8 - 29.7	58.8	.061	3960	262	193.	11.0

Four-Blade Bit (Berea Sandstone)

Table I-7. Four-blade bit results in Berea Sandstone at 100 rpm.

Data Pt. #	Penetration Interval [in]	R.O.P [ft/hr]	Depth of Cut [in/rev]	Weight on Bit [lbf]	Torque [ft×lb]	Rotary Speed [rpm]	Torsional Power [hp]
1	6.5 - 8.3	24.8	.051	900	68	97.	1.9
2	9.1 – 13.0	48.9	.100	1180	104	97.	2.6
3	13.9 - 18.9	53.4	.110	1230	105	97.	2.6
4	15.4 - 18.3	54.0	.111	1360	118	97.	2.9
5	19.0 - 21.7	62.0	.127	1510	129	98.	3.1
6	20.3 - 24.1	70.8	.146	1650	143	98.	3.3
7	22.8 - 25.5	81.3	.168	1730	156	98.	3.5
8	27.0 - 29.7	84.1	.174	1780	156	98.	3.5

Table I-8. Four-blade bit results in Berea Sandstone at 150 rpm.

Data Pt. #	Penetration Interval [in]	R.O.P [ft/hr]	Depth of Cut [in/rev]	Weight on Bit [lbf]	Torque [ft×lb]	Rotary Speed [rpm]	Torsional Power [hp]
1	7.2 - 9.9	40.8	.056	970	75	146.	3.2
2	9.8 - 10.8	61.9	.083	1090	88	146.	3.6
3	10.3 - 12.3	64.5	.087	1110	91	146.	3.7
4	13.6 – 16.0	71.7	.099	1300	105	146.	4.0
5	15.8 - 19.2	91.5	.123	1520	124	148.	4.6
6	16.8 - 20.4	102.9	.141	1720	141	149.	5.0
7	20.2 - 24.0	106.9	.146	1770	148	149.	5.2
8	21.1 - 24.5	127.7	.173	1960	162	149.	5.7

Table I-9. Four-blade bit results in Berea Sandstone at 200 rpm.

Data Pt. #	Penetration Interval [in]	R.O.P [ft/hr]	Depth of Cut [in/rev]	Weight on Bit [lbf]	Torque [ft×lb]	Rotary Speed [rpm]	Torsional Power [hp]
1	6.5- 7.2	30.5	.031	850	57	195.	3.8
2	7.8 - 9.7	59.5	.060	960	77	195.	4.3
3	8.9 - 10.9	84.8	.087	1150	95	196.	5.2
4	10.2 - 12.5	87.8	.090	1210	105	197.	5.6
5	12.4 - 14.7	96.5	.097	1270	113	198.	5.7
6	13.1 - 17.0	96.6	.098	1340	123	198.	6.1
7	16.6 - 19.8	120.9	.124	1570	135	198.	6.7
8	19.4 - 21.4	136.0	.138	1800	161	199.	7.5

Five-Blade Bit (Berea Sandstone)

Table I-10. Five-blade bit results in Berea Sandstone at 100 rpm.

Data Pt. #	Penetration Interval [in]	R.O.P [ft/hr]	Depth of Cut [in/rev]	Weight on Bit [lbf]	Torque [ft×lb]	Rotary Speed [rpm]	Torsional Power [hp]
1	7.5 – 10.0	53.3	.104	1110	101	102.	2.8
2	10.2 - 14.3	65.1	.127	1310	118	102.	3.1
3	15.1 - 20.3	82.5	.161	1530	138	103.	3.5
4	26.8 - 25.7	96.2	.189	1770	160	103.	3.9
5	31.0- 31.6	110.1	.217	2070	187	103.	4.4

Table I-11. Five-blade bit results in Berea Sandstone at 150 rpm.

Data Pt. #	Penetration Interval [in]	R.O.P [ft/hr]	Depth of Cut [in/rev]	Weight on Bit [lbf]	Torque [ft×lb]	Rotary Speed [rpm]	Torsional Power [hp]
1	7.3 - 9.7	63.7	.083	1010	85	152.	3.9
2	8.3 - 11.3	65.5	.085	1020	87	152.	4.0
3	11.0 - 12.6	80.0	.105	1200	99	152.	4.3
4	11.7 - 13.4	85.3	.112	1220	101	152.	4.3
5	13.1 - 16.3	95.9	.126	1360	110	153.	4.6
6	13.6 - 18.7	101.6	.133	1380	113	153.	4.6
7	17.0 – 20.0	103.5	.135	1410	115	153.	4.7
8	19.3 - 22.5	104.4	.138	1470	121	153.	4.9
9	20.2 - 22.8	117.9	.155	1550	125	154.	5.0
10	23.2 - 27.8	118.1	.155	1570	128	154.	5.0

Table I-12. Five-blade bit results in Berea Sandstone at 200 rpm.

Data Pt. #	Penetration Interval [in]	R.O.P [ft/hr]	Depth of Cut [in/rev]	Weight on Bit [lbf]	Torque [ft×lb]	Rotary Speed [rpm]	Torsional Power [hp]
1	6.8 - 7.5	53.7	.054	930	79	196.	4.6
2	7.7 - 9.4	70.4	.071	940	86	197.	4.9
3	10.4 - 13.3	88.6	.090	1080	94	198.	5.2
4	13.9 - 18.1	124.7	.127	1420	124	198.	6.3
5	19.8 - 22.3	148.1	.151	1590	144	198.	7.0

Bit-Comparison (Sierra White Granite & Berea Sandstone)

Table I-13. Detournay parameters and statistics for tests performed in Sierra White Granite and Berea Sandstone.

Bit Type	Rotational Speed [rpm]	SWG μγ [.]	BSS μγ [.]
Ulterra 4-Blade	100	0.84	0.74
Ulterra 4-Blade	150	0.79	0.84
Ulterra 4-Blade	200	0.73	0.87
Ulterra 5-Blade	100	0.97	0.94
Ulterra 5-Blade	150	0.74	0.98
Ulterra 5-Blade	200	0.66	1.00

Table I-14. Torque and RPM oscillations observed for tests in Sierra White Granite.

Bit Type	Rotational Speed [rpm]	Torque Range [lb-ft]	RPM Range [rpm]	Reference WOB [lbf]
4-Blade	100	134	29	3940
4-Blade	150	87	21	3820
4-Blade	200	51	8	3820
5-Blade	100	128	27	4100
5-Blade	150	101	16	4090
5-Blade	200	82	14	3960

Table I-15. Percent differences in ROP achieved between 4 & 5 bladed bits in Sierra White Granite.

Weight on Bit [lbf]	100 RPM [%]	150 RPM [%]	200 RPM [%]	Average [%]
2200	8.21	11.37	7.72	9.10
2350	13.23	10.20	-4.23	6.40
2580	9.83	7.03	0.93	5.93
2820	9.68	10.13	3.00	7.60
3080	17.31	11.21	8.68	12.40
3300	16.67	9.30	15.36	13.77
3550	18.63	9.38	17.76	15.26
3820	13.28	10.10	15.52	12.97
Average [%]	13.36	9.84	8.09	10.43

Table I-16. Percent differences in ROP achieved between 4 & 5 bladed bits in Berea Sandstone.

Weight on Bit [lbf]	100 RPM [%]	150 RPM [%]	200 RPM [%]	Average [%]
960	74.61	49.86	61.04	61.84
1080	19.85	13.11	20.89	17.95
1220	24.23	14.71	11.16	16.70
1380	36.76	26.69	21.05	28.17
1550	29.66	17.08	22.53	23.09

1550	-	23.05	-	23.05
1590	-	21.54	-	21.54
1720	-	9.00	-	9.00
Average [%]	38.86	21.88	28.53	29.76

APPENDIX J. SDOF DRILLSTRING SIMULATION

This page intentionally left blank.

Four-Blade Bit (Berea Sandstone)

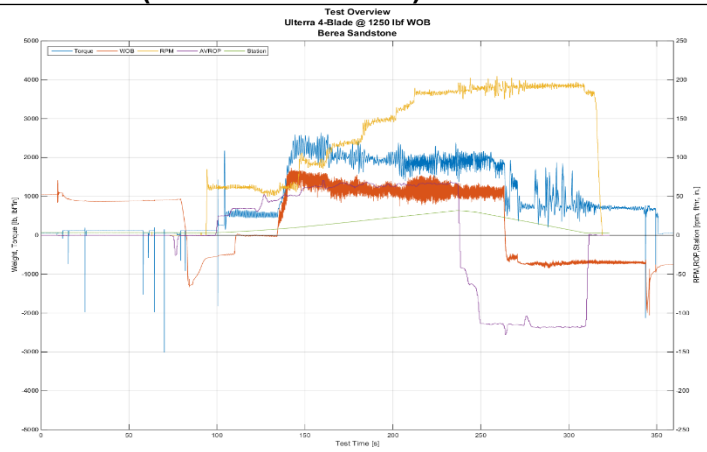

Figure J-1. Test overview for 4-blade bit in Berea Sandstone at 1250 [lbf] WOB and 60-180 [rpm] (Test2_081915_1571_2).

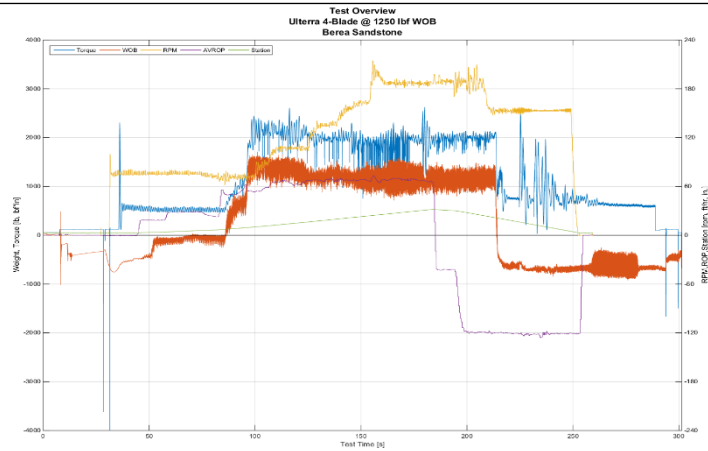

Figure J-2. Test overview for 4-blade bit in Berea Sandstone at 1250 [lbf] WOB and 70-190 [rpm] (Test3_081915_1528_2).

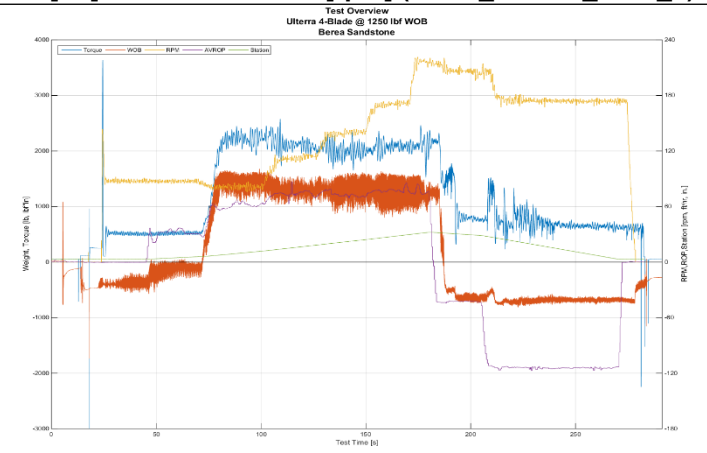

Figure J-3. Test overview for 4-blade bit in Berea Sandstone at 1250 [lbf] WOB and 80-200 [rpm] (Test4_081915_1537_2).

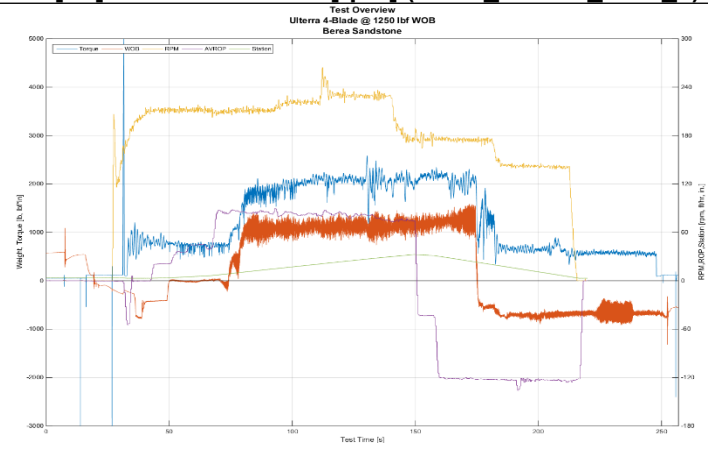

Figure J-4. Test overview for 4-blade bit in Berea Sandstone at 1250 [lbf] WOB and 210-230 [rpm] (Test5_081915_1553_2).

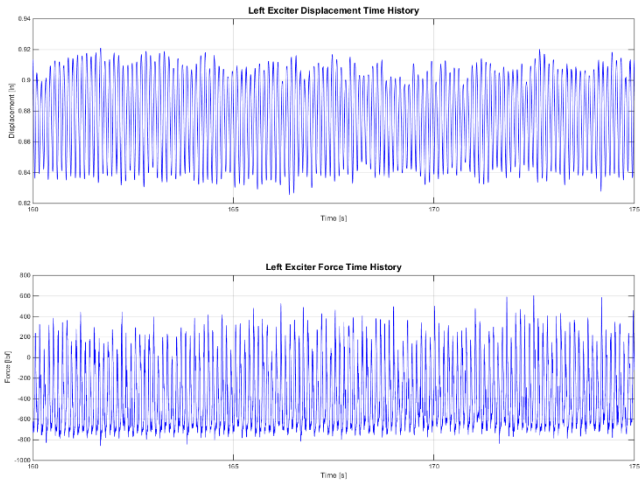

Figure J-5. Left exciter displacement and force time histories.

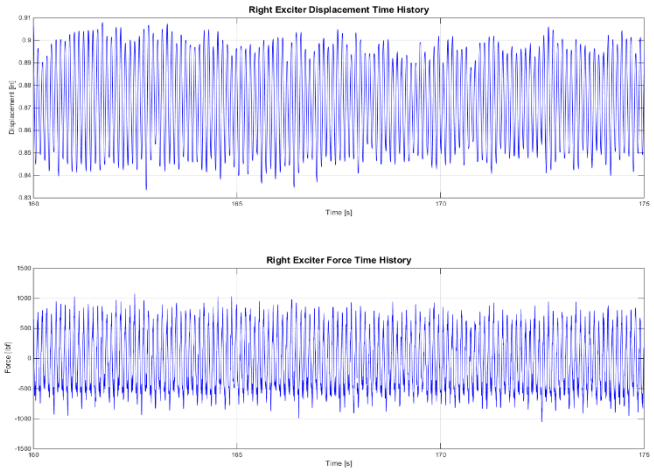

Figure J-6. Right exciter displacement and force time histories.

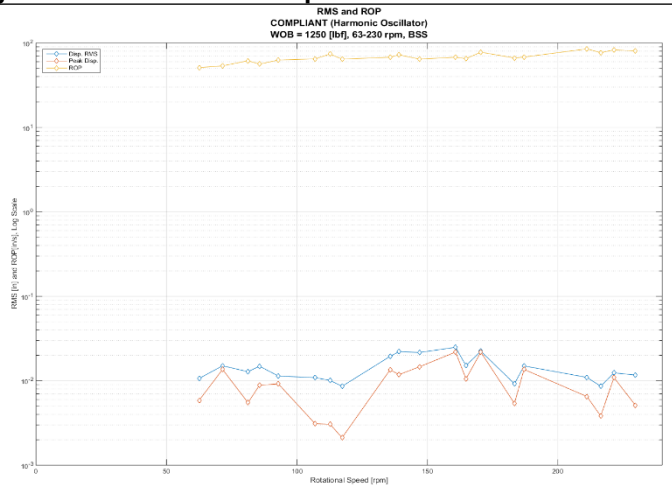

Figure J-7. Root mean square (RMS) and Rate of Penetration (ROP) vs. rotational speed semi-log plot.

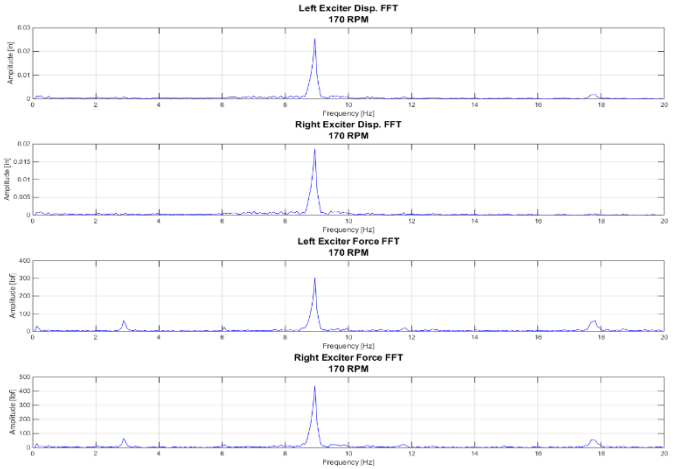

Figure J-8. Left and right exciter displacement and force FFTs.

Five-Blade Bit (Berea Sandstone)

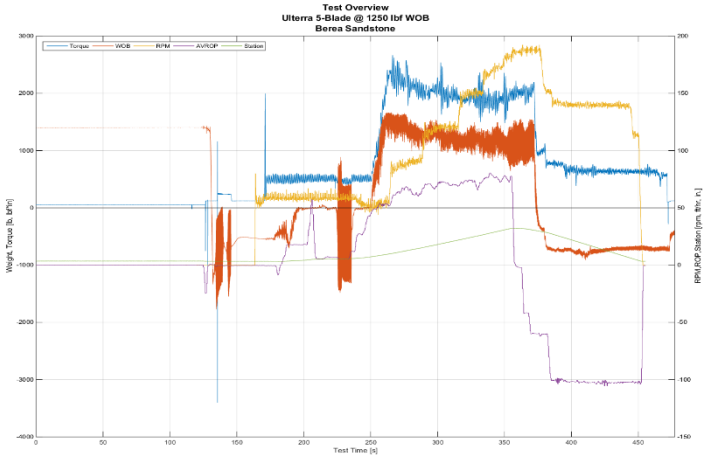

Figure J-9. Test overview for 5-blade bit in Berea Sandstone at 1250 [lbf] WOB and 60-180 [rpm] (Test4_081815_1448_2).

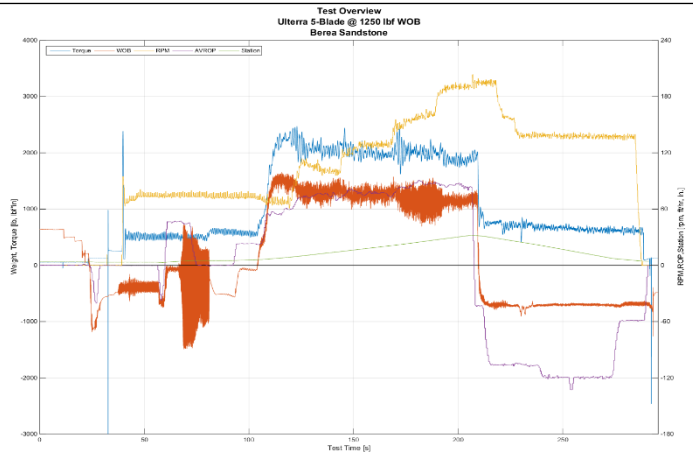

Figure J-10. Test overview for 5-blade bit in Berea Sandstone at 1250 [lbf] WOB and 70-190 [rpm] (Test5_081815_1518_2).

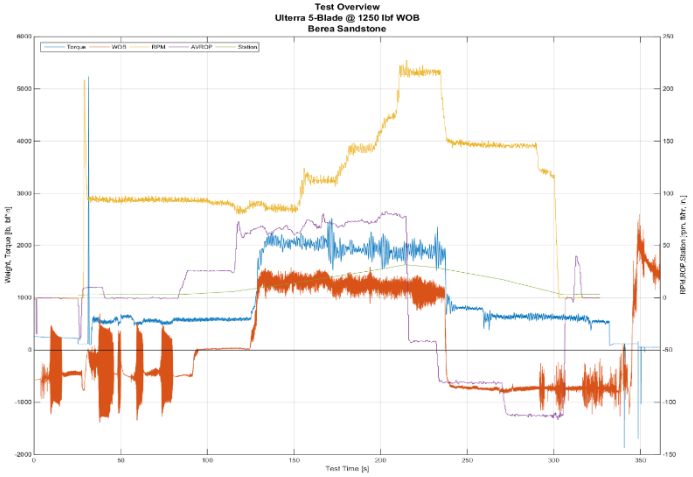

Figure J-11. Test overview for 5-blade bit in Berea Sandstone at 1250 [lbf] WOB and 80-200 [rpm] (Test5_081815_1533_2).

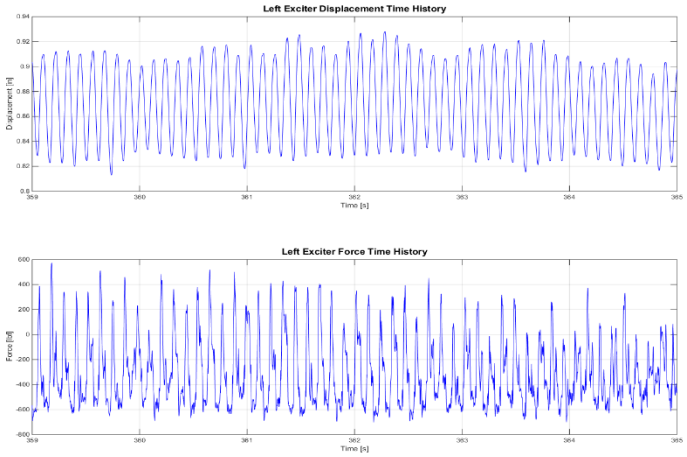

Figure J-12. Left exciter displacement and force time histories.

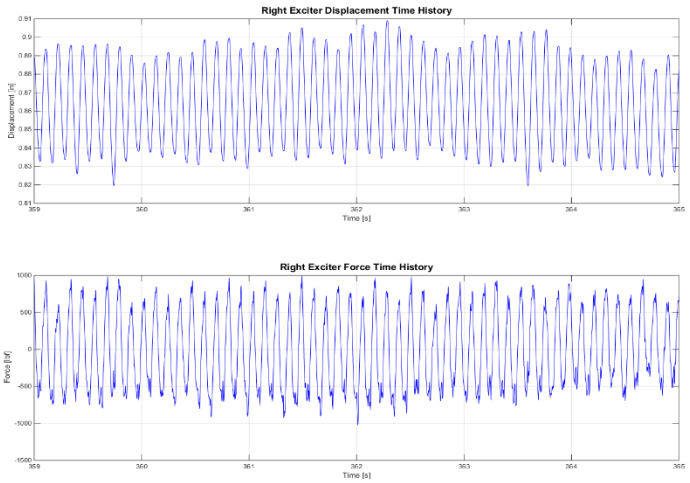

Figure J-13. Right exciter displacement and force time histories.

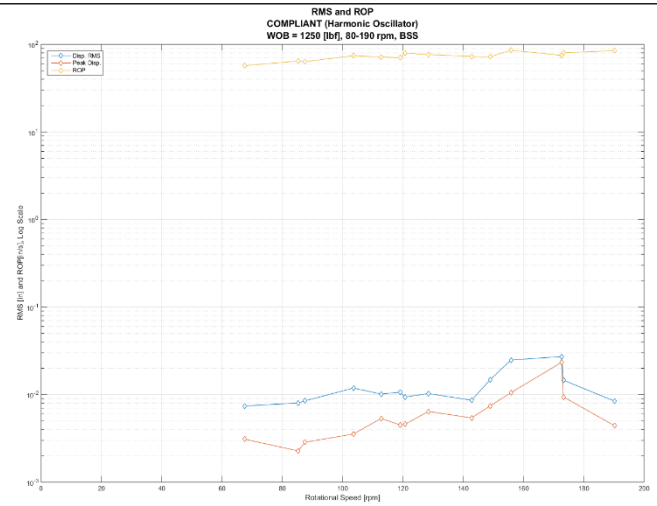

Figure J-14. Root mean square (RMS) and Rate of Penetration (ROP) vs. rotational speed semi-log plot.

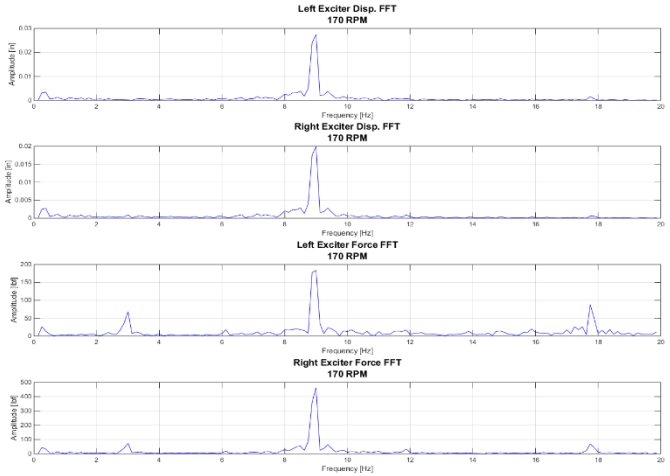

Figure J-15. Left and right exciter displacement and force FFTs.

APPENDIX K. HRDF COMPLIANT DRILLSTRING TESTING WITH VRSF INSTALLATION

This page intentionally left blank.

Five-Blade Bit (Berea Sandstone)

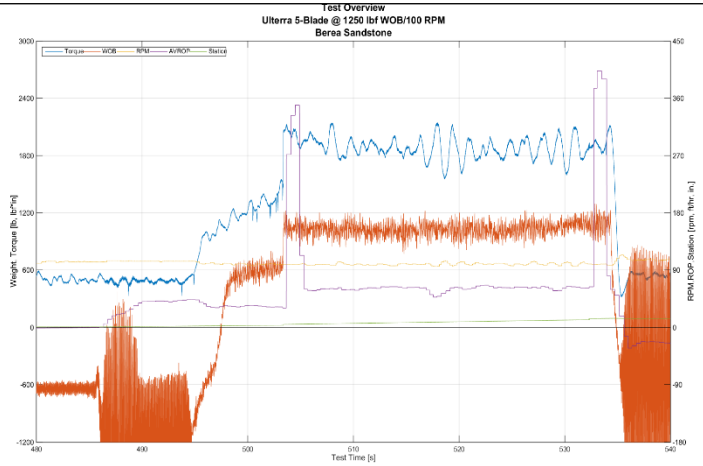

Figure K-1. Test overview for 5-blade bit in Berea Sandstone with rigid VRSF (VRS_load_test_10_091115_1622_2).

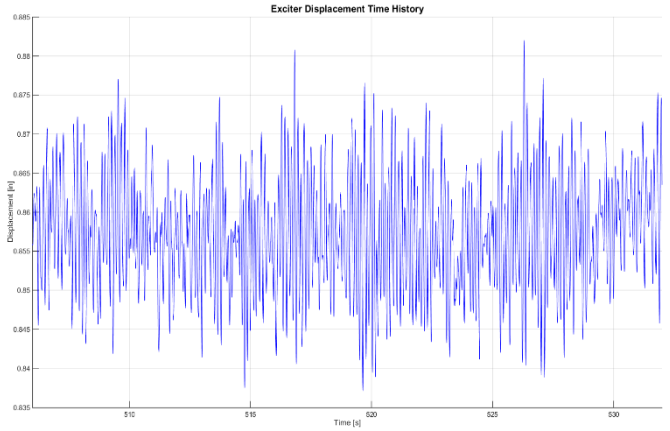

Figure K-2. Time history for averaged left and right exciter displacements with rigid VRSF.

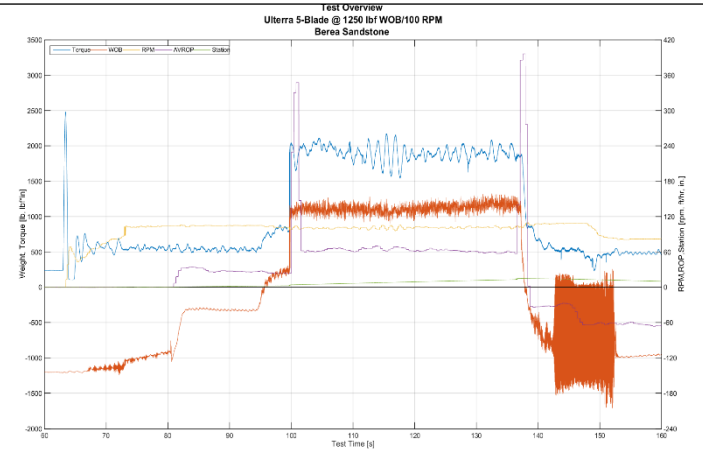

Figure K-3. Test overview for 5-blade bit in Berea Sandstone with VRSF module 4 active (VRS_load_test_11_091115_1758_2).

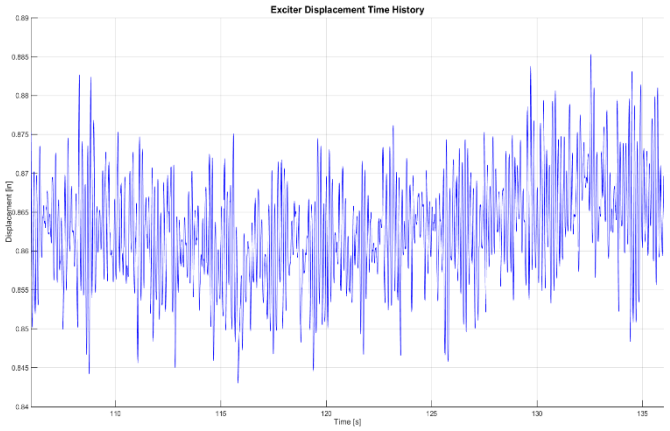

Figure K-4. Time history for averaged left and right exciter displacements with VRSF module 4 active.

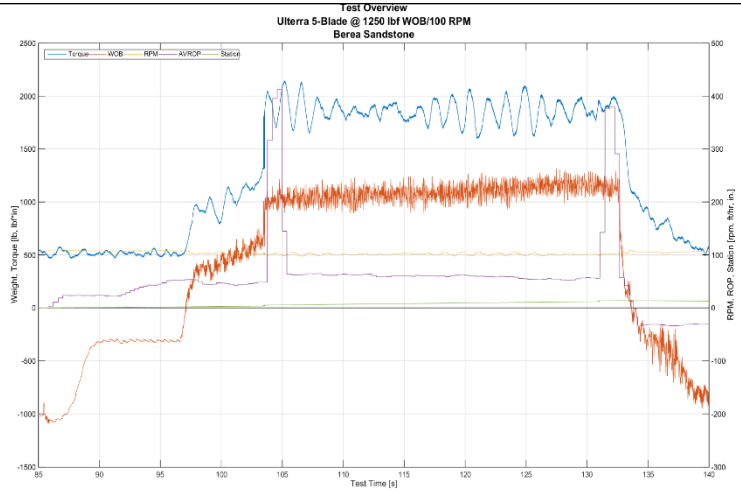

Figure K-5. Test overview for 5-blade bit in Berea Sandstone with VRSF module 3 active (VRS_load_test_12_091115_1815_2).

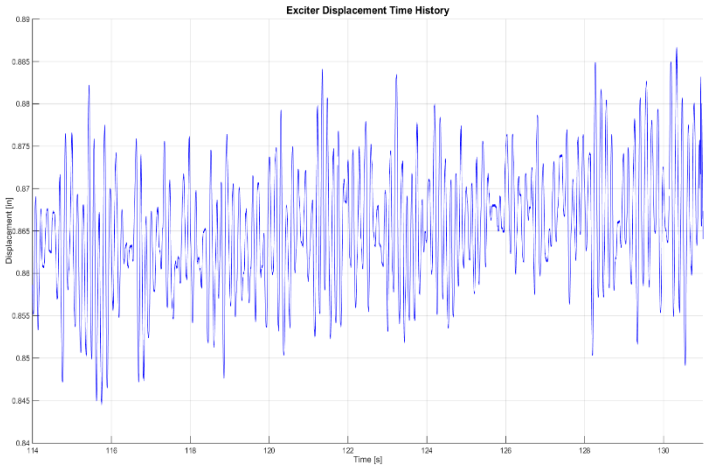

Figure K-6. Time history for averaged left and right exciter displacements with VRSF module 3 active.

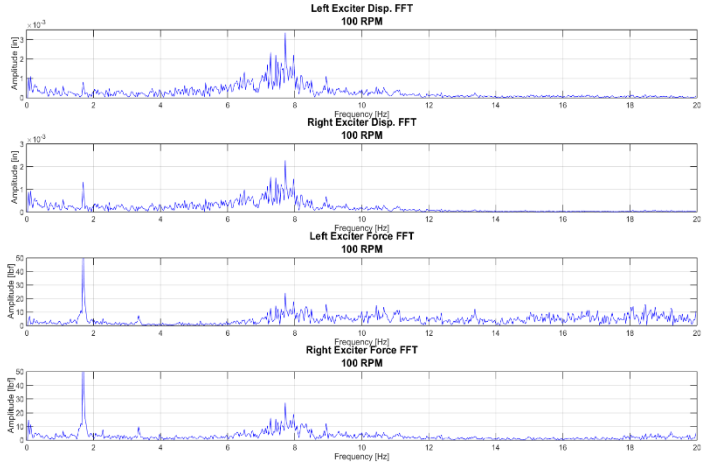

Figure K-7. Left and right exciter displacement and force FFTs with rigid VRSF.

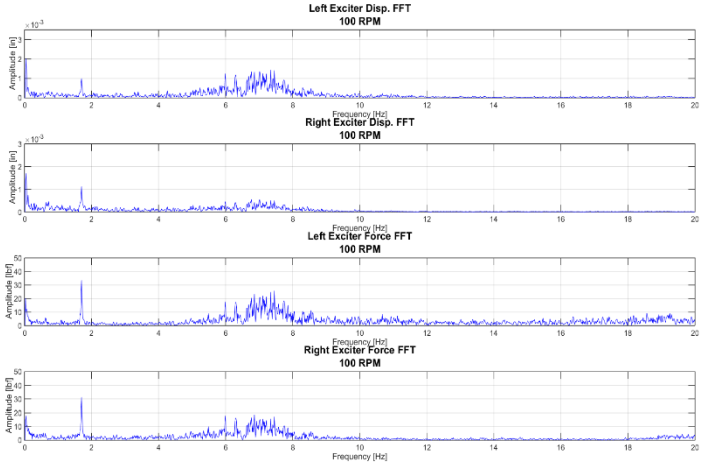

Figure K-8. Left and right exciter displacement and force FFTs with VRSF module 4 active.

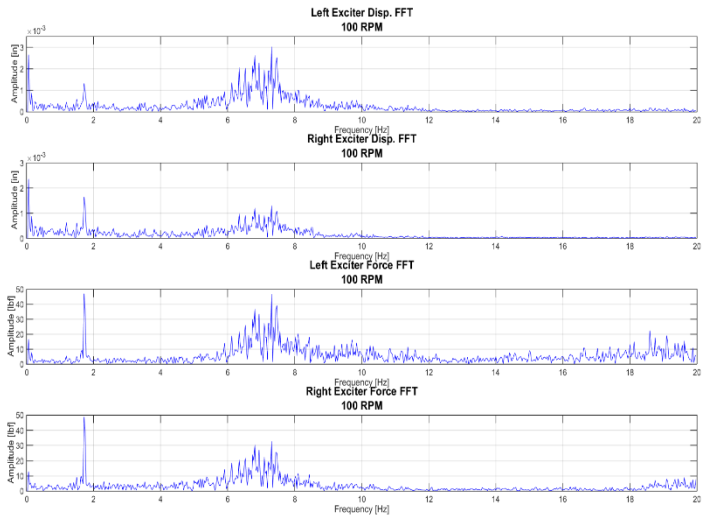

Figure K-9. Left and right exciter displacement and force FFTs with VRSF module 3 active.

RMS Values for Varying Spring States

Table K-1: RMS values corresponding to the averaged left and right exciter displacements.

VRSF Test No. (Description)	Displacement RMS [in.]	Axial Accelerometer RMS [ft/s^2]
10 (Rigid)	.0073	.2576
11 (Module 4 Active)	.0067	.2274
12 (Module 3 Active)	.0073	.2271

DISTRIBUTION

4 Lawrence Livermore National Laboratory
Attn: N. Dunipace (1)
P.O. Box 808, MS L-795
Livermore, CA 94551-0808

1	MS0346	Mikhail Mesh	01523
1	MS0701	Peter B. Davies	06900
1	MS0724	James M. Chavez	06000
1	MS0735	Erik K. Webb	06910
1	MS0754	Patrick V. Brady	06910
1	MS1010	Stephen Buerger	06533
1	MS1033	Douglas A. Blankenship	06916
1	MS1033	Avery Ted Cashion	06916
1	MS1033	Gregorz Cieslewski	06916
1	MS1033	John T. Finger	06916
1	MS1033	Adam Foris	06916
1	MS1033	Dennis K. King	06916
1	MS1033	Steven D. Knudsen	06916
1	MS1033	William T. Radigan	06916
10	MS1033	David W. Raymond	06916
1	MS1033	Jiann-Cherng Su	06916
1	MS1033	Elton K. Wright	06916
1	MS0899	Technical Library	9536 (electronic copy)

For LDRD reports, add:

1	MS0359	D. Chavez, LDRD Office	1911

For CRADA reports add:

1	MS0115	OFA/NFE Agreements	10012

For Patent Caution reports, add:

1	MS0161	Legal Technology Transfer Center	11500


Sandia National Laboratories